

Parametric Development of Cold Metal Transfer Wire Arc Additive Manufacturing

by

Conyers John Coupland

A thesis submitted to the Graduate Faculty of
Auburn University
in partial fulfillment of the
requirements for the Degree of
Master of Science

Auburn, Alabama
December 16, 2017

Keywords: additive manufacturing, wire arc additive manufacturing (WAAM),
cold metal transfer (CMT),

Copyright 2017 by Conyers John Coupland

Approved by

Lewis N. Payton, Associate Research Professor, Mechanical Engineering
Ruel A. (Tony) Overfelt, Professor, Materials Engineering
Robert Jackson, Professor, Mechanical Engineering

Abstract

Current commercial metal additive manufacturing techniques offer great accuracy and detail in small parts but are characterized by low deposition rates, high cost, and limited scale. This research seeks to develop, review, and establish new standards for the Wire Arc Additive Manufacturing (WAAM) technique utilizing a Fronius Cold Metal Transfer (CMT) welder. CMT is a new and proprietary Gas Metal Arc Welding (GMAW) process that provides increased process stability and control and while reducing excess heat input in deposition. WAAM uses an electric arc to melt and deposit metal alloys at much greater rates than other additive manufacturing techniques. This technology can be scaled to produce large parts, using a wide variety of filler metals, directly from 3D CAD drawings. This technology offers an alternative to low-volume casting or subtractive manufacturing, reducing the time to manufacture, reducing wasted material, and saving on tooling.

Wire Arc Additive Manufacturing (WAAM) as a process has been considered since 1925, with Cold Metal Transfer (CMT) based WAAM being the most technologically advanced iteration of this process. This study builds off a prior research at Auburn University on GMAW based WAAM using a 3-axis gantry CNC.

In the integration of the Fronius CMT welder, several new feedback control loops were added to increase process stability and deposition accuracy. Problems with varying contact tip to work distance are solved by the use of a probing loop.

To evaluate the capabilities of deposition, multiple geometries were printed. These include thin and thick-walled structures as well as complex geometries. These objects were

printed using three filler metals, a carbon steel (ER70S-6), an aluminum alloy (ER4043), and a stainless steel (ER308).

Optimal weld parameters were studied with respect to thick-walled and thin-walled deposition with the goal of finding the best practices for welding the different geometries. The surface roughness was evaluated by correlating it to the percent yield, calculated as the ratio of the net size after machining to material deposited.

The tensile strength was evaluated in multiple orientations for ER70S-6, ER308, and ER4043. The tensile strengths were determined to be at or above manufactures specifications and isotropic, or independent of direction, for carbon steel and aluminum. However, the tensile strength for ER308 stainless steel did not show isotropic results, with the transverse direction and longitudinal direction at 95 and 100% manufacturers spec, respectively.

The microstructure was examined for ER70S-6, ER308, and ER4043. Layer interfaces could be seen on the edges of ER308 and throughout the ER4043 sample. A uniform microstructure was observed throughout ER70S-6. Little to no porosity or void space was noticed throughout all the samples evaluated. A fine equiaxed grain structure was observed for all the materials.

Acknowledgments

Many people contributed to this project and deserve recognition for its success. I would like to thank my committee for their guidance. My advisor, Dr. Payton, deserves much recognition for allowing me the opportunity to attend Auburn University and to work in the Design and Manufacturing Laboratory. I would like to thank him for his assistance in this project and in the procurement of the new Fronius CMT unit. I would like to thank Dr. Overfelt for his guidance and technical expertise.

I am also grateful for my fellow researchers' assistance. Wesley Hunko's help in integrating the welder, controls development, and electrical knowhow was invaluable. The project would not have achieved such great results without help from Fronius representatives Jake Ross, Lucas Barron, and Kevin Barton who assisted me with setup, troubleshooting, and dialing in parameters. I would like to thank Jonathan Pegues of Auburn Universities FAME Lab for assisting me with tensile testing and microstructural evaluation.

Most importantly, I would like to thank my family and my fiancé, for their continued support and sacrifice over the past two years. I want to thank you for your unwavering support and interest in this project, it really did keep me going.

Table of Contents

Abstract.....	ii
Acknowledgments.....	iv
Table of Contents.....	v
List of Tables.....	ix
List of Figures.....	xii
I. Introduction.....	i
II. Literature Review.....	2
Metal Additive Manufacturing.....	2
Wire Arc Additive Manufacturing (WAAM).....	7
MIG Deposition Processes.....	8
WAAM using MIG Short-Circuit Transfer.....	13
WAAM Using Cold Metal Transfer GMAW.....	38
Parameterization of Cold Metal Transfer GMAW.....	73
Path Planning Strategies for WAAM.....	75
Evaluation Techniques for CMT WAAM.....	80
Summary of Research Opportunities.....	82
III. Scope and Objectives.....	85
IV. Design and Construction of Equipment.....	87
Previous Machine Design.....	87
CMT Weld System.....	90
Robot – Welder Integration.....	95

Instruments.....	101
Materials	107
ER308:	107
ER70S-6:.....	107
ER4043:	108
V. Methodology and Statistical Design of Experiments.....	109
Geometry Evaluation Methodology.....	109
Tensile Strength Evaluation Methodology	112
Mechanical Hardness Methodology	116
Microstructure Examination Methodology.....	117
Miscellaneous Methodology.....	118
Repeatability Study.....	119
Statistical Design of Experiments.....	127
Single-Bead Geometry Study	127
Thick-Bead Geometry Evaluation	128
Mechanical Properties.....	131
VI. Results.....	132
Standard Specimen Data Sheet	132
Closed Loop Process Control.....	134
ER70S-6 – Geometry Evaluation Results.....	136
Single-Bead Geometry Study	136
Thick-Bead Geometry Study	139
Short Wall Study.....	144

Two Wall Study	146
Cylinders and Boxes	151
Angled Deposition	157
X/Crossover Geometry	158
Bracket	161
ER308 – Geometry Evaluation Results	163
Single Bead Geometry Evaluation.....	163
Weave Geometry Evaluation	166
Short Wall Study.....	169
Two Wall Study	171
ER4043 – Geometry Evaluation Results	175
Single-Bead Geometry Study	175
Overhang Geometry Study	181
Thick-Bead Geometry Study	185
ER70S-6 – Mechanical Properties Evaluation Results.....	187
Temperature Study.....	187
ER308 – Mechanical Properties Evaluation Results	192
Temperature Study.....	192
Long Wall	196
ER4043 – Mechanical Properties Evaluation Results	201
ER70S-6 – Microstructure Evaluation Results	207
ER308 – Microstructure Evaluation Results.....	213
ER4043 – Microstructure Evaluation Results.....	218

Non-Planar Deposition Evaluation Results	221
VII. Discussion	222
CMT vs. GMAW Discussion.....	222
Closed Loop Process Controls Discussion	222
Geometry Discussion	223
Non-Planar Toolpath Discussion	224
Mechanical Properties Evaluation Discussion.....	225
Microstructure Examination Discussion.....	226
VIII. Conclusions and Recommendations for Future Work	227
Recommendations for Future Work.....	228
Omitted Objectives	229
References.....	230
Appendix I: Data Results	237
Appendix II: Data Sheets	245
Appendix III: Mach3 M-Codes.....	254
Appendix IV: Statistical Analysis.....	258
Appendix V: Weld Wire Data Sheets	271
Appendix VI: Wiring Diagram	276

List of Tables

Table 1. Interactions observed by Dickens, et al. [20].....	17
Table 2. Three bead models and the related bead height, bead width, and bead area (top) and the curve fitting of the mathematical models [40]	63
Table 3. Results of ISO-V toughness tests [3].....	70
Table 4. Results of tensile tests [3]	71
Table 5. Effect of changes in process variables on weld attributes [7].....	73
Table 6. Machine codes used to operate the welder.	97
Table 7. ER308/308L filler material properties.....	107
Table 8. ER70S-6 filler material properties.....	108
Table 9. ER4043 filler material properties.	108
Table 10. Average and standard deviation of yield stress, ultimate tensile strength, modulus of elasticity and hardness for repeatability study.....	121
Table 11. P-values for combinations of Walls 1 & 2 two sample t-tests.....	123
Table 12. P-values for transverse vs. longitudinal walls two sample t-tests.....	124
Table 13. P-values for combinations of Walls 3 & 4 two sample t-tests.....	124
Table 14. Rockwell hardness values from repeatability study.	125
Table 15. P-values for combinations of hardness two sample t-tests.	126
Table 16. Preliminary geometry study factors and levels.....	128
Table 17. Steel weave geometry study factors and levels.	129
Table 18. Steel “short wall” study factors and levels.	129
Table 19. Aluminum geometry study factors and levels.	130
Table 20. Overhang geometry study factors and levels.....	130

Table 21. Interpass cooling time study factors and levels.	131
Table 22. Weave geometry test 1 results.	140
Table 23. Weave geometry test 2 results.	142
Table 24. Weave geometry test 3 results.	143
Table 25. Short wall study measured results.	146
Table 26. Two wall study geometry results.	147
Table 27. Two wall study parameters.	147
Table 28. Two wall study results – mechanical properties.....	149
Table 29. Welding parameters used in the thick-walled box geometry study.....	154
Table 30. Weld parameters used in the bracket print.....	162
Table 31. Stainless, single-bead, CMT+Pulsed pyramid cylinder welding parameters.	164
Table 32. Stainless, single-bead, CMT pyramid cylinder welding parameters.	164
Table 33. Welding parameters for the weave geometry study.....	167
Table 34. Stainless steel weave geometry study 1 parameters.	167
Table 35. Stainless steel weave geometry study 2 parameters.	168
Table 36. Stainless short wall study results.	170
Table 37. Geometry factors used in stainless steel short wall study.....	170
Table 38. Stainless two wall study parameters.	171
Table 39. Stainless two wall study geometry results.	172
Table 40. Stainless two wall study mechanical properties results.	173
Table 41. Welding parameters used for initial single-bead aluminum prints.	175
Table 42. Aluminum OvAl welding parameters.....	178
Table 43. Welding parameters used in the overhang study.	182
Table 44. ER70S-6 temperature study welding parameters.....	187
Table 45. As-printed data for walls produced in the temperature study.	187

Table 46. ER70S-6 temperature study summary of mechanical property results.....	188
Table 47. Temperature study transverse wall as-printed data.....	190
Table 48. ER70S-6 temperature study mechanical property results for longitudinal and transverse specimen.	190
Table 49. Welding parameters used for ER308 Temperature Study.	192
Table 50. ER308 temperature study as-printed results.	192
Table 51. Stainless temperature study tensile properties results.....	193
Table 52. As-printed results for stainless long wall.....	196
Table 53. ER308 long wall tensile results grouped by orientation.	197
Table 54. Stainless steel long wall transverse data with respect to location.....	200
Table 55. Stainless steel long wall longitudinal data with respect to location.	200
Table 56. Aluminum big box 1 welding parameters.....	201
Table 57. Aluminum big box 2 welding parameters.....	203
Table 58. Aluminum big box 2 measured results.	204
Table 59. Aluminum tensile test results.....	205
Table 60. Summary of the particle size analysis.....	214
Table 61. Summary of particle size analysis ER308 long wall (top).....	215
Table 62. CMT-WAAM weld schedule.....	224
Table 63. Mechanical property results for all three materials in each orientation.....	225

List of Figures

Figure 1. Typical powder bed system setup [2].....	3
Figure 2. Typical powder fed system [2].....	5
Figure 3. Typical wire feed system setup [2].....	6
Figure 4. GMAW Process [1].....	7
Figure 5. Scheme of a modern inverter-based GMAW power source [10].....	9
Figure 6. MIG Short-circuit transfer [1].....	10
Figure 7. MIG globular transfer [1].....	10
Figure 8. MIG spray arc transfer [1].....	11
Figure 9. The Cold Metal Transfer process [1].....	12
Figure 10. Graph of current and voltage for different welding processes [10].....	13
Figure 11. Baker's patent [11].....	14
Figure 12. Box produced by Dickens, et al. using MIG process [20].....	16
Figure 13. Hollow pyramid produced by Dickens, et al. using MIG process [20].....	17
Figure 14. Geometries studied by Spencer et al [21].....	19
Figure 15. Voids and porosity in adjacent beads as shown in dye penetrant testing by Spencer et al. [21].....	20
Figure 16. First successful integration of CAD and welder controls [23,24].....	21
Figure 17. Procedure for depositing adjacent layers by Spencer et al. [21].....	21
Figure 18. Complex geometry produced by Ribeiro, et al. [26,27].....	22
Figure 19. Relationship between layer width and travel speed by Ribeiro et al. [22].....	23
Figure 20. Part with the same layer start point (left) and varied start point (right) [30]...	26
Figure 21. Wall without start and end control (top) and with control (bottom) [30].....	27

Figure 22. Integrated welding and milling machine created by Song et al. [31]	27
Figure 23: Thin-walled part before and after machining by Song et al. [31,32]	28
Figure 24. Microstructure observed by Song et al. [32]	28
Figure 25. Solid part before and after machining by Song, et al. [33].....	29
Figure 26. Building strategies for solid layers [33]	30
Figure 27. Sprocket made via the low-cost open-source MIG printer by Anzalone [35].	32
Figure 28. WAAM machine produced at Auburn University [4].....	33
Figure 29. Outward and inward facing geometry test (left) and bridging test (right) [4].	34
Figure 30. Stainless steel nozzle as-printed and post-machining [4].....	35
Figure 31. Wire diameter study voltage results (left) and current (right) [4]	35
Figure 32. Tensile test results ER70S-6 steel (left), ER308 stainless steel (right) [4]	36
Figure 33. Voids found between Layers in Steel (ER70S-6) Parts [4].....	37
Figure 34. Microstructure of steel (ER70S-6) sample before heat treatment (left) and after heat treatment (right) [4].....	37
Figure 35. High-speed photography images a CMT cycle [7].....	38
Figure 36. Manual GTAW and automated CMT-GMAW sample profiles [7]	41
Figure 37. Optical macrographs of CMT welds showing the effect of different shielding gases mixtures a) He (30%), b) He (50%) and c) He (70%), balance argon [8].....	43
Figure 38. Predicted first order 3D response surface model for the effective wall width as a function of the wire diameter and the WFS, for constant WFS/TS ratio of 20 [8]..	44
Figure 39. Hybrid layer manufacturing (HLM) machine [36].....	45
Figure 40. Parabolic cross-sectional profile of the bead [36]	47
Figure 41. Geometry of the overlapping parabolic beads and the fillet [36].....	48
Figure 42. Comparison of the actual profile with the profile predicted by the model in two different welds [36].....	49
Figure 43. Distortion verification along the longitudinal direction [37]	50
Figure 44. Longitudinal stress along the normal direction [37].....	51

Figure 45. Temperature and stress field around a welding heat source [5]	52
Figure 46. Macrograph of WAAM sample showing EWW and Wav [5]	54
Figure 47. EWW, Waviness, and ALH as functions of TS and WFS [5].....	55
Figure 48. Heat input distribution plot [5]	56
Figure 49. Temperature distribution of trials with 5 second inter-pass cooling (left) and the residual temperature of the midpoint after each layer (right) [5].....	57
Figure 50. Clamping fixture with water cooled backing plate used by Almeida [19].....	58
Figure 51. Macrograph of single-bead with measurable factors shown and defined [19]	59
Figure 52. CMT WAAM “turbine blade” [39]	61
Figure 53. Tangent overlapping model (TOM) [40].....	64
Figure 54. Diagrams of the TOM for cases of $d > d^*$ (left) and $d < d^*$ (right) [40].....	64
Figure 55. Multilayer deposition at $d = 0.667w$ (top) and $d = 0.738w$ (bottom) [40]	65
Figure 56. Macrostructure of Inconel 625 wall [1].....	66
Figure 57. Location of specimens for microstructural investigation [3]	67
Figure 58. Microstructure investigation on “black areas” (Pos. 2) [3].	69
Figure 59. Etched macroscopic cross sections (top) and microstructure in light optical investigation (bottom). a) Pos. 1, b) Pos. 2, c) Pos. 3 d) Pos. 4 [3]	69
Figure 60. Location of Charpy and tensile test specimens (left) and position of notch in relation to the microstructure (right) [3]	70
Figure 61. Range of produced orientations achievable by the CMT process [41]	72
Figure 62. Travel speed and the effect on weld quality at a constant WFS/TS ratio [6] ..	75
Figure 63. Walls showing the changing bead geometry at the start and end of weld [44]	76
Figure 64. Comparison of layers produced by the proposed MAT path patterns (a & c) and the traditional contour path patterns (b & d) [45]	78
Figure 65. Direct crossing (top) and opposite angle method (bottom) [46].	79
Figure 66. Build orientation nomenclature [50]	81
Figure 67. Orientation of tensile specimens [50].....	81

Figure 68. Gantry CNC machine used as base for WAAM research [4].....	88
Figure 69: Build plate design [4]	89
Figure 70: Mach3 CNC software interface.....	90
Figure 71. Fronius weld system [52]	91
Figure 72. Fronius CMT Advanced 4000 MV R Power Source [52].....	91
Figure 73: Fronius VR 7000 CMT Wire Feeder [52].....	92
Figure 74: Fronius Robacta 5000 Drive/Torch [52]	93
Figure 75: Fronius Wire Buffer [52].....	94
Figure 76. Sealevel RS-485 Modbus RTU (left) and I/O terminals (right).....	96
Figure 77. Fronius welder interface.....	100
Figure 78. Cincinnati Arrow VMC-750 CNC Mill	102
Figure 79. Bridgeport Series I 2 HP Vertical Milling Machine.....	102
Figure 80. Do-All 2013-V Vertical Band Saw (left) and the Wellsaw 1118 Horizontal Band Saw (right)	103
Figure 81. Model HR-150 Rockwell Hardness Tester.....	104
Figure 82. MTS Q-Test 100.....	104
Figure 83. MTS Landmark Servohydraulic load frame.....	105
Figure 84. Keyence VHX 1000 E 3D microscope.....	106
Figure 85. Geometries proposed for thick deposition.....	111
Figure 86. ASTM E8 Subsize Specimen dimensions	113
Figure 87. Longitudinal (left) and Transverse tensile specimens (right).....	120
Figure 88. Engineering stress – strain curve for repeatability study walls 1-4.....	121
Figure 89. Standard data sheet for tensile specimen.....	133
Figure 90. Side view of a single weld bead, showing direction of travel.	137
Figure 91. Single-bead wall, ER70S-6.	137
Figure 92. Profile measurement, ER70S-6 single-bead wall.....	138

Figure 93. ER70S-6 single-bead cylinders made with the spiral method (right) and layer-by-layer method (left)	139
Figure 94. ER70S-6 weave geometry study results (bottom) and weld paths (top).	140
Figure 95. Weave geometry study 3, from left to right, square 1, zig zag 1, concave 1, square 2, zig zag 2, concave 2.....	143
Figure 96. Geometries and dimensions (mm) used in the short wall study, from left to right: zig zag, modified square, and concave.	144
Figure 97. Short wall samples before and after machining, from top to bottom: zig zag, square, and concave. Black circles highlight porosity.....	145
Figure 98. Two wall study 1.75 mm wall (close) and 1.25 mm wall (far)	148
Figure 99. Engineering stress – strain curves for two wall study.	150
Figure 100. Thick walled box corner test results and paths.....	151
Figure 101. Current (top) and voltage (bottom) of corner test.	152
Figure 102. Thick walled cylinder geometry evaluation results and paths.....	153
Figure 103. Thick-walled cylinder and box.....	155
Figure 104. 3D scan of the as-printed surface of the thick-walled box.	156
Figure 105. From left to right, 15, 30, and 45-degree attempted walls.	157
Figure 106. The first crossover print attempt, X1. Arrows denote path direction.....	158
Figure 107. X1 corner detailed view.....	159
Figure 108. The third attempt, X3.	160
Figure 109. The second attempt, X2.....	160
Figure 110. X3 corner, detailed view.....	161
Figure 111. Bracket geometry toolpath and as-printed.....	162
Figure 112. Stainless, single-bead, pyramid cylinder geometry: path generation.	163
Figure 113. Stainless, single-bead, pyramid cylinders: CMT+Pulsed (left), and standard CMT (right).....	165
Figure 114. Voltage (dotted lines) and current (solid lines) vs. layer for CMT (black) and CMT+Pulsed (grey) in the deposition of the single-bead pyramid cylinders.	166

Figure 115. Stainless Steel Weave Geometry Test 2. From left to right, zig zag-1.25 1 & 2, convex 1 & 2, and zig zag-1.75 1 & 2.	169
Figure 116. Stainless steel two wall study, zig zag 1.25-mm wall (top) and zig zag 1.75 - mm wall (bottom)	172
Figure 117. Stainless two wall study – engineering stress strain curves.	173
Figure 118. Dogbones of ER70S-6 (left) vs. ER308 (right).	175
Figure 119. Aluminum single-bead cylinder.	176
Figure 120. Excess heat effect on aluminum wall.	177
Figure 121. Aluminum OvAl 2.	179
Figure 122. Aluminum OvAl 1	179
Figure 123. Aluminum OvAl 3.	180
Figure 124. As welded macrostructure of the side of oval 1.	181
Figure 125. Aluminum single-bead 15-degree overhang.	182
Figure 126. Aluminum single-bead 30-degree overhang.	183
Figure 127. Welding current and voltage of the last 200 seconds of welding for aluminum overhang 15 and 30-degree shapes.	184
Figure 128. Aluminum thick-bead geometry evaluation, from right to left: square, zig zag, ladder, sine, concave, and parallel bead.....	185
Figure 129. Aluminum flat spiral 1.....	186
Figure 130. Aluminum flat spiral 2.....	186
Figure 131. ER70S-6, the effect of pause duration on Ultimate Tensile Strength.	189
Figure 132. ER70S-6 transverse and longitudinal engineering stress strain curves.	191
Figure 133. Ultimate tensile strength, yield stress, and modulus of elasticity vs. pause duration for ER308.	194
Figure 134. Temperature at the end of welding vs. layer number for the walls printed in the temperature study.....	195
Figure 135. ER308 long wall showing minor residual stress bending.	196
Figure 136. ER308 long wall showing the location of the tensile specimen.....	197

Figure 137. Ultimate tensile strength, yield stress, and toughness for wall P90, and long wall transverse and longitudinal. Lines denote manufacturers spec.....	198
Figure 138. Long wall transverse vs. longitudinal engineering stress-strain curves.	199
Figure 139. Start point gap bridge, big box 1.	202
Figure 140. Aluminum big box 1.....	202
Figure 141. Aluminum big box 2. Arrows indicate start points.	203
Figure 142. Tensile specimen as-machined and a table of the measured sizes. Note that the specimens shown are transverse specimens 1, 2, and 3 and are incorrectly labeled.	204
Figure 143. ER4043 engineering stress-strain curve, dashed lines are transverse orientation.	206
Figure 144. Grain structure of Temperature Study Wall P90.....	207
Figure 145. Layer interface from side of wall P90 (right images) and repeatability study wall 1 (left) and the locations of the samples on the original wall.	208
Figure 146. Microstructure of repeatability study 1 wall at top edge (top), and at the bottom of the wall, in from the edge (bottom).....	209
Figure 147. Microstructure of temperature study wall P30 at top edge (top), and just below the top edge (bottom).....	210
Figure 148. Repeatability Study Wall 1, composite micrograph from the top down, showing the multiple microstructures present.	211
Figure 149. A 37 μ m void seen on sample taken from wall P180.....	212
Figure 150. ER308 microstructure observed at the bottom of the long wall.....	213
Figure 151. ER308 microstructure shown in Figure 149 processed with ImageJ, cropped (left), threshold applied (center), and particle size measurement (right).	214
Figure 152. Schaeffler diagram of 1948, with linear boundaries [55].....	215
Figure 153. ER308 microstructure observed at the top of the long wall.	216
Figure 154. ER308 layer interface observed at the side of the long wall.	217
Figure 155. ER4043 layer boundary, on the side, at the top.....	218
Figure 156. ER4043 samples mounted and polished.....	218
Figure 157. ER4043 stitched image of two layer boundaries 2.674 mm apart.....	219

Figure 158. ER4043 side profile layer boundary, bottom. Radius =1.946 mm.....	219
Figure 159. ER4043 top bead, viewing down toward the baseplate.....	220
Figure 160. Non-planar toolpath examination results.....	221

I. Introduction

Additive manufacturing of metals can be performed by using a wire feedstock and a welder to deposit material layer-by-layer and is known as wire arc additive manufacturing (WAAM). WAAM uses an electric arc to melt and deposit metal alloys at much greater rates than other additive manufacturing techniques and can be scaled to produce large parts out of a wide variety of filler metals. A Fronius Cold Metal Transfer (CMT) welder, a new and proprietary gas metal arc welding (GMAW) welding process, is well suited for utilization in WAAM. The CMT process provides increased process stability and control and while reducing excess heat input in deposition.

A Fronius CMT welder system was integrated into an existing 3-axis gantry-style CNC based WAAM platform for evaluation. New machine code was developed to integrate the welder and expand the functionality. New feedback controls were added to solve issues experienced in the previous system.

Three materials were evaluated, a carbon steel (ER70S-6), an aluminum alloy (ER4043), and a stainless steel (ER308). An evaluation of ideal deposition parameters and the ability to produce different geometries followed. Mechanical properties were evaluated for the three materials with respect to layer orientation. Microstructural analysis and the evaluation of the layer interface was observed and documented.

II. Literature Review

This literature review will first give a general background of the state of current metal additive manufacturing technologies. Wire arc additive manufacturing processes will be discussed, first giving background on the different metal transfer welding processes. Prior work in gas metal arc welding based additive manufacturing will be covered prior to focusing on the work of researchers using cold metal transfer.

Metal Additive Manufacturing

Additive Manufacturing (AM) is a process where parts are created from 3D CAD data by adding material layers upon layers. AM is also known as Additive Layer Manufacturing (ALM), Rapid Prototyping (RP), Direct Material Deposition (DMD), Free Form Fabrication (FFF), and Hybrid Layer Manufacturing (HLM). The first step is slicing the 3D geometric model into 2D layers, creating a 2D cross section profile of the part in successive layers. Each layer is built one layer at a time. This technique started in the late 80's and over the past few decades, the development and application of AM has been significantly increasing [1].

Additive manufacturing comes with significant advantages including, reduced material waste, the ability to build near net-shape parts with highly complex geometries directly from 3D CAD models without tooling, good mechanical properties compared with castings, and reduced lead times in manufacturing processes. The AM process has disadvantages including, slow manufacture speed compared to traditional methods,

difficult and expensive control systems, and degraded surface quality thus requiring a finishing process [1].

Metal additive manufacturing systems can be generalized into two broad categories: powder feed systems and wire feed systems [2, 1]. Each system comes with its own drawbacks and advantages that must be identified and evaluated for each end user's needs.

The powder based process is capable of fabricating parts with small size and high geometrical accuracy [1]. For powder based materials there are two feed system possibilities, powder feed system and powder bed system [2]. Figure 1 shows, a typical powder bed system which deposits the powder by raking it across the work area. The energy source (electron beam or laser beam) is programmed to deliver energy to the surface of the bed melting or sintering the powder into the desired shape. Additional powder is raked across the work area, and the process is repeated to create a solid three-dimensional component.

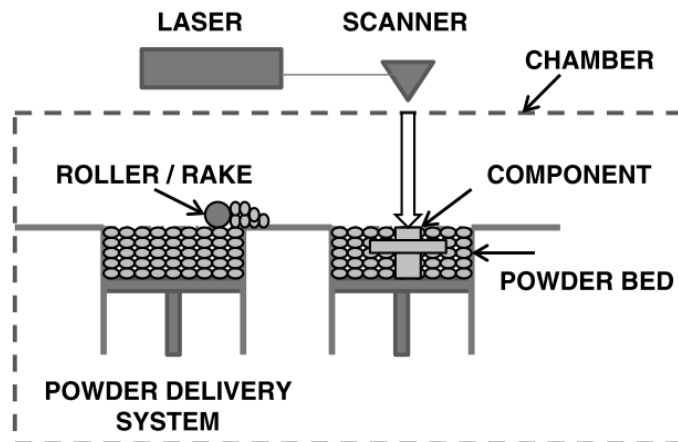


Figure 1. Typical powder bed system setup [2]

The advantages of this system include its ability to produce high resolution features, internal passages, and maintain accurate dimensional control [2]. Powder bed systems are not without their drawbacks. They are costly to purchase and operate and potentially expose

operators to a hazardous powder environment [1]. Additionally, since the entire machine is filled with material, powder bed systems often waste a large amount of un-sintered powder. Even if the excess powder is reclaimed, there is still a portion that is partially sintered that cannot be reused. Powder bed systems have low material deposition rates due to the repeated process of dispersing powder over the bed. Each layer is typically 30 – 60 μm or less.

Powder feed systems, like the one shown in Figure 2 work on a similar concept to powder bed systems. The build volumes of these systems are generally larger (e.g., $>1.2 \text{ m}^3$ for the Optomec LENS 850-R unit). The powder feed systems lend themselves more readily to build volume scale up than do the powder bed units. In these systems, powder is conveyed through a nozzle onto the build surface. A laser is used to melt the powder into the shape desired. This process is repeated to create a solid three-dimensional component. There are two dominate types of systems in the market. In the first, the work piece remains stationary, and deposition head moves. In the second type, the deposition head remains stationary, and the work piece is moved. The advantages of this type of system include its larger build volume and its ability to be used to refurbish worn or damaged components” [2]. Powder fed systems still have relatively low deposition rates and are incapable of producing internal passages and features.

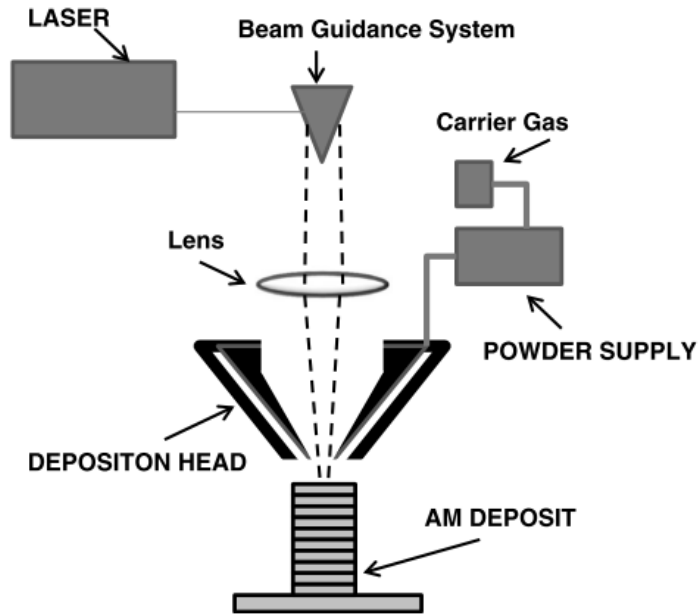


Figure 2. Typical powder fed system [2]

Wire feed systems, like the schematic shown in Figure 3, use wire feed stock to deposit material and build layers. “The energy source for these units can include electron beam, laser beam, and plasma arc. Initially, a single bead of material is deposited and upon subsequent passes is built upon to develop a three-dimensional structure. In general, wire feed systems are well suited for high deposition rate processing and have large build volumes; however, the fabricated product usually requires more extensive machining than the powder bed or powder fed systems do” [2]. Compared to powder based systems, it is important to note that wire fed system processes offer higher material usage efficiency, higher deposition rate, energy efficiency, safe operation and lower cost [1]. “For bigger 3D shaped components like wings, turbine plates and valves, economic considerations are more dominant and it is necessary to reduce the additive manufactured component costs by, e.g., replacement of the more expensive powder by a less expensive wire and the reduction of the manufacturing equipment costs by use of a cheaper heat source” [3]. Wire

fed machines are ideal for near net shape manufacturing of large structural objects with low material waste which greatly reduces the amount of subtractive machining post processing. “Wire feed systems do not require complex powder distribution hardware and are easily integrated to a gantry style CNC machine” [4]. Figure 3 shows an illustration of a wire feed system using an electron beam energy source and an external wire feeder being used.

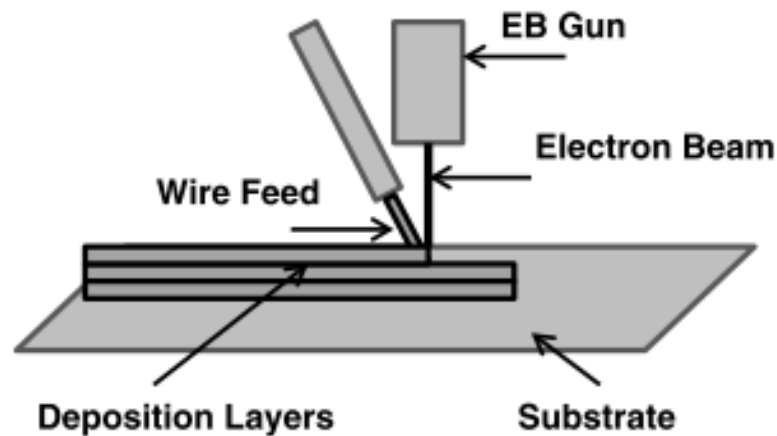


Figure 3. Typical wire feed system setup [2]

“Depending on the energy source used for metal deposition, wire-fed AM can be classified into three groups, namely laser based, arc welding based, and electron beam based. Among these, arc welding based AM has shown promise due to its combined advantages of higher deposition rate, energy efficiency, safe operation and lower cost”[5]. "The two types of wire fed additive manufacturing systems use a repurposed and modified Tungsten Inert Gas (TIG/GTAW) or Metal Inert Gas (MIG/GMAW) welding power source [6]. GTAW uses an energy source (laser, electron beam, or electricity) to melt metal filler wire in an inert gas environment. The GTAW process uses a tungsten electrode from which an arc is generated to provide the heat for the addition of the filler material, creating a large temperature differential between the filler and the work piece [7]. GTAW requires a highly skilled operator when performed manually. The process typically necessitates an operator

to use both hands to execute the weld: one for holding the torch and the other for feeding in filler to ensure maximum precision [7]. The MIG process, Figure 4, uses a consumable wire electrode, that acts not only as the filler but also the heat conductive electrode. The filler wire is melted by electricity and deposited in an inert gas environment [7].

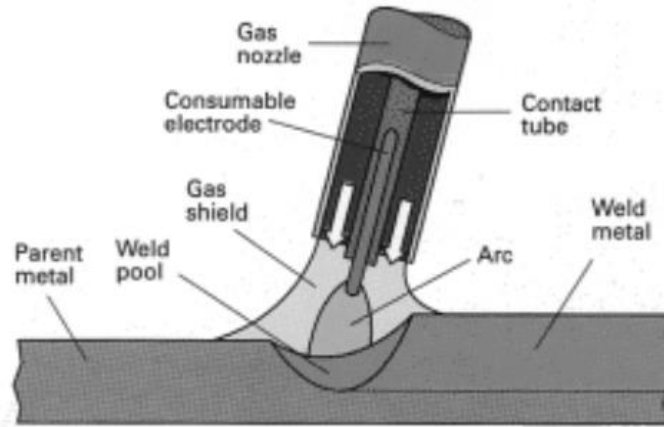


Figure 4. GMAW Process [1]

Wire Arc Additive Manufacturing (WAAM)

Wire and Arc Additive Manufacturing (WAAM) using either the GMAW or the GTAW process is a promising technology for manufacturing components of medium to large size in terms of productivity, cost competitiveness and energy efficiency [1]. “Both the GMAW deposition process and the GTAW deposition process have advantages and drawbacks when being applied to WAAM. The GMAW, or MIG, process results in easier control because it requires less moving components than the GTAW, or TIG process. The TIG process requires movement of an electrode and the deposited metal wire. The MIG process only has one moving component because the deposited metal wire is the electrode. Additionally, the MIG process does not require orientation of the deposited metal wire. The TIG process requires appropriate orientation of the wire as well as the arc source which

results in complicated toolpath generation. The TIG process, however, is less prone to electric arc wandering and a better surface finish is consequently easier to achieve [6]” [4]. Comparatively, the main drawback of GTAW is still the substantial lower deposition rate capability, when compared with GMAW based process, where deposition rates can be several times greater [8].

MIG Deposition Processes

The MIG process, Figure 4, appeared in the 1920s, but only in 1948 was this process fully developed and ready to be used by all types of industries [1]. “This welding process has significant advantages when compared with other welding processes, it can weld all types of commercially available metals and alloys, it can weld in all positions, it does not have the same restrictions in electrode’s dimensions when compared with shielded metal arc welding, it has higher welding speeds, and does not need heavy slag removal operations. However, it needs a more complex and more costly equipment than shielded metal arc welding, as shown in Figure 5” [1]. “Whenever possible, MIG is the process of choice: the wire is the consumable electrode, and its coaxiality with the welding torch results in easier tool path generation” [6]. Metal transfer is accomplished by fed wire being melted and deposited on a substrate. MIG welding has four methods of deposition depending on the amperage and voltage of the welding machine, short-circuit transfer, globular transfer, spray arc transfer, and relatively new Cold Metal Transfer (CMT) process [9, 10].

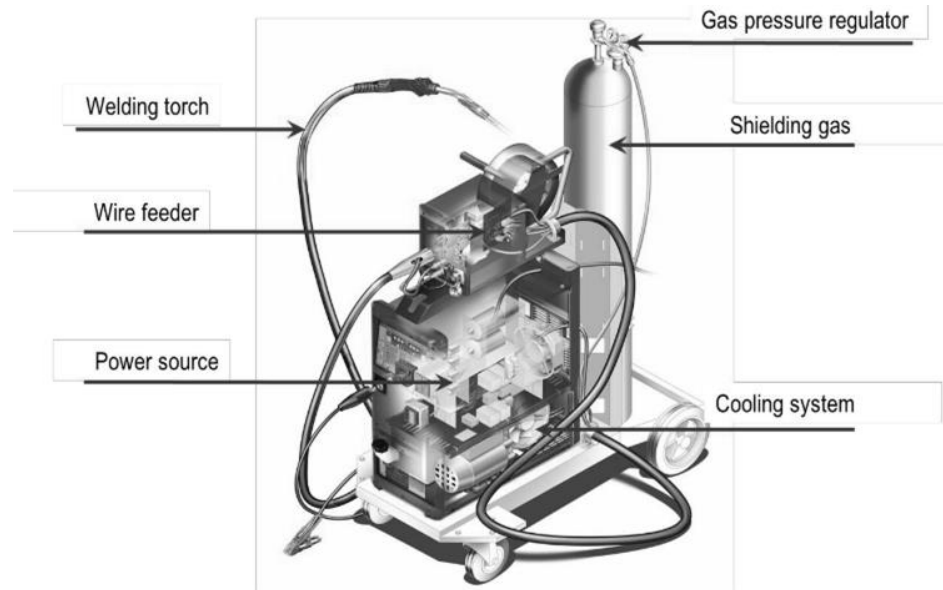


Figure 5. Scheme of a modern inverter-based GMAW power source [10]

Short-circuit transfer, also known as dip transfer, is the traditional MIG process as illustrated in Figure 6. “Short-circuit transfer is determined by low arc current and voltage, and characterized by low heat input. Because of lower current and consequently heat input, this type of transfer mode is used to weld thin materials. This type of metal transfer produces a fast freeze weld pool. The metal is transferred from the electrode to the work piece only during the time the electrode contacts with the weld pool. There are about twenty to two hundred contacts per second between the electrode and the weld pool” [1]. While short-circuit transfer is not as capable of as high deposition rates as spray arc transfer, the characteristic lower heat input and relatively high deposition rate make this process favorable. A potentially negative consequence of this low heat behavior is a lack of complete weld fusion when attempting to weld thick metals [9]. However, the additive manufacturing process requires less heat input than a traditional weld which requires full heating and penetration of two pieces of base metal. In the additive manufacturing process, only enough energy to penetrate the relatively thin previously deposited layer is required.

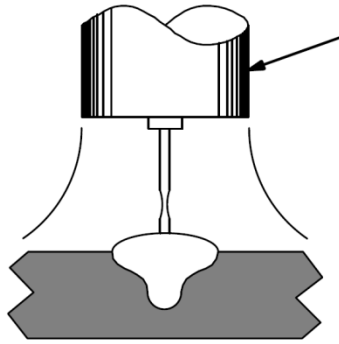


Figure 6. MIG Short-circuit transfer [1]

Globular transfer, shown in Figure 7, occurs when globs of hot metal accumulate on the fed wire electrode and are discharged onto the base metal. Instead of a small amount of metal being deposited during a brief short circuit, a large amount of metal accumulates on the electrode before it is deposited. “Globular transfer is often seen as the worst transfer mode in MIG/MAG welding, because it tends to produce high heat, poor weld surface and spatter” [1]. This makes it a poor choice for application in additive manufacturing.

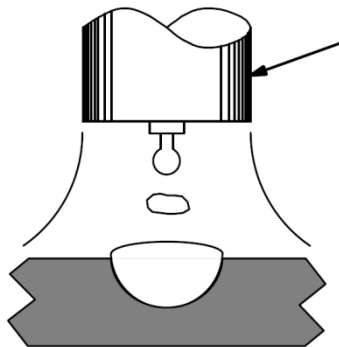


Figure 7. MIG globular transfer [1]

“With a current level above the transition current and with Argon shielding gas, it’s possible to achieve the transition from globular transfer to spray transfer. Spray transfer is characterized by small droplets transferred between the electrode and the work piece, and by spatter free welds” [1]. As shown in Figure 8, spray arc transfer occurs when a stream of tiny drops flow from the fed wire electrode to the base metal. Spray arc transfer has the

advantage of a high deposition rate and deep weld penetration. However, spray arc transfer does require higher power input to the weld and consequently adds more heat [9]. This behavior makes spray arc transfer not conducive to the ideally low thermal input additive manufacturing process.

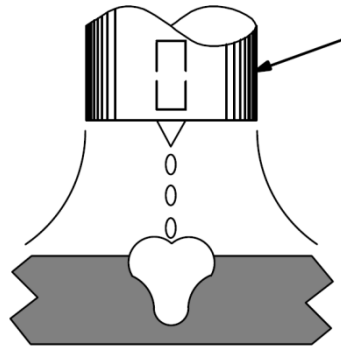


Figure 8. MIG spray arc transfer [1]

The final MIG welding technique is Cold Metal Transfer (CMT) is illustrated in Figure 9. In 2005, Fronius introduced a revolutionary new arc welding process called CMT. CMT is classified as a dip transfer process and characterized by low heat input when compared to the conventional GMAW [1]. The CMT presents an innovative solution, which is determined by the motion of the electrode directly assisted by the process control mechanism. When the arc plasma is developed, the filler wire moves to the weld pool until the wire touches the weld pool and short-circuiting takes place. Then the current becomes lower and the electrode is retracted enhancing the droplet detachment [1, 10]. The process is then repeated. This process has the advantage of lower thermal input than other MIG welding techniques. The electrical power melting the wire is more precisely controlled which results in an overall lower process temperature [6].

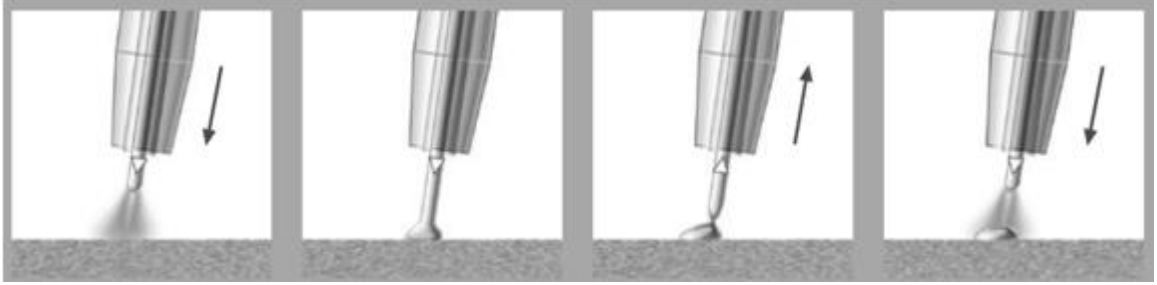


Figure 9. The Cold Metal Transfer process [1]

In CMT welding the current and voltage cannot be changed independently and are linked together via synergic control, a linear mathematical relationship developed by Fronius and based on predetermined relationships of voltage, current, and wire feed speed. Synergic welding is described as “single dial” control, or the manipulation of multiple welding parameters based on a single user defined characteristic. The synergic algorithm incorporates voltage and amperage control based on the wire feed speed and is dependent on the thermal and electrical resistivity of the substrate, the filler wire used and its diameter, and the shielding gas composition [7].

The standard CMT process can “altered” in three ways to manipulate deposition for different situations. The CMT Pulsed process combines a pulse cycle with CMT welding, increasing the flexibility but at the expense of inputting more heat into the weld. CMT Advanced is an even “cooler” process than CMT and is characterized by reversing the polarity of the welding current in the short-circuit phase. The results yield tightly controlled thermal input, extremely high gap bridgeability and an up to 60% higher deposition rate. CMT Pulsed Advanced combines the negatively polled CMT cycles and the positively polled pulsing cycles and results in a slightly higher heat input than CMT advanced. [10]. A graph of the voltages and currents of the different processes can be found in Figure 10.

COMPARISON OF ARC TECHNOLOGIES

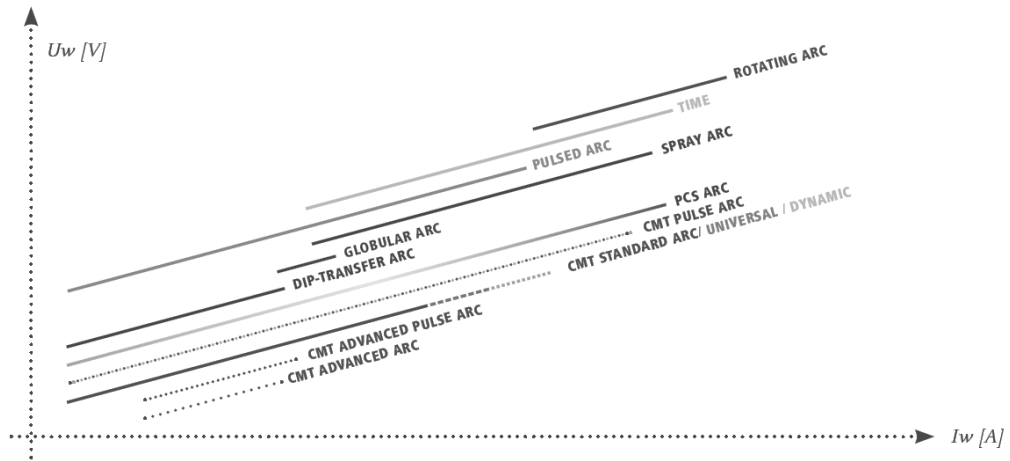


Figure 10. Graph of current and voltage for different welding processes [10].

WAAM using MIG Short-Circuit Transfer

Wire arc additive manufacturing was first recorded in a patent by Baker in 1925, entitled “Method of Making Decorative Articles.” The patent presented a new method of creating objects using a metal electrode and electricity to deposit material in fused subsequent layers to form an object. The patent included drawings of two objects and a close-up of built up layers as shown in Figure 11. In the patent text, Baker identified that the current was related to the speed of the moving electrode and the thickness of the layer. Additionally, Baker moved the electrode in a tight circular manner to create the deposit. Baker focused on creating decorative objects that did not have any mechanical value. The process was not mechanized and relied upon the operator for movement of the welding tip [11].

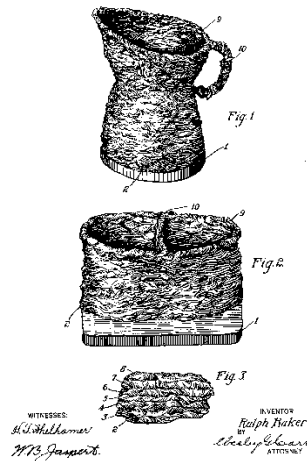


Figure 11. Baker's patent [11]

In 1925, Eschholz deposited single layers of metal to form ornamental letters. Eschholz determined that the important process parameters were substrate material, arc current, travel speed, bead width, bead height, and penetration depth [12]. Shockey in 1932 used the novel wire and arc deposition method in his patent for “Machine for Reclaiming Worn Brake Drums”. In the patent, single layer weld beads were deposited on worn brake drums so they could be returned to service. After depositing the material, the brake drum was machined to the correct size. The mechanization of the deposition process of the weld head was the major improvement in this patent method, prompting Shockey to note the impact of travel speed and electrical current on the geometry of the deposited bead. In 1933, Noble filed a similar patent for a cost-effective method of enlarging shaft diameters. Noble proposed near net shape manufacturing of a collar on a shaft instead of machining a large diameter shaft with great material waste [13].

In 1943, a significant development was made as evidenced in a patent by Carpenter and Kerr. Using the Submerged Arc Welding (SAW) process to manufacture large shafts with increased strength when compared to traditionally manufactured objects, it was

determined that the substrate must be preheated to permit a high rate of metal deposition. Preheating seemed to allow a greater feed rate [14]. The SAW process continued to be refined in a 1962 patent by White in which rollers were used to apply pressure to the previously deposited layer. White observed large variability in the process and noted that the pressure roller improved the surface of the layer and created a more consistent process [15]. In patents filed in 1967 and 1970 by Ujiie, SAW was carried out with the addition of an inert shielding gas and three simultaneous parallel welding nozzles to achieve a high deposition rate. This created a larger weld pool but resulted in degraded grain structure and voids when compared to the single wire electrode objects. When using a smaller weld pool resulting from a single welding nozzle, Ujiie hypothesized that the pressure vessel's good mechanical properties resulted from the tempering effects of subsequent layer deposition [16]. In a 1974 patent, Brandi and Luckowon determined that the welding power and temperature of the substrate and subsequent layers were critical factors that could be controlled [17].

In 1990, Acheson was granted a patent titled "Automatic Welding Apparatus for Weld Build-up and Method of Achieving Weld Build-up." He included a nozzle for a shielding gas that moved with the fed arcing wire in a process similar to the Gas Metal Arc Welding (GMAW)/Metal Inert Gas (MIG) welding. Acheson focused on the mechanical design of nozzle with shielding gas to additive manufacturing but did not provide any testing or evaluation of his invention [18]. However, this patent marked the beginning of the current trend of focused research of the MIG based wire and arc additive manufacturing process.

With the proliferation of Computer Numerical Control (CNC), the wire and arc additive manufacturing process has been increasingly researched and developed focusing on the GMAW process. Recognizing the potential of this additive manufacturing technique to be a disruptive technology, Rolls-Royce in the early 1990s internally investigated the application of this technique to the aerospace industry. The focus of the research was on lowering cost by producing near net shape high performance alloys with low waste [19, 20].

At the University of Nottingham in 1992, UK, Dickens, *et al.* conducted a notable preliminary study of additive manufacturing using MIG based methods. A commercially available welding robot was used, and the researchers noted significant advantages to the process when compared to conventional manufacturing techniques. These techniques included robotic control and automation, consistent material properties, rapid manufacturing times, and material efficiency. The team used mild steel welding wire to produce a square box and a truncated pyramid shown in Figure 12 and Figure 13 [20].

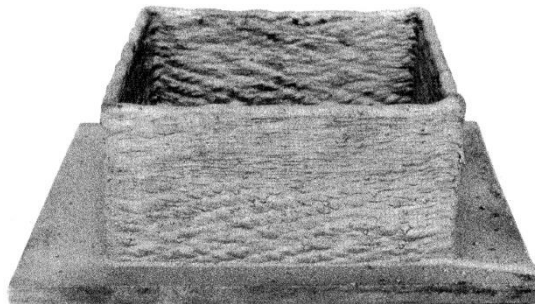


Figure 12. Box produced by Dickens, et al. using MIG process [20]

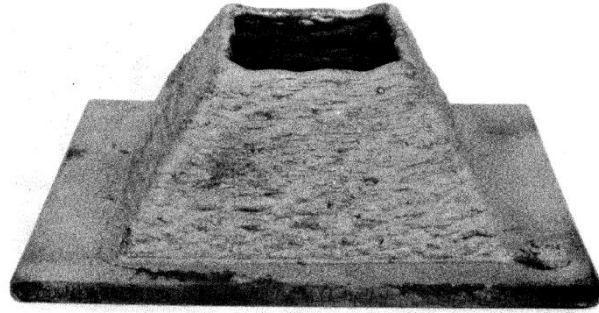


Figure 13. Hollow pyramid produced by Dickens, et al. using MIG process [20]

Dickens emphasized the importance of geometry of the produced weld bead and conducted numerous trials of singular weld beads with varying parameters. The authors studied voltage, wire feed rate, wire stickout distance from the nozzle, wire diameter, and welding velocity in observing their effect on arc voltage, arc current, layer width, and layer height. The authors observed that the geometry of the weld bead was dependent upon these factors and summarized the general trends presented in the Table 1. It was observed that the shape of the weld bead could be modified from a wide and flat bead to a narrow bead when producing vertical walls by varying the velocity of the welder [20].

Table 1. Interactions observed by Dickens, *et al.* [20]

Increasing Variable	Effect on Measured Variable			
	Arc Voltage	Current	Bead Width	Bead Height
Voltage	↑	=/↑	↑	↓
Wire Feed	↓	↑	↑	↑
Stickout	↑	↓	↓	↑
Wire Diameter	↓	↑	↑	↑
Velocity	=	=	↓	↓

Dickens, *et al.* also conducted a brief (not statistically significant) post process mechanical and microstructure evaluation of the manufactured square box wall sections. The microstructure was largely equiaxed ferrite and perlite with a grain size of

approximately 60 μm . Hardness tests showed an increase in hardness from the base of the wall to the top and microstructurally the top was much less equiaxed and more columnar. They hypothesized that these interactions were the result of the tempering of the lower layers due to repeated reheating during deposit of subsequent layers. Tensile tests were conducted parallel and orthogonally to the layers, and there was found to be very little difference in ultimate tensile strength in the two directions; however, a statistical study was not performed [20]. The researchers recommended heat treating the object to ensure a uniform microstructure, but they did not test this hypothesis. Additionally, there were no voids or cavities in the material when a sample was polished and observed under a microscope.

Dickens *et al.* concluded that to further develop the MIG based additive manufacturing technique there must be significant software development. Additionally, a sensing feedback loop between the welder and the robot controller was identified as necessary to improve the consistency of the process and create surface finishes similar in quality to cast objects. The authors recommended that the sensing feedback loop provide the wire offset distance to the controller. The controller would then maintain the wire offset distance to a constant value [20].

Further research at the University of Nottingham of the MIG additive manufacturing technique was published by Spencer *et al.* in 1997. The team used a commercially available three-axis robot and MIG welder with a Siemens controller to build layers on a platform that could tilt and rotate manually, allowing orientation of the part at different angles to the welder so geometries could be made without supports [21].

Three test parts, a hollow box, a vertical wall, and a horizontal slab, were studied and are shown in Figure 14. The geometries were 82 layers totaling 100 mm high copper coated mild steel wire that was 1 mm in diameter. The layer width of the resulting weld bead was 3.5mm. It was found that the layer widths between 3 and 6 mm were possible. Attempting to build walls of thicknesses greater than 6mm resulted in excessive heat input and poor bead profile to due to insufficient cooling of built up heat [21].

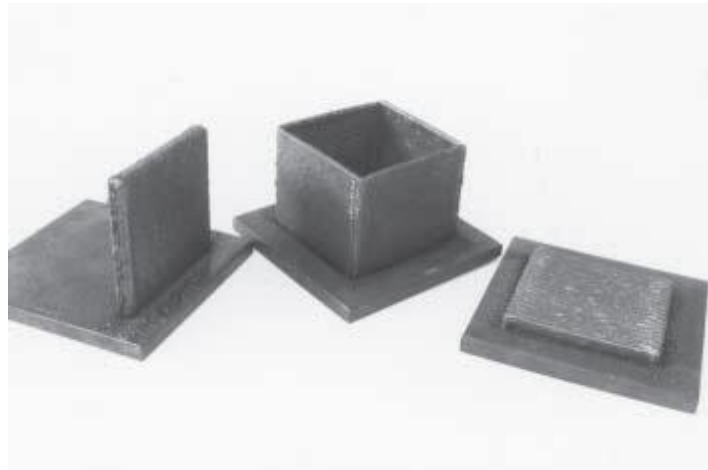


Figure 14. Geometries studied by Spencer et al [21]

Spencer *et al.* attempted to manufacture thicker walls by placing multiple beads beside each other, but this resulted in incomplete penetration of the substrate and neighboring bead. Attempts to angle the welding torch to deposit multiple adjacent beads were unsuccessful due to an unpredictable bead profile. The dye penetrant test, shown in Figure 15, demonstrated the lack of fusion when attempting to deposit adjacent beads. Instead of attempting to deposit the beads directly next to each other, the authors deposited beads at a pitch approximately double the width of the weld bead crest. As illustrated in Figure 17, material was then deposited in the root channel formed by the two beads separated by the pitch distance. According to tensile tests, the researchers concluded that

this method of adjacent layer deposition created excellent mechanical properties. The tensile test standard used was not recorded.

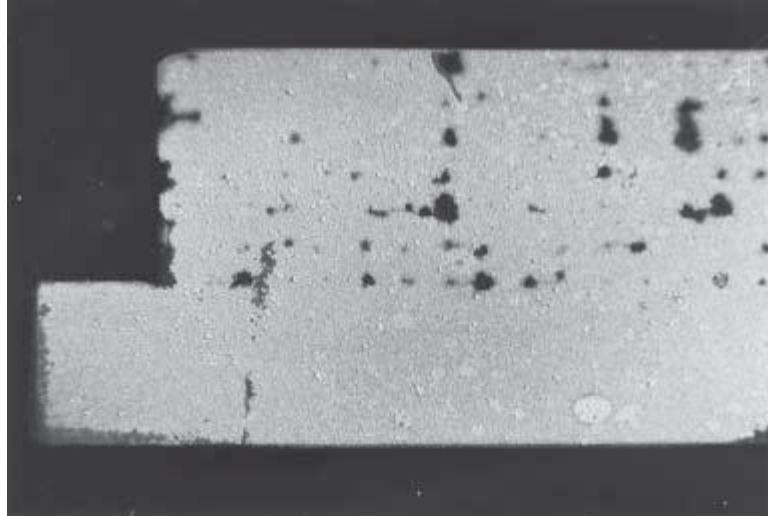


Figure 15. Voids and porosity in adjacent beads as shown in dye penetrant testing by Spencer et al. [21]

Spencer *et al.* implemented temperature control to ensure the previous layer had sufficiently cooled before depositing the next layer. An infra-red sensor was used to measure temperature. The operators set a maximum allowable temperature at which welding was to be performed. The computer prevented welding until the part reached an acceptable temperature. After implementing temperature control, the authors achieved an improved surface finish at the cost of over doubling the build time [21]. Spencer *et al.* observed that the microstructure of the upper surface had a martensitic structure due to rapid cooling. The recrystallization and slower cooling of the lower layers resulted in finer and uniform ferrite/pearlite grain structure [21].

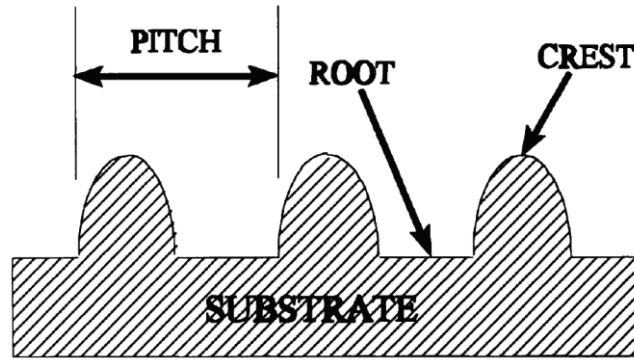


Figure 17. Procedure for depositing adjacent layers by Spencer et al. [21]

The work of Dickens, *et al.* and Spencer *et al.* did not include Computer Aided Design (CAD) integration, rather the machine code was written by hand and only simple geometries were created [22]. Ribeiro *et al.* at Canfield University in 1994 developed a process for generating machine code directly from a CAD drawing. Their proprietary, unpublished software package translated a CAD file into movements interpreted by the software controlling the industrial robotic arm welder. The weld parameters were kept at predefined constants and were controlled by the internal circuitry of the welding robot. Ribeiro *et al.* successfully produced a circular metal vase out of mild steel with this process as shown in Figure 16 [23, 24].

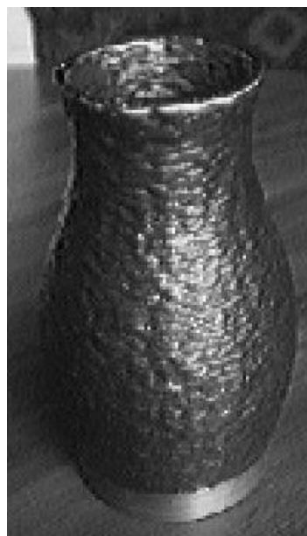


Figure 16. First successful integration of CAD and welder controls [23,24]

Although he was just performing a software process evaluation, Ribeiro, *et al.* recorded conclusions from the brief experiment. The authors identified that the curved geometry of the vase created a variable distance between the arcing wire and the previous layer during deposition. Additionally, it was observed that the quality decreased with time which was likely due to heat buildup. Ribeiro, *et al* recommended weighing the base plate before building an object to calculate how much material was deposited [23, 25].

To illustrate the software capabilities and evaluate the geometric accuracy, an additional hollow object was created with refined software by Ribeiro, *et al* in 1996 and is shown in Figure 18. The authors concluded that bead geometry (layer height and width) was of utmost importance and must be properly estimated for the slicing parameters to function correctly. Additionally, during the build process, the distance between the arcing wire and the previous layer was variable and required manual adjustment during the process. The inward taper of the component was considered to be the cause of this issue and closed loop control was recommended as the solution [26, 27].



Figure 18. Complex geometry produced by Ribeiro, et al. [26,27]

For greater control of the MIG arc welding process, Ribeiro, *et al.* developed a mathematical model to determine the welding parameters to use in the slicing software. The inputs of the model were layer width, layer height, welding current, and welding voltage. In testing, machine travel speed was varied between 500 and 2500 mm/min, and the welding current was varied between 120 and 160 Amps. The wire feed speed was not considered independently [22]. The welder used a synergic control algorithm to control the pulsing of the power source and the wire feed speed. The synergic algorithm varied the welding power based upon the wire feed rate. The welder was attached to a robotic welding arm for testing [22].

Ribeiro *et al.* performed their experiments with Inconel 718 wire of 1.0 mm in diameter and used a shielding gas of commercial argon. During the experiments, the layer width varied between 3.8 and 10 mm and the layer height varied between 0.44 and 1.24 mm. The authors observed a relationship between welding speed and layer width as shown in Figure 19 [22].

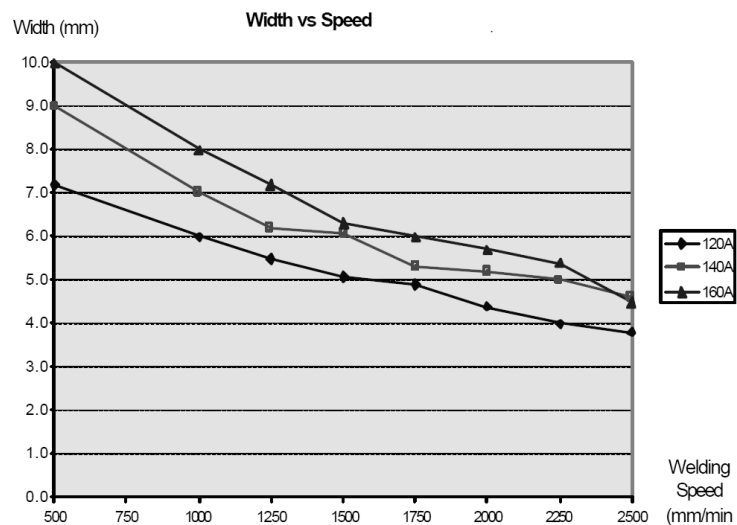


Figure 19. Relationship between layer width and travel speed by Ribeiro et al. [22]

To develop the parameter input algorithm for the slicing software, Ribeiro *et al.* used empirical results as inputs for a regression analysis to determine the relationship between four measurable coefficients of welding speed, welding current, layer height, and layer width. The created mathematical model was incorporated into the software so the user could input a desired layer height, and the computer would automatically set the welding speed and current. To evaluate the software, three test objects of desired layer width were manufactured. The greatest observed absolute layer width error was 0.4mm with an expected layer width of 8.0 mm. The authors considered this layer width error to be relatively small [22].

While Ribeiro *et al.* were successful in creating an appropriately sized geometry, their preliminary study failed to consider many parameters (*e.g.* wire feed speed, weld characteristics, wire offset, wire diameter) previously identified as important by other researchers [19]. Additionally, the authors failed to study the influence of the internal controls of the welder. Finally, the model was purely based upon empirical data for Inconel 718 deposited by the studied welder, and generalized equations that could be applied to other materials and hardware were not created.

In research at Southern Methodist University, Kovacevic, *et al.* used a 24 Volt MIG welder with ER70S-6 mild steel wire, 95% Argon and 5% CO₂ shielding gas, and the machine traveled at a constant speed of 6.4 mm/sec. The researchers proposed controlling the metal transfer process by turning the electrical current to the welder on and off based upon the size of the metal droplet formed at the end of the electrode. To observe the metal transfer process, a high speed digital camera capable of 800 frames per second with a resolution of 128X128 pixels was used [28]. Kovacevic, *et al.* determined that the

deposited metal bead size and penetration could be controlled by the pulsing electrical current. Therefore, this strategy could be used for increased control and consistency during the deposition process [28]. Kmecko, *et al.* continued this research in 1999 by applying real time image processing to the system in an effort to reduce welding spatter. The developed system measured the voltage and current used by the welder. In addition, the system featured an infrared pyrometer and a light sensor. While the system was capable of real time image capture, no reference of successful closed loop control was presented. Kmecko, *et al.* were convinced that the closed loop control was necessary to improve the process and reducing welding spatter [29].

In 2002, Zhang, *et al.* at the University of Kentucky published an improved MIG based additive manufacturing process with a more sophisticated CAD model slicing strategy. The team developed unpublished slicing software that could vary the infill method and layer height throughout different sliced regions. To evaluate the varying start point strategy, Zhang *et al.* created tube shaped parts with and without varying start points. As shown in Figure 20, the accumulated error from buildup at the start point of the deposited layer path is significant. Figure 20 presents a tube-shaped part with a varied layer start point. As a result, the effects of the accumulated start point error are mitigated [30].

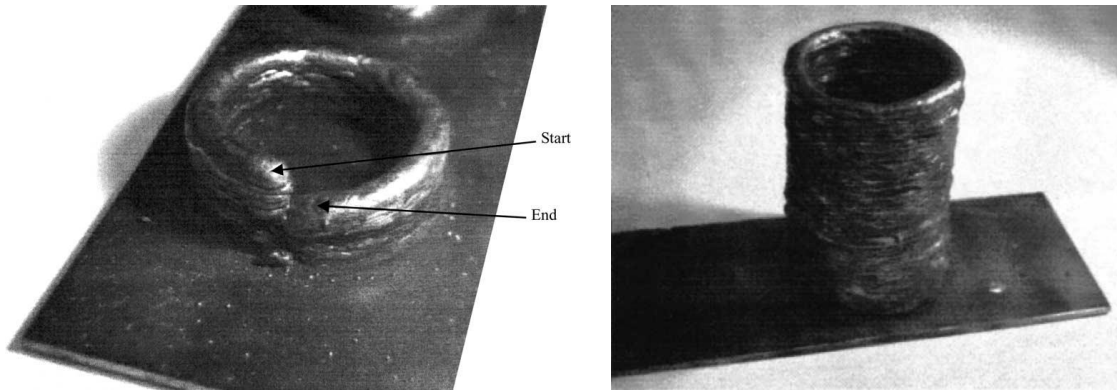


Figure 20. Part with the same layer start point (left) and varied start point (right) [30]

The software was also capable of speed control over the start and end points of a deposited line. The researchers observed buildup of the layer at the start of the path and a decreased amount of material at the end of the path. To counteract this effect, the authors increased the machine travel speed at the beginning of the path and slowed the machine travel speed at the end of the path while the wire feed speed was kept constant. Additionally, a second pass was added to the end region of the path to further level the deposited layer [30]. As shown in Figure 21 (top), the wall is not level with material buildup at the start point of the path and lacking material at the end of the path. Figure 21 (bottom) presents a wall section with control of the start and end points. As a result, the build up at the start point is decreased, the end point is not lacking material, and the wall section is more even [30].

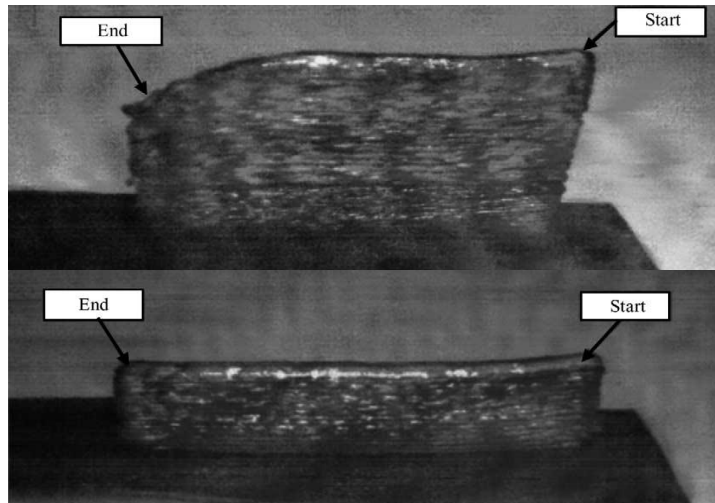


Figure 21. Wall without start and end control (top) and with control (bottom) [30]

In 2004, Song, *et al.* published a technique based upon MIG additive manufacture coupled with a subtractive manufacture milling machine shown in Figure 22 [31]. The authors proposed a machining process after each layer was deposited. Additionally, the build plate was heated to 200 °C before welding with a built-in heater. The researchers hypothesized that preheating the build plate would reduce thermal stress build up during deposition but did not perform experiments to confirm this [32].

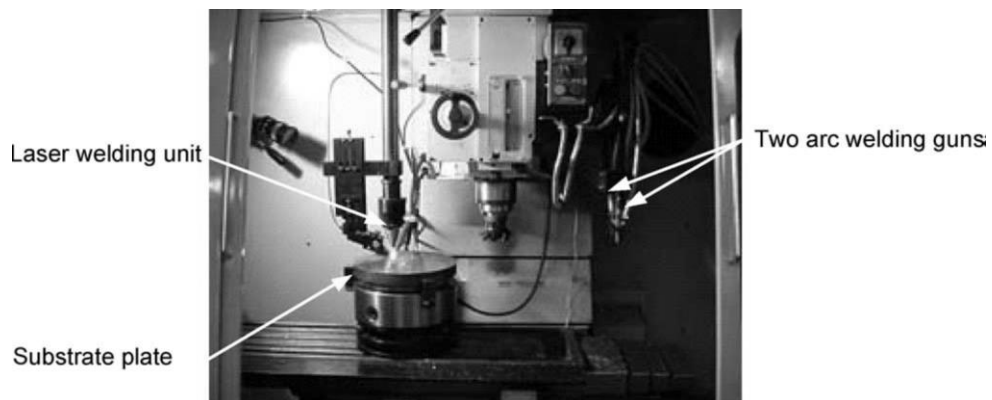


Figure 22. Integrated welding and milling machine created by Song et al. [31]

To evaluate the welding and milling process, the authors constructed test parts with a constant welding voltage of 19 volts and a constant welding current of 120 Amps with a

welding speed of 1.2 m/min. During the process, the authors deposited layers and then milled the object, as shown in Figure 23. The object had a layer height of 0.8 mm, a layer width of 4 mm. After machining, the object had a wall thickness of 1 mm. Song, *et al.* examined the microstructure of a machined and polished sample. As shown in Figure 24, the sample had large grains in the upper region of the wall (region a) and fine grains in the lower region of the wall (region b). This is consistent with the observations of Ribeiro, *et al.* [32].

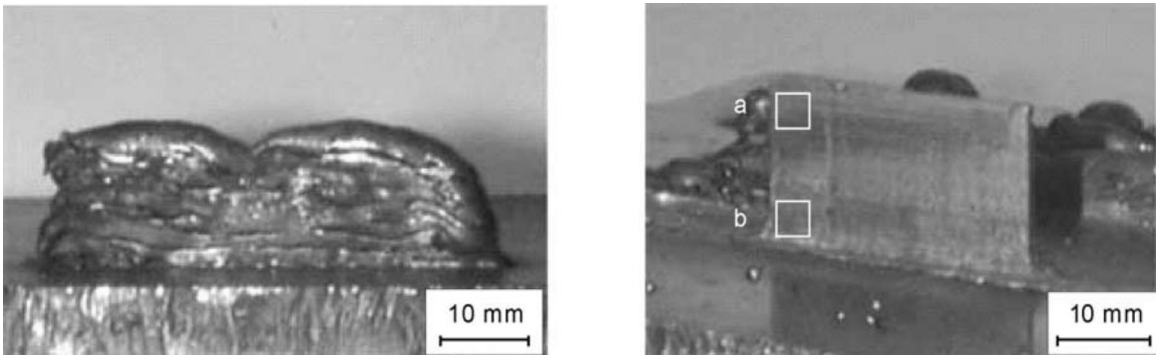


Figure 23: Thin-walled part before and after machining by Song et al. [31,32]

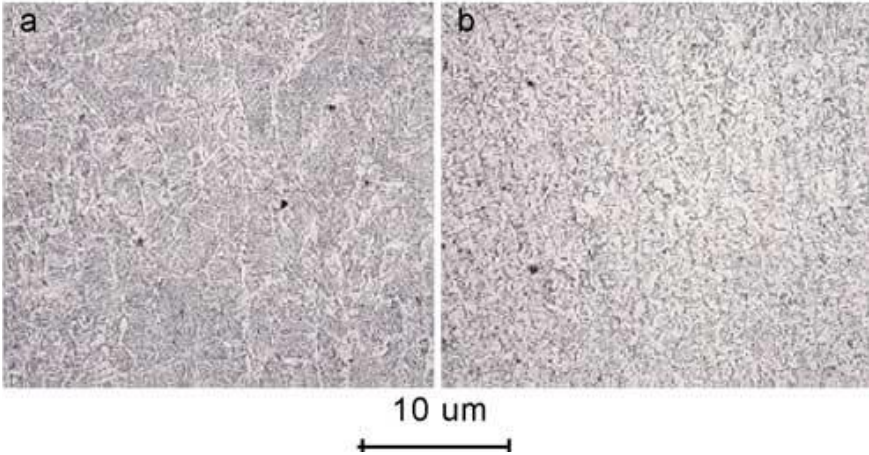


Figure 24. Microstructure observed by Song et al. [32]

In addition to a thin wall, Song, *et al.* manufactured a test rectangular solid object as shown in Figure 25. The object had a layer height of 0.8 mm and a deposited layer offset of 2.8 mm. The solid test object was measured to have a dimensional accuracy of ± 0.5 mm before machining and a dimension accuracy of 20 μm after machining.

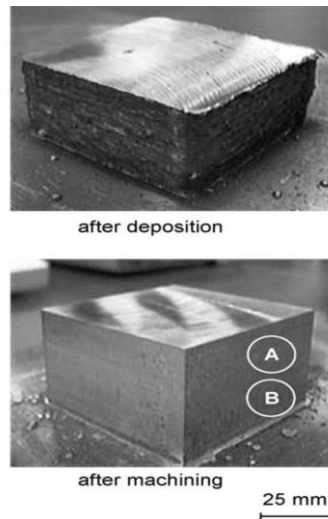


Figure 25. Solid part before and after machining by Song, *et al.* [33]

Song, *et al.* also performed a tensile test in the longitudinal direction, or parallel to the layers of the deposited material, and observed that the object had a tensile strength of 620 MPa which was compared to the deposited wire material which had a tensile strength of 550 MPa [32]. Song, *et al.* did not perform a tensile test in the transverse direction, or normal to the direction of deposited layers.

In a continuation of the previous study, Song, *et al.* optimized their welding and milling technique using statistical methods. The authors chose to optimize welding voltage (varied between 14 and 26V), wire feed speed (3 to 8 m/min), wire offset (6 to 8 mm), and the shielding gas composition (CO_2 varying from 30 to 10%). The weld spatter and deposited layer width were chosen as the two main functions of the welding parameters [33]. To quantify the weld spatter, a spatter index was created which was the ratio of the

mass of the spatter divided by the mass of the welded wire. The mass of the spatter was determined by collecting and measuring the spatter beads after the completing the deposition. The mass of fed wire was determined based upon the fed wire speed [33].

Song, *et al.* determined that the welding voltage, wire feed speed, and wire offset have a high impact on the spatter formation. However, the shielding had a negligible effect on spatter formation. When examining deposited layer width, the welding voltage and wire feed speed had significant impact. However, the wire offset and shielding gas composition have a small impact on the deposited layer width [33]. From these results, the authors concluded it was best to use the least expensive shielding gas with a CO₂ composition of 30% and reduce wire offset to the minimum of 6 mm to reduce spatter [33].

Song, *et al.* studied the distance between adjacent layers (bead offset), the direction of layer deposition, and alternating the direction of layer deposition, shown in Figure 26. To measure the studied factors, tensile tests and hardness tests were performed to see which building strategy had the best performance [33].

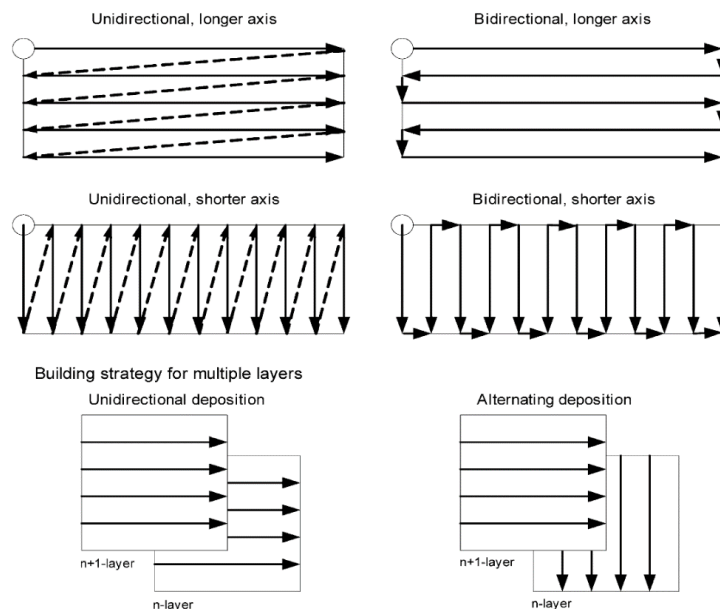


Figure 26. Building strategies for solid layers [33]

Results indicated that the deposition parameters have a negligible effect on the surface hardness, however, the team did not examine the surface hardness at different heights of the object. The researchers concluded that the orientation of the deposited layer determines the tensile strength and alternating the deposition direction between layers increases the tensile strength. The authors proposed that the method of alternating deposition direction between layers was stronger because voids were filled in the previous layer, increasing the surface quality and density of the layer [33].

In 2007, Clark, *et al.* with Rolls-Royce researched the viability of MIG based additive manufacturing of the nickel-based polycrystalline super alloy, Alloy 718, for aero engine applications. The researchers used a synergetic MIG power source with argon shielding gas. The welder was set to 35 volts, the wire stickout was 20 mm, the travel speed was 10 mm/s, and the wire feed speed was 10 mm/s. The deposited layers had a nominal width of 12.8 mm and nominal height of 1.7 mm [34]. Clark, *et al.* performed multiple deposition geometries and examined the polished and etched samples with a scanning electron microscope for microstructural analysis and x-ray for chemical analysis. When performing the trials, the authors waited until the previous layer had cooled to 80⁰C before deposited the subsequent layer. This was to prevent latent heat buildup in the deposited object and a created approximately a 10-minute cooling duration between welds. The resulted in lengthy build times because each deposited layer required over 10 minutes [34]. When examining the microstructure, Clark, *et al.* concluded that the results were highly dependent upon the deposition factors. The authors concluded that controlling the cooling rate in particular was necessary for a uniform part and the prevention of crack formation.

In 2013, Anzalone, *et al.* at Michigan Technological University developed a low cost (less than \$2000) open-source, MIG based, 3-D printer shown in Figure 27. The machine was a three-axis delta robot that was designed for Fused Deposition Modeling (FDM) plastic extrusion printing without any feedback. The authors used readily available open-source Cura software created for Fused Deposition Modeling (FDM) The system used 75% Argon and 25% CO₂ shielding gas at a rate of 20 CFH, a tip offset of 6 mm, and ER70S-6 wire [35]. As a proof of concept, the sprocket shown in the figure was created by the authors. The object had a layer height of 1.75mm and was created with a wire federate of 3.5 cm/s [35].



Figure 27. Sprocket made via the low-cost open-source MIG printer by Anzalone [35]

Additionally, Anzalone, *et al.* examined the microstructure of a polished and etched sample. Similar to the results of previous research, the Anzalone, *et al.* concluded that the microstructure was finer at lower layers when compared to upper layers. This was due to reheating of the lower layers during the deposition of consecutive layers. The researchers

concluded their results proved that this was a feasible process for the economical production of metal parts [35].

Recent research performed at Auburn University in 2015, sought out to produce a low-cost metal additive machine and to measure parameters and validate their importance as a way to validate the machine's capabilities [4]. These components included a standard Miller welder, Mach3 CNC control software, gantry style 80/20 framing, Probotix CNC motor controller and stepper motors, along with standard linear rails and ball screws. Figure 28 shows the finished machined Gaddes produced at Auburn University.

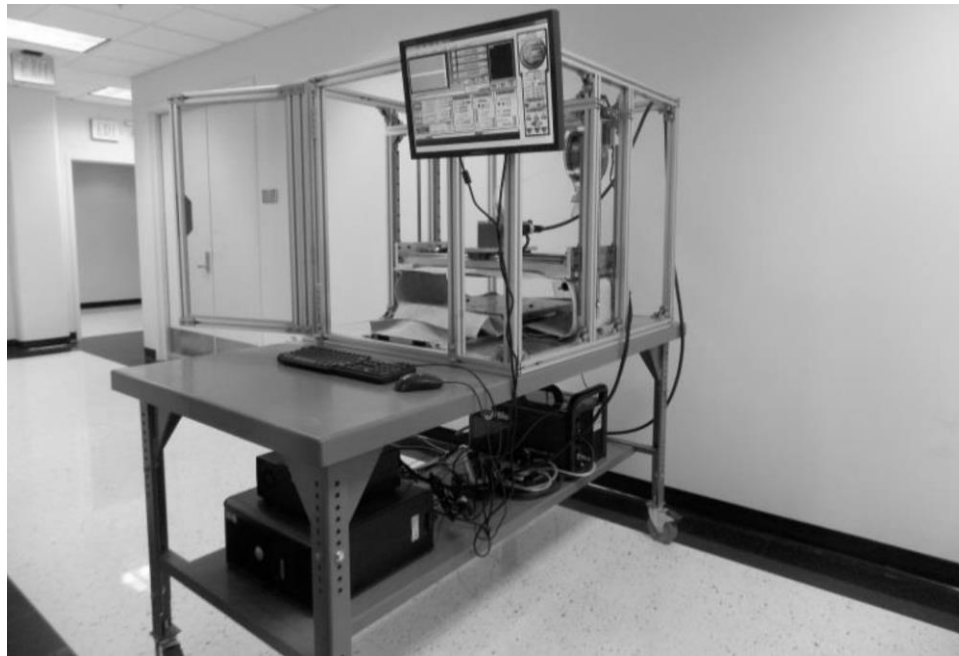


Figure 28. WAAM machine produced at Auburn University [4]

Gaddes' first study was a geometry evaluation. Test prints were created to evaluate infill strategies (zigzag patterns vs. parallel patterns), step-over, ability to "bridge" parts, overhangs, layer heights, as well as post-processing. For infill strategies tested, Gaddes found that making a parallel infill part or a spiral shape where the material was swept across the geometry produced a better result than having an infill with bordering "shells" [4].

The machine's ability to perform more complicated geometries was also tested. Figure 29 show parts that were produced to test these capabilities [4]. Gaddes concluded that having the layer height helix along the parts vertical produced the best results due to the start and end of each layer being slightly different thickness than the steady-state layer height. He noted that randomizing start points did help but the error was still existent due to starting and ending build-up [4].



Figure 29. Outward and inward facing geometry test (left) and bridging test (right) [4]

“As a demonstration of a useful part, two stainless steel printed nozzles are shown in Figure 30. The part on the right was turned on a lathe after printing while the part of the left was only removed from the build plate after printing. No voids were observed on the surface after turning. Before turning, the large diameter of the part was 1.770 in. with a wall thickness of 0.172 in. After turning, the part was 1.667 in. diameter with a wall thickness of 0.087 in” [4].



Figure 30. Stainless steel nozzle as-printed and post-machining [4]

Gaddes studied the effect of varying wire diameters on the voltage and current of the welder while producing the same geometries. The two graphs in Figure 31 show the results of this study [4]. Varying wire diameters had no effect on the power input required by the machine even for the different materials.

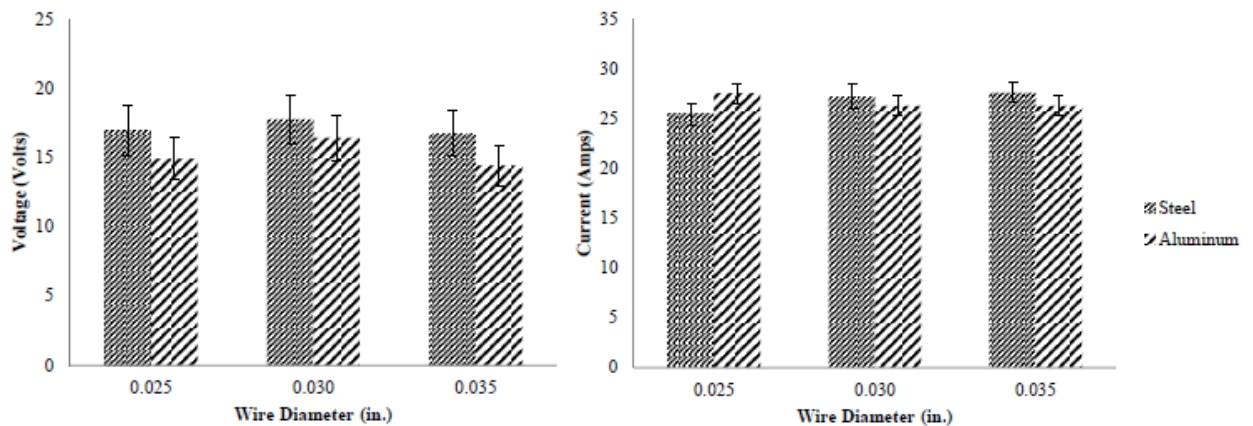


Figure 31. Wire diameter study voltage results (left) and current (right) [4]

The next study performed by Gaddes was a comparison of layer strength vs. material strength by comparing tensile tests at different deposition orientations. By producing prints and machining dog bones parallel and perpendicularly to the deposition direction, tensile tests could be performed to compare parts' properties in orthonormal

planes. Figure 32 shows the results of part of this study [4]. As one can see, both materials were orthotropic in behavior, with the transverse (vertical) specimens resulting in lower ultimate tensile strengths. Repeatability issues in the ER70S-6 vertical specimen should also be noted, with wall 1 and wall 2 varying drastically. The repeatability greatly improved in the ER308 specimens, shown on the right of Figure 32, although orthotropic behavior persisted and the manufacturers specification was not reached.

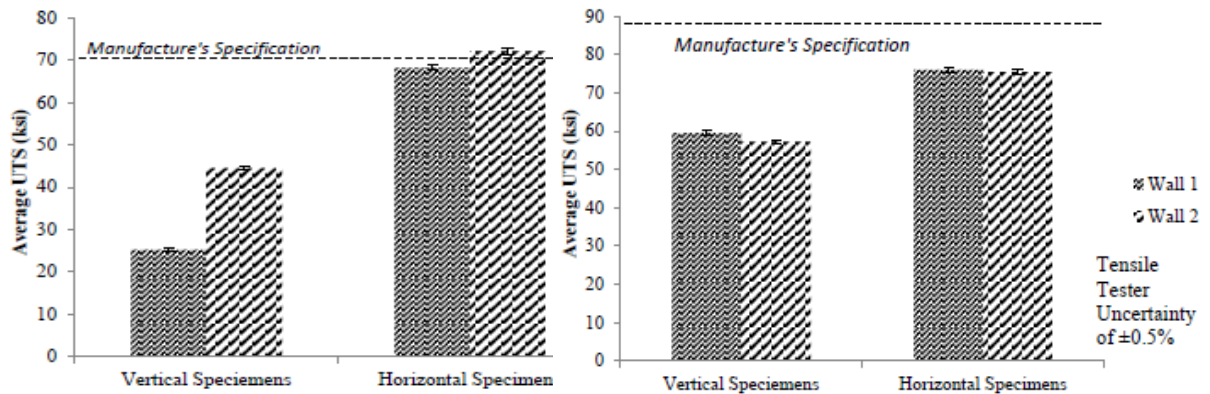


Figure 32. Tensile test results ER70S-6 steel (left), ER308 stainless steel (right) [4]

The cause of these issues (orthotropic, repeatability, low strength) was attributed to lack of control over the MIG transfer process, creating porosity in the prints. Figure 33 shows voids between layers that were observed by Gaddes. Gaddes noted that post-process heat treatment did improve the microstructural voids. Figure 34 shows the microstructural results of a Steel Specimen before and after a heat treatment cycle [4].

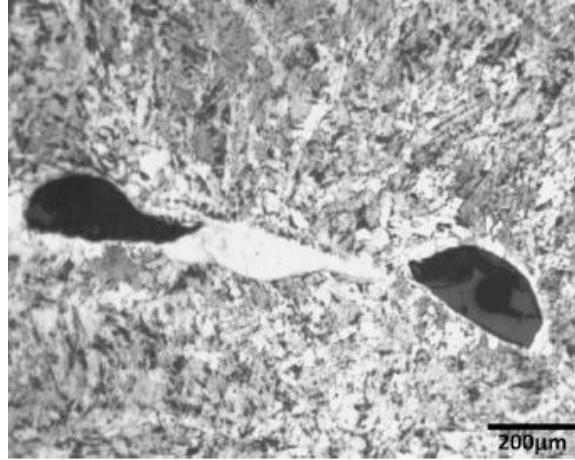


Figure 33. Voids found between Layers in Steel (ER70S-6) Parts [4]

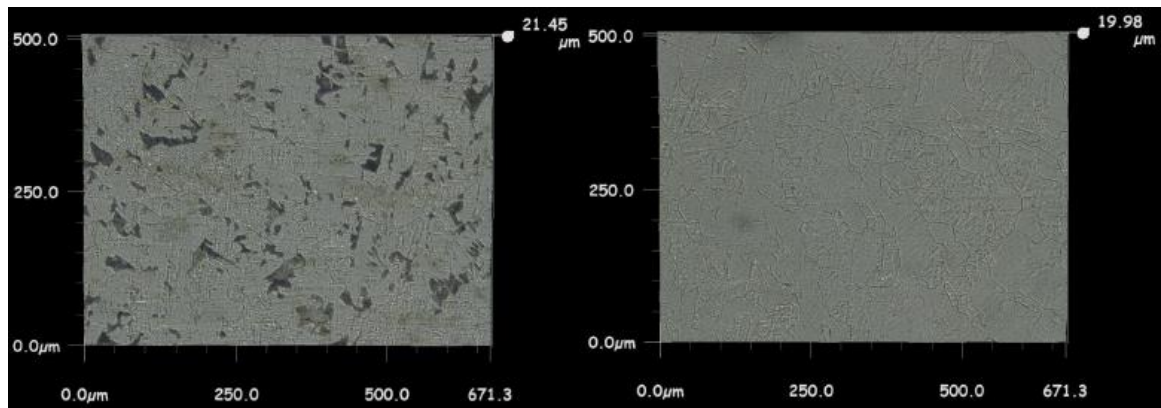


Figure 34. Microstructure of steel (ER70S-6) sample before heat treatment (left) and after heat treatment (right) [4]

A few of Gaddes' listed suggestions for future work to “provide greater control of the process” were as follows:

- “A cold-water tip cooled MIG gun would assist in the deposition of aluminum and copper.
- A pulsed MIG gun would assist in controlling the heat buildup in the deposit.
- A cold metal transfer MIG process would result in greater control of the weld bead” [4].

WAAM Using Cold Metal Transfer GMAW

Previous research has demonstrated that the GMAW process is a viable method for additive manufacturing. In 1999, Kmecko *et al.* stated that the “primary barrier to achieving quality welds in GMAW is the irregularity of the metal transfer process, i.e. the irregular growth and detachment of the droplets” [29]. By changing the welding current and depositing metal one drop at a time through precise process monitoring, Kmecko hoped to increase accuracy, lower the heat input, reduce the spatter, and have shallower weld penetration. While the system was unable to demonstrate successful closed loop control, the authors did highlight the current limitations of GMAW WAAM, all of which are improved upon by the development of CMT welding seven years later.

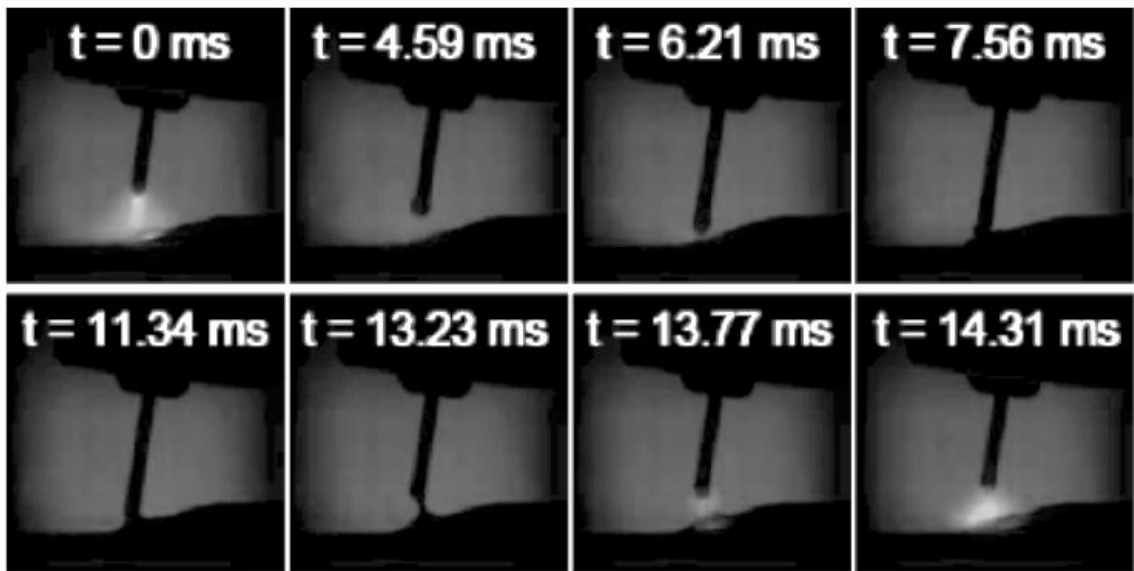


Figure 35. High-speed photography images a CMT cycle [7]

The development and application of the CMT process into WAAM provides increased features and control to improve the stability and viability of this technology. The CMT-GMAW is a fully digital, micro-processor-controlled inverter welding process that results in the introduction of a reduced amount of residual heat to the work piece and

produces a virtually spatter free weld. The improved weld quality is obtained via a digital process-control that detects a short circuit, and then retracts the wire being feed so as to help detach and deposit a single molten droplet at a time [7]. Figure 35 shows one cycle of the CMT wire retraction process, with the arcing period being about 1/3rd the total cycle time of 14.31 ms [7]. “The rearward movement of the wire assists droplet detachment during the short circuit. In this way, the arc itself only inputs heat very briefly during the arcing period. The thermal input is immediately reduced after arc is extinguished, creating an oscillating hot/cold weld pool. During the CMT-GMAW process, the average current is kept very small by controlling the short circuit, resulting in virtually spatter free metal transfer” [7]. While Cold Metal Transfer is not “cold”, it is comparatively cold when set against its predecessor, conventional-GMAW, making CMT highly desirable for low thermal input fusion arc welding in most aerospace applications [7].

In research from Rensselaer Polytechnic Institute published in 2009, author Timothy Hasselberg performed a feasibility analysis on CMT-GMAW of Inconel 718, a nickel based superalloy. Hasselberg carried out his research using a six-axis robotic welding arm and a two-axis positioner, a rotary head mounted on a trunnion table, both manufactured by ABB. Hasselberg angled the torch between 5-10 degrees from vertical when welding to pull the weld, producing a bead with maximum penetration and a narrow convex shape. This allowed for maximum shielding of the weld pool. Shielding gas of pure argon was used with a flowrate between 30-35 CFH. Four geometries were used for evaluation, a single-line bead with 1 mm oscillation, a circular weld with three layers of buildup and 1 mm oscillation, a straight-line 8 mm weave pattern bead, and edge welding. Hasselberg’s tests were conducted at wire feed speeds between 290 to 110 ipm, with

traverse speed held constant at 14 ipm; however, the author does not go into details on the size and shape of the resultant bead or work toward optimal parameters. The layer height for the multi-layer circular shapes or the reasoning for lowering the wire feed speed after step-up was also not discussed. In the welding of thicker geometries Hasselberg employed a weave method of infill rather than performing multiple passes but did not specify the parameters of the weave pattern.

Hasselberg performed a comparative study between geometries manually welded by a GTAW process and automated CMT-GMAW process, with CMT wire feed set at 205 ipm. Hasselberg noted an increase in material deposition rate, noting the single pass of CMT weld deposits four times the amount of material as the three passes of GTAW. As shown in Figure 36, the GTAW sample has increased distortion of the build plate due to the higher thermal input increasing the residual stresses induced during solidification [7]. Performing hardness tests and tensile tests, at both 65°F and 1100°F, on the specimens, Hasselberg found equivalent results for everything with the exception of ductility.

The CMT samples exhibited an average of twice the percent elongation, percent reduction in area, and strain at break when compared to the GTAW samples [7]. The CMT samples fracture surface exhibited more cleavage and visible slip planes, a sign of ductile failure. “In general, it has been shown that with larger grain size, there is a corresponding decrease in ductility. The temperature exhibited during the solidification process governs grain size and the subsequent dendrites that form. The GTAW process inherently induces a greater amount of heat input during welding; therefore, upon solidification, the solidification rate will be small and the local solidification temperature will be larger. When the solidification conditions become sufficiently slow, the dendrites and the separation

between them become large, in addition to the grain size. This will decrease the ductility of the weldment (as with the GTAW specimens), whereas the CMT-GMAW has been shown to have a lower thermal input. The lower thermal input will create a smaller local solidification temperature and will result in smaller, more finely, precipitated grains that will increase the ductility” [7].

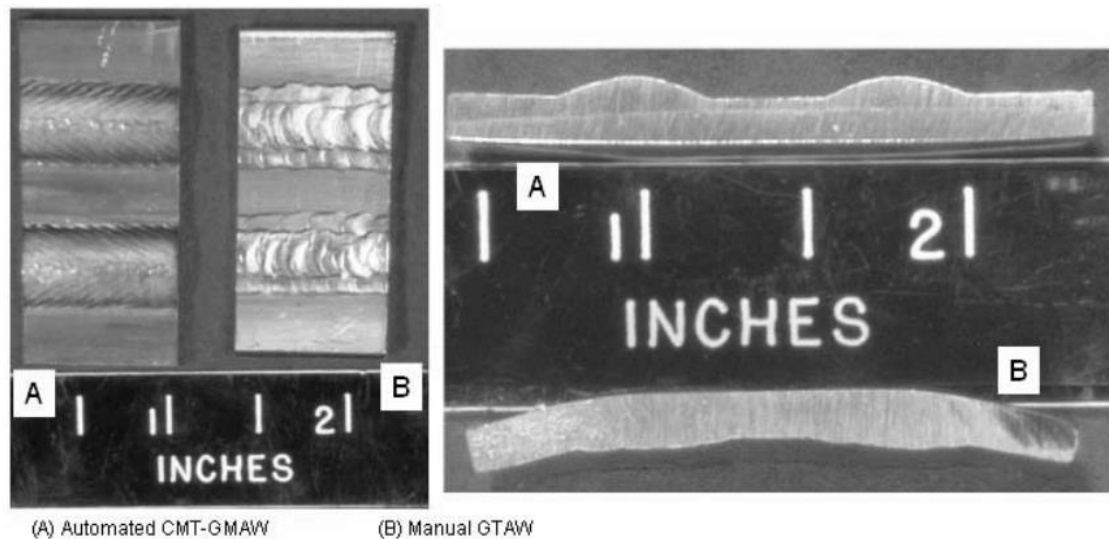


Figure 36. Manual GTAW and automated CMT-GMAW sample profiles [7]

Prior to welding, Hasselberg performed thermal treatment in order to place the base material in a fully solutioned (weldable) condition and to obtain complete recrystallization and maximum softness. Hasselberg performed solution heat treatment on all samples post welding to resolve any residual stresses and dissolve any secondary phases to homogenize the sample prior to aging [7].

In 2010, research at Cranfield University, carried out by Almeida and Williams, sought to develop a process model for multilayer Ti-6Al-4V deposition using CMT based GMAW in order to predict optimum welding parameters to achieve a target wall width/height requirement and maximize deposition efficiency. Using four welding

deposition processes, namely CMT, Pulsed GTAW (GTAW-P), Gas Tungsten Constricted Arc Welding (GTCAW), and Direct current electrode positive GMAW (DCEP-GMAW), single and multilayer Ti-6Al-4V deposits were welded for evaluation. Welding torches were coupled to a six-axis ABB industrial manipulator and shielded in an effectively inert atmosphere via two trailing shielding gas devices where 30 L/min/nozzle of 100% Argon flow was introduced around the weld. “In order to comply with a consistent build up strategy each subsequent layer was laid on top of the previous layer only when the latter had cooled down and stabilized at room temperature. An infrared pyrometer was used to monitor the substrate temperature between layers” [8]. Including the cooling time, a deposition rates of 2.58 kg/h to “in excess of 3 kg/h” were reported.

The welding parameters used for the CMT process included: 1.2 mm wire diameter, 8.5 m/min wire feed speed, 0.567 m/min travel speed, I_{AVG} of 145.8A, V_{AVG} of 14.6V, heat input of 224.1 J/mm, gas of Ar-He (50%/50%) at 15 L/min, contact tip to work distance of 13 mm. The average instantaneous power (AIP) method, Equation 1, was employed by the authors to calculate the arc energy in watts and thereafter input to calculate the heat input per unit length measured in Joules per millimeter.

$$AIP = \sum_{i=1}^n \frac{I_i * V_i}{n} \quad \text{Equation 1}$$

where, AIP (W) is the average instantaneous power

I (A) is the current

V (V) is the voltage

$$HI = \eta * \frac{API * 0.06}{TS}$$

Equation 2

where, HI (J/mm) heat input per unit length

η is the efficiency factor, 0.9 is used for CMT

API (W) is the average instantaneous power

TS (m/min) is the travel speed

Almeida and Williams performed an in-depth microstructural analysis on single pass Ti-6Al-4V deposited CMT weld beads to study the effects of different shielding gasses on the grain size and morphology in the fusion zone. Three different compositions were used, with 30%, 50%, and 70% He (remaining balance Ar) tested. Measured heat inputs of the three compositions were 290, 324, and 363 J/mm respectively, with the hotter arc promoted by the higher helium content. The authors noted finer prior β grains, a structure common in titanium weldments, are obtained at higher He content shielding gas, as seen in Figure 37, and attributed this to a variety of different mechanisms, both metallurgical and process related.

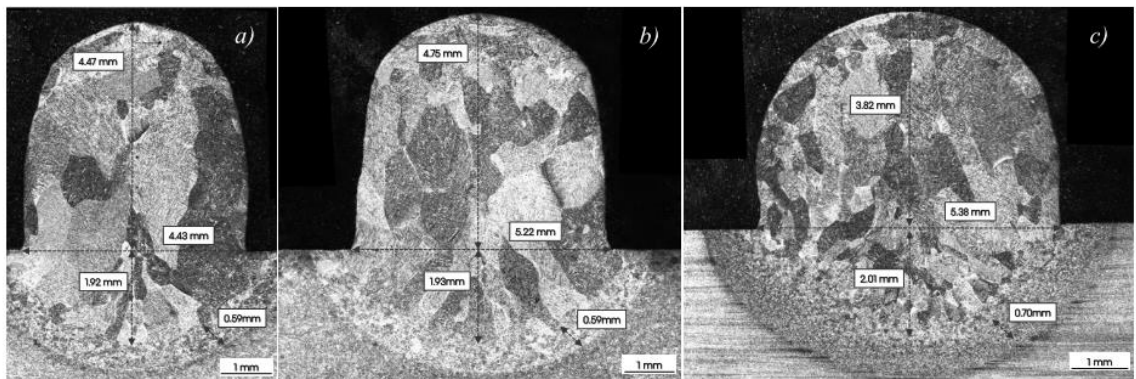


Figure 37. Optical macrographs of CMT welds showing the effect of different shielding gases mixtures a) He (30%), b) He (50%) and c) He (70%), balance argon [8]

Almeida and Williams assert that the success of fully automated WAAM is “strongly dependent on accurate predictions of the optimum welding process parameters in order to achieve a target weld bead geometry”[8]. In parameter optimization, the authors aimed to create a model for predicting bead width, the effective wall width, and the step increment between layers. Effective wall width, defined as the target wall width dimension after undergoing the post processing machining stage, is a key factor in the metal utilization efficiency, the ratio of the metal deposited to the net shape of the total delivered metal volume. For this analysis, the authors varied the wire feed speed (WFS) between 2 - 12 m/min, the WFS/TS ratio of which 15, 20, and 25 were evaluated, and the welding wire diameter using 0.9 and 1.2 mm. The authors only reported the results for effective wall width and deposition efficiency via a single 3D response surface for one of the WFS/TS ratios, Figure 38. While effective wall widths of 3.2 to 5.2 mm are reported, all with a deposition efficiency of over 80%, the authors do not publish any data for the individual factor levels. Additionally, the lack of recommendations or conclusions on favorable parameters leaves the research open ended [8].

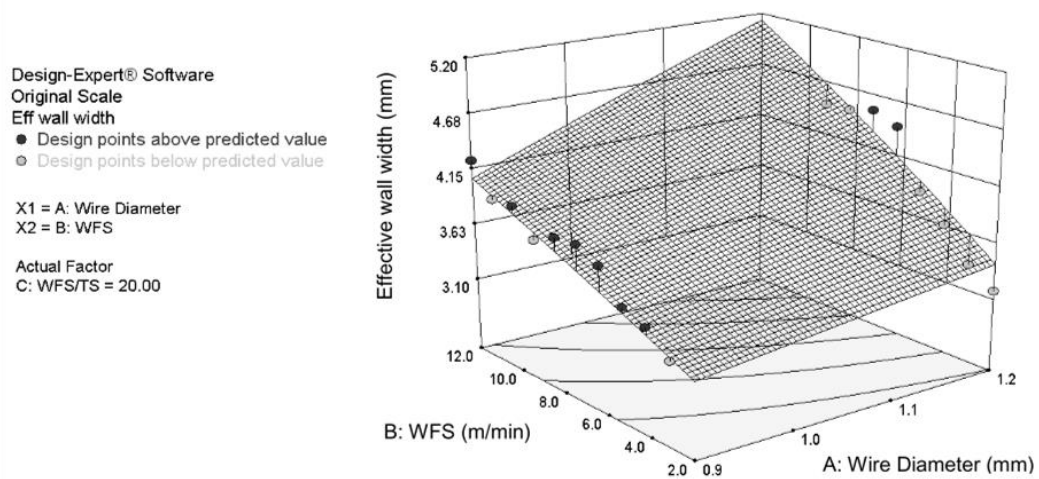


Figure 38. Predicted first order 3D response surface model for the effective wall width as a function of the wire diameter and the WFS, for constant WFS/TS ratio of 20 [8]

In 2011 research at the Indian Institute of Technology by Suryakumar *et al.*, a three-axis hybrid layer manufacturing (HLM) machine was built to integrate additive and subtractive manufacturing in one, as seen in Figure 39. The process employed two Fronius CMT units (TPS 4000 and TPS 2700) capable of either using the same material wire of different diameters, with the thicker wire for infill and the thinner for boundary contours, or using wires of different material for building composite objects. In the HLM, after every layer is deposited, the surface is milled to remove the scalloped top layer and provide a flat surface for further deposition. Face milling adds to the inefficiency of the process, measured by the yield, the ratio of the material remaining with the object to the material deposited [36]. For this reason, the authors sought to accurately model weld bead geometry and optimize the process to create beads that when placed side by side require the least amount of material removal in flattening by the interlayer milling operation.



Figure 39. Hybrid layer manufacturing (HLM) machine [36]

“While high productivity and high penetration are important considerations in joining applications, higher resolution, spatter-free/stable operation and less heat input are important in deposition applications so as to minimize distortion and finish machining allowance” [36]. Suryakumar *et al.* identified filler wire diameter, filler wire speed, welding torch speed, and the distance between consecutive beads (step over increment) as being influential parameters to study in the optimization of the HML process. Identifying a failure in past research to adequately approximate the bead geometry, the authors developed a model that relates the single-bead geometry to the process parameters and approximate the shape to be a symmetric parabolic cross-section of the form $y = a + cx^2$ [36]. As shown in Figure 40, the bead height (h), and width (w) can be introduced into the equation by substituting in $a = h$, and $c = -\frac{4h}{w^2}$, and the expression can be reduced down to:

$$y = h \left[1 - \left(\frac{2}{w} x \right)^2 \right] \quad \text{Equation 3}$$

The area can be expressed in terms of the process parameters, wire feed speed, wire diameter, and travel speed, via the equation:

$$A (mm^2) = \frac{2}{3} h * w = \frac{\pi * WFS * d^2}{4 * TS} \quad \text{Equation 4}$$

where, WFS is the wire feed speed in m/min, d is the wire diameter in mm, and TS is the machine travel speed in m/min. The bead width can be expressed by the equation:

$$w = \frac{3 * \pi * WFS * d^2}{8 * h * TS} \quad \text{Equation 5}$$

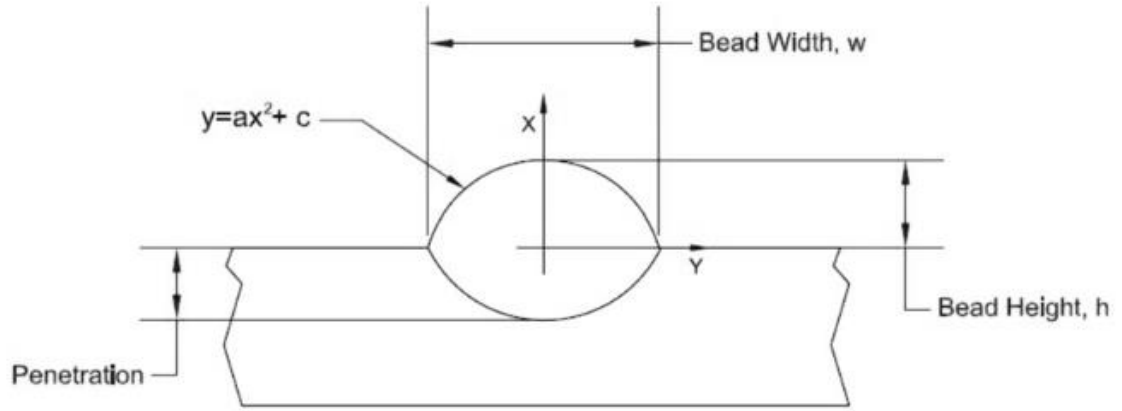


Figure 40. Parabolic cross-sectional profile of the bead [36]

Based on values obtained for bead height from 42 trials, and assuming a parabolic cross section, a second-degree regression model solves for bead height as a function of wire speed is generated as follows:

$$h = C_1 WFS^2 + C_2 TS^2 + C_3 WFS * TS + C_4 WFS + C_5 TS + C_6 \quad \text{Equation 6}$$

where, $C_1 = 0.29945E-02$, $C_2 = 0.25610E+01$, $C_3 = -0.13833E+00$,

$C_4 = 0.18947E+00$, $C_5 = -0.49778E+01$, $C_6 = 0.30299E+01$

In the 42 trials that create the model, seven wire feed speeds were used, from 4.7 to 10.4 m/min, and six torch velocities or travel speeds were used, from 0.6 to 1.1 m/min [36]. It is important to note that the authors did not section each bead to measure it and relied upon the assumption the cross section was parabolic and of the form of Equation 3, allowing for just the bead height and width to be measured for verification.

Multiple beads next to one another are modeled as overlapping parabolic beads, as shown in Figure 41. The parabolic beads have the equations:

$$p_1: y = h \left[1 - \left(\frac{2}{w} x \right)^2 \right] \quad \text{and} \quad p_2: y = h \left[1 - \left(\frac{2}{w} (x - p) \right)^2 \right] \quad \text{Equation 7}$$

and the fillet c has the equation:

$$\left(x - \frac{p}{2}\right)^2 + (y - m)^2 = R^2 \quad \text{Equation 8}$$

where, p is the step over distance, R is the radius of the fillet, and m is the height of its center

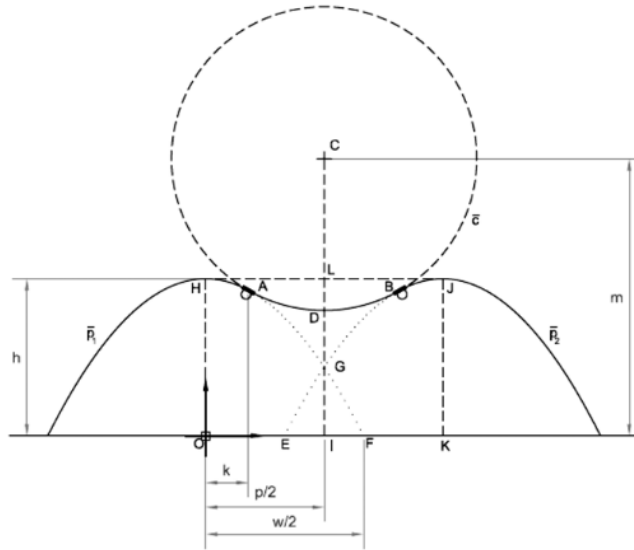


Figure 41. Geometry of the overlapping parabolic beads and the fillet [36]

In solving for the optimal step over, where the radius of the fillet is decreased to approximately a straight line, a numerical solution exists. Thus the optimal step over is:

$$p = \frac{2}{3}w \quad \text{Equation 9}$$

“For a given wire and torch speed, bead width can be calculated from the database created through single bead experiments involving only height measurements. Thus, the optimal step over increment can be set equal to two-thirds of the width” [36]. In verification trials, it is found that the model presented approximates actual bead geometry, as shown by the outline in Figure 42. The model presented by Suryakumar *et al.* “helps in the identification of the optimal process parameters corresponding to maximum yield as well as minimization of heat input”[36]. Using the model of multi-bead deposition, the

authors can predict the layer thickness and the yield as a function of the process parameters. Wire speed is an indication of the rate of heat input as is torch travel speed. For the range of wire feed and torch speed that produce a stable arc, the authors suggest using the lowest possible wire speed and fastest possible torch speed to minimize distortion, internal stresses and machining allowance. Using those speeds, and inputting the values into Equation 5 and Equation 10, the bead height and width can be solved for. Using Equation 10, the step over is obtained. These values, the authors assert, “correspond to maximum yield, minimum heat input, better geometric resolution and better heat distribution” [36].

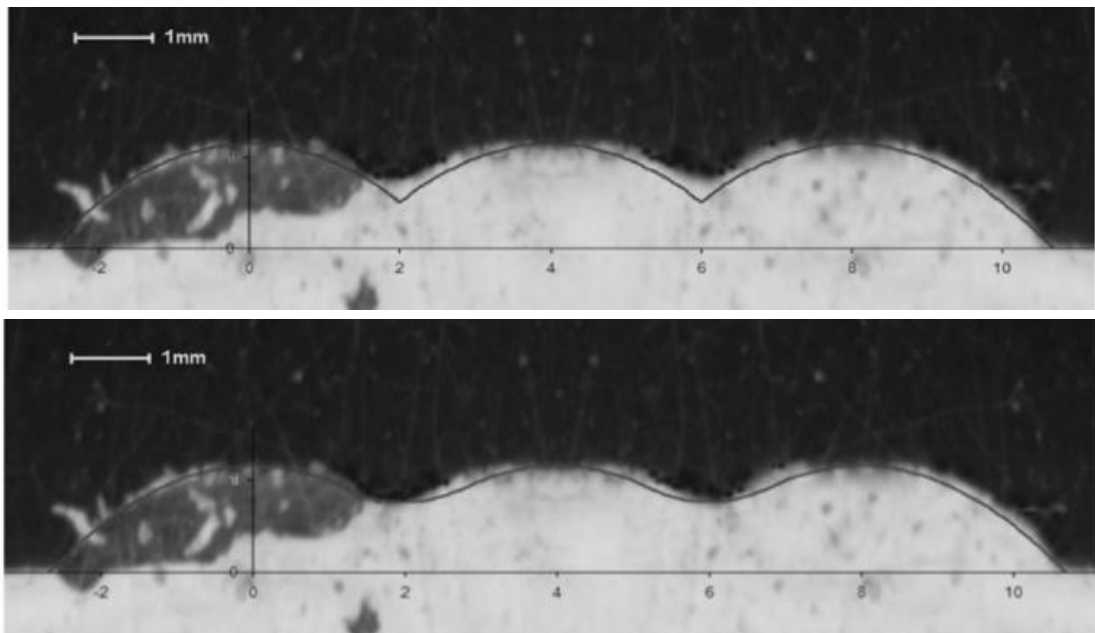


Figure 42. Comparison of the actual profile with the profile predicted by the model in two different welds [36]

Further research at Cranfield University by Ding *et al.* in 2011 was conducted to create a finite element (FE) model “to analyze the thermo-mechanical performance of the WAAM process on a 500 mm mild steel multi-layer wall structure” [37]. Four layer walls with straight-line weld beads 500 mm long were deposited with a reported bead width of 5mm and height of 2 mm. Welding wire with a diameter of 1.2 mm was used at a wire feed

speed of 10 m/min, travel speed of 8.33 mm/s. The CMT welding process had a calculated heat input of 269.5 J/mm with an assumed efficiency of 0.9 used, calculated using the Average Instantons Power method of Equation 1 & Equation 2. “A water-cooled aluminum backing plate was utilized in order to cool the sample more rapidly. A waiting time of 400 s was used between subsequent layers enabling the sample to cool below 50 °C before new layers were deposited” [37]. Temperature of the baseplate was recorded by four thermocouples installed at various locations, two along the centerline of the weld at a depth of 12 mm and 8 mm, and two on the surface of the build plate with 5 mm and 12mm offset from the centerline. Two thermal models were created, with both giving an accurate prediction of the temperature at the four thermocouple positions. The validation of the mathematical model showed accurate predictions of residual stresses and distortion as shown in Figure 43. The conclusions drawn by the authors are “that stress across the deposit is very uniform with very little influence of the preceding layers on the following layers. A significant stress redistribution is observed after unclamping. The stress at the top of the deposited wall has a much lower value than at the interface due to the bending distortion of the sample,” as shown in Figure 44 [37].

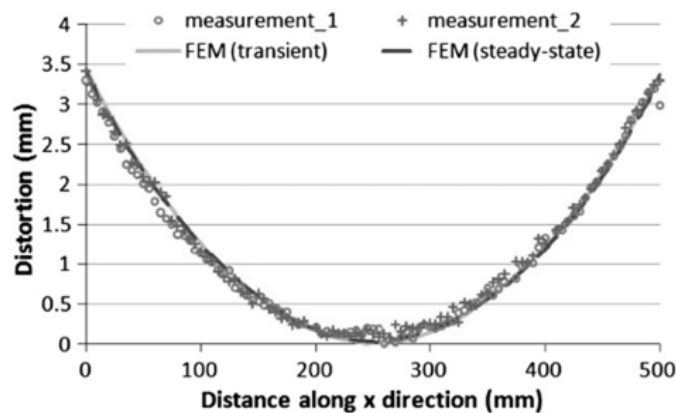


Figure 43. Distortion verification along the longitudinal direction [37]

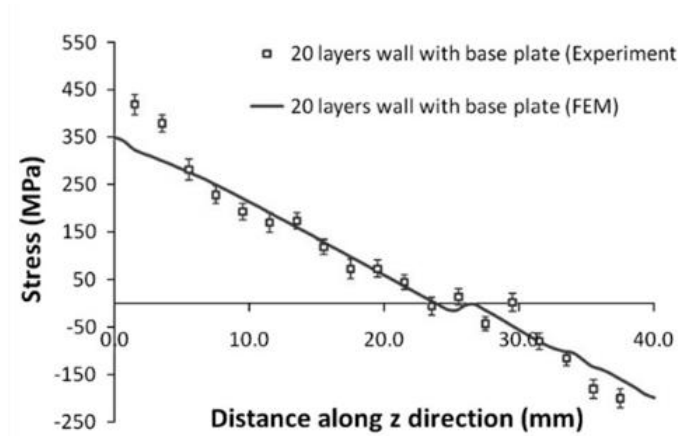


Figure 44. Longitudinal stress along the normal direction [37]

The following year, in a continuation of the study at Cranfield University, Jialuo Ding, studied different deposition parameters and build path strategies with finite element models (FEM) to reduce residual stresses and distortions. As illustrated in Figure 45, a large area of compressive stresses is generated in front of the fusion zone due to thermal expansion of the heated material with is being constrained by the surrounding cold material, with stresses in the fusion zone being very low due to the high temperature. After the heat source passes, the rapid cooling rate results in high tensile stresses due to material contraction being restrained by surrounding cold material [5]. “Classified by different directions, residual stresses contain three components. These are the longitudinal stress in the direction of welding, transverse stress which is perpendicular to the direction of welding and normal stress through the thickness of the material” [5]. The longitudinal stress is typically the dominant stress, with the normal stress being comparatively small.

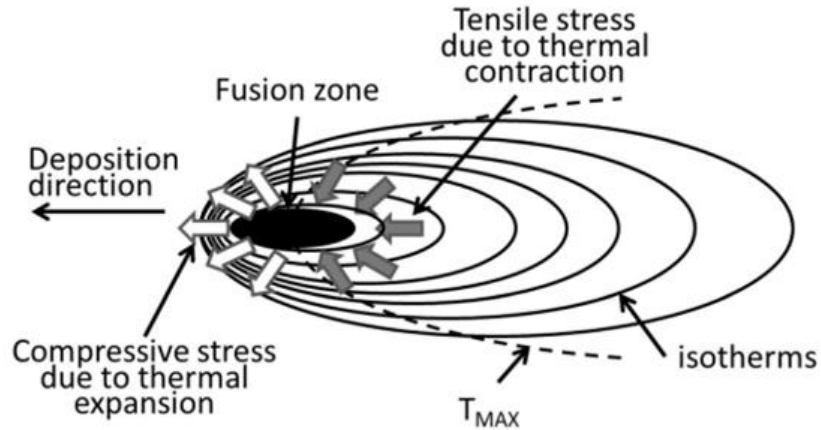


Figure 45. Temperature and stress field around a welding heat source [5]

Ding outlines many methods that have been developed for minimizing the effects of residual stresses, placing them into two categories depending on whether additional processing is required or not. Techniques such as applying a proper clamping system, prebending, preheating, thermal tensioning, global mechanical tensioning, local mechanical tensioning, and post-weld processing are the main methods for mitigating residual stresses or distortions in welding process with extra manufacturing process and facilities [5]. In contrast, by optimizing welding parameter and the welding sequence, the residual stresses can be controlled without the need for additional effort. Lowering the heat input results in a narrower tensile and residual stress zone and lower stress magnitude. With respect to travel speeds, welds exhibit the same level of maximum longitudinal stresses, however the slower travel speed results in a larger area of the longitudinal residual stress. In building components with thick walls, using a spiral pattern from the outside to the inside results in the lowest the lowest level of deformation and distortion [5].

Ding highlights the ability of the FEM of the prior paper to make detailed and accurate predictions on temperature distribution, stress distribution and the distortions, noting the drawback of this method being that it is highly computationally expensive. Using

a mechanical model with steady-state thermal data, computational time can be reduced by over 99%, from 51 hours to 10 minutes in one case. This simplified model is used to provide estimations for residual stress and distortions in the optimization of CMT process parameters.

Ding identifies the wire feed speed (WFS) and the travel speed (TS) as the most influential controllable factors. Research was carried out by Ding using a CMT welder attached to a six-axis industrial robot. Steel wire 0.8 mm in diameter was used. Build plates were attached to a water-cooled backing plate to cool the samples rapidly with a waiting time of 400 seconds was used between each layer, the same mode of operation as previous research. The study was carried out with a contact tip to work distance (CTWD) of 13 mm. A total of 43 trials were conducted with wire feed speed varied from 3 to 15 m/min at six factor levels and travel speed varied between 0.1 and 0.9 m/min in increments of 0.1 m/min. Not all levels of travel speed were used for each level of wire feed speed since unstable conditions resulted. The output of the study included the effective wall width (EWW), surface waviness (Wav), average layer height (ALH), heat input (HI), penetration (P), and length of the heat source (LoHS). Walls 10 layers high and 250 mm long were deposited. “EWW and P were measured from the etched cross-sectional macrophotographs, Figure 46. Wav was measured utilizing a high-resolution scanning type confocal optical microscope. ALH was taken the average value of the step increments after four layers of the wall. The values of LoHS were obtained by measuring the length of the isotherms noticeable from the weld pool surface ripple markings after the first layer of the deposition pass” [5]. Heat input was calculated using the Average Instantons Power method from Equation 1.

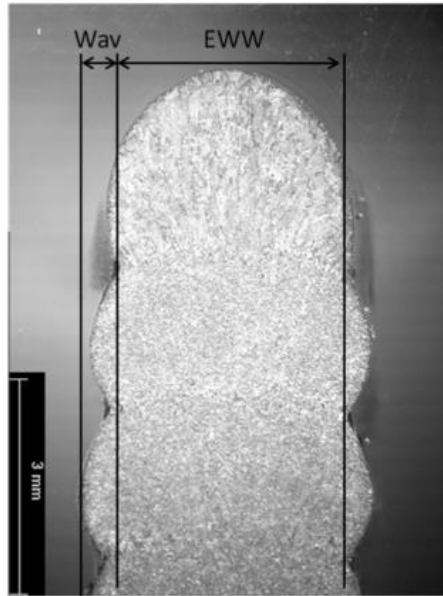


Figure 46. Macrograph of WAAM sample showing EWW and Wav [5]

The influence of the process parameters on the geometry of the deposited wall is illustrated by the contour graphs in Figure 47 where all 43 trials are plotted. The graph of EWW indicates that higher WFS with lower TS result in wider deposited wall. From graph b, it can be seen that WFS does not have a significant effect on the surface waviness while TS has a strong impact when it is below 0.4 m/min. An area of low levels of surface waviness is seen with TS value is higher than 0.4 m/min and WFS is smaller than 12 m/min. Graph c, indicates that in general higher WFS with lower TS result in taller deposited layers. The average layer height is comparably stable in the area where TS is higher than 0.5 m/min, which varies from around 0.8 mm to around 1.5 mm [5].

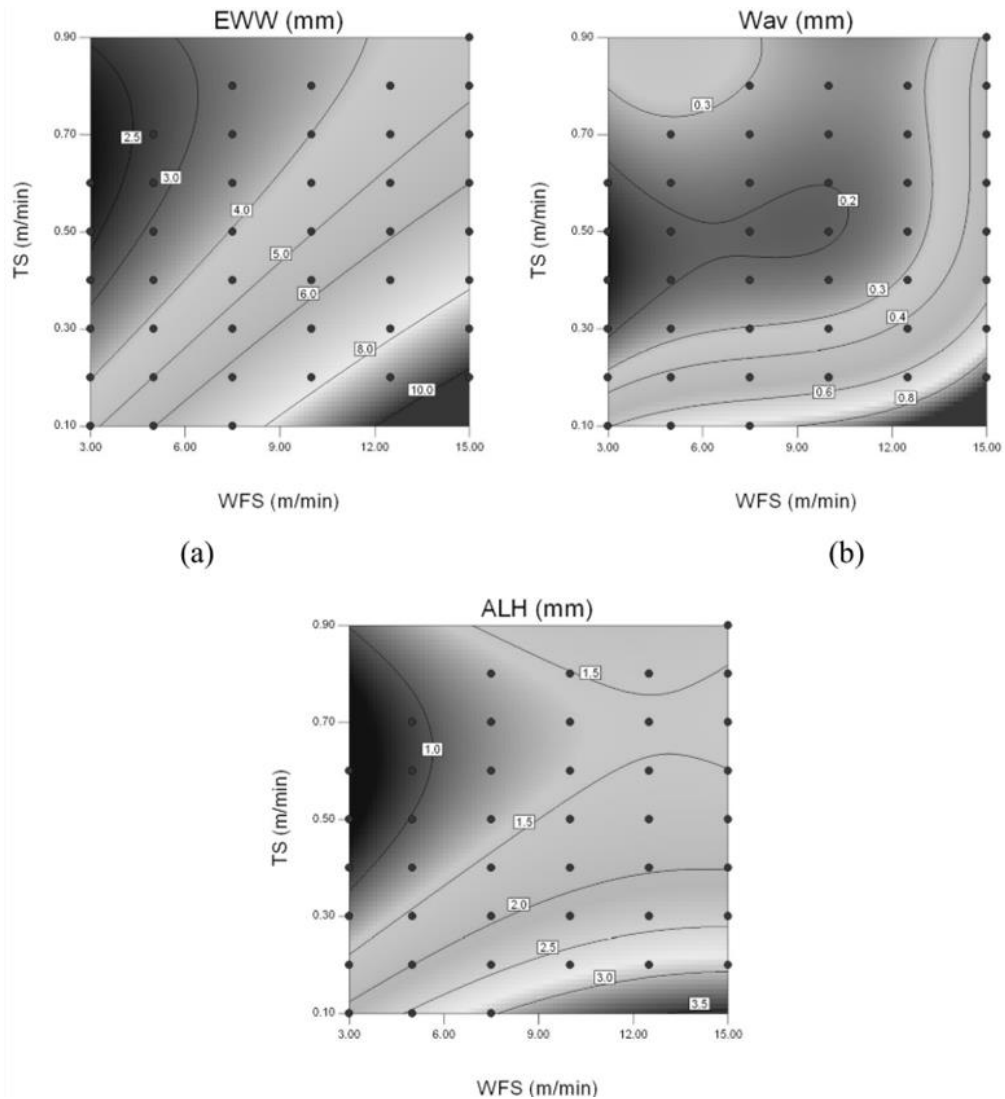


Figure 47. EWW, Waviness, and ALH as functions of TS and WFS [5]

Evaluating the relationship between deposition parameters and stress distributions was done using FEM in which 24 trials were conducted. The wire feed speed was varied between 5 and 12 m/min at eight levels. Each level featured three iterations of wire feed speed/travel speed ratio at 10, 15, and 20. Five layer tall walls were simulated using a cooling time of 300 seconds. The trials indicate that low WFS/TS ratios (faster travel speeds) results in a much narrower stress zone than the higher ratios. Comparing different wire feed speeds within the same ratio, the stress zones generated by the lower WFS values

are slightly narrower. “Higher WFS/TS ratio causes higher heat input level. In consequence, it results in a wider area of high temperature where the thermal strain exceeds the yield strength during the thermal cycle, which causes a wider stress zone” as shown in Figure 48 [5]. This data suggests the ideal parameters would be a lower wire feed speed and faster travel speed, a similar conclusion to that made by Suryakumar *et al.* [36].

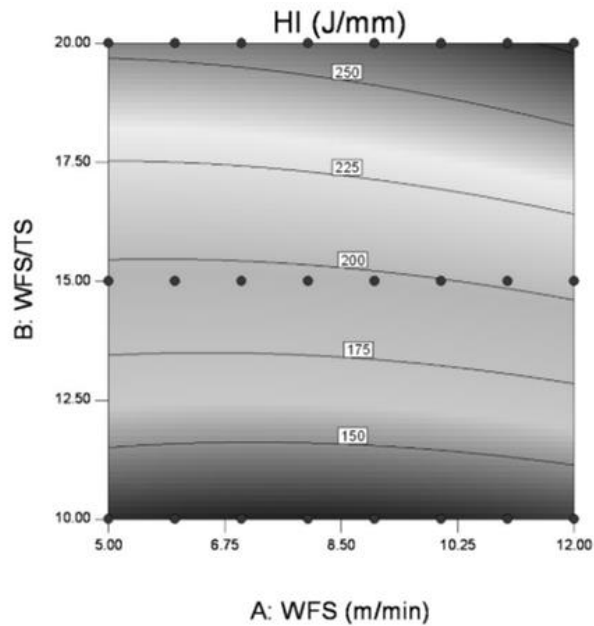


Figure 48. Heat input distribution plot [5]

The effect of inter-pass cooling time was studied, with 5 second cooling time evaluated against the 400 second cooling time used in the rest of the study. As shown in Figure 49, the 5 seconds is not enough for the component to cool down before the subsequent layer of material is being applied, and the temperature keeps rising. The first layers are effected by the cooled backing plate, but beyond the fourth layer, the melt pool reaches steady state and the residual temperature increases linearly. With respect to residual stresses, the 5 second inter-pass cooling time results in lower stress in both the transverse and longitudinal direction. “The results would seem to favor short inter-pass time because of lower residual stress level, distortion and higher production yield. However, in practice

the residual temperature needs to be limited to a certain level, otherwise the residual temperature may cause problems like loss of dimension tolerances and poor surface finish” [5]. Only two factor levels were compared for this research, one being effectively zero cooling, and one being total cooling. Additional levels would be of interest to find an optimum value.

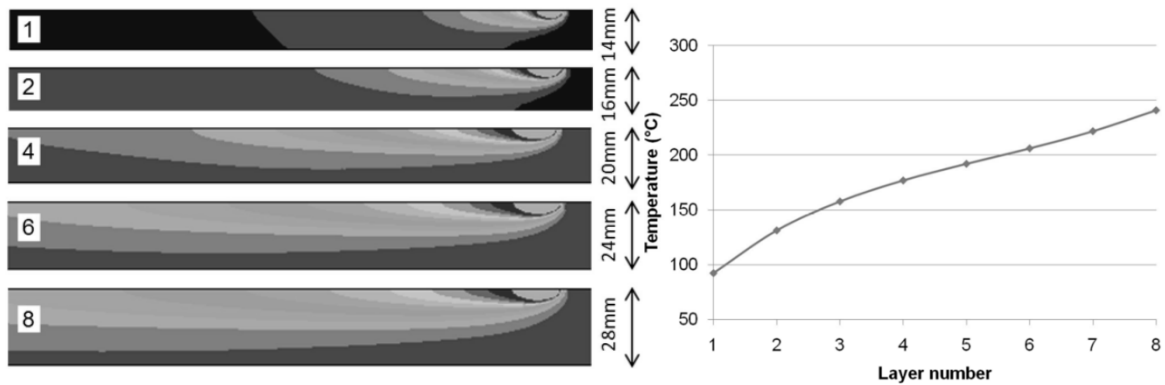


Figure 49. Temperature distribution of trials with 5 second inter-pass cooling (left) and the residual temperature of the midpoint after each layer (right) [5]

In the study of a robot program generator, Ding notes the current process of programming robot movements is tedious and time-consuming for complicated WAAM parts. The author also notes that, “Tool path generation can be accomplished by “mirroring” milling paths generated from CAM module in commercial CAD/CAM software” [5]. Using a program developed for their specific robotic arm, slicing and welding path generation is brought together to convert stl files directly into robot paths. Key parameters for the welding process can be easily set by the users from the graphic interface, including welding process parameters such as travel speed of the welding torch, waiting time between layers, building sequence for the part with several subparts, etc.

Research continued at Cranfield in 2012 with the dissertation of Pedro Miguel Sequeira Almeida offering the most in depth and comprehensive overview of CMT-

WAAM to date. Almeida stated that the CMT process is appropriate for WAAM applications based on the excellent deposition characteristics, process behaviour and arc welding stability. “The constant current static volt-ampere characteristic of the power source ensures constant current flow conditions through the workpiece. The digital process control offered by the cold metal transfer process, allied with a variable wire feed speed control feature, allows the arc-length to be maintained nearly constant during processing with respect to variations in contact tip to work distance” [19].

One unique aspect of Almeida’s setup is the use of an Aluminum water cooled backing plate for fixturing the build plates to, as shown in Figure 50. “The water cooled base plate was intended to provide a larger heat sink to improve the heat flow during the manufacturing cycle and therefore reduce the waiting time between subsequent deposited layers” [19]. Additionally thermal imaging was used to capture the heat flow, with “a FLIR A320 thermal video camera at up to 30 Hz over a 7.5-13 μm spectral range, with a field of view of 25° by 18.8°, and a minimum focus distance of 0.4 m”[19].

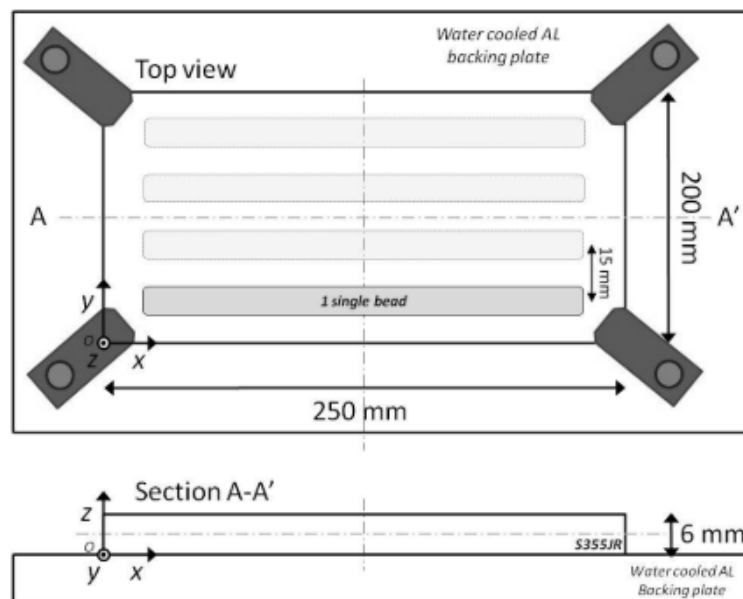


Figure 50. Clamping fixture with water cooled backing plate used by Almeida [19].

Almeida defined the parameters of interest of his single-bead geometry study as bead width, bead height, remelting ratio, penetration depth, dilution, deposition rate, contact angle, penetration area, reinforcement area, and aspect ratio, all displayed in Figure 51.

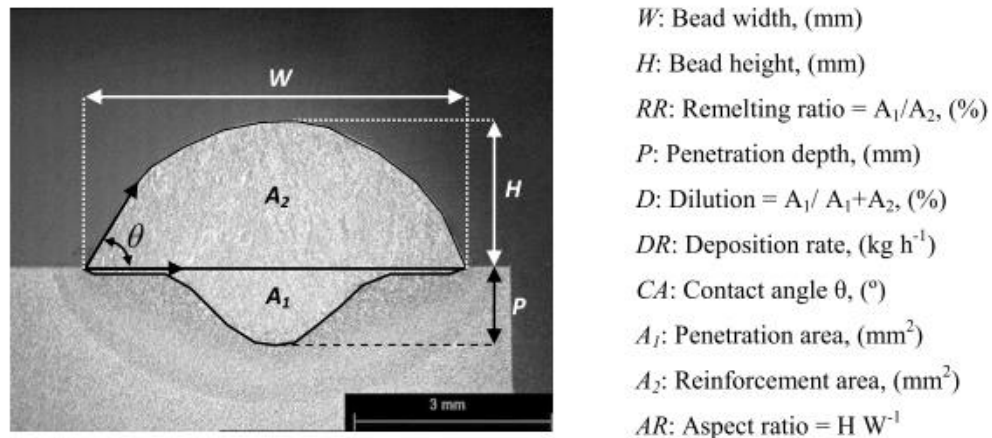


Figure 51. Macrograph of single-bead with measurable factors shown and defined [19]

In the deposition of Ti-6Al-4V, Almeida found that the CMT process results in spatter free deposition with greatly improved weld bead straightness and uniformity compared to the GTAW or PAW processes. Studying the mechanical properties of CMT compared to GTAW, Almeida found the static mechanical performance of material showed better average ultimate and yield tensile strength both in the horizontal and vertical directions.

Research carried out in 2014 by Gu *et al.* at Cranfield University, CMT based WAAM of aluminum and issues with porosity and low mechanical properties are studied. “The implementation of traditional welding process for WAAM aluminum is currently limited by solidified defects. Porosity is the main problem in aluminum alloys, which are far more susceptible to this defect than all other structural metals. This is because merely trace levels of hydrogen usually exceed the threshold concentration needed to nucleate

bubbles in the molten pool” [38]. Four modes of operation are present in the CMT Advanced 4000 R used by the authors, traditional CMT, CMT pulsed (CMT-P), a variant of this process is where conventional spray is mixed with the dip transfer mode, and two advanced variants (CMT-ADV and CMT-PADV). This variant allows for polarity reversal and therefore AC operation.

A Fronius CMT Advanced 4000 R was used as the power source and connected to a six-axis ABB robotic arm. ER2319 aluminum alloy wire was used and shielded with 100% Ar at a flow of 25 L/min. CTWD was kept at 15 mm while depositing walls 500 mm long and 200 mm high. All four variants of the CMT process were employed using variable WFS and TS. “All specimens were naturally aged prior to tests for a minimum of 30 days after deposition” [38].

Analysis of the microstructure show that the CMT-PADV process effectively eliminated porosity compared to a wall built by the pulsed CMT (CMT-P) process. “Conventional processes, which generate high levels of porosity due to their high thermal heat input level, the narrow finger-shaped molten pool and the coarse grain structure, are considered not suitable for the WAAM process for aluminum” [38].

Research presented in 2014 by Gerhard Posch of Fronius International offers a comprehensive technology overview of the CMT process along with the creation of “turbine blade” geometry out of duplex stainless steel. On CMT welding Posch notes, “the standard wire diameter for the CMT process in general is 1.2mm. In this combination, minimum wall thicknesses of around 4-5 mm can be realized, depending on the wetting characteristics during the metal transfer from the wire tip to the weld pool. Broader cross

sections can be realized by torch weaving during welding and/or putting a certain number of welds side by side – up to establishing complete overlays” [39].

In the welding of turbine blades, such as the one shown in Figure 52, inclined planes can be made by offsetting the welding torch with respect to the previous layer. If the base is fixed, planes up to 15% from vertical can be established, but if the base is mounted on a commercial turntable, very complex 3D shapes can be produced although, programming effort rises exponentially [39]. Posch sees this 15% incline or decline to be the maximum limit of angled walls but it is not clear if this is only for single-bead wall thickness or extends to multi bead thick structures.



Figure 52. CMT WAAM “turbine blade” [39]

Posch states that, “care has to be taken in respect to the heat input caused by the electric arc: the smaller the cross section, the less the heat input has to be to prevent excessive remelting and in further consequence a “burn through” of the already welded seams. This means in practice that the welding current has to be limited and after each seam

a certain time for cooling down of the already piled up seams has to be given” [39]. Posch does not state his inter-pass cooling time used in the fabrication of the turbine blade geometries but does affirm the consensus that inter-pass cooling is necessary.

In the mechanical and technological investigation of duplex stainless steel blade geometry, Böhler CN 22/9 N-IG welding wire was used with a diameter of 1.2 mm, to produce the blades having dimensions of 200 mm x 200 mm x 10 mm. The blades were made of 136 layers and welding took 87 minutes including inter-pass cooling times. Layer height can be extrapolated to be approximately 1.5 mm. The total deposition rate was around 1.7 kg/h. “The blades were established on a horizontal mounted base plate. The decline from the vertical was achieved by a 0.5 mm horizontal sideward adjustment of the torch after each layer” [39].

The mechanical properties of the weld are reported as follows: yield strength of 660 MPa, tensile strength of 830 MPa, 28% elongation, toughness of 85, and delta ferrite content between 30 – 60 FN. However, Posch does not specify the direction of the tensile test and does not perform multiple examinations.

Research from Wollongong University published in 2015 by Ding *et al.* reexamines the single and multi-bead weld model, to build understanding and accuracy in deposition in multi-bead overlapping parts. “It was shown that the optimal model for the bead profile is largely dependent on the ratio of wire feed rate to welding speed” [40]. The author identifies a failure in previous research, such as that performed by Suryakumar *et al.*, where only bead height and width are measured and the cross section is assumed to fit the model. “The relative errors of bead cross-sectional area predicted by their models were as high as 15–20% in certain circumstance” [40].

Experimental tests were conducted using a six-axis robotic arm and a Fronius welder with copper coated steel wire 1.2 mm in diameter with a wire feed rate of 5 m/min. Welding travel speed was varied from 200 – 550 mm/min with CTWD set at 18 mm and 82% Ar, 18% CO₂ was used to shield the weld pool at a flow rate of 22 L/min. “A 3D laser profile scanner with a resolution of 0.02 mm was used to accurately measure the cross-sectional profile of the weld beads at different locations along the welding direction. Each bead profile was scanned 200 times” [40]. As shown in Table 2, the parabola, cosine, and arc models all approximate and can accurately predict single-bead shape with R² values greater than 0.975. Only one wire feed was used by the authors at 8 different welding speeds, reported by λ , the ratio of wire-feed rate to welding speed.

Table 2. Three bead models and the related bead height, bead width, and bead area (top) and the curve fitting of the mathematical models [40]

Models	Model function	Bead height, h	Bead width, w	Bead area
Parabola model	$y = ax^2 + c$	c	$2\sqrt{-\frac{c}{a}}$	$A_p = \frac{4c}{3}\sqrt{-\frac{c}{a}}$
Cosine model	$y = a \cos(bx)$	a	$\frac{2a}{b}$	$A_c = \frac{2a^2}{b}$
Arc model	$y = \sqrt{a^2 - x^2} + b$	$a - b$	$2\sqrt{a^2 - b^2}$	$A_a = \text{arc cos}(-b/a) - b\sqrt{a^2 - b^2}$

S. no.	Process parameters		Parabola model			Cosine model			Arc model		
	V_w (mm/min)	Ratio λ	a	c	R^2	a	b	R^2	a	b	R^2
1	200	25	-0.0840	3.3418	0.9989	3.395	0.2411	0.9937	7.010	-3.720	0.9990
2	250	20	-0.0955	3.0176	0.9996	3.071	0.2716	0.9969	6.216	-3.251	0.9841
3	300	16.7	-0.1040	2.7210	0.9994	2.765	0.2971	0.9951	5.715	-3.042	0.9859
4	350	14.3	-0.1144	2.5420	0.9976	2.592	0.3248	0.9991	5.220	-2.727	0.9786
5	400	12.5	-0.1262	2.4615	0.9934	2.483	0.3461	0.9968	4.941	-2.571	0.9915
6	450	11.1	-0.1221	2.1919	0.9943	2.239	0.3625	0.9988	4.866	-2.717	0.9923
7	500	10	-0.1405	2.1513	0.9934	2.198	0.3925	0.9982	4.299	-2.194	0.9967
8	550	9.1	-0.1511	2.0704	0.9873	2.123	0.4173	0.9961	4.052	-2.034	0.9943

In the flat-top overlapping model (FOM) of Suryakumar *et al.*, highlighted earlier in this literature review, adjacent beads have a valley between them represented by a straight line connecting the peaks of beads, Figure 41. The authors propose a new model, after observing a “critical valley” that better approximated the cross section of multiple

welding beads. The principle of the tangent overlapping model (TOM), shown in Figure 53, is that there is a critical center distance d^* for which the center distance d must exist at.

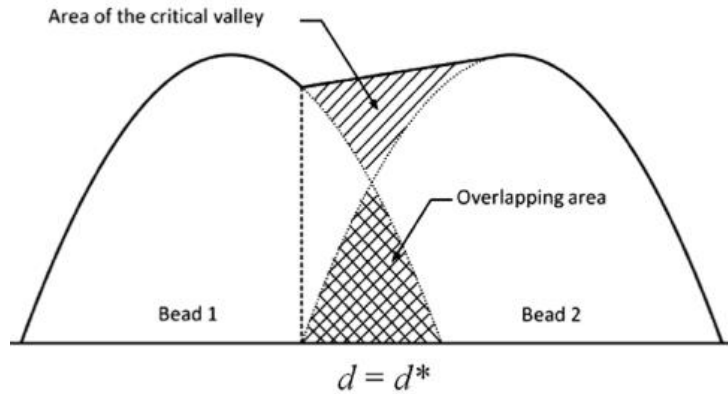


Figure 53. Tangent overlapping model (TOM) [40]

For the case shown in Figure 53, where $d=d^*$, a numerical solution exists for the critical distance as a function of bead width:

$$d^* = 0.738w \quad \text{Equation 10}$$

For the case where $d > d^*$, excessive waviness results as the valley is not filled in, creating an unstable deposition and leading to greater problems as the weld progresses to multiple layers, as shown in Figure 54. When the step over is less than the critical distance, $d > d^*$, the second weld bead is deposited and excessive overlapping results in uneven layer height and thickening of the internal layers with external layer slumping as the weld progresses.

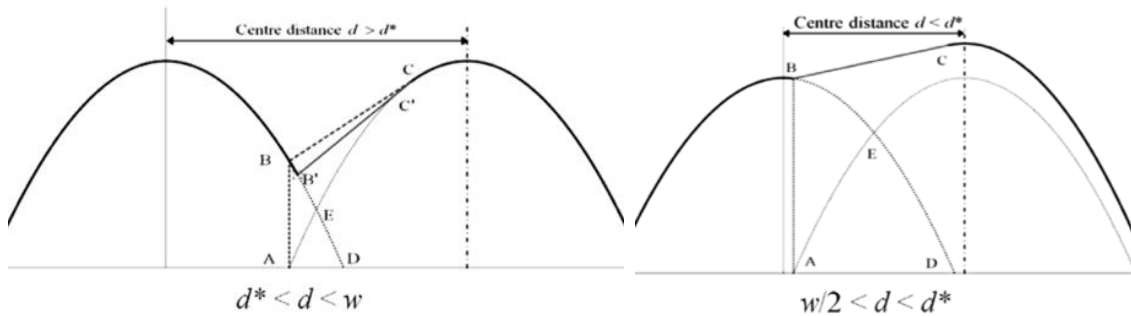


Figure 54. Diagrams of the TOM for cases of $d > d^*$ (left) and $d < d^*$ (right) [40]

The FOM of Suryakumar *et al.* proposed an optimal center distance of $d=0.667w$ [36]. According to the TOM, this would lead to unstable results, as this is less than the critical distance. While the research of Suryakumar *et al.* was focused on HLM where the deposits were machined after each layer, the work of Ding *et al.* and the model proposed is for multi-bead and multi-layer deposits, without inter-layer machining. To verify the model, Ding *et al.* deposited six parallel beads at both distances ($0.667w$ and $0.738w$) and repeated the process over 5 layers, scanning the surface after the first, third, and fifth layers. As shown by the results at the top of Figure 55, using the FOM model, the first bead drops off (shown on the left) and becomes much shorter after five layers are deposited. The variation of the height of the across the entire surface of TOM model is smaller, however the waviness of the surface is of greater magnitude. Ding *et al.* reported the yield of the FOM and TOM two to be 75.7% and 84.1% respectively, indicating the TOM is more material efficient [40].

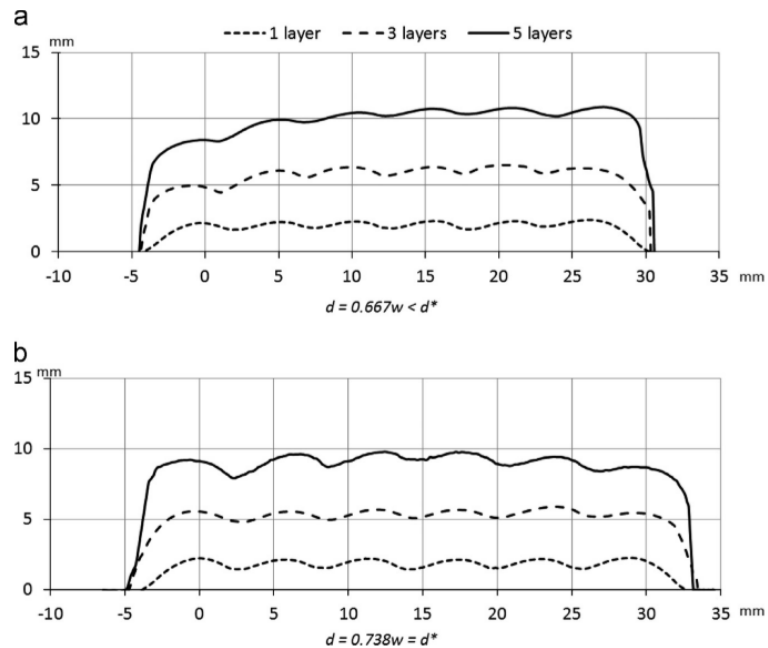


Figure 55. Multilayer deposition at $d = 0.667w$ (top) and $d = 0.738w$ (bottom) [40]

In research published in 2015 by Inês Pinto out of Técnico Lisboa, the CMT WAAM process is applied to the deposition of Nickel components, specifically Inconel 625. Walls 120 mm in length and 17 mm high were deposited using wire 1 mm diameter wire, 20 L/min Argon shielding gas, and austenitic stainless steel build plates. A Fronius CMT Advanced 4000 was employed and mounted on a Kawasaki JS6 robotic arm. For investigations in the macrostructure, such as layer width, size, and scale, the software Scentis was used, Figure 56. In the trials performed by Pinto, current and travel speed were the two control variables and were varied between 90 – 130A and 200-300 mm/min. Pinto counted the number of layers the wall required to reach 17 mm and calculated the total heat input [1]. The results of this study were insignificant and not of statistical importance. The ranges of welding parameters evaluated were narrow and the welding was poor quality.

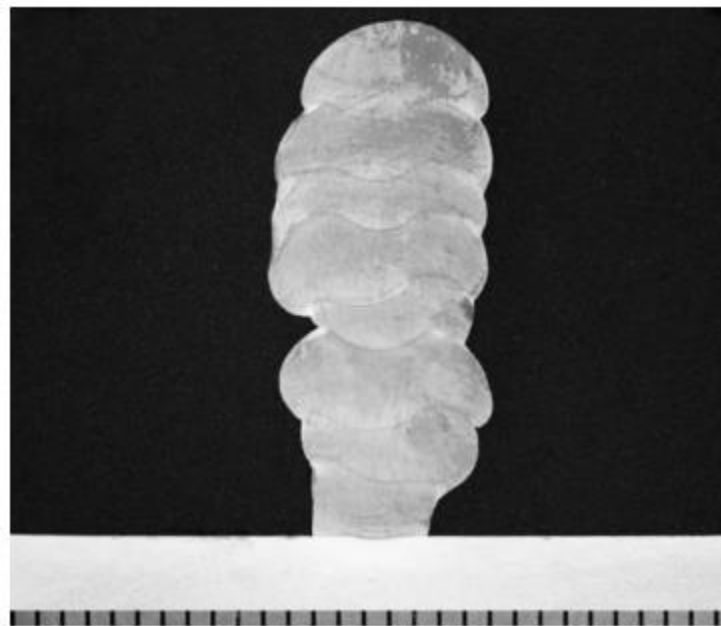


Figure 56. Macrostructure of Inconel 625 wall [1]

Research published in 2017 by Gerhard Posch *et al.* continues on his aforementioned earlier work with the “turbine blade” geometries and includes a more in-

depth exploration on microstructure evaluation. Duplex stainless steel filler wire 1.2 mm in diameter is used with 0.5 mm horizontal step over. “The welding parameters were kept constant for all layers: the wire feed rate was set to 4.2 m/min, the welding speed was 36 cm/min. The amperage was 145 A, the voltage 11.9 V, and the CMT frequency was 100 Hz. Shielding gas composed of 98% Ar and 2.5%CO₂ was used. Additionally, the CMT torch oscillated 8 mm at a frequency of 2 Hz” [3]. Posch does not go into any more detail about the 8-mm torch oscillation. Posch reports a wall thickness of 8-10 mm [3]. It is not clear if the welding travel speed accounted for the additional movements of the torch.

Expanding on his past work, Posch investigates the surface quality of the as welded blade and finds it to be comparable in roughness to sand castings, hot rolling, or flame cutting, with an Ra value of 24.5 μm. Chemical analysis showed that the measured composition was very similar to the composition of the filler wire. Sectioning the blade in different regions, four specimens are created for further microstructural examination, as shown in Figure 57.

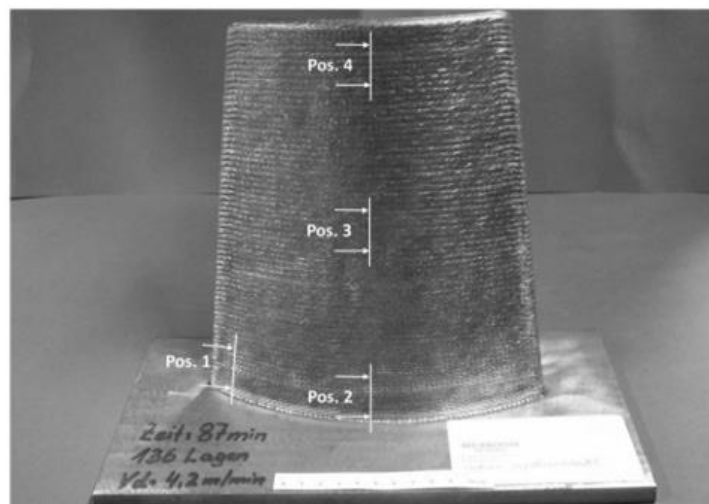


Figure 57. Location of specimens for microstructural investigation [3]

Approximately eight layers are sampled in each of the four different regions, the welding start area (Pos. 1), the first layers in the middle of the blade (Pos. 2), the middle of the structure (Pos. 3), and the upper layers (Pos.4). Performing hardness tests on the samples from the bottom layers (Pos. 1&2) across the profile and covering the first five layers revealed a constant hardness level of 266 HV and 270 HV respectively for Pos. 1 and Pos. 2. These fit the typical hardness values associated with duplex stainless steel weld material of 240-320 HV10. Investigation into the hardness of the other samples was not performed.

“Although it is well known that the applied horizontal welding position is in general not prone to pore formation or lack of fusion, a closer look was done on polished specimens using light optical microscopy (LOM) and scanning electron microscopy (SEM)” [3]. No porosity or lack of fusion was observed, however numerous non-metallic, Si-Al-O containing inclusions, in sizes up to 1 μm were observed by Posch. Only a few inclusions in the range 1–4 μm were detected uniformly at all sample positions; “such types of inclusions are typical for GMAW weld metals and are small slag particles” [3].

“For the light optical investigations, a Beraha II etching agent (mixture of water, hydrochloric acid, ammonium bifluoride, potassium metabisulfite) was applied. The resulting microstructures of the different cross sections are shown in Figure 59” [3]. Columnar-like grain growth is visible, with austenite (white) in a colored δ -ferrite matrix.

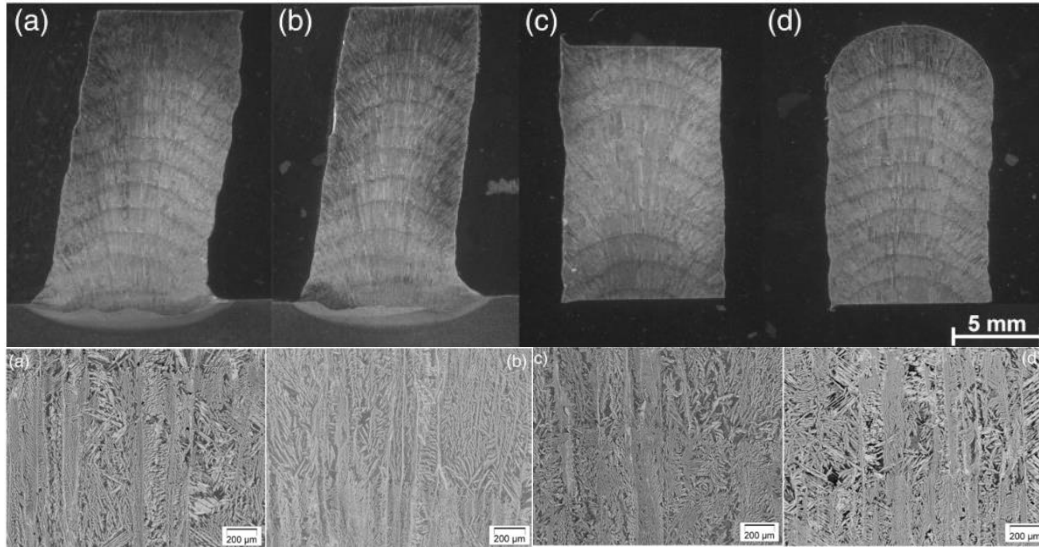


Figure 59. Etched macroscopic cross sections (top) and microstructure in light optical investigation (bottom). a) Pos. 1, b) Pos. 2, c) Pos. 3 d) Pos. 4 [3]

“The first look at the duplex stainless steel weld metal microstructure of the CMT-MAM sample at lower magnification with light optical microscopy raised some concerns about “black areas” (Figure 58 left). SEM examination at higher magnification (Figure 58 right) identified the “black areas” as a very fine microstructure, but no porosity or undesirable phases were detected. This fine microstructure occurs mainly in the transition zone between two seams” [3]. An ion argon beam polisher was used to create the samples.

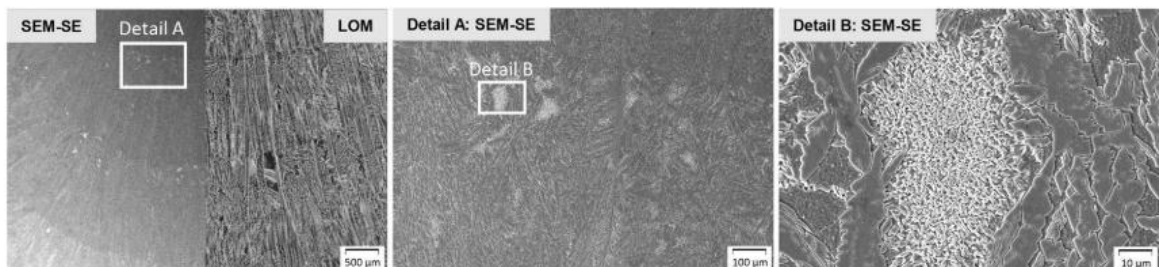


Figure 58. Microstructure investigation on “black areas” (Pos. 2) [3].

To evaluate the mechanical properties of the CMT blades, tensile and toughness tests were carried out using samples created at the locations shown in Figure 60. Specimen length 55 mm and height at 10mm but the thickness for transversal specimens was 7.5 mm while longitudinal samples were 5 mm. “The impact strength of the blade is nearly the same under all conditions, independent on the examination area. Only the location of the notch in case of longitudinal testing has a marginal influence on the variation” [3]. “The impact strength showed that all toughness values are in general high compared to around 100 J achieved with standard ISO-V specimen size as stated on the filler metal data sheet” [3]. Results are shown in Table 3.

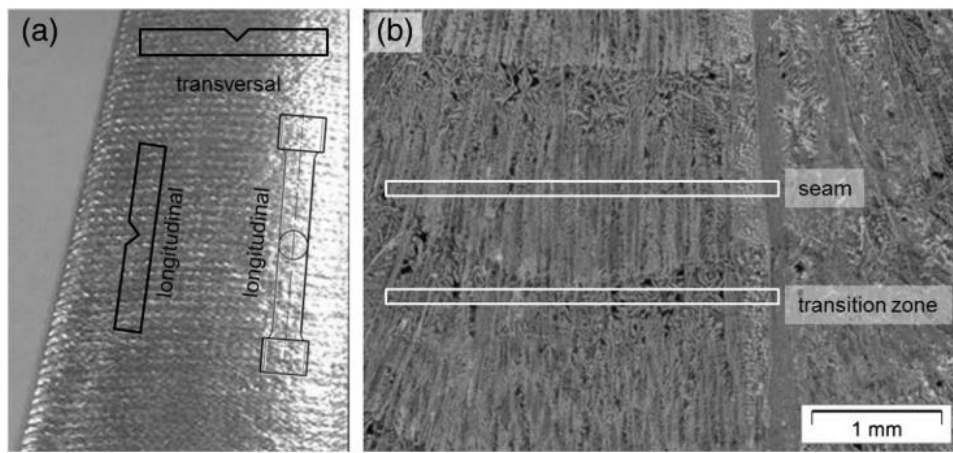


Figure 60. Location of Charpy and tensile test specimens (left) and position of notch in relation to the microstructure (right) [3]

Table 3. Results of ISO-V toughness tests [3]

		Charpy size	Absorbed energy	Impact strength	
	Sample position	Notch position	[mm]	[J]	[J/cm ²]
CMT blade	Transversal		55 × 10 × 7.5	77 ± 3.3	129 ± 5.9
	Longitudinal	Transition zone	55 × 10 × 5	51 ± 3.4	129 ± 8.3
	Longitudinal	Seam	55 × 10 × 5	51 ± 5.2	128 ± 11.9
All weld metal	Transversal		55 × 10 × 10	70	~100

“Three tensile test specimens, according to DIN 50125—special geometry with a size $\varnothing 6 \times 30$ mm, were tested according to DIN EN 6892-1 at room temperature. The test area was in transverse weld direction, which is different to the test area of all-weld test samples for filler metal data sheets, where the examination area is in longitudinal direction of the weld. The measured values of yield strength ($R_{p0,2}, R_{p1,0}$), tensile strength (R_m), Young’s modulus (E), elongation (A; $L_0 = 5d_0$) and reduction in area (Z) in comparison to data sheet values are given in Table 4.” It is not clear how many replicates of the tests were performed by Posch for the tensile test or the Charpy tests [3].

Table 4. Results of tensile tests [3]

	$R_{p0,2}$ [N/mm ²]	$R_{p1,0}$ [N/mm ²]	R_m [N/mm ²]	E [N/mm ²]	A [%]	Z [%]
Mean value	455	576	717	195	28	68
Data sheet	510	550	700	–	25	–

A case study published in 2017 by The Welding Institute (TWI) evaluates the CMT WAAM process and their ongoing research efforts creating aluminum components. The researchers produced walls by performing multipass welds noting, “the production of vertical walls was easily achieved with a standard vertical torch alignment, the experimental trials showed that structures could be produced with a range of orientations by varying the torch angle in line with the desired orientation” [41]. The inclined structures and the torch inclination can be seen in Figure 61. Increased geometric complexity can be attained with additional axis of motion, paralleling what Posch stated [39, 3]. TWI achieved these results using the inclination of the torch while Posch stated, “if the base is mounted on a turntable which allows an additional movement, much more complex geometries can be established” [3]. TWI does not report the maximum inclination of the walls or any

welding parameters aside from 1mm diameter 5183 grade aluminum wire, bead heights of between 1-3 mm and bead width between 1-5 mm, and a deposition rate of 0.94 kg/hour [41].

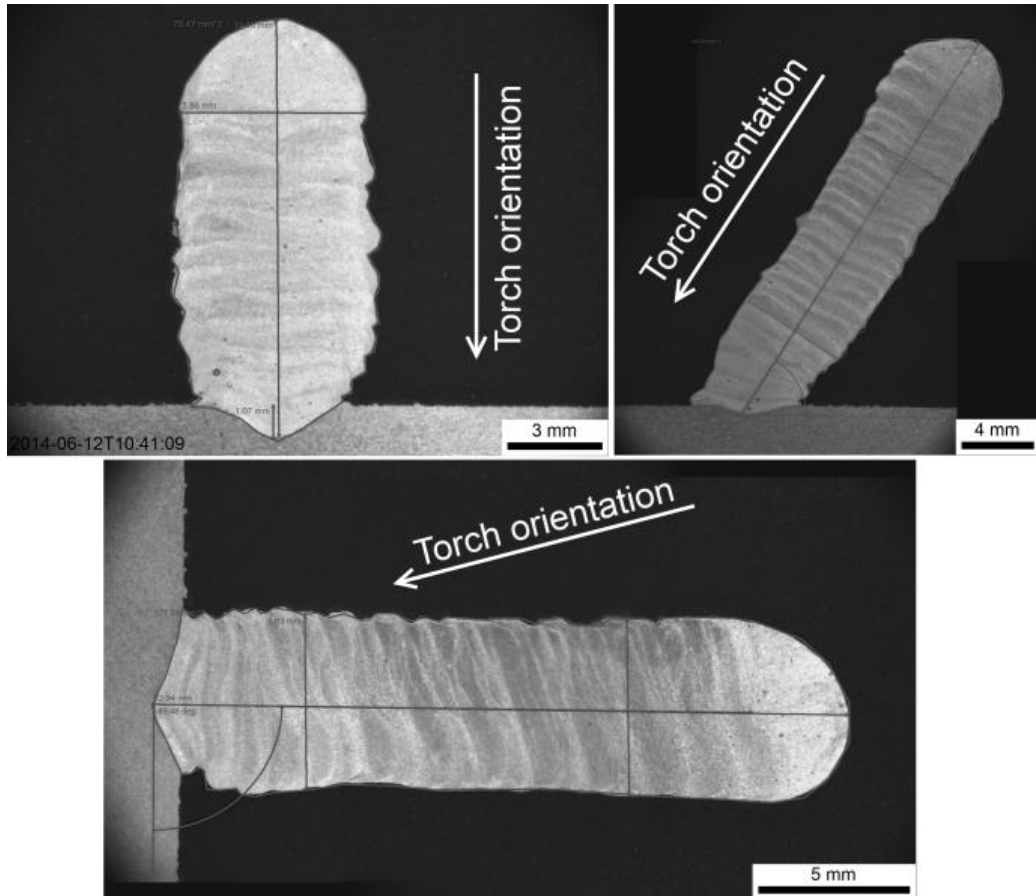


Figure 61. Range of produced orientations achievable by the CMT process [41]

Parameterization of Cold Metal Transfer GMAW

“A key element of the successful application of WAAM is the development of a process model that enables the prediction of weld bead geometry from the process parameters” [8]. The most important variables of any GMAW process, which affects the weld penetration, bead geometry, and overall weld quality are: (1) welding current (wire feed speed), (2) polarity, (3) arc voltage (arc length), (4) travel (traverse) speed, (5) electrode extension, (6) torch angle, and (7) electrode diameter [7]. These variables are not independent and affect each other and changes that are made to one variable will require altering additional parameters. The effect of the changes in welding parameters and the resultant changes in the weld bead are shown in Table 5.

Table 5. Effect of changes in process variables on weld attributes [7]

<i>Welding variables to change</i>	Desired Changes							
	<i>Penetration</i>		<i>Deposition rate</i>		<i>Bead size</i>		<i>Bead width</i>	
	<i>Increase</i>	<i>Decrease</i>	<i>Increase</i>	<i>Decrease</i>	<i>Increase</i>	<i>Decrease</i>	<i>Increase</i>	<i>Decrease</i>
Current and wire feed speed	Increase	Decrease	Increase	Decrease	Increase	Decrease	Little effect	Little effect
Voltage	No effect	No effect	Little effect	Little effect	Little effect	Little effect	Increase	Decrease
Travel speed	No effect	No effect	Little effect	Little effect	Decrease	Increase	Decrease	Increase
Electrode extension	Decrease	Increase	Increase (a)	Decrease (a)	Increase	Decrease	Decrease	Increase
Electrode diameter	Decrease	Increase	Decrease	Increase	Little effect	Little effect	Little effect	Little effect
Shield gas %	Increase	Decrease	Little effect	Little effect	Little effect	Little effect	Increase	Decrease
Torch angle	Drag	Push	Little effect	Little effect	Little effect	Little effect	Push	Drag

(a) Will result in desired change if current levels are maintained by adjustment of wire feed speed

Arc voltage is the electrical potential between the electrode and the work piece, which is generally lower than the voltage measured at the power source. Arc voltage is related to arc length as an increase in the voltage will result in a longer arc. High voltage can lead to porosity, spatter issues, and undercutting, therefore process optimization and

control over this voltage is crucial [7]. In the CMT welding process, arc length is acquired and adjusted mechanically, keeping the arc stable. CMT uses a self-correcting mechanism as the distance between the tip and the workpiece changes. In conventional GMAW, as the gap increases, the arc voltage and the arc length would increase. In CMT welding, the welding current decreases, while the mechanical wire feed drives in the torch adjust to maintain a constant arc length [7]. Conversely, a shortened distance will push current higher to counteract the lower voltage and compensate for the shorter wire stickout.

Conventional GMAW is sensitive to fluctuations in wire feed speed leading to decreased arc stability disturbing the welding process [42]. Changes in wire feed speed causes welding current to fluctuate with varied arc length in response to slight changes in the arc voltage. Unlike conventional GMAW, in CMT welding the current and voltage cannot be changed independently and are linked together via synergic control, a linear mathematical relationship developed and propriety to Fronius based on predetermined relationships [42, 7]. Synergic welding is described as “single dial” control, or the manipulation of multiple welding parameters based on a single user defined characteristic. The synergic algorithm incorporates voltage and amperage control based on the wire feed speed and is dependent on the thermal and electrical resistivity of the substrate, the filler wire used and its diameter, and the shielding gas composition [7]. Therefore, for a weld schedule, the shielding gas composition will solely be determined by the synergic profile used. The synergic line is highly repeatable and precise and the fundamental mathematical relationships should not be altered.

Machine travel (traverse) speed has a large effect on the weld quality. With decreasing travel speed, the filler metal deposition per unit length increases and the welding

arc deposits on the molten weld pool rather than the base material, reducing penetration and widening the bead. As travel speed is increased, the thermal energy per unit length is at first increased because of the arc directly contacting the base material, however further increases in travel speed impart lower thermal energy. With high travel, there is a tendency for undercutting on the bead edges because of insufficient deposition [43].

According to Williams *et al.* “travel speed (TS) has the largest effect on deposits quality. As shown in Figure 62, for a given wire feed speed/TS ratio of 30 (keeping the WFS/TS ratio constant ensures that both the amount of material per unit of length and the heat input are kept constant), the lowest TS of 0.2 m/min resulted in the best deposit; the quality progressively deteriorated for increasing TSs, and finally, deposits were unacceptable for a TS of 0.5 m/min” [6].

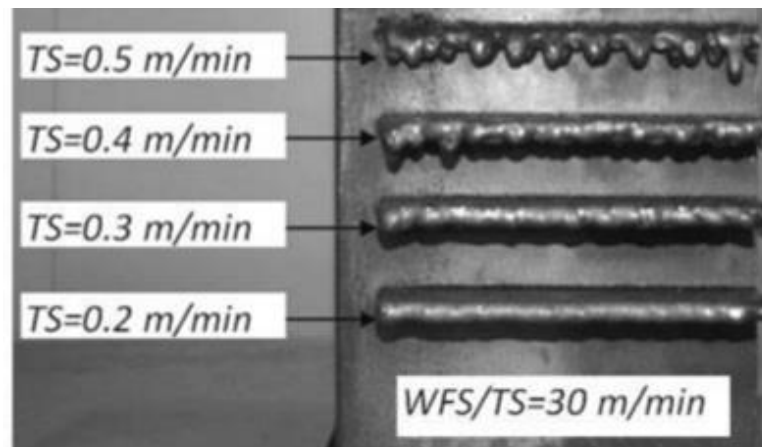


Figure 62. Travel speed and the effect on weld quality at a constant WFS/TS ratio [6]

Path Planning Strategies for WAAM

“Slicing software refers to the software package that is used to generate the machine code that controls the machine. The input to a slicing software is a CAD file and the output is the machine code. For 3D printing, the CAD file is in the form of the de facto industry

standard stereolithography (.stl) file format. Several slicing software packages that were developed for the FDM 3D printing process are freely available online” [4].

Proper welding path generation is necessary for improving the surface accuracy of the built parts and is based upon the weld bead models covered in the prior section. “Uneven weld bead geometry may lead to an accumulation of errors in the vertical direction after the deposition of several layers” [44] Figure 63 shows an example of thin walls built by weld deposition where there are significant differences in bead geometry at the start and end of the weld paths. To overcome these issues, researchers have adjusted deposition parameters at the start and end of the weld. Research in path planning carried out by Ding *et al.* has proposed a path planning algorithm that is able to generate a continuous toolpath to fill a large class of geometries without starting or stopping, thus eliminating the issues associated with starting and stopping [44].



Figure 63. Walls showing the changing bead geometry at the start and end of weld [44]

Ding *et al.* highlighted the requirements of a toolpath strategy for WAAM as:

1. Geometrical accuracy: as the resolution of arc welding is relatively low, the outlines of 2D geometries should be fabricated by contour patterns which could effectively improve the geometrical quality of the part.
2. Minimize the number of toolpath passes: the cumulative deviations introduced by the uneven weld bead geometry at the start and end portions of each welding pass will limit the maximum number of layers that can be added together before vertical build errors become problematic. Therefore, the number of welding passes should be minimized to reduce starting-stopping sequences within each layer. A continuous path is preferred here.
3. Minimize the number of toolpath elements: toolpath elements are a series of line segments representing the travel path of the tool. In general, at the ends of toolpath elements, the wire feed rate should be adjusted to avoid a deposition error caused by a rapid change of toolpath travel direction. To improve surface accuracy, the number of toolpath elements should be minimized.
4. Simple algorithm with rapid implement: the path planning algorithms should be simple and quick to implement to reduce the pre-processing computational time. Domain decomposition is a frequently used technique in computational geometries that is also useful in AM for path planning [28]. It divides arbitrary layer geometries into a set of simpler shapes, such as monotone polygons or convex polygons, which become easier for path generation. The algorithm for generating zigzag patterns is relatively simple. Therefore, the domain decomposition of 2D geometries and the filling of the interior

area of 2D geometries with zigzag patterns are important to simplify the toolpath generation algorithm [44].

In a continuation on his research, Ding *et al.* published a follow-up journal article in 2015 that evaluated a technique of medial axis transformation (MAT) for producing toolpaths without gaps associated in the traditional contour toolpaths, as shown in Figure 64. The authors evaluate the material efficiencies of the depositions for comparisons on the toolpath strategies. In their evaluation, the authors find that the material efficiency for different step over distances is minimal for solid structures, while it is significant for thin walled structures. “In choosing the optimal step-over distance, material efficiency could be increased by 2.4 times from 38.63% to 94.15%. This indicates that step-over distance plays an important role on material efficiency when fabricating thin-walled structures using WAAM technology” [45].

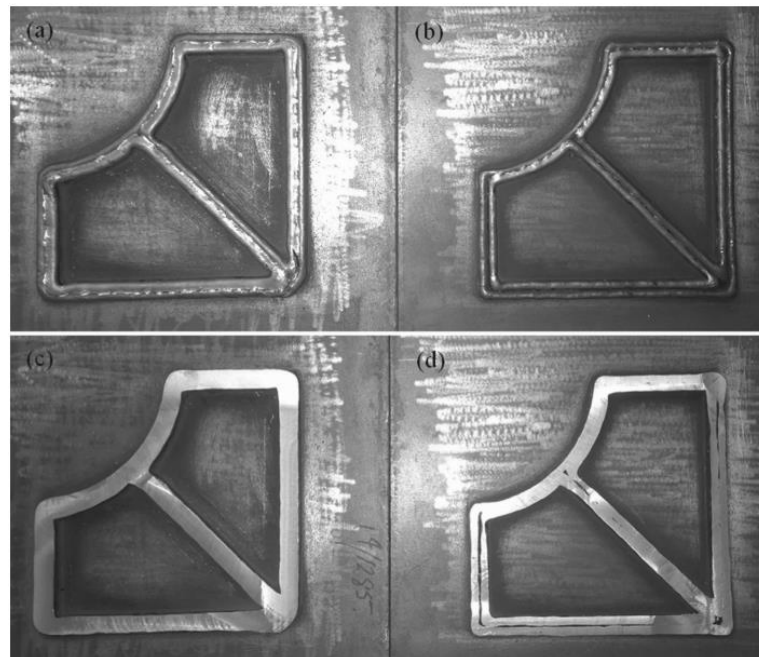


Figure 64. Comparison of layers produced by the proposed MAT path patterns (a & c) and the traditional contour path patterns (b & d) [45]

Ding *et al.* continued in 2016 to further highlight the challenges of path planning, moving toward an automated robotic arc-welding-based AM system to move from CAD to finished part. Ding notes that one of the biggest challenges in complex part construction is at a location where weld paths meet and must cross. “Crossings in thin-walled structures make path planning more complex. Thin-walled structures are most commonly seen in aerospace components, which are attractive applications for AM due to their high buy-to-fly ratios. Crossings always exist in the case of these structures. Experiments reveal that directly crossing paths produce peaks where the weld beads overlap at the crossing points as shown in Figure 65 (a). In addition, sharp angles in the intersections can concentrate stresses” [46]. Ding found that by using the opposite angle method, as shown in Figure 65 (b), demonstrated the best crossings with smooth radii in corners [46].

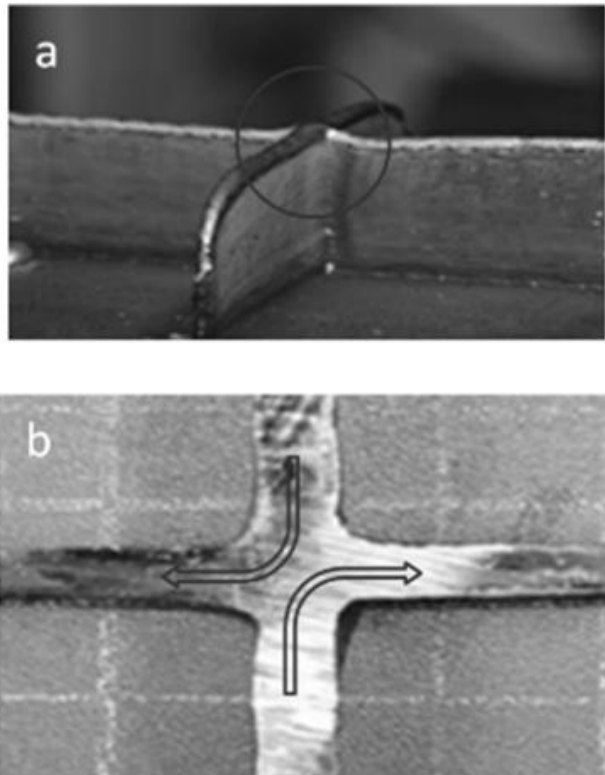


Figure 65. Direct crossing (top) and opposite angle method (bottom) [46].

Evaluation Techniques for CMT WAAM

As noted by Posch, “For technical applications, reliable mechanical and technological properties of the manufactured component within certain limits are required” [3]. Evaluation of the mechanical properties of deposited materials is of paramount importance. The American Society for Testing and Materials (ASTM) has published the *Standard Guide for Evaluating Mechanical Properties of Metal Materials Made via Additive Manufacturing Process*, designation F3122 –14. The standard outlines applicable procedures for measuring deformation properties and material fatigue properties [47].

When measuring material properties, the tension and hardness are to be considered according to the previously published procedures common to materials manufactured by conventional processes. ASTM Standard E8 covers the tension testing of metallic materials in any form at room temperature and provides guidance on specimen production and dimensions [48]. ASTM Standard E18 covers the determination of the Rockwell hardness and the Rockwell superficial hardness of metallic materials by the Rockwell indentation hardness principle [49].

When reporting results, the ASTM requires previously published guidelines for the individual test to be followed. Additionally, information about construction procedure for the additive manufactured part must be reported. The information reported must include location and orientation of the part in the additive manufacturing system build volume. As shown in Figure 66 & Figure 67, tensile specimens must be labeled in accordance with the axis rotation of the figure. This is due to the potential anisotropic behavior of additive manufacturing [50]. Many of the standards specifically apply to plastic extrusion 3D printing and therefore do not pertain.

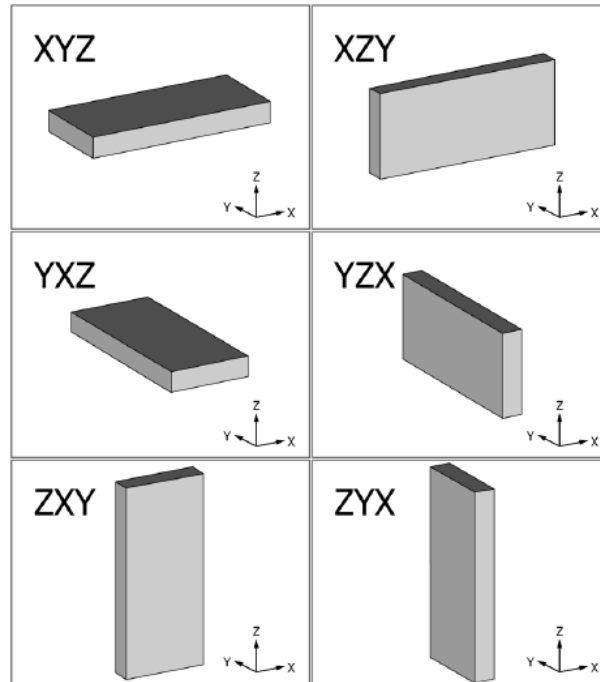


Figure 66. Build orientation nomenclature [50]

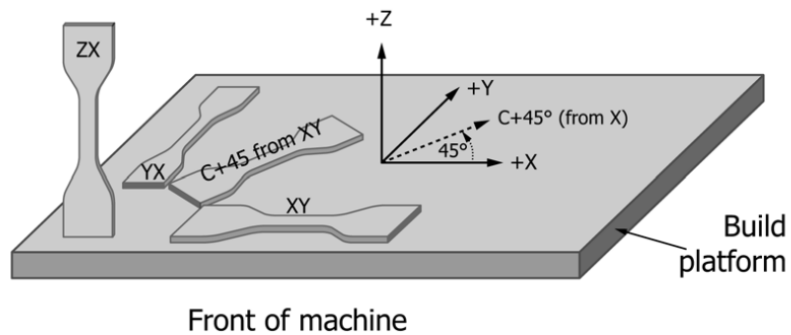


Figure 67. Orientation of tensile specimens [50]

Since the WAAM process is similar to sand casting in finished surface roughness [3], sand casting standards may be used to evaluate parts. The ASTM *Standard Practice for Steel Castings Surface Acceptance Standards Visual Examination* establishes surface texture criteria. The surface texture should be between A1 to A4 in the Steel Castings Research and Trade Association (SCRATA) graded reference comparators [51]. When examining mechanical requirements, the ASTM *Standard Specification for Common*

Requirements for Iron Castings for General Industrial Use contends that the mechanical properties of the part should be sufficient for the need of the particular application. Additionally, the standard provides a list of specifications for specific type of castings. The evaluation techniques used for castings are techniques common to other processes and referenced inside the standard F3122 –14 [47].

Previous researchers of CMT-WAAM, highlighted in the prior section, have used numerous techniques including: visual inspection, tensile testing, ISO-V toughness testing, fatigue testing, crack propagation testing, hardness testing, microstructure evaluation of a polished and etched samples under optical microscopes and scanning electron microscopes, electron backscatter diffraction with argon ion beam cross section polishing, X-ray inspection, surface profilometry by laser optical systems and stylus profilometers, chemical composition analysis, neutron diffraction strain scanning, etc.

Summary of Research Opportunities

Short circuit transfer WAAM as a process has been considered since 1925, with CMT based WAAM being the most technologically advanced and newest iteration of the technological development. CMT offers numerous improvements to legacy problems, including increased process stability and control and lower heat input. Researchers have integrated CMT into WAAM and investigated the construction of basic geometries, including single wall sections, curved geometries, and large multi-layer mold sections. Different models of single-bead geometry, and multi-bead cross sections have been evaluated. Parameterization has been examined as a method of controlling heat input and residual stresses as well as a way to create predictable bead geometries. All but one of the CMT researchers evaluated in this review used a commercial six-axis robotic arm for torch

control so a large research gap exists for gantry style 3D WAAM. Methods of creating larger shapes and more complex geometries need to be evaluated for three-axis deposition. Some researchers employed torch oscillation or weaving to create wider bead deposits without the need of parallel beads, however no research work was carried out to study bead geometry or process optimization concerning this method.

Researchers identified the need for closed loop control for greater consistence in the process. Kovacevic, *et al* performed a preliminary study of the application of closed loop control hardware; however, the authors failed to fully implement the strategy [28]. With the added control features of the CMT welder, control and monitoring in real time is feasible and the addition of monitoring processes need to be reevaluated.

Inter-pass cooling was employed by all of the researchers dealing with CMT, however the results of varied cooling times was only minimally evaluated by one study. Some researchers employed a temperature monitoring method, where a layer would be paused to allow temperature to drop below a set point, while other employed a timed pause of various duration. Cooling and the effect on the final structure and mechanical properties has yet to be studied for CMT WAAM.

With regard to welding path generation, Gaddes determined that using the Slic3r program to produce welding paths was an issue due to excessive buildup when starting or stopping a weld. Gaddes employed a method of non-retraction toolpaths and maintained welding constantly to mitigate this issue in a similar manner as researchers at The University of Wollongong [44, 45, 4]. Since there are no dedicated software packages for wire and arc additive manufacturing, machine toolpath creation using various open-source 3D printing slicing software needs to be reevaluated for the Fronius based CMT unit due

to greater control over the starting and stopping point of the weld with added features like no-burn back weld stop and multi-step start current. Additionally, no research efforts on the generation of non-planar deposition toolpaths, where all three axes are moving in three dimensions rather than 2D layer slices, is ongoing.

III. Scope and Objectives

There is a lack of parameterization and study of the Wire Arc Additive Manufacturing (WAAM) process using Cold Metal Transfer Gas Metal Arc Welding (CMT-GMAW). Researchers noted a lack of control over suggested key parameters of interest including: voltage/current/wire feed speed relationship, process temperature, and wire offset distance.

Specific primary objectives for the research include:

- Adapt existing 3-axis WAAM printer previously operating using short-circuit transfer GMAW, to new Cold Metal Transfer (CMT) welder.
- Document the printer's adaptation.
- Demonstrate the ability to create standard geometric shapes (hollow and solid cylinders, walls, rectangular shapes, hourglass, overhangs).
- Establish a statistical design of experiments (DOE) with different factor levels to include travel speed, wire feed speed, material, etc. Measurable outcomes include tensile strength, porosity, hardness, grain structure.
- Investigate the relationship of interpass cooling on material properties and deposition quality.
- Study and compare the tensile strength of specimens made with different materials to the published strength of the materials used. Specimens will be tested parallel and perpendicular to the direction of deposition.

- Study and compare the hardness of specimens made with different materials to the published hardness of the materials used.
- Study the macrostructure and microstructure of specimens.
- Compare dimensional accuracy of finished parts to original models.
- Investigate the development of a closed loop process control method for maintaining wire offset distance throughout the process.
- Investigate different methods of deposition toolpath and infill strategies including parallel bead and weave pattern.
- Investigate the use of “rafts” as baseplates to increase ease of specimen removal.
- Develop standard output data from the Fronius welder to document performance.
- Compare measured current and voltage data to that of the machine in its previous configuration.
- Develop easy to ‘print’ files/programs to create traditional standard test specimen for subsequent Auburn University researchers.

Specific secondary objectives of this research include:

- Investigate limitations of deposition angle for creating overhangs and bridges
- Investigate the development of a G-code post (machine specific M-codes, G-codes, etc.) for the machine to produce future prints quickly and easily.
- Investigate non-planar deposition and the development of 3D toolpaths, moving both the x, y, and z axis simultaneously.

IV. Design and Construction of Equipment

Previous research conducted by Gaddes at Auburn University on WAAM involved construction of a purpose built, 3-axis, gantry-style CNC machine. A build volume of 18” x 18” x 18” was specified to meet the requirement of evaluating the construction of large objects while providing room for future expansion. “Cartesian style machine was chosen with a build plate that traversed horizontally (y) and not vertically (z)” [4]. Gaddes chose to integrate a commercially available and reliable Miller model 190 welder via a custom-built wire feeder head attached to the x-axis carriage. A Fronius CMT 4000 Advanced welder was specified for advancing the research and integrated into the printer for this study. A complete overview of the equipment and retrofitting procedure is included in the following section.

Previous Machine Design

Auburn University’s WAAM printer was previously configured for research utilizing an off the shelf welder. This machine is used as a base for the current research. Figure 68 shows the printer in its previous configuration [4]. The frame of the machine is constructed from 80/20 aluminum extrusions that allow for easy modification. The build plate travels on two linear guide rails via four ball bearing carriages in the y-axis and is driven by a single ball screw and ball nut. The z-axis moves along four linear rails and carriages and is driven by two ball screws connected by an L-series belt and timing pulley. The welding torch is carried upon the x-axis and is driven by a single ball screw between

two linear rails and carriages. The custom ball screws are 16 mm in diameter and the linear rails are 20 mm wide.



Figure 68. Gantry CNC machine used as base for WAAM research [4]

The axes are driven by stepper motors. The stepper motors used are NEMA 23 with $1.8^\circ/200$ steps per revolution and have 420 oz-in. of holding torque. The stepper motors are connected to the ball screws by an elastomer coupler to help with possible binding.

The build plate assembly, shown in Figure 69, consists of multiple layers to provide thermal and electrical isolation [4]. The first layer is a piece of machined aluminum plate that connects to the carriages and the ball screw nut. Next, a 1-inch-thick ceramic fiber electrical and thermal insulation board called Duraboard 3000. In addition to being an electrical insulator, this ceramic board has a maximum operating temperature of 3000°F and a very low thermal conductivity of 0.8 at 1000°F . The thermal insulation is important to protect the mechanism beneath from the heat generated during the WAAM process. The

electrical insulation is important to protect the operator and the machines electronics. Above the ceramic insulator, an 18 x 18 x 0.5 in. steel plate is bolted to the aluminum plate with counter-bored ceramic inserts to maintain isolation. The steel plate features threaded holes (1/2-13 UNC) in a 4-in. spacing pattern to allow attachment of build plates.

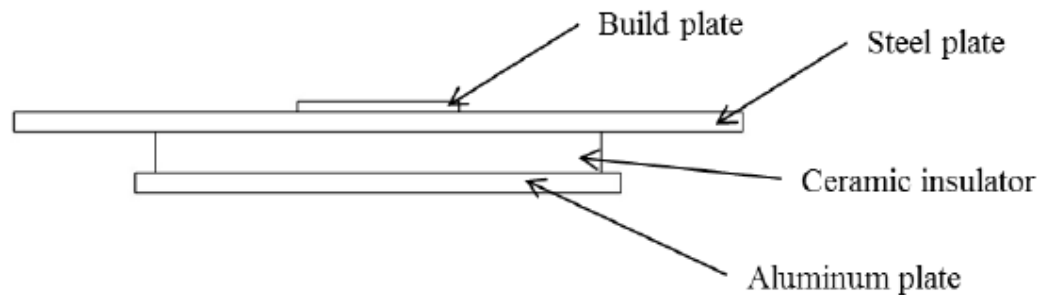


Figure 69: Build plate design [4]

The machine is controlled by the CNC control software Mach3, with the interface shown in Figure 70. The software runs on a dedicated computer and accepts standard CNC G-codes and M-codes. It also has its own post processor downloadable for most CAM packages. The Mach3 software is configured to control the three axes movements. The wire feed mechanism was configured as a variable speed spindle, and later changed to be driven by a stepper motor with a direct drive feed gear. Mach3 communicates with the machine via a standard parallel port breakout board. The breakout board distributes signals to stepper motor drivers to control the motors.

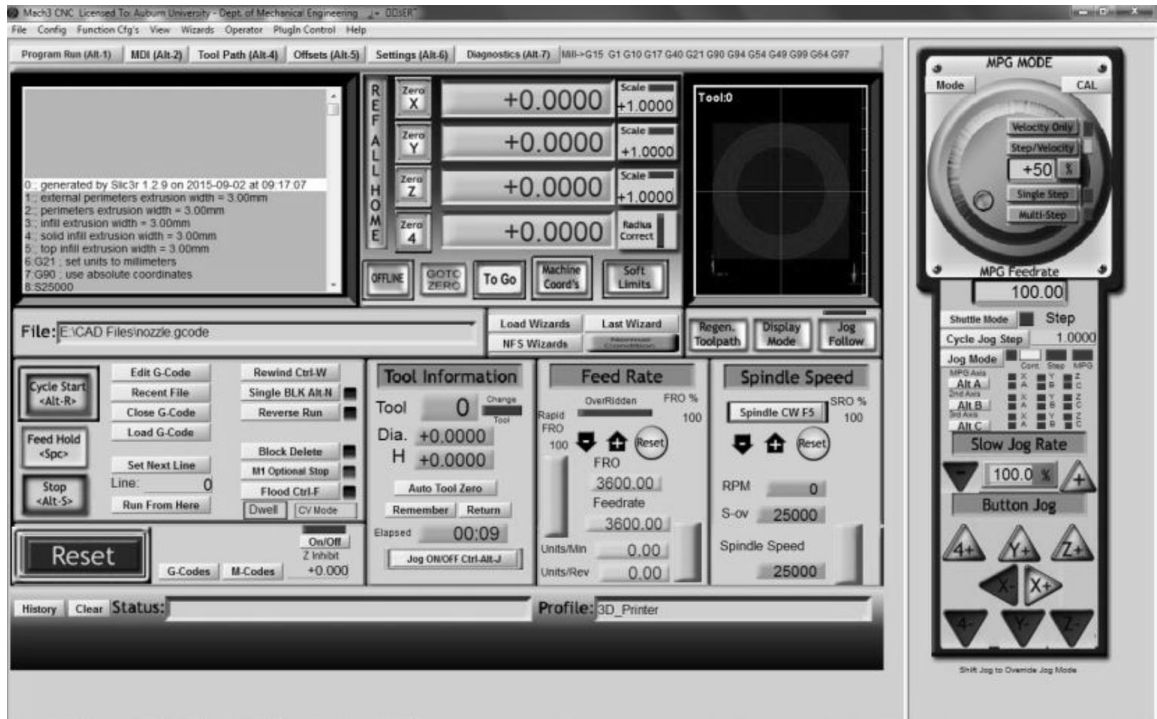


Figure 70: Mach3 CNC software interface.

CMT Weld System

The equipment listed below encompasses the Fronius weld system, as shown in Figure 71.

- Fronius CMT Advanced 4000 MV R power source
- Fronius VR 7000 CMT wire feeder
- Robacta 5000 Welding Torch
- Robacta drive CMT
- Cooling unit
- Shielding gases from Airgas

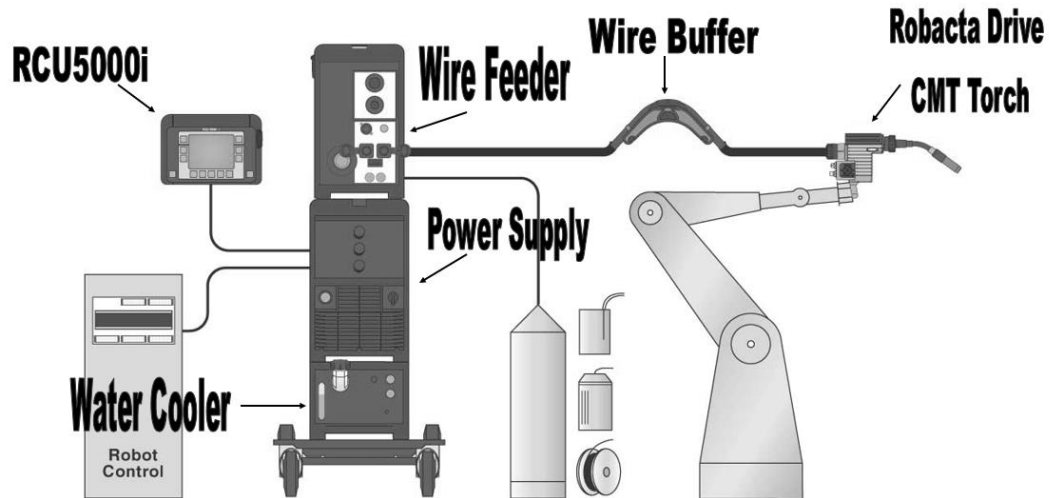


Figure 71. Fronius weld system [52]

Fronius CMT Advanced 4000 MV R Power Source

The Fronius CMT Advanced 4000 MV R Welder is shown in Figure 72 below. The accuracy of the machine with respect to displayed values is noted at a max of +/- 8 % of the load for voltage, and a max of +/- 10 % of the load for current. The table shown in Figure 72 displays the specs for the welder. The power source transforms energy into the appropriate form for use in the welding process. The digital process control ensures quality and repeatable welding results [52].



		CMT-A 4000 MV
Mains Voltage Range	3 x 240	200 - 240 V
	3 x 460	380 - 460 V
Mains Tolerance		+/- 10%
Mains Frequency		50/60 Hz
Fuse Protection, slow-blow	3 x 240	63 A
	3 x 460	35 A
Primary Continuous Current (100% dc)		n/a
Primary Continuous Power (100% dc)		13.0 - 16.0 kVA
Electrical Efficiency		n/a
Welding Current Range	MIG	3 - 400 A
Welding Voltage Range	MIG	14.2 - 34.0 V
Max Welding Voltage		n/a
Open Circuit Voltage		90 V
Duty Cycle (77°F)		85% @ 400 A
		100% @ 380 A
Duty Cycle (104°F)		40% @ 400 A
		60% @ 350 A
		100% @ 290 A

Figure 72. Fronius CMT Advanced 4000 MV R Power Source [52]

Fronius VR 7000 CMT Wire Feeder

The VR 7000 wire feeder, shown in Figure 73, was created specifically for the CMT welding process. The wire feeder can utilize large spool sizes or externally fed drums for higher production jobs. Being as that the feeder is designed for CMT it can operate with a push/pull process torch or a normal push only torch [52]. The wire feeder replaces the wire drive unit of Gaddes' system. It is longer controlled through the use of the spindle motor in Mach3.



Figure 73: Fronius VR 7000 CMT Wire Feeder [52]

The wire feeder unit uses four drive rollers for feeding the filler wire through the hosepack to the torch. The two profiles for the feed rollers are U-Groove and H-Groove. The U-Groove profile is a semicircular shape and is good for most materials, but specifically for steel and stainless wire. These rollers have four points of contact and are to be set to a tension of $\sim 2.5 - 3$ on the tensioner. The H-Groove profile is a trapezoidal geometry that creates a hexagon when used in conjunction with another roller. This profile is best for aluminum and silicon bronze. These rollers have two points of contact and the tension is to be set at $\sim 1.5 - 2$ on the tensioner [52].

Robacta 5000 Welding Torch and Drive CMT W

The Robacta 5000 is a “water-cooled” drive/torch unit for the CMT welding system. The term “water-cooled” is misleading as it utilizes proprietary coolant from Fronius. This unit is designed to be mounted to a CNC control unit and not be used manually. The unit does have the capability to feed and retract wire as well test gas flow. The torch uses either a conical or counter bored tip. The conical tips guide the filler wire through, acting as a funnel. The counter bore tips allow the wire liner to enter the tip and guide the filler wire through. This allows softer materials to be used without deformation [52]. Figure 74 shows the Robacta Drive with the Robacta Torch attached.



Figure 74: Fronius Robacta 5000 Drive/Torch [52]

FK 4000 Cooling unit

The FK 4000 cooling unit is the standard cooling unit for most of Fronius’ MIG and TIG packages. It has an internal reservoir and a closed loop system that flows to the Robacta Drive for cooling purposes. The unit is fuse protected for over-voltage damage [52].

Wire Buffer

The wire buffer provides tension in the wire when the drive motors switch from push to pull operation during the CMT process. This prevents binding in the system and insures the torches dynamic functions are not hindered. The unit is to be mounted no more than 1.6 m from the Robacta Drive [52]. Figure 75 shows the wire buffer.



Figure 75: Fronius Wire Buffer [52]

RCU 5000i

The RCU 5000i is a universal remote unit for the Fronius welder. It is required for the CMT process and allows the operator to choose between the different operating modes (CMT, Pulse, or Standard). The unit also allows the user to adjust and set the weld parameters prior to and during the welding process [52].

Shielding Gases

Shielding gases for the welding process provide a stable environment for the weld pool. Depending on the specific material being welded and the synergic line being used a different composition of gases is specified. The Fronius welder controls the flow rate

which is calculated based on the diameter of the wire. Fronius states that the flow rate in l/min of gas flow for the weld process should be 10 – 12 times the diameter of the wire in mm. Therefore, for 1.2 mm (0.045”) diameter wire 12 to 14.4 l/min are required (25 – 30 CFH) [52].

Robot – Welder Integration

The equipment and instruments listed below were used together to create the WAAM printer and interface the welder into the existing setup. The equipment listed includes the gantry based CNC, the welder, upgrades to the machine, software and hardware, and machine I/O logic interface.

- Auburn University’s WAAM Printer
- Fronius Weld System (outlined in previous section)
- Fronius RCU 5000i
- Fronius ROB 5000
- Fronius Xplorer Software
- Sealevel RS-485 ModBus RTU Interface (SeaI/O-410M-OEM)
- RS-485 PCI Express Card
- Probotix 3-Axis Monster Mill Stepper Motor Driver Kit
- Mach3 CNC Control Software
- LocalNet RS-232 PC Connection Cable
- Passive Splitter
- LocalNet Cables
- Mean Well 12 Volt DIN Rail Power Supply
- Dell Optiplex 755 PC (Windows XP)

Integrating the Fronius CMT welder into Auburn University’s WAAM machine was accomplished via the ROB 5000 Discrete I/O interfaced to Mach3 with the RS-485 Modbus protocol. The ROB 5000 features interface signals that are individually wired for connection to the robot automation controller to provide communication between the welding system and the robot controller. Figure 76 (left) below shows the Sealevel RS-485 Modbus RTU interface. It utilizes 16 I/O ports to communicate between the welder’s ROB 5000 controller and Mach3. Figure 76 (right) shows the I/O setup on the SeaI/O-410M-OEM Modbus.

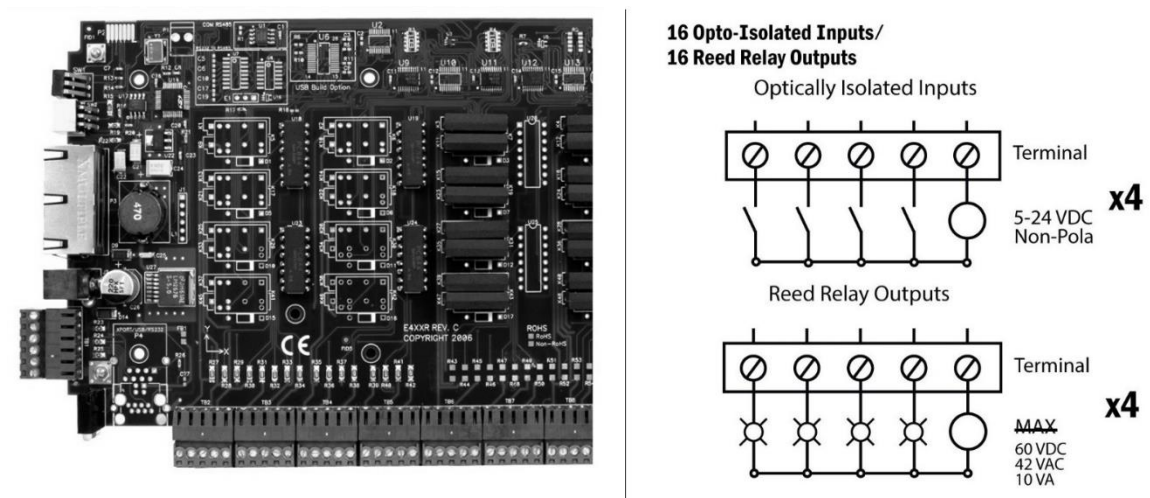


Figure 76. Sealevel RS-485 Modbus RTU (left) and I/O terminals (right).

The Fronius LocalNet interface, connects the welder as a slave to the controller, in our case Mach3 CNC software. Digital input signals to the welder (output signals from Mach3), are accomplished and actuated using machine codes (m codes) that were created in Mach3 to activate and deactivate the various output signals to the welder. The digital signals are based on a 2-level logic, represented by the voltage difference between the signal and ground. The two levels are logical high and low, corresponding to active hi/low status of the output signal. These outputs were designated to ports & pins in Mach3 to

control the various signals available. Table 6 shows the setup coming from Mach3 to the ROB 5000 with the designated M-codes assigned. In Mach3 M-codes above 100 are designated for user functions, therefore M-codes begin with M1XX. The second number in the designation indicates what output pin the function is on the Modbus board. The third number in the designation indicates the relay status as high/low (1/0, I/O). Appendix III details the specifics of each M Code.

Table 6. Machine codes used to operate the welder.

M Code	Function
M111/M110	Welding Start/Welding Stop
M121	Quick Stop (Active Low)
M120	Robot Ready
M131/M130	Gas Test Start/Stop
M141	Touch Sensing
M151/M150	Wire Retract Start/Stop
M161	Source Error Reset
M171	Blow Through
M181/M180	Wire Feed Start/Stop

The robot ready signal, M120, indicates that the robot is communicating, functioning and ready to weld. This is one of two signals required for any sort of operation of the welding system. By making the signal active-low, meaning that while the logic level is low, the signal will output high, Mach3 will communicate its status of robot ready unless disabled using the quick stop command, M121. By doing this, the operator will not have to explicitly tell the welder that the robot is ready every time that welding is to take place. The source error reset signal, M161, is designed to clear any error state the welder is in. For proper use, this signal should be toggled on and then off again, therefore the signal does not have a corresponding M160 command to deactivate the signal. The M161 command activates the signal, pauses, and deactivates the signal without additional

operator action. The welding start signal, M111, will start the welding process, beginning with pre-welding (gas pre-flow, hot start) and then automatically move to the welding process. When an M110 welding stop code is read by Mach3 and the output signal goes low, the post welding process (crater fill, and gas post-flow) will start automatically. The gas test signal, M131 is used to purge gas. It can be used as a gas pre-flow or post-flow as necessary. Wire inching and wire retract, M181 and M151 respectively, are used to move the wire forward or backward. These codes should be used carefully, as the wire will not stop until an M180 or M150 code deactivates the signal or the RESET button is pressed. The blow through signal, M171, actuates a compressed gas purge blow through to clean the welding nozzle to remove any spatter that may have accumulated. This signal is actuated and then automatically turned off [52].

The ROB 5000 allows for the selection of welding modes via the robot interface using a combination of three signals, X2:6, X8:1, X8:2. This allows for the selection between standard program, pulsed arc program, job mode, parameter selection internal, manual, CC/CV, TIG, or CMT/special process. For our application, parameter selection internal was hardwired by wiring X2:6 High, X8:1 High, and X8:2 Low. This allowed process selection using the RCU 5000*i*. Welding jobs can be called in a similar way, with several bits joined together to form a binary number between 0-99. The set of bits used tells the welder what weld schedule to use. This feature was deemed unnecessary for our application and was not used [52]. Future use could include the direct call of welding programs from the job bit, however the programs could just be selected on the RCU5000*i*.

Digital input signals (output from the welder) to the robot controller are read via the assigned ports & pins designated in Mach3. The inputs from the ROB 5000 to Mach3

are arc stable, power source ready, and process active; and are connected to pins 1,2, and 4 respectively. Arc stable is a signal sent from the ROB 5000 “once an arc has been started and that arc is within acceptable parameters as determined by the welding power source.” Arc stable functions as the touch sensing input signal, with the input going high once contact has been made between the electrode and the base. The power source ready signal is sent from the ROB 5000 “when the power source has established successful communication and there are no errors that will interfere with the function of the welder.” The process active signal is sent from the ROB 5000 “once the welding process has started (after a “welding start” signal) beginning with the gas pre-flow if set by the welder (note this signal will not go high if the gas is controlled by the robot instead)” [52].

The ROB 5000 features analog outputs for welding voltage, welding current, wire drive current, wire feed speed, and arc length via a 0 – 10V signal. These outputs are used for displaying and documenting the process parameters and monitoring the weld. These signals were unused in our initial application, however future use could use them for feedback control. Noticing spikes in the voltage could be accomplished and welding parameters changed in real time.

The Fronius Xplorer software was used for monitoring and logging of all weld data. Data is logged ten times a second and includes the mean, max, and average voltage, current, and wire feed speed for that tenth of a second. The data is stored by the weld seam, and exported from Fronius Xplorer in excel format.

The welder interfaces with the computer, RCU 5000*i* handheld controller, and ROB 5000 via the LocalNet. Figure 77 shows the complete layout of the interface.

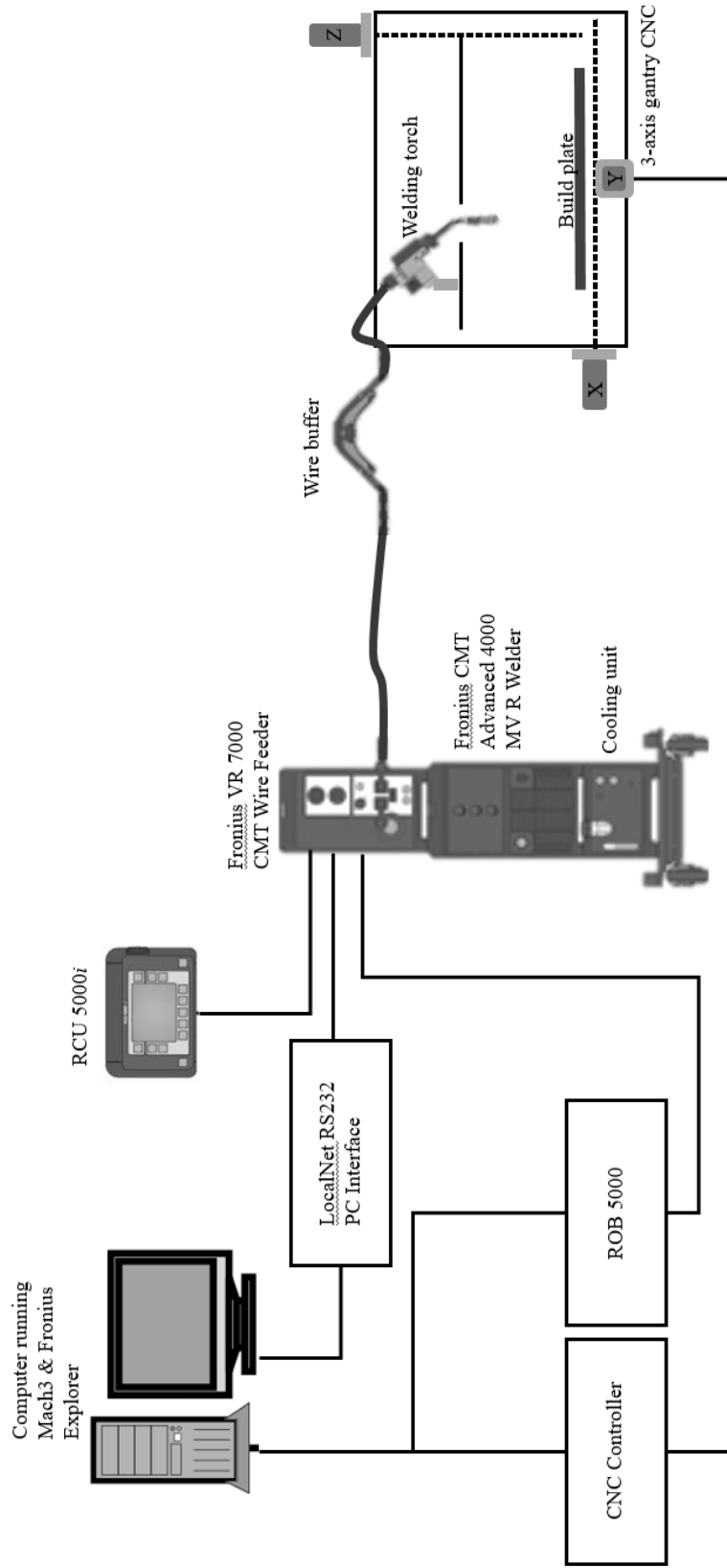


Figure 77. Fronius welder interface.

Instruments

The following equipment was used in this research to prepare or test specimens and create any custom fixtures or tooling required. The material testing equipment used to obtain the material properties of the final specimens is included in this section. Software used for design and post processing of data is also listed.

- Cincinnati Arrow VMC-750 CNC mill
- Bridgeport Series I 2 HP vertical milling machine
- Southbend 450 lathe
- Do-All 2013-V vertical band saw
- Wellsaw 1118 horizontal band saw
- Wilton belt sander
- Model HR-150 Rockwell hardness tester
- MTS Q-Test 100 tensile tester
- Keyence VHX 1000 E 3D microscope
- Keyence VR-3000 wide-area 3D measurement system
- Dassault Systems Solidworks modeling software
- Autodesk HSMWorks CAM software
- Mathworks MatLab 2016b
- Microsoft Excel 2016
- Microsoft Word 2016
- R statistical analysis software
- Minitab 18 statistical analysis software
- ImageJ microscope software

The Cincinnati CNC milling machine, shown in Figure 78, was used to machine the tensile samples from each sample as well as prepare fixtures, jigs, and components for/of the machine. G-code was generated on a separate PC and then loaded via USB stick onto the CNC machine.



Figure 78. Cincinnati Arrow VMC-750 CNC Mill

The Bridgeport milling machine, shown in Figure 79, was used to create machine components as well as prepare fixtures/jigs. The Bridgeport was used to flycut the surface of all walls.



Figure 79. Bridgeport Series I 2 HP Vertical Milling Machine

The Southbend 450 lathe was used to create machine components as well as prepare fixtures/jigs/specimen. The vertical band saw seen in Figure 80 (left) was used to cut the walls after the dogbones were machined. The horizontal band saw seen in Figure 80 (right) was used to separate the specimens from the build plates.



Figure 80. Do-All 2013-V Vertical Band Saw (left) and the Wellsaw 1118 Horizontal Band Saw (right)

The Wilton belt sander was used to for various purposes including the removal of burrs from specimens generated during the machining process. The belt sander was also used for initial sanding of the samples after coming out of the mill.

Figure 81 shows the HR-150A Rockwell hardness tester used to test the samples. Accuracy and repeatability of the tester is +/- 2 HRB. Standard test blocks were used both before and after hardness measurements were taken to ensure the accuracy and calibration.



Figure 81. Model HR-150 Rockwell Hardness Tester

The MTS Q-Test 100 tensile testing machine used can be seen in Figure 82. The tensile testing machine moves at a constant displacement rate and records the forces applied to the load cell. The jaws used for the tensile testing of the metal samples were of the screw clamping type. A screw collar is tightened which clamps down on the piece. The jaws are designed so that as the pulling force increases the clamping force does as well.



Figure 82. MTS Q-Test 100



Figure 83. MTS Landmark Servohydraulic load frame.

An MTS Landmark Servohydraulic load frame Model 370.10, shown in Figure 83, was used for tensile testing. The tensile testing machine moves at a constant displacement rate and records the forces applied to the load cell. Featuring a high-resolution force transducer with a range of 100 kN (22 kip), the MTS Landmark provides highly accurate force measurements with a maximum error in tension of 0.05 %. The jaws used for the tensile testing of the metal samples are hydraulically actuated grips. When combined with precision alignment fixtures the machine delivers tightly controlled and constant zero specimen loading.



Figure 84. Keyence VHX 1000 E 3D microscope

A Keyence VHX 1000 E 3D microscope, shown in Figure 84, was used in the study of weld specimen microstructure. It is a two-stage microscope with the first stage having a magnification range of 100x to 1000x and the second stage magnification range of 500x to 5000x. The resolution of this microscope is +/- 0.05 microns and a repeatability of +/- 0.5 microns.

Materials

The materials chosen for this experiment are listed below along with the source from which they were obtained. The initial hardness temper or level of hardness is also listed for each material as they were specifically chosen prior to ordering. Available data sheets can be found in Appendix V.

ER308:

- Stainless steel consumable wire
- Westward 0.045" diameter 30lb spool purchased from Grainger
- Balanced chromium and nickel levels provide enough ferrite in the weld for high resistance to hot cracking
- Dual classification ensures the maximum carbon content is 0.03%
- 0.03% carbon content increases resistance to intergranular corrosion

Table 7. ER308/308L filler material properties.

ER308/308L Wire Properties and Chemistry				
Tensile Strength (As Deposited) [ksi]			87 - 90	
Yield Strength (As Deposited) [ksi]			57 - 61	
Elongation (As Deposited)			41%	
Reduction of Area (As Deposited)			60%	
Shielding Gas (%Ar/%CO2)			98% / 2%	
% C	% Cr	% Ni	% Mo	% Mn
0.08 Max	19.5-22	9.0-11.0	0.75 Max	1.0-2.5
% Si	% P	% S	% Cu	
0.3-0.65	0.03 Max	0.03 Max	0.75 Max	

ER70S-6:

- Mild steel consumable wire
- Washington Alloy 0.045" diameter

- High levels of manganese and silicon deoxidizers tolerate medium to heavy mill scale surfaces
- More puddle fluidity
- Excellent wetting action

Table 8. ER70S-6 filler material properties.

ER70S-6 Wire Properties and Chemistry				
Tensile Strength (As Deposited)				70,000 psi
Yield Strength (As Deposited)				58,000 psi
Elongation (As Deposited)				24%
Reduction of Area (As Deposited)				60%
Shielding Gas (%Ar/%CO2)				90% / 10%
% C	% Mn	% S	% Si	% P
0.1	1.7	0.015	1	0.01
% Cu	% Cr	% Ni	% Mo	% V
0.5 Max				

ER4043:

- Aluminum consumable wire, EN ISO 18276 designation AlSi5
- AlcoTec Almigweld 4043 3/64” diameter
- Designed for welding heat-treatable base alloys, specifically the 6000 series alloys
- Lower melting point and more fluidity than the 5000 series filler alloys
- Low sensitivity to weld cracking with the 6000 series base alloys

Table 9. ER4043 filler material properties.

ER4043 Wire Properties and Chemistry				
Tensile Strength (As Deposited)				27,000 psi
Yield Strength (As Deposited)				18,000 psi
Elongation (As Deposited)				8%
Shielding Gas (%Ar)				100%
% Al	% Si	% Fe	% Cu	% Mn
Remainder	4.5-6	0.8 Max	0.3 Max	0.05 Max
% Mg	% Be	% Zn	% Ti	Other
0.05 Max	0.0003 Max	0.1 Max	0.2 Max	0.15 Max

V. Methodology and Statistical Design of Experiments

The methodology for the design and testing of CMT based Wire Arc Additive Manufacturing and the production of specimens for geometric evaluation, mechanical testing, and microstructural examination is detailed in the following section.

Geometry Evaluation Methodology

For preliminary assessment of geometry, evaluation of the geometric deposition capabilities and different print strategies will be performed. Replicating the process of prior researchers, multiple geometries will be created and printed at a variety of parameters. Objects will be printed with ER70S-6 steel, ER4043 aluminum, and ER308 stainless steel wires all of 0.045 in. diameter.

Weld paths will be drawn using Solidworks and G-code created using HSMWorks add-in. The creation of G-code is accomplished in HSMWorks by mimicking a milling toolpath using a trace function. For this research G-code will mostly be created and post-processed by hand.

Single bead width print geometries, created with different two step-up methods, are proposed for evaluation. The ‘spiral vase’ method is characterized by a single-bead, constant z-axis retraction path. In this method, the welder continuously welds while retracting and spiraling up, and eliminating layer changes and starts and stops. Hollow objects will also be created with the traditional layer change method, referred to as “layer-by-layer” and characterized by planar deposition at discrete layers, stopping the welding process when complete, moving to the next layer start point, and resuming.

For the deposition of thicker wall widths and solid layers, multiple methods of infill will be analyzed and are shown in Figure 85. Parallel bead deposition features straight lines or curves stacked next to one another and separated by a step-over distance. This method of infill is a favorite among researchers and was the primary method of deposition used in prior research at Auburn University. The square deposition strategy is a basic weave pattern, with lines separated by a step-over distance. The zig zag weave method, employed at the recommendation of Fronius representative Jake Ross, uses straight lines, angled back and forth by a set step-over distance in the x-axis each move. Zig zag may benefit from a short pause at the peaks of the lines, allowing for balanced deposition across the cross section. The ladder weave method features 90° arcs, offset by a step-over distance from one another and linked with straight lines. The curlicue weave method also features 90° arcs and a step-over distance in the x-axis, from the base of the arc to its sharp inflection point. This method is an overlapping weave pattern. The convex weave method has characteristic 90° arcs and set x-axis step-over. This method may also benefit from a short pause at the inflection points. The triangle weave method is an overlapping pattern, whose geometry is determined by the distance between the vertical lines and their length. The triangle has its apex slightly off-center, to make a 45-45-90 triangle. The final weave method is a sine wave, with defined period and amplitude.

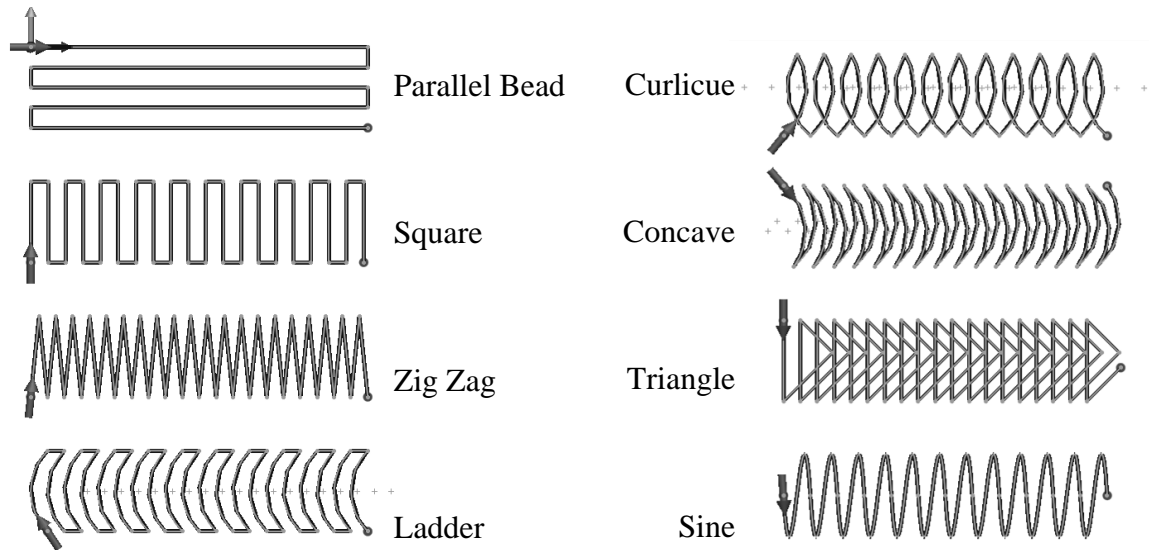


Figure 85. Geometries proposed for thick deposition.

All the methods will be first evaluated by studying the deposition of a single layer with variations in the geometry parameters (i.e. step-over, pause distance) for optimization. Printing geometries that show promise will be used to print short walls for evaluation of macrostructure, ease of production, print-to-fly ratios, and hardness. For the weave methods, a phase shift will be used when printing multiple layers to ensure any gaps between the peaks of the prior layer will be filled in.

The ability to create complex structures like ‘bridges’ or overhangs will be studied for feasibility. While multiple researchers showed the potential to create bridges and overhangs using robotic arms and two-axis positioners, minimal research using 3-axis deposition has been attempted. This bridging and overhang geometry is created by shifting deposition over to the side of the previously deposited layer, building outwards from vertical. The limitations of angled deposition with respect to vertical will be studied and be of value in future adaptation of WAAM into design limits.

The relationship of interpass cooling, or pausing between layers for a set increment of time or until a temperature set point is reached, will be studied with respect to print

geometry and macrostructure. Decreased surface finish and sagging were noted by Gaddes in previous research when excessive heat built up in the upper regions of the print.

Tensile Strength Evaluation Methodology

It is imperative to classify the material properties of the printed structures since welds commonly behave differently from wrought structures, which generally are more homogeneous and have finer grain sizes, and subsequently enhanced tensile strength. Tensile tests provide information on the strength and ductility of materials under uniaxial tensile stresses and is useful in comparisons of materials, alloy development, quality control, and design. Tensile tests will be conducted in accordance with ASTM standards covered in the literature review.

Tensile strength evaluation begins with sample preparation. Walls were chosen as the desired print geometry due to wide acceptance among other researchers in the literature review, direct comparison to past research, ease of deposition, simple G-code modification, and the ability to print multiple replicates in one structure. Producing tensile test samples, or dog-bones, from the walls will start with the removal of the print from the build plate using the horizontal band saw. Walls will then be machined square and faced flat, with care taken to remove an equal amount of material from each face of the wall to reduce the thickness and produce samples from the center of the wall. A final machining pass will be done using a fly cutter to improve the surface finish and decrease sanding time. Once to size, the dog-bones will be CNC machined from the walls using the Cincinnati CNC vertical mill with a 0.25-inch diameter end mill. Orientation and location of the tensile specimens within each wall will be recorded. The tensile test specimens were created according to the *ASTM E8* standard which dictates a specimen with a gauge length of

1.000±0.003 inches, a neck width of 0.250±0.005 inches, and a thickness of 0.250±0.005 inches, as shown in Figure 86 [48]. After machining, the samples will be sanded using the following schedule: 80-grit, followed by 120, 180, 240, 320, 400, 500, 600. Prior to pulling the specimens, the precise dimensions of the tensile test bars were verified using dial calipers with accuracy ±0.001 inches.

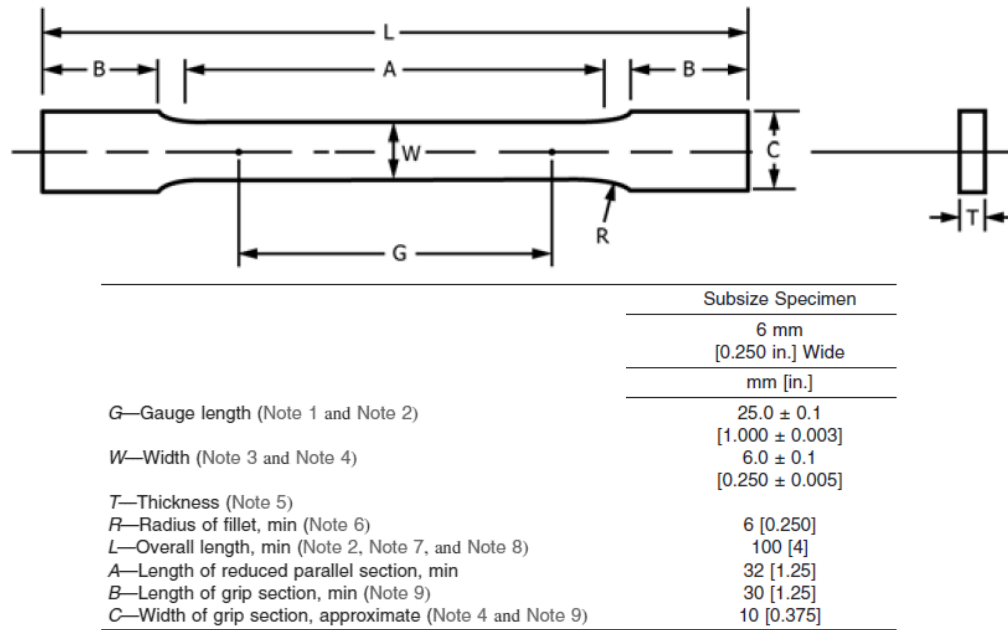


Figure 86. ASTM E8 Subsize Specimen dimensions

Tensile data is output in the form of a comma separated values (csv) file with data for time, load, and axial displacement. Knowing the width and thickness of the sample, the engineering stress (S) can be calculated via Equation 11 [53].

$$S = \frac{P}{A_0} \quad \text{Equation 11}$$

P is the axial force (kN) and A_0 is the original cross-sectional area in mm^2 . The maximum value of S is called the the ultimate tensile strength S_U . The engineering strain, e , is based on the original gage length and is given by,

$$e = \frac{l - l_0}{l_0} \quad \text{Equation 12}$$

l is the instantaneous gage length and l_0 is the original gage length. The instantaneous gage length can be calculated by adding the elongation to the original gage length. The engineering stress does not account for the change in cross-sectional area and therefore will be less than the true stress, σ , given by

$$\sigma = \frac{P}{A} \quad \text{Equation 13}$$

A is the instantaneous cross-sectional area. The true strain, ε , is based on the instantaneous gage length and is given by

$$\varepsilon = \int \frac{dl}{l} = \ln\left(\frac{l}{l_0}\right) \quad \text{Equation 14}$$

For small strains (less than 0.2 percent) the engineering stress is approximately equal to the true stress, and the true strain is approximately equal to the engineering strain. The 0.2 percent offset can also be used an arbitrary point to find the yield strength or yield stress (S_y), with $S = S_y$ at this point, as noted in the Determination of Yield Strength section of ASTM E8 [48]. After yielding, large inelastic deformations occur and the values of engineering stress/strain and true stress/strain are no longer equal. A constant volume assumption can be made such that up to necking, $A_l = A_0 l_0$. The following relationships can be made:

$$\sigma = S (1 + e) \quad \text{Equation 15}$$

$$\varepsilon = \ln(1 + e) \quad \text{Equation 16}$$

Equation 15 and Equation 16 are valid up to necking which takes place when the ultimate tensile strength has been reached. After this point, plastic deformation becomes localized and strain is no longer uniform.

The reduction of area can be calculated by measuring the area of the fracture surface after testing (A_f) and using the equation:

$$\%RA = 100 \frac{A_0 - A_f}{A_0} \quad \text{Equation 17}$$

The true fracture strain, ϵ_f , or ductility can be calculated by:

$$\epsilon_f = \ln \left(\frac{A_0}{A_f} \right) \quad \text{Equation 18}$$

The true fracture strength, σ_f , can be calculated from taking the axial force at fracture and dividing it by the area of the fracture surface but it is usually corrected for necking. This is done easily using the Bridgman correction factor for cylindrical specimens but a simple solution does not exist for square sample [53].

The toughness of a material is the ability of a material to absorb energy and plastically deform without fracturing. It is calculated by taking the area under the stress strain curve but due to the limitations of calculating true stress and true strain past the ultimate tensile strength, the engineering stress and engineering strain will be substituted into Equation 19.

$$Toughness = \int \sigma d\epsilon = \int S de \quad \text{Equation 19}$$

To produce multiple tensile test replicates in each wall, with a milling allowance for step-over in the gauge neck region, walls 120 mm in length and 100 mm in height will be printed. This size wall allows for the production of multiple replicate dog-bones to be

machined from each sample. Allowing for material removal on the sides, walls will be oversized with an as-printed thickness of approximately 12.5 mm (0.5 inches).

In accordance with standard procedures, tensile test specimens will be created and tested parallel and perpendicular to the layers of deposition. Tensile testing will be carried out on different print strategies and weave patterns. Tensile testing will be used to validate the effects of interpass cooling and design for ideal cooling levels. Walls will be printed at different interpass cooling pause times, with the temperature of the wall recorded prior to welding. Temperature and the effect that it has on tensile strength will be evaluated for future integration of a feedback control loop, pausing between the layers until a set temperature is reached.

Mechanical Hardness Methodology

The term hardness is defined as the ability of a material to resist permanent indentation or deformation when in contact with an indenter under load. Hardness testing is perhaps the simplest and the least expensive method of mechanically characterizing a material since it does not require an elaborate specimen preparation and is relatively quick. The theoretical and empirical investigations have resulted in fairly accurate quantitative relationships between hardness and other mechanical properties, such as ultimate tensile strength, yield strength, and strain hardening coefficient and fatigue strength and creep [7].

Hardness testing will be performed on samples, including the dog-bones prior to being pulled and after sanding and polishing according to the schedule outlined in the prior section. Samples will be tested on the Rockwell B scale in accordance with ASTM-E18.

Microstructure Examination Methodology

The purpose of the microstructural-analysis of this research was to classify the general microstructure of the solidified weld pool formed during the CMT-GMAW process. This analysis is accomplished by examining the weld geometry in various planes of view (i.e. longitudinal, planar, and transverse).

In a similar fashion to previous research, the metallurgical details of the deposited steel structure will be examined. The samples to be examined are to be cut from the walls manufactured for the tensile test specimens. Samples will be selected from locations which show the microstructure in the middle of a weld bead and at the interface between layers. Metallographic samples shall be prepared with care to avoid thermally disrupting the specimen in sectioning. The samples will be mounted in fast setting resin (epoxy) pucks and polished in Auburn's Materials Engineering Rough and Fine Polishing Laboratory. Specimens will be manually plane ground using rotating abrasive silicon carbide grinding paper, with grit sizes from 120 to 2000 (ANSI grit). Final polishing was accomplished using 3 μm followed by 0.5 μm alumina suspension. Samples were then dried using an air drier to and care was taken to avoid contacting the surface.

Macroscopic and microscopic examination will take place in the Materials Engineering department using optical microscopy to evaluate the grain structure. The selection of the proper etchant will follow ASTM E407 guidelines. For ER70S-6, a Nital etchant will be used with 3 mL nitric acid mixed in 100 mL of ethanol. For ER308L, Kroll's reagent will be used, a mixture of 10 mL nitric acid, and 20 mL hydrochloric acid diluted with 30 mL water. For ER4043, Keller's reagent will be used, a mixture of 190 mL distilled water, 5 mL nitric acid, 3 mL hydrochloric acid, and 2 mL hydrofluoric acid.

The ImageJ Software will be used to analyze the images. Opening the images in ImageJ is relatively straightforward. The first step in all image processing involves setting the scale by drawing a line on the scale bar and relating the number of pixels to the known length. Next, the images are converted to 8-bit monochromatic. For analysis of particle size, a threshold image is created to define the brightness values of the particles and isolate them. The threshold image will define the entire image as either black or white. The ImageJ toolbox contains a particle analysis tool that summarizes the sizes the particles in the threshold image and displays the results.

Miscellaneous Methodology

The development of a closed loop process control method for maintaining contact tip to workpiece distance (CTWD), or wire offset distance, throughout the process will be evaluated. Many researchers noted the importance and challenges of maintaining a constant CTWD. Without a process in-place to maintain CTWD, the welding program will make all z-axis steps at a distance set in the G-code. Unless the distance set to exactly the right retraction, the print will either deviate and move closer and closer to the welding nozzle or further from the welding nozzle. The Fronius welder will react to an increased CTWD by sensing increased resistance and increasing the wirefeed speed (WFS) to deposit more wire and narrow the gap. The opposite is also true, with a decreased CTWD leading to a lower WFS. In this sense, the system will act to maintain CTWD and return to the ideal distance of 14 mm.

Standard output data from the Fronius welder will be evaluated to document performance. Measured current and voltage data will be compared to that of the machine in its previous configuration. The Fronius Xplorer software provides monitoring of real-

time welding data including voltage, current, and WFS. The recorded data will be exported for analysis in Microsoft Excel.

A manual will be created that covers the operation of the welder and details the process for routine 'print' creation. A fundamental understanding of the base machine will be assumed after reading the design and construction of equipment section of this thesis and information can be found in the manufacturers' manuals for basic functions.

Easy to 'print' files/programs will be developed to create traditional standard test specimen for subsequent Auburn University researchers. In addition to creating some standard programs and storing them for future use, an easy to use script file will be created using Mathworks Matlab program to prompt the user for parameters and compile a G-code file instantly. For geometries like walls and cylinders, the script file will prompt for the parameters of length, width, and height of desired print, the welding parameters such as travel speed or interpass cooling time, and the geometry parameters like step-over distance. The program will compile the data and create a G-code file output as a text document.

The use of rafts for easy print removal will also be evaluated. Graphite mesh will be used, with different sizes and thickness' of meshes evaluated. The feasibility of this process and the effect on the print structure and stability will be evaluated.

Repeatability Study

Prior to establishing a statistical design of experiments (DoE), it is necessary to validate the capability and repeatability of the 3D printer to serve as a basis for the DoE. Related to the gantry CNC machine, Gaddes noted "repeatability studies show that the machine is accurate to ± 0.0005 inches" [4]. This system is proven to provide repeatable and precise movements; therefore, repeatability analysis will not consider this as a factor.

To examine repeatability of the prints, four walls were printed using the same welding program, producing walls 120 mm in length and 12 mm in width. The zig zag pattern with a layer-by-layer phase shift was used with a 1.25-mm step-over distance, 8 mm oscillation distance, and 0.2 second pause duration at the inflection points. Travel speed was set at 720 mm/min. The CMT 1362 synergic line was used with a wire feed speed of 95 ipm, 15% arc length correction, -1.2% dynamic correction. The first two walls were printed one week apart from each other and the second pair was printed one day apart from each other. All the walls underwent the same post-processing per the previously outlined schedule. Six replicate dog-bones were machined from each wall, with dog-bones transverse to the layers being made from Walls 1 and 2 and longitudinal samples made from Walls 3 and 4.

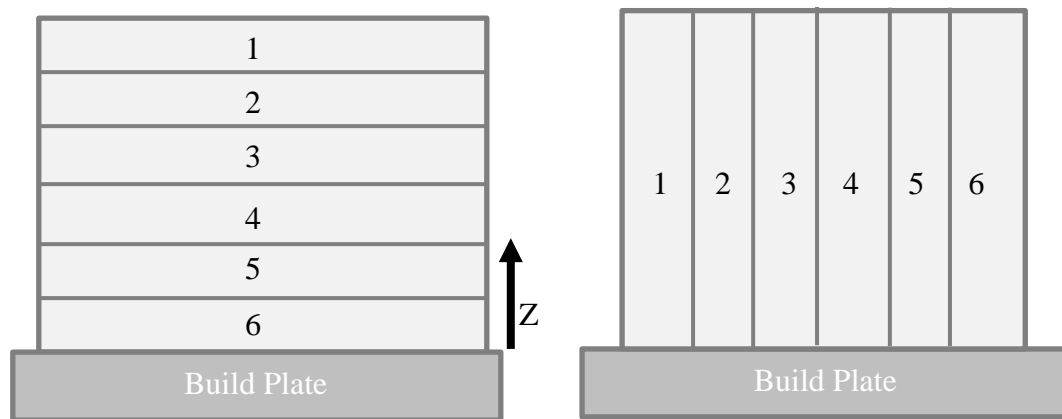


Figure 87. Longitudinal (left) and Transverse tensile specimens (right).

For walls 1 & 2, the tensile test specimens were pulled on a MTS Landmark Servohydraulic tensile testing machine, walls 3 & 4 were pulled on the MTS Q-Test 100, both were pulled at the same rate of 0.15 ipm. The load, time, and extension were recorded from which engineering stress/strain curves were generated and the ultimate tensile strength (UTS), yield strength, and Young's modulus were calculated, see Table 10 and Figure 88.

Table 10. Average and standard deviation of yield stress, ultimate tensile strength, modulus of elasticity and hardness for repeatability study.

Sample orientation	Wall		Yield Stress	Ultimate Tensile Strength	Young's Modulus	Average Hardness
	No.		ksi	ksi	ksi	HRB
Transverse	1	Avg.	53.34	67.90	6924.52	76.56
		SD	2.242	0.257	163	0.57
	2	Avg.	52.17	67.59	6706.15	76.21
		SD	2.407	0.269	336	0.96
Longitudinal	3	Avg.	51.48	69.52	1228.09	75.91
		SD	2.865	1.037	262	0.51
	4	Avg.	50.41	69.15	1342.50	75.79
		SD	1.133	0.822	119	0.85

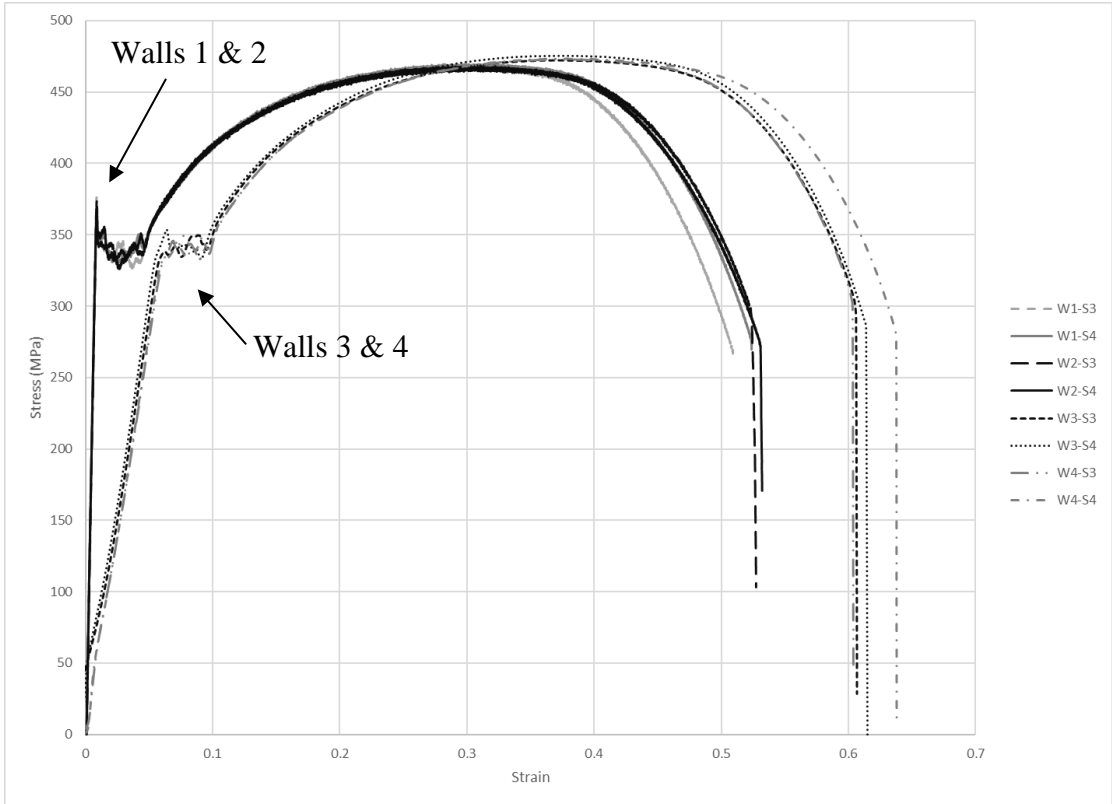


Figure 88. Engineering stress – strain curve for repeatability study walls 1-4.

When looking at the data and the plot above, the magnitude of the difference between the tests jumps out at you. Shown in Figure 88 is a sample of two stress strain curves for each wall, with sample 3 and 4 plotted for each. The curves that take off steeper, and yield first are walls 1 and 2, pulled on the MTS Servohydraulic Load Frame. The other curves, that have the shallow slope of stress vs. strain are walls 3 and 4, pulled on the Q-test. The yield points for walls 3 and 4 seems to be shifted from the other curves by the same amount that the final fracture point is shifted. The values for modulus of elasticity is very different than that of any steel, and the difference from Wall 1 and 2 to Wall 3 and 4 is tremendous. For example, 1018 steel has a modulus around 29,000 ksi, while our values for Walls 1 and 2 were around 6800 ksi and Walls 3 and 4 are around 1250 ksi, orders of magnitude less. The data output for the MTS Q-Test is different than that of the MTS Landmark Servohydraulic load frame. While the raw data output is similar in format, the software calculates stress, strain, and modulus of elasticity for every sample. The rate of data acquisition is also about 50 times less than that of the other machine, resulting in smaller and less accurate data sets. The MTS Q-Test software generated values for stress were correct, however when checked against calculated values, the software generated strain values were half of the actual engineering strain. The calculated modulus of elasticity, using a slope fit, was around one-third that of the reported modulus. Checking the calibration on the machine, the certifications for displacement, crosshead speed, and force calibrations were all expired. This may be the source of error, but this does not account for the shift in data. The values independent of displacement, i.e. ultimate tensile strength and yield stress seem accurate, so future testing on this machine will only consider them valid. However, the yield strength cannot be calculated using the 0.2% offset and it

must be found as the maximum point of the linear region, or the elastic limit. Toughness cannot be calculated for this repeatability study as the values would vary drastically from wall 1/2 to wall 3/4. However, although toughness is an elongation dependent value, it can be calculated and used as a point of comparison, regardless of the machine used, as long as all the samples pulled on the same machine.

T-tests were performed using Minitab 18 comparing the ultimate tensile strength (UTS) and yield stress within each wall, from outside to inside and top to bottom, and from wall to wall. The t-tests compare the walls to each other and test the hypothesis that the mean UTS or yield stress are equal. For a p-value greater than 0.05, the walls are statistically equal, and therefore we can assume the samples are the same. For wall 1 and wall 2, comparing the outer samples (1 and 6) to the inner samples (3 and 4) resulted in p-values greater than 0.05, meaning the walls are the same from outside to inside. Comparing all samples of wall 1 to wall 2, p-values greater than 0.05 were observed for both UTS and yield stress, meaning the walls were statistically equal, see Table 11.

Table 11. P-values for combinations of Walls 1 & 2 two sample t-tests.

Combination	Factor	P-Value
Wall 1 Outer to Inner	UTS	0.430
	Yield	0.134
Wall 2 - Outer to Inner	UTS	0.084
	Yield	0.225
Wall 1 - Wall 2	UTS	0.068
	Yield	0.407

This process was repeated comparing wall 3 to wall 4, the upper samples (1 and 2) were compared to the lower samples (5 and 6), and wall 3 was compared to wall 4. P-values greater than 0.05 were observed in all combinations for both UTS and yield stress, as shown in Table 13.

Table 13. P-values for combinations of Walls 3 & 4 two sample t-tests.

Combinations	Factor	P-Value
Wall 3 - Top to Bottom	UTS	0.485
	Yield	0.743
Wall 4 - Top to Bottom	UTS	0.406
	Yield	0.424
Wall 3 - Wall 4	UTS	0.643
	Yield	0.323

Comparing the tensile test results from walls 1 and 2 to walls 3 and 4 was done to see if the material properties were isotropic. As shown in Table 12, the p-value is greater than 0.05 for yield stress but not for UTS. This result signifies that walls produced have statistically the same yield strength regardless of orientation but have different UTS. A possible source of error here arises when you consider that the dogbones were pulled on different machines. Therefore, in further analysis and testing both orientations must be studied for UTS until the process reaches isotropic behavior. When looking at the averages for UTS compared to the manufacturer's specifications, the walls fall short of reaching the 70 ksi mark. While this is currently below the level reported by the manufacturer, this level represents a large leap forward from past research at Auburn.

Table 12. P-values for transverse vs. longitudinal walls two sample t-tests.

Combinations	Factor	P-Value
Wall 3&4 to Wall 1&2	UTS	0.00002
	Yield	0.094

In order to design a statistical experiment to study various effects of controllable factors, it is necessary to establish a sample size based of the statistical confidence limit. Sample size is dictated by how accurate the results must be, or how large a margin of error that can be tolerated. For the current study, the confidence interval (CI) was set to be at

95%. Using the data from the repeatability analysis, a power analysis was performed to determine the minimum number of samples necessary to achieve a statistical confidence of 95%.

$$\eta = \left(\frac{z\sigma}{E}\right)^2 \quad \text{Equation 20}$$

Where, z is the z-score, equal to 1.959964 based on 95% CI

σ is the standard deviation of the population

E is the margin of error

Using Equation 20, it was determined that four replicates were necessary to be within one standard deviation from the mean for tensile strength in the transverse and longitudinal orientations at 95% CI. For additional details of the analysis see Appendix IV.

Prior to testing the tensile strength, hardness testing was performed for each wall's six sample dog-bones and analyzed for repeatability. Hardness was tested in duplicate at two locations, the top and bottom of the samples in the grip region. A summary of the measured hardness values is shown below in Table 14.

Table 14. Rockwell hardness values from repeatability study.

Sample orientation	Wall		Hardness		
	No.		Top/Right	Bottom/Left	All
Transverse	1	Avg.	76.88	76.25	76.56
		SD	0.59	0.35	0.57
	2	Avg.	76.63	75.79	76.21
		SD	0.52	1.17	0.96
Longitudinal	3	Avg.	75.92	75.90	75.91
		SD	0.70	0.30	0.51
	4	Avg.	75.71	75.88	75.79
		SD	0.89	0.89	0.85

For walls 1 and 2, hardness tests were located along the top and bottom of the wall, for walls 3 and 4, hardness was tested along the right and left sides of the wall. In a similar fashion to tensile strength, t-tests were performed testing if the values were equal from outside to inside, top to bottom, left to right, comparing Wall 1 to Wall 2, Wall 3 to Wall 4, and Walls 1 & 2 to Walls 3 & 4. In comparison, p-values greater than 0.05 were observed in all combinations of t-tests with the exception of the tops of walls 1 & 2 to the tops of walls 3 & 4. The statistical summary and p-values can be seen below in Table 15.

Table 15. P-values for combinations of hardness two sample t-tests.

Combinations		P-Value
Wall 1	Top to Bottom	0.087
	Outer to Inner	0.496
Wall 2	Top to Bottom	0.114
	Outer to Inner	0.439
Wall 1 - Wall 2	All	0.236
Wall 3	Right to Left	0.936
	Top to Bottom	0.920
Wall 4	Right to Left	0.689
	Top to Bottom	0.582
Wall 3 - Wall 4	All	0.635
Wall 1&2 to Wall 3&4	Top to Top	0.031
	Bottom to Bottom	0.797
	Top to Bottom	0.107

Analyzing the results from the repeatability study, it was determined that walls were uniform and the hardness tests were constant and repeatable with all results falling within the accuracy of the machine. It is important to note that since the hardness values are independent of deposition direction, a comparison between transverse and longitudinal is not completed; however, the location of the measurement is of greater significance and compared (top to bottom). A power analysis was performed to determine the minimum number of samples necessary to achieve a statistical confidence of 95%. Similar to tensile

strength, it was determined that four replicates were necessary to be within one standard deviation from the mean for hardness at 95% CI. The standard deviations for the walls were 0.781 comparing the tops, 0.726 for the bottoms, and 0.770 for all the samples. For additional details of the analysis see Appendix IV.

Statistical Design of Experiments

Single-Bead Geometry Study

Experimentation will begin with single-bead geometry evaluation for steel and aluminum. This study aims to develop ideal deposition practices and highlight the capabilities and limitations of 3-axis WAAM; the results from this study will influence all further studies. This study will focus on ER70S-6 and ER4043 and omit the use of ER308 due to similarities in deposition behavior arising from comparable material properties between stainless steel and mild steel filler material. Using the wire feed rate and travel speed that was recommended by Fronius representatives during training as a starting point, two methods of buildup will be analyzed for the production of single-bead width multi-layer parts, spiral vase and layer-by-layer. Cylinders will be produced via the two buildup methods. The effect of interpass cooling will be studied by pausing between layers in layer-by-layer deposition, or not pausing at all in the spiral vase method. Observations will be made including, visual inspection, ease of buildup, slumping, and consistency. Measured data will include, bead width, as-printed size, and number of beads deposited. This study will also involve the printing of single-bead width walls.

Table 16. Preliminary geometry study factors and levels.

Factors	
Material	Method
ER70S-6	Spiral Vase - No Pause
ER4043	Layer-by-layer - With Pause

Thick-Bead Geometry Evaluation

For the evaluation of printing thicker beads using steel, multiple methods of infill will be examined in a preliminary analysis. All eight proposed methods will be used to print 50 mm long, 12 mm wide, single layer beads. After printing one group of eight, the geometry parameters will be altered based on the findings. Three batch runs will be done to optimize each geometry. The initial parameters will be set using a constant volume of filler material assumption while holding constant the wirefeed speed at 95 ipm. Travel speeds will be adjusted for each path such that all geometries deposit the same volume of wire. Knowing that the zig zag method with a travel speed of 720 mm/min produces a good result, as evidenced by the repeatability study, the amount of material deposited can be calculated by measuring the length of the weld path. Performing this analysis for each geometry and setting the volume of wire deposited equal to that of the zig zag layer, travel speed was calculated for each path and used as an initial set point. For each geometry, observations will include visual inspection, presence of porosity, undercutting, rounding, ease of buildup and consistency. These will be weighted and assigned a value comparatively from 1-8, with 1 being the best and 8 being the worst among the group. The weighted numbering system will be used to identify quality and feasible geometries, and thus be reflected in a lower score. Measurable data will include as-printed width and height for comparison. The results of the weave tests will indicate which weave patterns and

geometries are feasible for use in WAAM and deserve further analysis, while the other geometries will be abandoned along the way.

Table 17. Steel weave geometry study factors and levels.

Factors	
Material	Geometry
ER70S-6	Square
	Zig Zag
	Ladder
	Curlicue
	Concave
	Parallel
	Triangle
	Sine

Using the best geometries from the weave tests, secondary analysis will be conducted by building up multiple layers to form “short walls”. These walls will be 75 mm long and 12 mm wide. Observations will be conducted and weighted in the same manner as the preliminary analysis. Measurements of height and width will be taken as-printed, then the walls will be machined along the sides until they are clean and free of any weld surface. The tops of the walls will then be milled flat. Measurements of thickness and height will be taken and compared to the as-printed measurements to calculate the yield, or the “print-to-fly” ratio. Hardness testing will be done on the top surface to provide an estimation of material properties. Analysis will be conducted with the aim of selecting one geometry with the best all-around properties to use throughout the rest of this study.

Table 18. Steel “short wall” study factors and levels.

Factor	Levels
Material	Geometry
ER70S-6	1st, 2nd, etc.
ER308	

For aluminum deposition, a similar study will be conducted but geometries will be limited to non-overlapping weave patterns, as the build up needs to be kept to a minimum. Only parallel bead, square, zig zag, ladder, convex, and sine will be used. Wirefeed speed will be reduced as heat builds up. Travel speeds will be set using the constant volume assumption and be based off of preliminary work with Fronius representatives. Any feasible thick-bead geometries will be used to perform a short wall study.

Table 19. Aluminum geometry study factors and levels.

Factors	
Material	Geometry
ER4043	Parallel Bead
	Square
	Zig-Zag
	Ladder
	Convex
	Sine

The thick-bead geometry study continues with the examination of the ability to create complex overhang structures. Using the method of deposition with the best results for each material, the limitation of overhang angle will be studied for 15, 30, and 45° angles with respect to vertical.

Table 20. Overhang geometry study factors and levels.

Factors	
Material	Overhang Angle
ER4043	15
ER70S-6	30
ER308	45

Mechanical Properties

Using the optimized geometry from the thick-bead results, walls will be deposited to produce dog-bones for evaluation of tensile properties. Walls will be printed with a programmed length of 120 mm and a width of 8 mm. Four dog-bones will be machined out of each wall. This will allow for excess material to be removed from the faces of the walls for yield calculations as well as producing samples for microstructural evaluation.

The first study conducted will evaluate four levels of interpass cooling time, or the duration of a pause between layers. Interpass cooling time durations of 30, 90, 120, and 180 seconds will be used for evaluation with two materials, ER70S-6 and ER308. Per the repeatability study, four dog-bones will be created at every cooling time/material factor combination, with a total of 8 walls produced. Hardness testing will be done on each wall before tensile testing, with four hardness needed per wall.

Table 21. Interpass cooling time study factors and levels.

Factors		
Geometry	Material	Interpass cooling times (s)
1	ER70S-6	30
		90
	ER308	120
		180

For the evaluation of the mechanical properties of aluminum, printing a wall will be attempted using the best geometry found in the geometry study. Aluminum deposition poses many challenges, therefore the geometry of the wall and the size of the tensile dog bones specimens may need to be revised to accommodate for this.

VI. Results

Standard Specimen Data Sheet

A standard data sheet was created to allow for the recording of all pertinent data of the print in one location and can be seen in Figure 89. The weld and geometry parameters sections of the data sheet would be filled out prior to the print. This section provides a large blank space to draw in the geometry pattern used. The post weld data features measurements from the walls as-printed, during the machining process, and at the end. This data sheet was made to assist in the making of dogbones, but it can be used for other prints as well, as the pertinent information remains the same in most of the sections.

The data sheet asks for a test code name and data save location to avoid lost data or misidentifying the parts. The code name is a short two to three letter abbreviations for the study being performed, for instance SWS (short wall study). The wall ID would be a unique feature of that sample, for instance a wall printed in the interpass cooling study with a 90 second pause duration would be identified P90. In the post machining data area, the specimens, typically dogbones, receive a number to track their width, thickness, hardness, and any notes that goes along with them. Below this section is a blank area where the operator would draw in the wall identifying the print orientation and location of the dogbones relative to this, for instance if sample 1 was machined from the top or bottom of the wall, or from the left or right. All data sheets can be found in Appendix II.

WAAM Print/Sample Info Sheet									
Name:					Geometry Printed:				
Date:					Study:				
Test Code Name:					Data Save Location:				
Weld Parameters									
Material	Gas	Synergic Line	WFS (ipm)	ALC (%)	Dyn. Cor. (%)	Burn Back (s)	Crater fill	Notes	
ER70S-6	90/10								
ER308L	98/2								
ER4043	100 Ar								
Geometry Parameters									
					FR/TS (mm/min)				
					FR Reduction?				
					Layer Time				
					Notes				
Post Weld Data									
Wall ID	As Printed			Layers Printed	Total Time	Material Removed		% Yield	Notes
	Height	Length	Width			Side 1	Side 2		
Post Machining Data									
Wall ID	Sample #	Orientation	Dogbone		Hardness (HRB)	Sanding Grit	Surface Defects?		
			Width	Thickness					

Figure 89. Standard data sheet for tensile specimen.

Closed Loop Process Control

Early testing and deposition revealed the importance of closed loop process controls. Therefore, before taking any data, work began on the development of closed loop feedback controls. The two main issues that were noticed were:

- 1) After receiving an M111 (Welding Start) command, the robot begins moving before welder arcs. The G-code reads the M111, activates the signal and moves on to the next line. The delay was very small, about 0.5-1 second but still noticeable.
- 2) Programing for discrete z-levels leads to increasing or decreasing contact tip to work distance (CTWD) if layer height is not properly set. Because of this, every few layers the operator would have to pause the program and reset the z-height and then restart the program.

Initial attempts to fix the first issue involved the use of an inserted pause after a M111 welding start command in a similar fashion to Ding et al. [45]. This was found to be helpful but not a great solution to the problem as the pause duration did not account for variance in the time it took to arc. The Fronius ROB 5000 features numerous output signals, including an Arc Stable signal that goes high when the filler material makes contact with the base plate. Coupling this signal to the robot movement was done using custom VB Scripts in Mach3 which are detailed in Appendix III. Essentially, once a M111 command is received, the CNC program is paused until the input is received, at which point the program is resumed. This code runs in the background and is unnoticeable in practice. simple code allowed for the welder to start at the correct point and not move prior to arcing.

To work around the issue of increasing or decreasing CTWD, initial work was carried out with the goal to develop a way to change the z-height in process. When the operator notices the distance getting too large, he could press a button, triggering the z-axis to move down or up by 1 mm. This idea was a patch to the problem but was abandoned for a less hands on probing program that would operate without any operator action. A probing program was created that utilized the touch sensing function of the Fronius welder and assigned to the M141 M-code. Once the M141 code is executed, touch sensing is activated on the welder, and the z-axis moves down until contact is made. When the electrode and the workpiece have made contact the ROB 5000 outputs an arc stable signal high. A VB script was created that contains the entire program and involves multiple loops and checks of initial conditions. The program first checks to see if contact is already made, if not it will begin to lower the z-axis at a lower federate of 100 mm/min until contact is made. Prior to changing the feed rate, the program reads the current feed rate and stores that to a variable, allow the feed rate to be reverted back at the end of the program. Once contact is made, robot is commanded to moves up relative to this point by a set distance and re-zero at that level. For a desired CTWD of 14 mm, the z-axis has to be lifted about 8mm when probing on the edge of a part due to burnback in the wire. When probing on the top of a weld bead the z-axis only needs to retract 3mm. To avoid having to change the VB script and additional program was created and given the M142 designation and will be used for probing the middle of a weld bead.

An unforeseen benefit of this probing feature is the added ease of creating programs. When making print in which the geometry remains constant throughout the entire program, only two, three, or four layers need to be programed followed by a M141

probe, then copied and passed until the desired number of layers is reached. For instance, a wall is desired with layer one printing at $Z = 0$, and layer two printed at $Z = 3$. A probe would take place and resets the zero prior to layer 3, allowing the same code for layer one and two to be used again without the operator having to change the z values on those layers or create and program every individual layer.

ER70S-6 – Geometry Evaluation Results

Single-Bead Geometry Study

Single bead tests, 70 mm in length, were first performed with wire feed speeds of 125, 150, and 175 ipm and WFS/TS ratios of 5, 10, 15, and 20. The results showed that the ideal WFS/TS ratio was around 7.5. Further analysis was performed that dialed in the WFS at 125 ipm at a TS of 400 mm/min, a ratio of 7.9.

For ER70S-6, ideal “speeds and feeds” for the deposition of single-beads were found to be a WFS of 125 ipm, a feed rate of 400 mm/min, arc length correction of 15%, and a dynamic correction of -1.2%. With these parameters, single-bead thicknesses of around 5.5 mm can be realized. In the deposition of a 120 mm long, single-bead wall, 32 layers were printed and can be seen below in Figure 91. The resulting height was measured to be 55 mm, or about 1.72 mm/layer. In this print, a pause time of 60 seconds was used between layers. Minimal surface roughness can be seen.

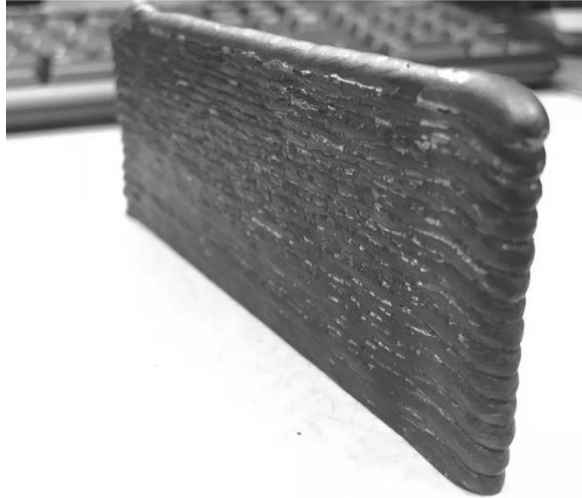


Figure 91. Single-bead wall, ER70S-6.

Examining the wall using the Keyence VHX 1000 revealed more details about the surface. As shown in Figure 90, a single bead at the bottom of the wall is flanked with a buildup of some precipitate both above and below the layer, as indicated by the arrows.

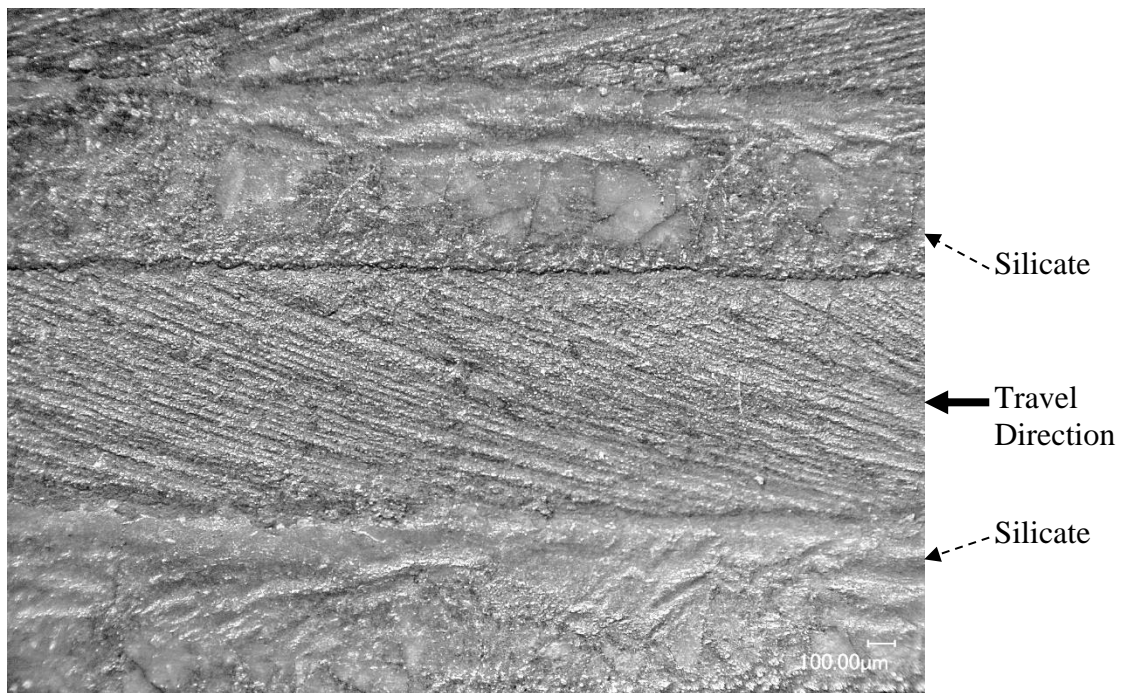


Figure 90. Side view of a single weld bead, showing direction of travel.

Speaking with Fronius representative Jake Ross, the precipitate buildup was found to be silicate. It is common a combination of silica, manganese, iron, and oxygen along with other trace alloys including the copper coating on the wire to prevent corrosion. While welding, the silicate floats on top of the liquid weld pool and aids in shielding the weld from impurities and puddle fluidity. The silicate cools and forms a glass that can be chipped away. In multilayer buildup, the silicate has been observed to flake off the surface and is easily removed after welding with a wire brush.

Using the Keyence 3D microscope to stitch together an image of an area representative of the surface, heights were calculated to quantify the roughness and the material that would need to be removed to generate a clean surface. As seen in Figure 92, just 0.2159 mm separated the lowest point from the highest point in the sample taken.

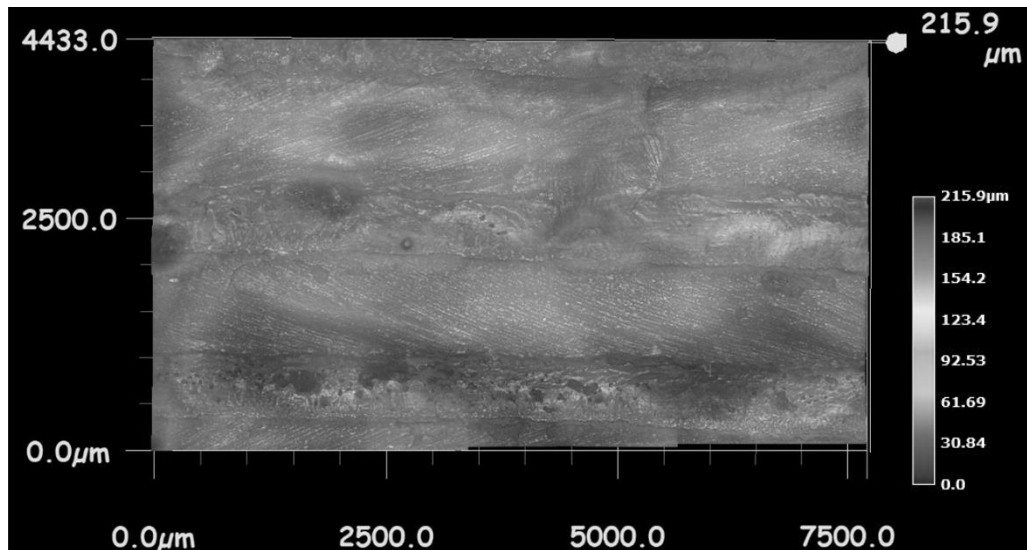


Figure 92. Profile measurement, ER70S-6 single-bead wall.

For ER70S-6, single-bead cylinders were made via a spiral and layer-by-layer method and can be seen in Figure 93. Both cylinders were programmed to be 35 mm in diameter. The spiral cylinder has a pitch of 2 mm and the layer-by-layer has a step up and probe between layers. The spiral cylinder printed without stopping, and the layer-by-layer

paused between layers. In total 16 layers were deposited, resulting in a 20.5 mm cylinder (1.28 mm/layer) that was 37.5 mm in external diameter and 28.75 mm internal diameter. The spiral cylinder is much shorter, due to the excess heat input the removal of cooling time between layers.



Figure 93. ER70S-6 single-bead cylinders made with the spiral method (right) and layer-by-layer method (left)

Thick-Bead Geometry Study

For the evaluation of deposition of thicker beads, eight weave patterns were tested and can be seen below in Figure 94. The image below the patterns is the cross section of the bead, cut with the build plate intact. This highlights the flaws of the geometries further expanding upon surface inspection. All of the beads were programmed to be 12 mm wide and 50 mm long. From left to right in Figure 94, we have square, zig zag, ladder, curlicue, convex, parallel bead, triangle, and sine. The geometries were evaluated based on their deposition quality and measurable dimensions.

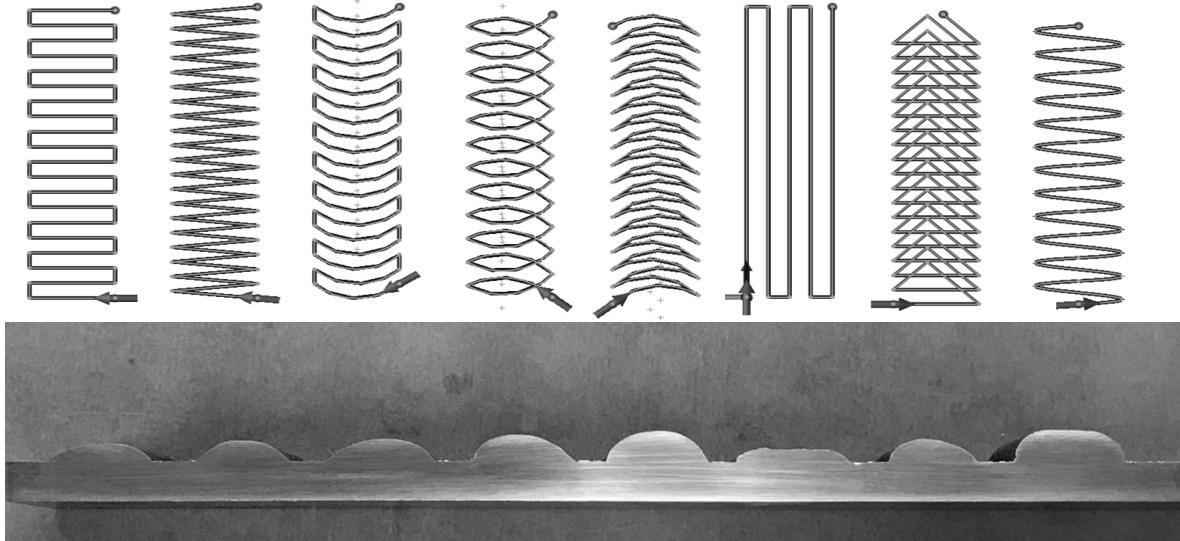


Figure 94. ER70S-6 weave geometry study results (bottom) and weld paths (top).

The geometries were visually inspected and ranked with results shown in Table 22 along the feed rate or torch speed used and the associated geometry step over. It was clear that many of these geometries showed some promise and just needed to be tweaked further, while other were worse.

Table 22. Weave geometry test 1 results.

Factors	Parameters		Observations			Measurables		
	Geometry	Step over (mm)	Feed Rate (mm/min)	Visual Inspection	Porosity	Consistency	Width (mm)	Layer Time (s)
ER70S-6	Square	2.6	448	6	Yes	No	13.7	40.4
	Zig Zag	1.25	720	1		Yes	12.6	42
	Ladder	2.5	483	5		No	14.6	53.5
	Curlicue	2	492	4	Yes	No	14.1	60.2
	Concave	1.5	648	2		Yes	14.3	78.1
	Parallel	3	410	8		Yes	15.7	39.8
	Triangle	2.5	801	3		Yes	13	42.6
	Sine	4	467	7		No	15.6	107.5

Based on monitoring the deposition and the results of the first weave geometry study three weave patterns were abandoned. Parallel bead, sine, and curlicue would no longer be considered. Parallel bead and sine produced an inconsistent height, with sine also

showing deep undercutting. Curlicue produced void space in the overlap region at the start and end of the bead and was observed to be very hot at the end of the weld.

For the second iteration of the weave geometry test, initial parameters were changed for all but the zig zag geometry. For that geometry, two iterations were done with changes in the dwell time; the first coming in the form of reduced feed rate at the corners and the latter coming in the form of a programmed pause, a 0.2 dwell at the inflection point. The reduced feed rate feature is an option in the CAD/CAM software used to program the paths and is typically used in milling applications to slow the feed rate in the corners to avoid chatter. The feed rate reduction is defined by a specified distance and reduced speed, both of which may require tweaking to get dialed in. When trying to figure out the feed rate and distance to use, comparisons in the time were simulated in HSMWorks to estimate the layer time. A feed rate reduction to 100 mm/min for 0.4 mm was decided upon based on a simulated time being equal to that of a zig zag path with a 0.2 second dwell at the inflection points.

The concave, ladder, and triangle were all modified slightly, with increases or decreases in the step over distance. The square profile was modified to include a slight draft on the sides, with a 3-mm lateral step over on the edges angling back by 0.5-mm when crossing over the middle to the other edge. The feed rates were all updated with the constant volume assumption constraint. The results of the weave geometry evaluation 2 can be seen in Table 23. In this weave geometry evaluation porosity was not noticed, therefore additional categories of rank were created. Alongside visual inspection the profile and consistency were ranked, with close ties being indicated by shared values.

Table 23. Weave geometry test 2 results.

Factors		Parameters			Observations			Measurables	
	Geometry	Step over (mm)	FR Reduction	Feed Rate (mm/min)	Visual Inspection	Profile	Consistency	Width (mm)	Layer Time (s)
E R 7 0 S 6	Modified Square	3, 0.5		464	4	1	4	14.3	44.2
	Zig Zag	1.25	↓ 100 m/min for 0.4 mm	720	1	2	1	14	50.2
	Ladder	2		558	3	4	3	15.6	64.3
	Concave	1.75		572	2	5	4	14.8	53.2
	Triangle	3		670	2	6	6	14.7	48.2
	Zig Zag	1.25	0.2 sec. pause	720	1	2	2	15.5	53.7

The results of the Weave Geometry Study 2 indicated better results, as the layer times were all closer together and the beads did not show any major glaring issues. The triangle geometry produced a very lopsided bead, with a higher height in the region where the apex of the triangle lies. For this reason, in the third iteration of the weave geometry evaluation, triangle would no longer be considered as viable for buildup. Concave did not produce great results but it might benefit from a reduced feed rate. The ladder geometry did not produce great results and due to the overlapping bead, sounded very unstable when printing. For this reason, I do not believe it would successfully produce multi layered parts and therefore will no longer be evaluated.

For Weave Evaluation 3, square, concave, and zig zag were the only geometries considered and were each duplicated twice. The modified square geometries varied in step-over and step-back, with “modified square 1” featuring a 3-mm step-over and 0.5-mm step-back and “modified square 2” featuring a 4-mm step-over with a 1-mm step-back. Zig zag 1 featured a 1.25-mm step over while zig zag 2 featured a 1.75-mm step over. The concave geometries both had a step over of 2-mm, with concave 2 diverging from the characteristic 90° arcs and featuring shallower 65° arcs. The feed rate reductions that were introduced in the weave geometry study 2 produced great results and added material to outside edge,

aiding in buildup of a flat profile. The feed rate reductions were added to weave geometry evaluation 3 and can be seen alongside the reduced feed rate distance shown in Table 24 below. Visual inspection was conducted between the iterations and focused on ranking the top parameters of each geometry. Bead height was added alongside width and layer time.

Table 24. Weave geometry test 3 results.

Factors		Parameters			Observations		Measurables		
	Geometry	Step over (mm)	FR Reduction	Feed Rate (mm/min)	Visual Inspection	Consistency	Height (mm)	Width (mm)	Layer Time (s)
E R 7 0 S 6	Modified Square 1	3, 0.5	↓85 m/min for 0.4 mm	464	2	6	3.2	15.3	47.1
	Zig Zag 1	1.25	↓100 m/min for 0.4 mm	720	1	1	3.6	14.7	51.9
	Concave1	2, 90°	↓100 m/min for 0.4 mm	516	2	5	3.9	14	42.6
	Modified Square 2	4, 1	↓85 m/min for 0.4 mm	419	1	4	3	15.4	44.7
	Zig Zag 2	1.75	0.2 sec. pause	536	2	3	3	13.3	39.9
	Concave 2	2, 65°	↓100 m/min for 0.5 mm	626	1	2	3.2	14.1	43.7

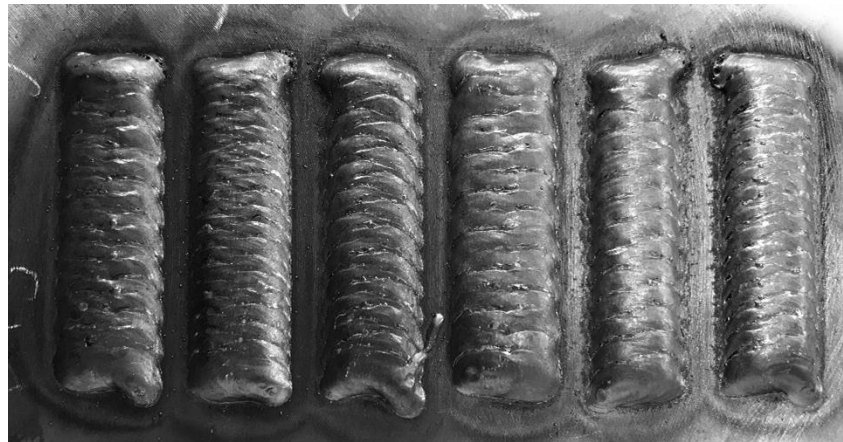


Figure 95. Weave geometry study 3, from left to right, square 1, zig zag 1, concave 1, square 2, zig zag 2, concave 2.

Based on the results of weave geometry study 3, modified square 2, concave 2, and zig zag 1 all warrant further analysis and testing as viable geometries for multilayer buildup. These three geometries were selected for continued study in the short wall study.

Short Wall Study

The modified square, concave, and zig zag geometries and the parameters from weave geometry study 3 have been selected, and shall be evaluated in the short wall study. This study will evaluate the ability of these three geometries to produce stable buildup and a clean machined surface. The study will also begin to look at the material properties to see if any variations exist.

Three 75 mm long walls will be printed simultaneously, with one for each geometry. Nine layers will be deposited, with a 35 second pause and probe cycle when moving between the walls. The weld path, feed rate, and feed rate reduction parameters can be seen in Figure 96. The welding parameters mimic the geometry study, with wire feed speed at 95 ipm, 15% arc length correction, and -1.2% dynamic correction. The results of the study are shown below in the images of Figure 97 and in Table 25.

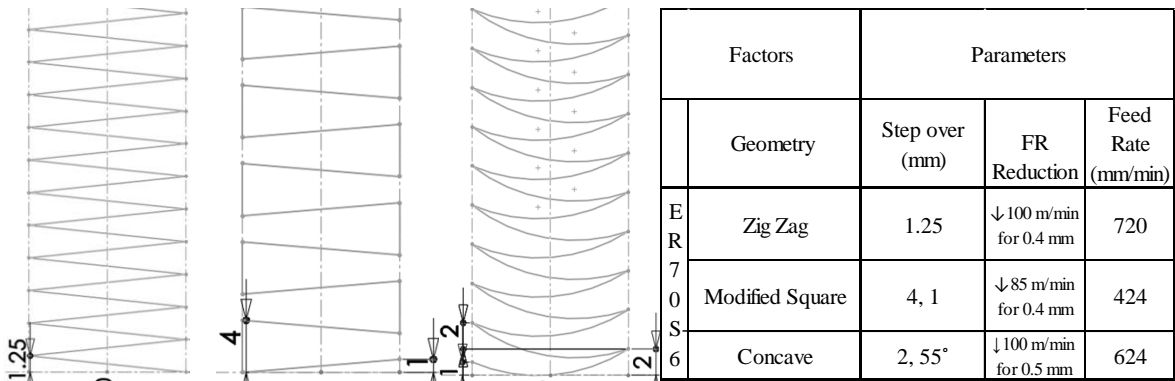


Figure 96. Geometries and dimensions (mm) used in the short wall study, from left to right: zig zag, modified square, and concave.

Yield was calculated based on the amount of material removed from one side in milling using Equation 21:

$$\% \text{ Yield} = \frac{\text{Original Width} - \text{Material Revoved}}{\text{Original Width}} * 100 \quad \text{Equation 21}$$

As illustrated on the left images in Figure 97, the modified square produced the roughest as-printed surface. This visual inspection is reflected in the data with this geometry having the lowest yield percentage. The lengths of the walls were all around the same values however the heights and widths varied, with the square wall much wider and shorter than the others. Due to the slow buildup and rough surface, the modified square geometry is not recommended as the best option. Between concave and zig zag, the results were very similar. A definite conclusion on the quality of the walls is hard to justify with almost equal as-printed heights and widths and negligible differences in the yield.

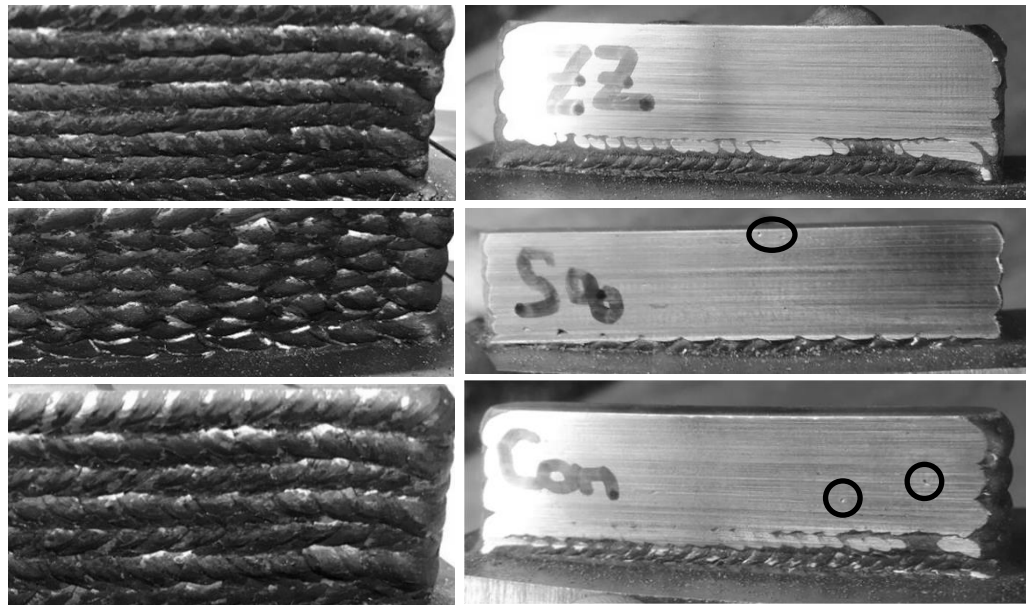


Figure 97. Short wall samples before and after machining, from top to bottom: zig zag, square, and concave. Black circles highlight porosity.

One major issue with concave was noticed upon closer inspection of the machined surface. Shown with circles in Figure 97, the presence of void areas or large porosity in the concave wall and the absence of any in the zig zag wall indicates a valid reason to focus

solely on the 1.25-mm zig zag for all future testing in ER70S-6. In addition, higher hardness values for the zig zag geometry in the results from six hardness tests taken across the top of each wall indicate better mechanical properties. A complete summary of the data can be found in Table 25.

Table 25. Short wall study measured results.

Factors		Measurables								
		Layer Time (s)	Length		Width			Height		
Geometry	Printed (mm)		Printed (mm)	Removed (mm)	% Yield	Printed (mm)	Removed (mm)	% Yield		
ER70S-6	Zig Zag	77.2	78	14.1	-0.5842	95.86%	24.9	-2.2225	91.07%	82.16
	Modified Square	66.8	79	15.5	-1.143	92.63%	20.3	-1.905	90.62%	80.46
	Concave	74.7	77	14.1	-0.635	95.50%	24.6	-2.413	90.19%	80.93

Two Wall Study

For final analysis of the weave geometry, two walls will be printed using a 1.25-mm and 1.75-mm zig zag. The walls will be printed at the same time and dog bones machined to evaluate the monotonic tensile properties and the difference in the walls. Dog bones would be made in the longitudinal direction for both walls to allow for direct comparison within the test and to compare to the manufacturers specification. Walls were programed to be 120 mm long, with 8 mm width and printed simultaneously, with a probe cycle between every layer. A summary of the geometry factors can be found in Table 27.

Table 27. Two wall study parameters.

Factors		Parameters		
	Geometry	Step over (mm)	FR Reduction	Feed Rate (mm/min)
E R 7 0 S 6	Zig Zag_1.25	1.25	↓80 mm/min for 0.5 mm	720
	Zig Zag_1.75	1.75	↓60 mm/min for 0.3 mm	525

Based on the results from prior analysis, the feed rate was reduced for both geometries in different manners. The 1.25-mm zig zag featured a longer feed rate reduction of 0.5 mm at a higher velocity while the 1.75-mm feed rate had a slower velocity but a shorter distance. In total, 35 layers were printed for each wall. The walls were separated from the build plate and machined on both sides, allowing for the calculation of yield on both faces. The measured results of the print and the two-sided yield values can be found in Table 26.

Table 26. Two wall study geometry results.

Factors		Measurables					
		Layer Time (s)	Width			Height	Length
Geometry			Printed (mm)	Removed (mm)	% Yield	Printed (mm)	Printed (mm)
E R 7 0 S 6	Zig Zag_1.25	98.9	12	-2.159	82.01%	91.8	122
	Zig Zag_1.75	83.4	11.3	-1.7272	84.72%	83.7	123.5

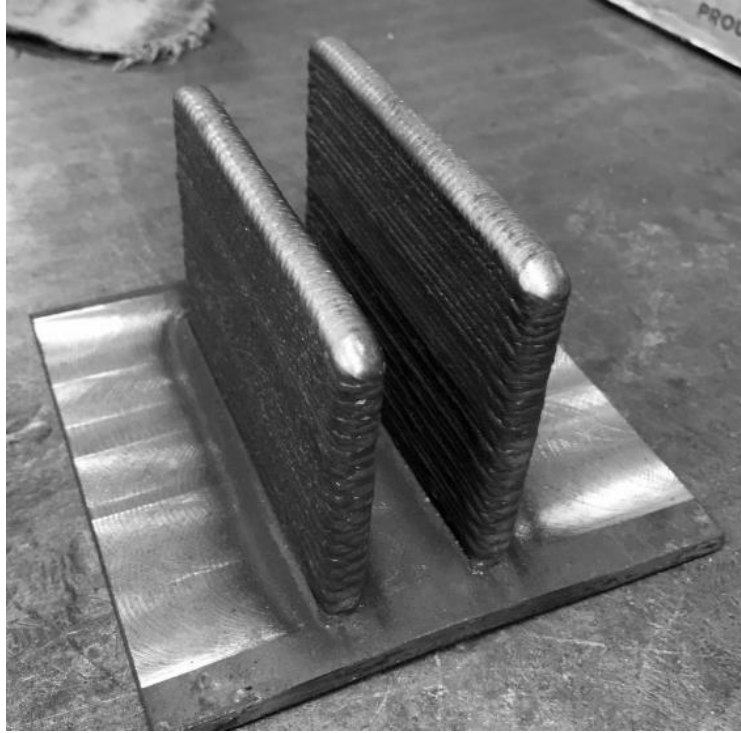


Figure 98. Two wall study 1.75 mm wall (close) and 1.25 mm wall (far)

During the study, the walls built up at different rates, as evidenced by the data in Table 26 and the image in Figure 98. In total, the walls differed by about 15 mm. This was the limiting factor in continuing the print, as after printing a layer on the 1.75-mm zig zag wall, the torch retracted up in the z-axis by 15 mm and moved to the other wall to probe. Once the clearance was reduced to the point where the torch would no longer clear the walls without contact, the program was stopped. While the yield difference looks significant, the actual difference in the material removed is on the order of a few thousandths of an inch difference, therefore this will not be the only factor used in evaluation.

Dog bones were machined and hardness test were performed on each sample prior to pulling them on the MTS Q-test. Since this machine was used, the values independent of displacement, ultimate tensile strength and yield strength will only be considered valid.

The results of the hardness tests and a summary of the data from the tensile tests can be seen in Table 28. The un-summarized data results can be seen in Appendix I.

Table 28. Two wall study results – mechanical properties

		Yield Stress	Ultimate Tensile Strength	Hardness	Reduction of Area	True Fracture Strain	Toughness
		ksi	ksi	HRB	%		$\int \sigma d\epsilon$
ZZ_1.25	Average	52.57	71.32	76.75	73.67	1.33	255.98
	SD	1.20	0.58	1.02	1.02	0.04	3.06
ZZ_1.75	Average	53.12	71.77	76.94	74.97	1.39	253.03
	SD	1.25	0.33	0.52	0.93	0.04	2.79
Manufacturers Spec		58	70		60		

Between the walls, the data shows a minor difference in the ultimate tensile strengths and yield strengths, with the 1.75-mm wall showing slightly higher values across the board as well as an increased reduction of area. The difference may be attributed to the reduced heat input due to shorter layer times for this wall. Performing a two-sample t-test on the data shows that the 1.25-mm zig zag wall and the 1.75-mm zig zag wall had statistically equal values for yield stress and ultimate tensile strength, the results can be seen in Appendix IV.

As shown in the engineering stress – engineering strain curve of Figure 99, the 1.25-mm zig zag tensile specimens, shown with the dashed lines, consistently have a higher strain value at fracture. Giving the 1.25-mm zig zag wall having a higher value for toughness than the 1.75-mm zig zag wall. Although the values are statistically equal, a decision has been made to utilize the 1.25-mm zig zag, as it produces quicker buildup of the wall, with average layer heights of 2.62 mm versus 2.39 mm of the 1.75-mm zig zag, and exhibits high toughness.

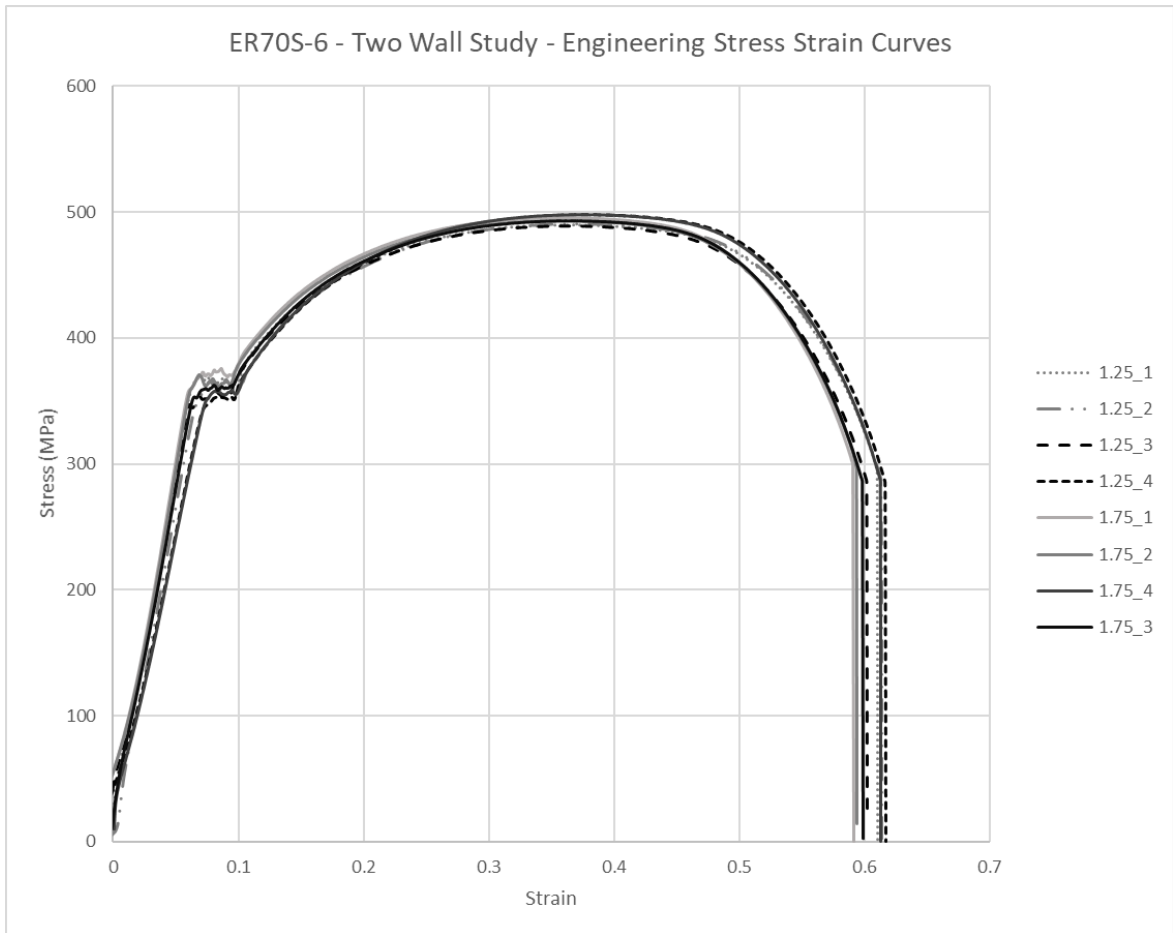


Figure 99. Engineering stress – strain curves for two wall study.

In the two-wall study, 100% manufacturers specification was achieved for ultimate tensile strength with the values exceeding 70 ksi when tested in the longitudinal direction. Prior research at Auburn was unable to produce tensile specimens with repeatable properties that meet manufacturers specifications. The yield stress values are about 90% the manufacturers specification of 58 ksi. This may be attributed to the residual stresses imposed on the weldment when clamped to the fixture plate and cooled.

Cylinders and Boxes

The evaluation of printing strategies for creating thick walled cylinders and square shapes followed. Each of these shapes present challenges when using the 1.25-mm zig zag pattern. For the cylinder, stretching the zig zag pattern around results in unbalanced deposition from the inside to the outside. For the square, the best method of turning the pattern around the corner can come in a number of different strategies.

As shown in Figure 100, four different weave corner strategies were programmed and tested on a single 50-mm square with an 8-mm wide travel path. The first strategy features the zig zag truncated into the corner and then connected by a vertical and horizontal line to the next leg. The second corner features the zig zag path rotated into a smaller zig zag separated by 1-mm from the last leg and gradually growing to full size. The third corner extends the legs of the end of the first zig zag path to a line parallel to the second path and offset by 2-mm. The fourth corner is the simplest, with the first zig zag path terminating at the corner and extending the last leg to connect to the second zig zag.

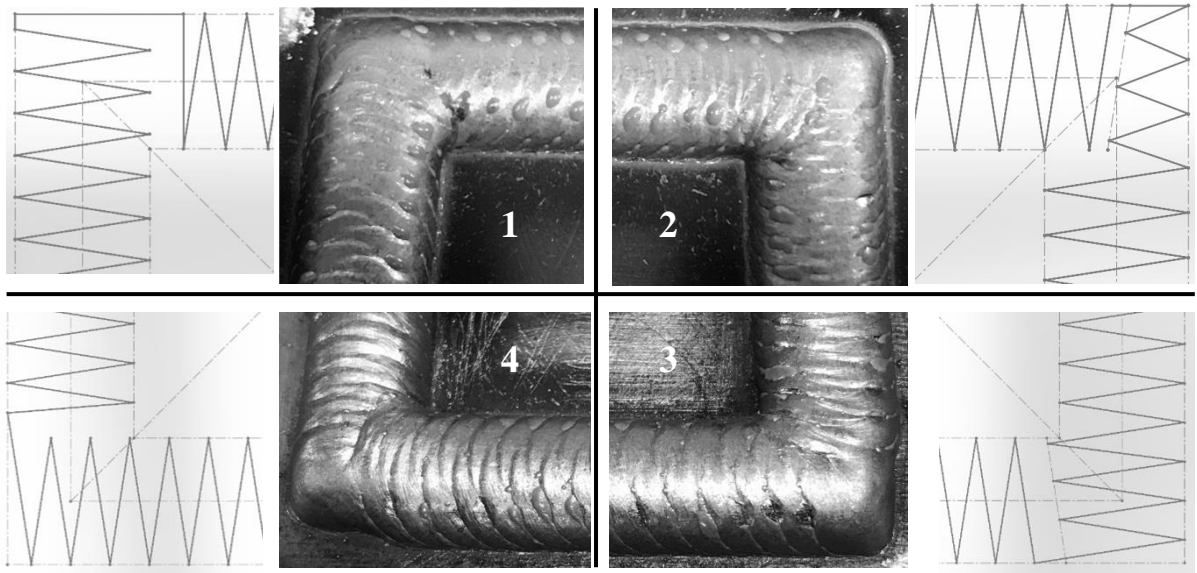


Figure 100. Thick walled box corner test results and paths.

The evaluation focused on observation while printing, visual observation after printing, and the measured voltage and current results. The first and fourth paths sounded the worst. The fourth corner failed to build up sufficient material and would result in a low yield percentage. The second and third paths both provided good results, with the third looking slightly better and doing a better job at filling the corner in and thus having a higher estimated yield percentage. The third was also the most stable, as shown in Figure 101.

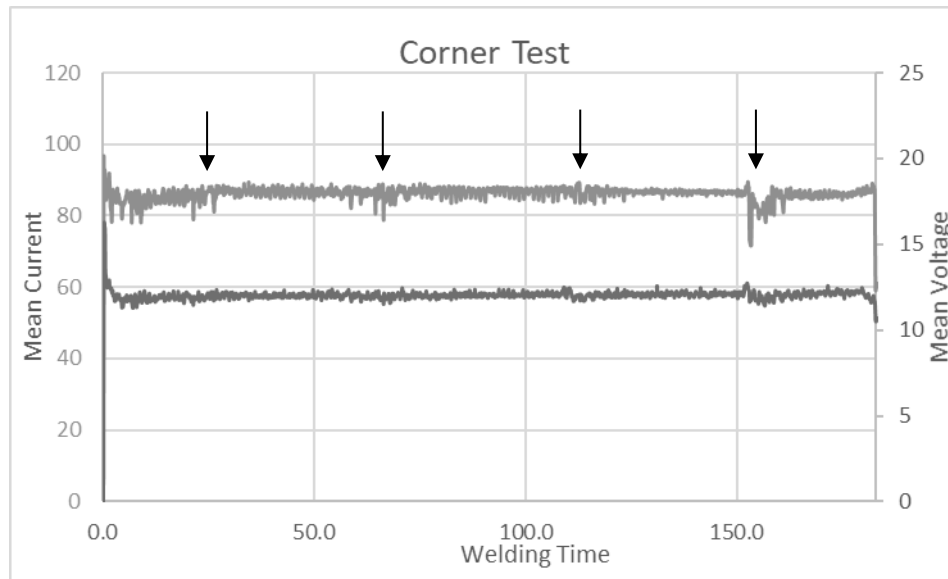


Figure 101. Current (top) and voltage (bottom) of corner test.

For the evaluation of the optimal geometry curved weave path, a cylinder, 75 mm in diameter, with a wall thickness of 8 mm was programmed to be printed. As shown in Figure 102, two paths were chosen for evaluation. The first, shown on top, is a standard zig zag path. To avoid depositing excess material on the inside of the cylinder, the reduction in feed rate was only applied to the external inflection points and was reduced from 720 mm/min to 85 mm/min for 0.4 mm. The second path shown below is a square weave, with the step over determined through a set angle offset; in this case 2° resulted in a 1.17 mm step over at the ID and a 1.45 mm step over at the OD. The feed rate here was also only

reduced at the external edge but was reduced to 85 mm/min for only 0.2 mm, since this path features twice as many corners as a zig zag does.

Both tested geometries were evaluated with the deposition of two layers, allowing for any problems with undercutting to be highlighted on the second layer, as seen in Figure 102 (top). The two geometries varied substantially in their layer times with the zig zag path taking 241.7 seconds and the square taking 163.4 seconds. The results show that the square weave is better for making a rounded profile and is more suited to bending than the zig zag. The square cylinder had an as-printed height of 6.5 mm, OD of 85.6 mm, and ID of 64.6 mm.

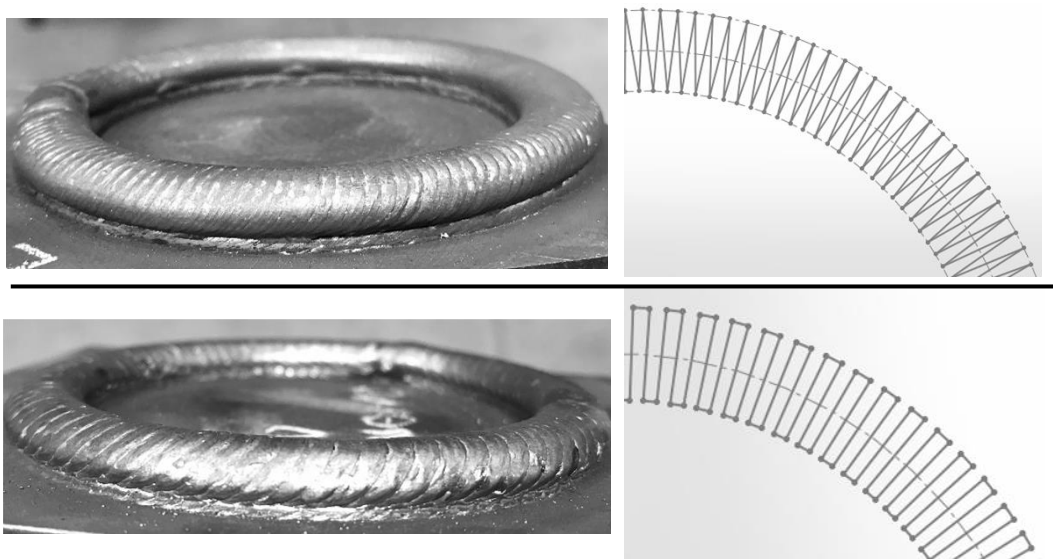


Figure 102. Thick walled cylinder geometry evaluation results and paths.

Applying the lessons learned in preliminary analysis, a multi-layer box and cylinder were printed and machined to highlight any defects or issues with the strategies decided upon. The cylinder was printed with a layer-by-layer phase shift to fill in any gaps left by the prior layer as well as four different start and stop points angled 90° from each other. 16 total layers were deposited with a layer time of 163.8 seconds and a pause time of 60

seconds, adding up to a one-hour print time. The as-printed height, OD, and ID were 44 mm, 85.4 mm, and 36 mm respectively.

For the box, the third corner geometry was used and altered slightly by increasing the step over in the corner from 1.25 to 1.3 mm. Layers were deposited with a phase shift as well as a reversal of direction layer-by-layer. Start and stop points were located in the corners and rotated every layer. A layer time was 180.7 seconds and a 60 second pause was used between layers. In total, 24 layers were deposited in one hour and seven minutes. The as-printed dimensions were 61.7 mm on the external, 36 mm internal, and 49.5 mm tall. The welding parameters can be seen in Table 29.

Table 29. Welding parameters used in the thick-walled box geometry study.

Filler Material	Shielding Gas	Synergic Line	WFS	ALC	Dyn. Corr.	Burn Back	Crater Fill	FR	FR Reduction	
			ipm	%	%	sec.	sec. and %	mm/min	mm/min	mm
ER70S-6	90/10	CMT 1362	95	15	-1.2	-0.03	0.7s at 40%	720	60	0.5

In machining the cylinder, excess material needed to be removed from the locations of the start and stop points in order to achieve a uniform surface. The defect could be best described as a dimple or an intrusion. Therefore, this geometry needed a great deal more material to be removed to provide a clean finish than the square box, as shown in Figure 103 bottom. In future path planning, additional material needs to be deposited at this point via a slight overlap in the final pass or a longer crater fill to compensate for this. The box geometry machined well, with a final width of 59.7 mm, after an approximate 0.5 mm was removed from the outside walls. The inside was machined with a 1/4" diameter end mill, leaving a quite sizeable radius at the corners with a few spots of machined surface. Due to a very small amount of material being removed from the outside of the box, the external corners still show signs of being un-machined.

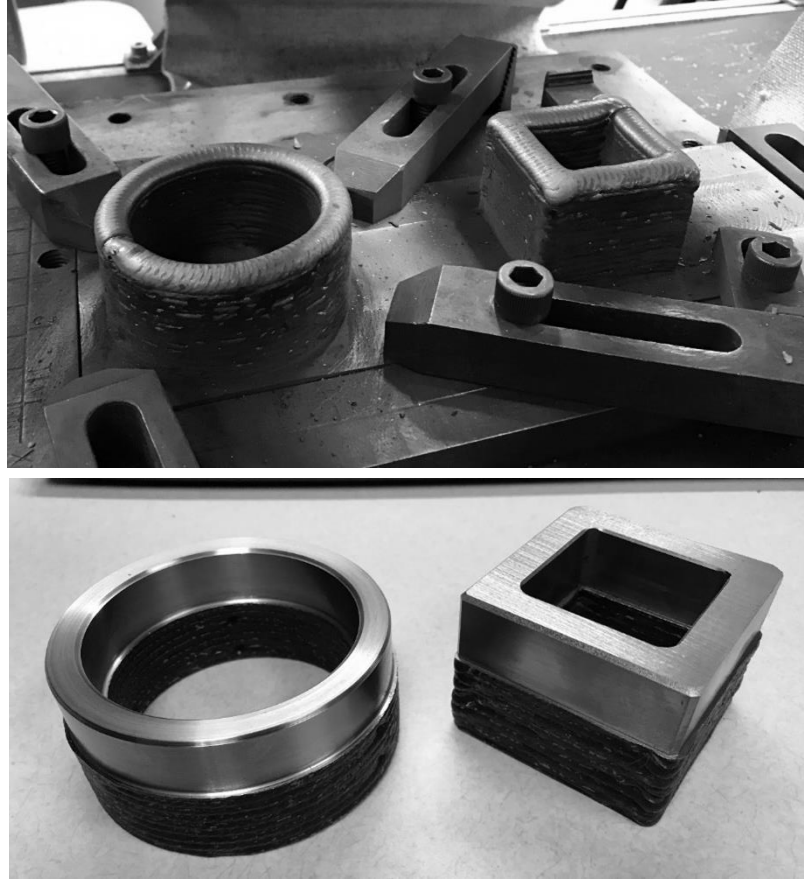


Figure 103. Thick-walled cylinder and box.

In a demonstration of the ability of a Keyence VR-3000 wide area 3D measurement system, the as-printed surface of the box was scanned as shown in the images at the top of Figure 104 below. As you can see from the scanned surface, the beads resemble rope stacked on top of one another, with the zig zag motion creating a woven appearance. The surface was analyzed and the surface profile plotted both in the transverse direction perpendicular to the direction of travel as well as across the top of a bead normal to the direction of travel. The surface plots can be seen at the bottom of Figure 104. The top plot is across the layers and reveals the layer height to be 2.73 and 2.8825 mm. The lower plot is along the bead, and reveals the waviness of the bead is 2.5 mm from peak to peak, which correlated to the period of the 1.25-mm zig zag geometry printed.

The other important measurement to note is the distance between the high point and low point of the scanned surface. The measure maximum was 0.4709 mm while the minimum was -0.4312 mm, so in total 0.9021 mm of waviness is present and would need to be milled to generate a clean surface. This matches value for yield obtained by measuring the material removed in milling the surface until it is clean and free of defects, verifying this method as an accurate measurement technique.

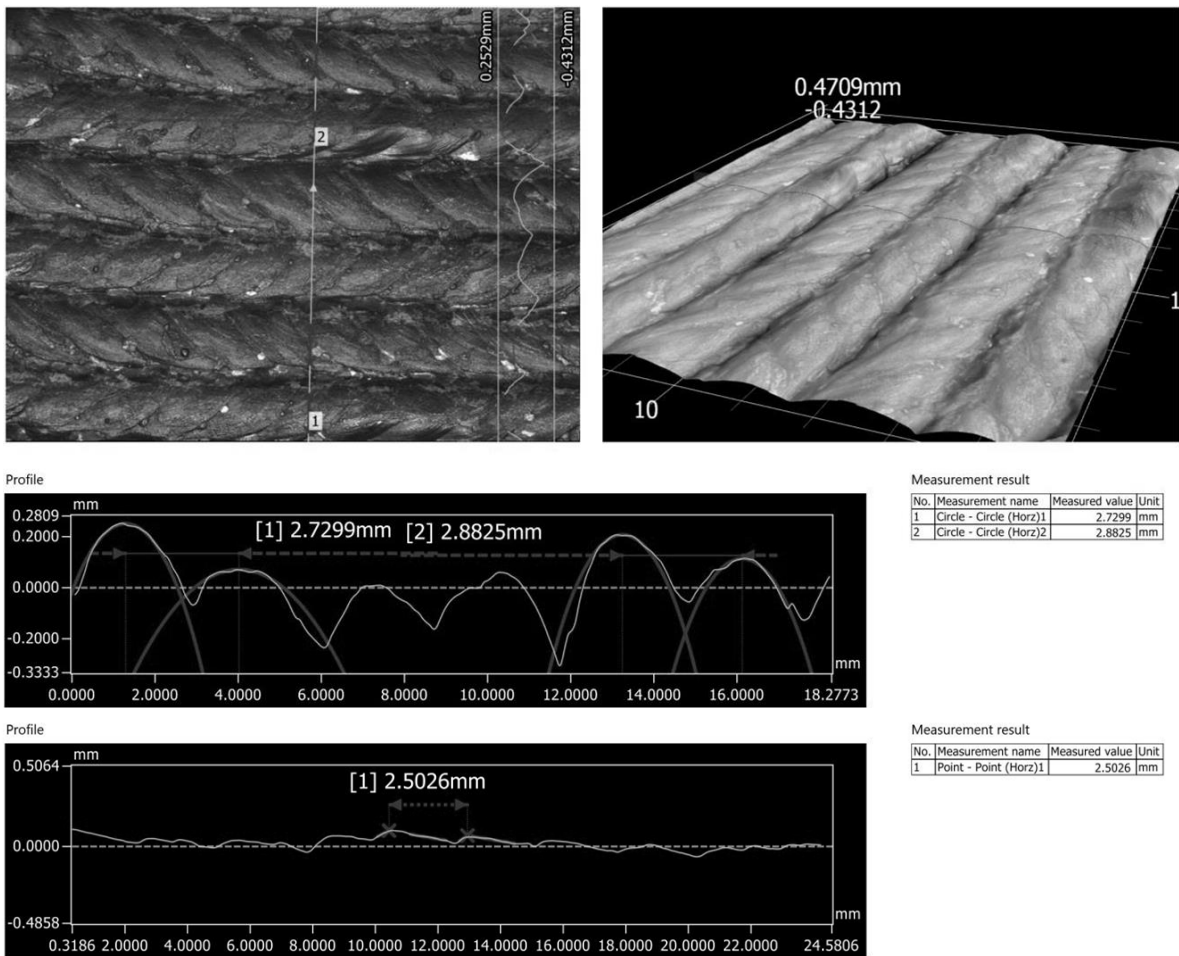


Figure 104. 3D scan of the as-printed surface of the thick-walled box.

Angled Deposition

Using the 1.25-mm zig zag weave, attempts to print at 15, 30, and 45-degrees from vertical were attempted. The eight layers were printed for each test, with the first two layers building directly on top of each other followed by angling out thereafter.

As shown in Figure 105, angled deposition was successful for overhangs of 15 and 30-degrees. In those attempts, walls were easily created and results were within about one or two degrees of the programmed angles. For the 45-degree overhang, slumping can be noticed in the result. When depositing at a higher angle, the deposited layer is only able to build on a fraction of the previous layer. When building up, it also must build outward upon itself, creating the slumping noticed in Figure 105. For this reason, the attempted 45-degree wall measured about 60 degrees from vertical (30 degrees from horizontal).

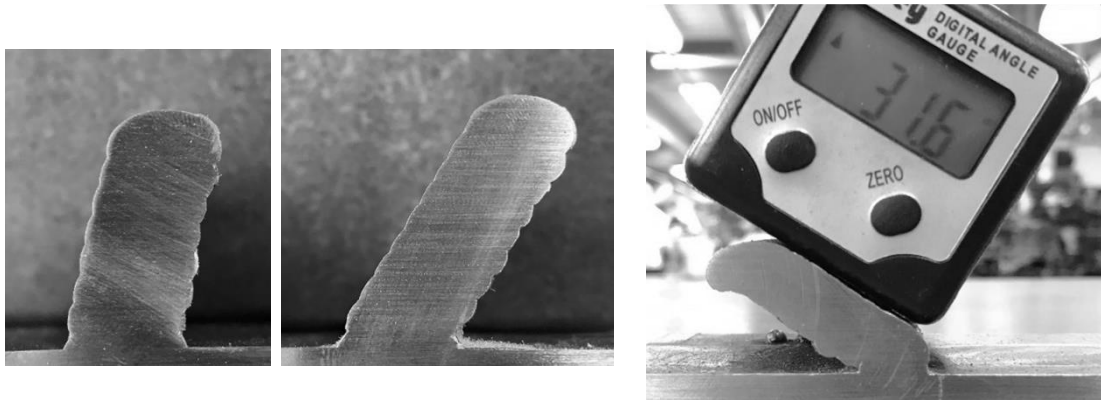


Figure 105. From left to right, 15, 30, and 45-degree attempted walls.

One important process note that arose out of testing was the location of start points and probe points. When probing for an overhang, the location cannot be on the front edge, as the probe will almost surely miss the part completely. This is also true for starting as trying to arc out in thin air will cause the wire to miss and contact low at the base of the build plate.

X/Crossover Geometry

An attempt was made at this point to try and print the crossover geometry or X-geometry studied by Ding *et al.* [46]. What makes this geometry so difficult is the un-equal build up in the middle. If you were to print two straight lines, you would create un-equal deposition and the center would rise up and spread out. Similar to the methods of Ding *et al.*, the X was broken down into two “V’s”. Using the 1.25-mm zig zag weave geometry along the legs, attempts to create a balanced X will be attempted.

The first attempt, referred to as X1, can be seen below in Figure 106 along with the weave pattern at the center of the structure. The pattern was created to avoid depositing too much material, but as you can see, it resulted in too little material being deposited in the corners on the sides of the V’s, with sharp in-cuts shown in the black circle on Figure 106. The feed rate reduction was removed from the center portion of the geometry to allow the welder to move through the path without depositing excess material. X1 featured start and stop points at the same location every layer, and therefore, slumping off occurred at the end of the legs. This problem was addressed by rotating the start point around.

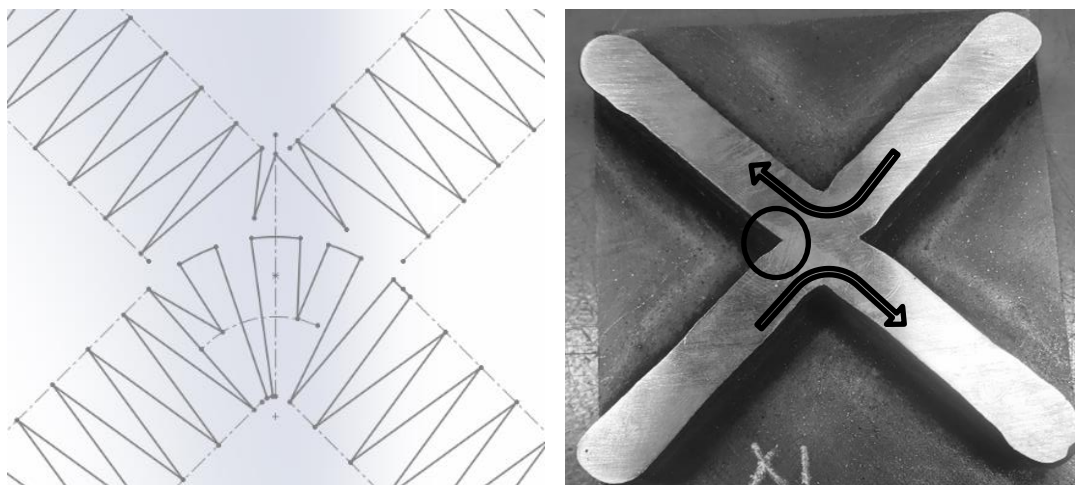


Figure 106. The first crossover print attempt, X1. Arrows denote path direction.

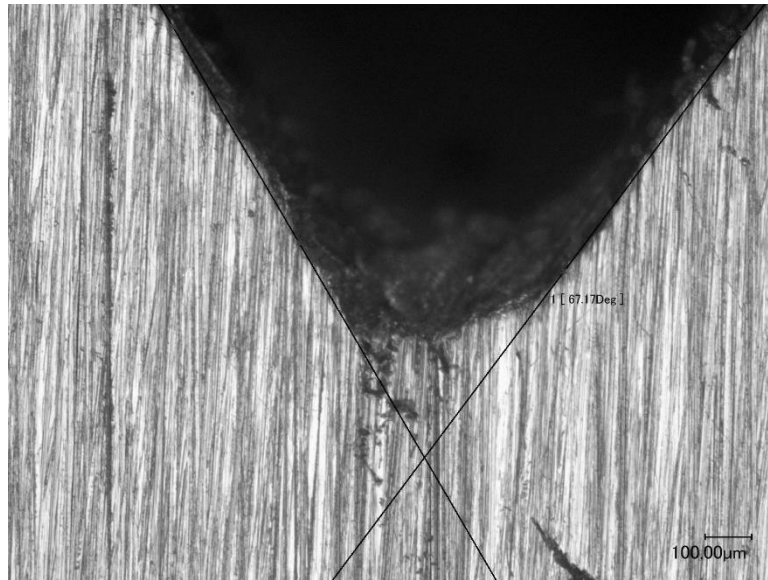


Figure 107. X1 corner detailed view.

Using the Keyence microscope to make a detailed inspection at the corner, shown in Figure 107, the lack of material is evident with high porosity noticed at the pit of the corner. In addition, the angle measured is acute, coming in at 67° . This means that the legs are necking down in size where they mesh. Material needs to be added here to avoid this.

The second attempt to produce a solid X-geometry is shown alongside the welding path in Figure 109. As you can see, this path attempts to get more out to the corners and deposit the material at these meeting points. The overall length of the path at the center was longer, so reductions in feed rate were deemed excessive, however this led to a lack of buildup at the center. It became clear from about the second layer that this was a major problem. The lack of buildup stemmed from the removal of the feed rate reduction at the inflection points in the center and resulted in the welder moving too quickly through the center path. The geometry was run for 10 layers and then machined flat. Over 3.5 mm had to be removed before reaching the middle and machining the entire surface. Aside from this, the corners of the V's did a better job at meshing and filling in the sharp in cuts.

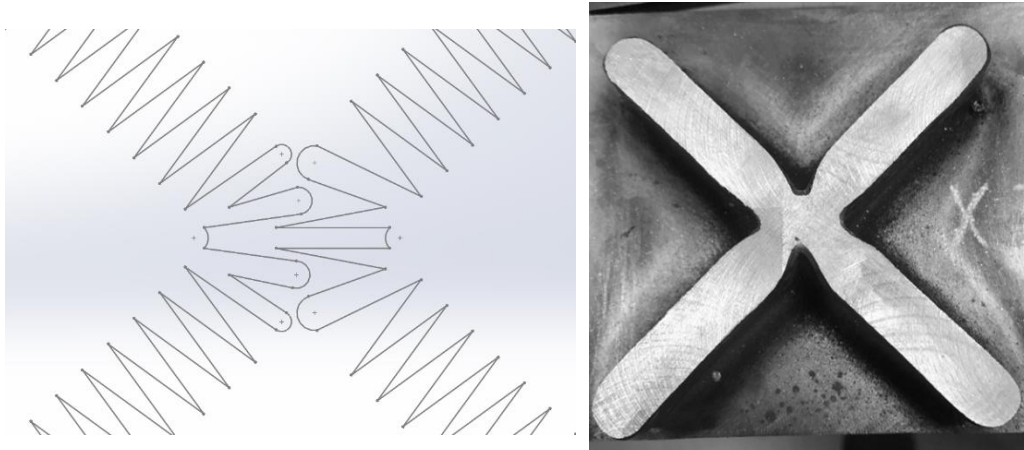


Figure 109. The second attempt, X2.

The third attempt, X3, featured the same weld path as X2, the only change was the re-addition of the feed rate reduction at the center of the X's. The feed rate was reduced from 720 mm/min to 85 mm/min for a distance of 0.4 mm. The layers start and stop point were shifted after each layer by rotating the path 90-degrees. A phase shift was used and the resulting surface finish was very smooth along the built-up walls. The as-printed results and as machined X can be seen in Figure 108.



Figure 108. The third attempt, X3.

A detailed view of the corner of X3 can be seen in Figure 110. As noted on the image, the angle measured 95 degrees, showing that the excess deposition with the feed rate reductions worked in adding back the material at this location. The lack of noticeable porosity is also reflected in this geometry.

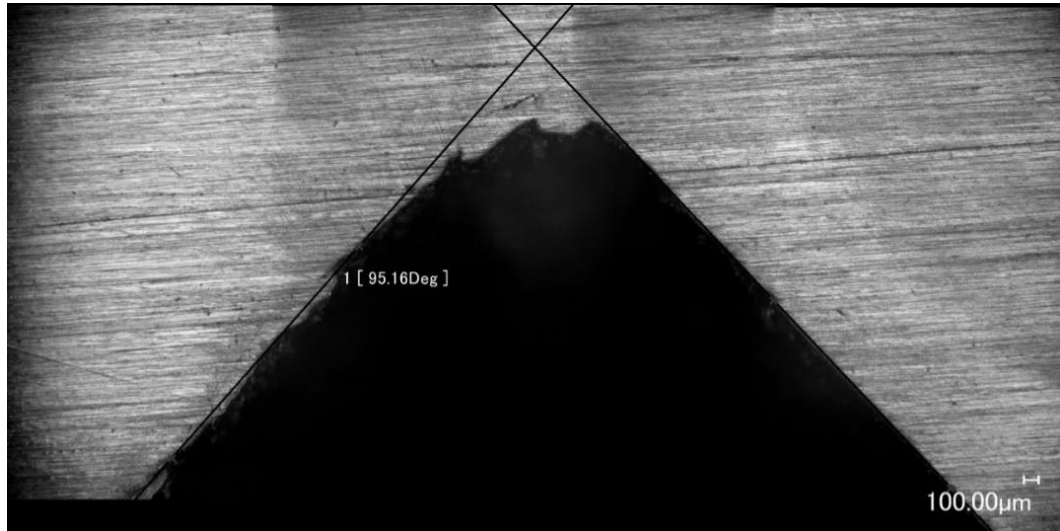


Figure 110. X3 corner, detailed view.

Bracket

At the recommendation of Dr. Overfelt, an attempt to build a bracket to show the ability of the process to: 1) utilize the base plate as a feature, 2) create something that typically is casted and machined, and 3) create a structural component. The design is simple, a 100 mm long, 8 mm thick wall is deposited followed by the angled back wall. The angled wall starts off as 62.5 mm long, and then every layer gets shorted by one zig zag, (1.25-mm x 2), thus after 25 layers the back brace would disappear and the front wall would remain. In total, 27 layers were printed with a 60 second pause between layers in 2 hours and 20 minutes. The weld parameters used in the print can be seen in Table 30, the toolpath focused at the intersection and the bracket itself can be seen as-printed in Figure

111

Table 30. Weld parameters used in the bracket print.

Filler Material	Shielding Gas	Synergic Line	WFS	ALC	Dyn. Corr.	Burn Back	Crater Fill	FR	FR Reduction	
			ipm	%	%	sec.	sec. and %	mm/min	mm/min	mm
ER70S-6	90/10	CMT 1362	95	15	-1.2	-0.03	0.7s at 40%	720	60	0.5

The intersection of the two zig zag paths is separated by a 2-mm gap to avoid excess buildup at this location. Upon visual inspection of the as-printed structure, a slight gap can be seen towards the base, with a flush 90-degree internal angle not achieved and some undercutting present. As the structure grew out of the base plate, the gap was eliminated. This could be due to the higher temperature causing the metal to flow together or could be due to residual stresses pulling the walls closer.

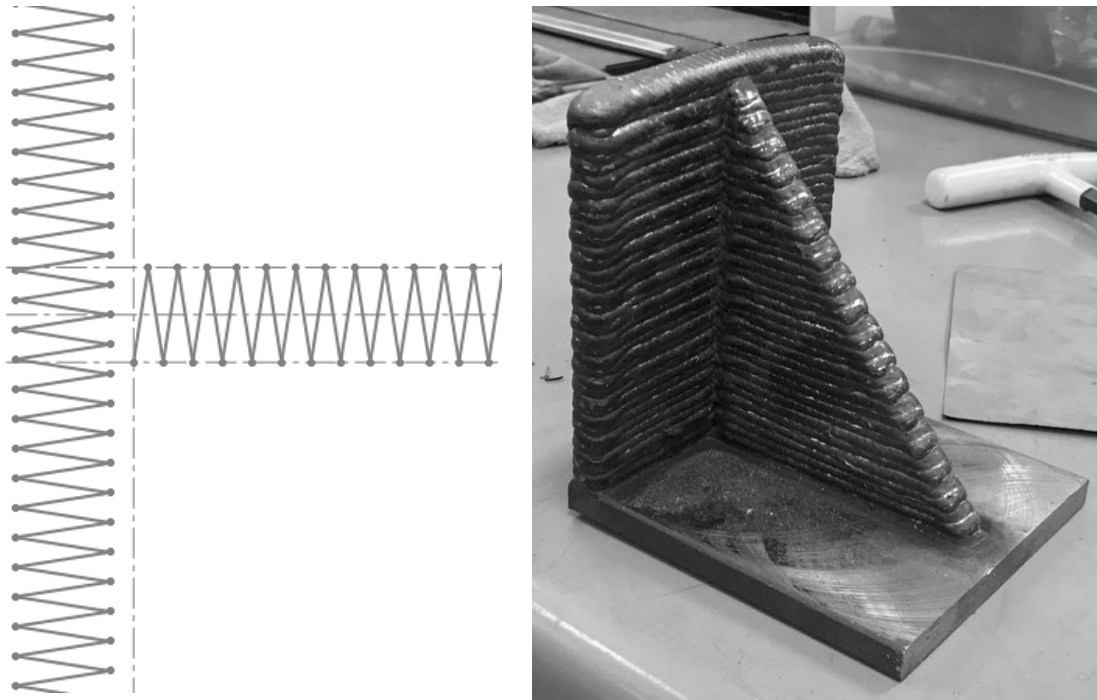


Figure 111. Bracket geometry toolpath and as-printed.

ER308 – Geometry Evaluation Results

Single Bead Geometry Evaluation

To evaluate the ability to create single-bead width structures in stainless steel, a challenging geometry was created that features a square pyramid, meeting a circular cylinder and meshing together. The structure is similar to the one created by Ribeiro and Norrish in 1996, seen in Figure 18 [27]. The structure designed was smaller but still large, having a base 85 mm square and the cylinder diameter of 48 mm. The pyramid ascends at a 20° angle with respect to vertical, meeting the cylinder 50 mm up. The entire structure is 80 mm tall. The toolpath was generated using a 3D contour toolpath in HSMWorks and programmed with a 1.5-mm layer height. Using the 3D contour for printing required some alteration, as it is usually used in 3D milling. The option of starting from the bottom up was selected to ensure that the layers were printed in order. The start and stop points were varied by using a smooth ramp between levels, which transitions up in the z-axis while moving along the contour. The structure can be seen in Figure 112. Probes were not used due to the non-uniform and repeating geometry, therefore the discrete z-step up method is employed.

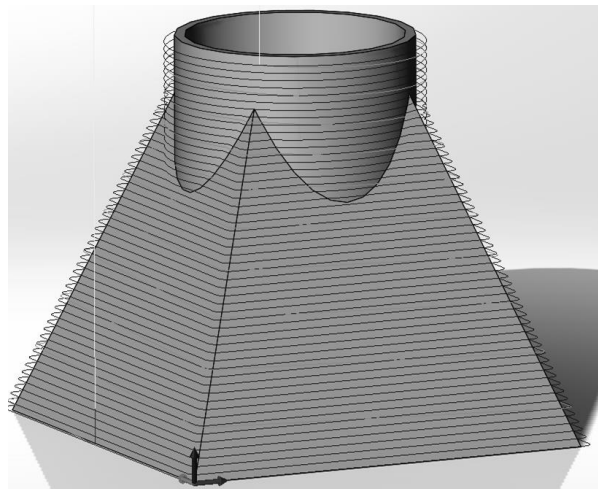


Figure 112. Stainless, single-bead, pyramid cylinder geometry: path generation.

Following a single-bead test where wirefeed speed, travel speed, and synergic line were all tested and varied, two sets of parameters were chosen for analysis; one using a CMT+Pulsed (CMT+P) synergic line the other using a standard CMT synergic line. CMT+P was chosen for evaluation in the single-bead testing for its ability to deposit a thicker bead with a lack of undercutting, however this comes at the price of a higher heat input. The following welding parameters were used, as shown in Table 31 and Table 32.

Table 31. Stainless, single-bead, CMT+Pulsed pyramid cylinder welding parameters.

Filler Material	Shielding Gas	Synergic Line	WFS	ALC	Dyn. Corr.	Burn Back	Crater Fill	FR
			ipm	%	%	sec.	sec. and %	mm/min
ER308	98/2	CMT+P 929	135	15	-1.2	0.05	0.3s at 50%	400

Table 32. Stainless, single-bead, CMT pyramid cylinder welding parameters.

Filler Material	Shielding Gas	Synergic Line	WFS	ALC	Dyn. Corr.	Burn Back	Crater Fill	FR
			ipm	%	%	sec.	sec. and %	mm/min
ER308	98/2	CMT 0908	150↓ 125	15	-1.2	0.05	0	400↑ 440

The result of this test can be seen in Figure 113. During the first print, the temperature of the CMT+P pyramid was observed to be getting too hot, an initial 30 second pause was programmed for after each layer but this was increased to a 55 second pause about halfway through. For the CMT+P structure, seen in Figure 113 on the left, the measured height was exactly 80 mm and the measured angle of the pyramid base was 21.7°, quite close to the programmed value. The bead thickness was measured to be 7.1 mm, much thicker than previous single-bead work. Noticeable build up at the start/stop points can be seen as the “lumps” on the sides of the wall. For this reason, crater fill was reduced to zero for the following print.

While heat was the main issue for the CMT+P print, while running the standard CMT pyramid, decreasing contact tip to work distance was the biggest challenge. This

problem is usually alleviated with a probe, however, the increased programming effort made adding a probe time consuming. The CMT bead was much taller than the CMT+P bead and built up at a faster rate, growing closer to the torch on every pass. For this reason, the wire feed speed was turned down to 125 ipm, and the feed rate was increased to 440 mm/min. During one pause, the z-axis had to be lifted and re-set to bump up the distance. The CMT pyramid cylinder, seen in Figure 113 on the right, measured 91 mm in height at an angle of 19.5 °, much more upright than the last attempt. The wall thickness, measured at the top of the cylinder portion, was only 4.5 mm., a reduction in almost 40% comparatively.

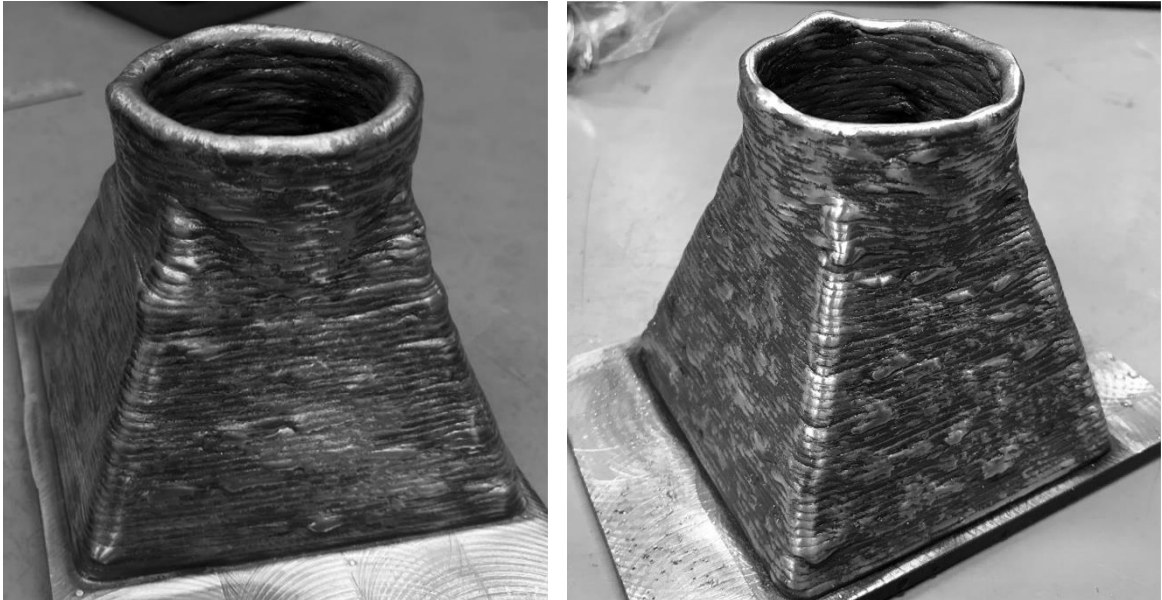


Figure 113. Stainless, single-bead, pyramid cylinders: CMT+Pulsed (left), and standard CMT (right).

Evaluating the heat input of the two different synergic lines used, the voltages and currents were compared. The CMT+P welded with higher current and voltage, inputting more power into the weld and resulting in a hotter deposition. As shown in the voltage and current plot of Figure 114, the current averaged about 20 A less and voltage averaged 6 V

less for the standard CMT process. Deviations in the CMT plot for current and voltage are due to the decreasing CTWD and the decreasing wire feed speed.

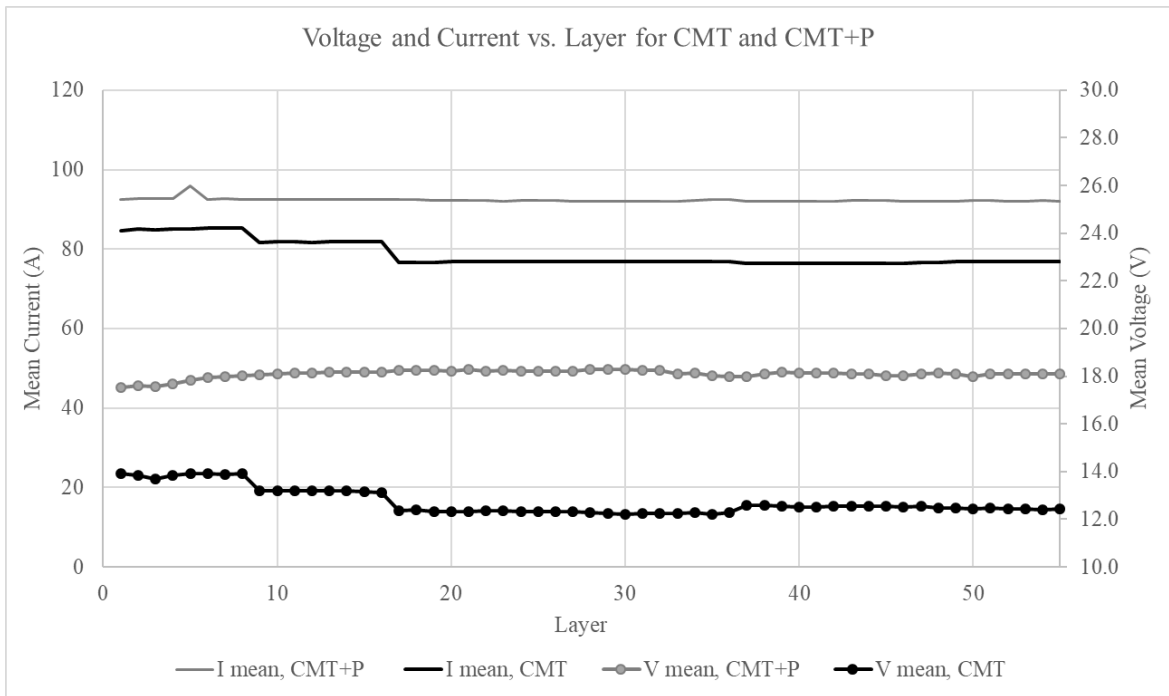


Figure 114. Voltage (dotted lines) and current (solid lines) vs. layer for CMT (black) and CMT+Pulsed (grey) in the deposition of the single-bead pyramid cylinders.

Due to the decreased heat input and visually better results, the standard CMT process will be used in further evaluations of stainless steel.

Weave Geometry Evaluation

For the evaluation of deposition of thicker beads, six weave patterns were tested and can similar to the weave study done for ER70S-6. The modified square geometry, zig zag, ladder, concave, and parallel bead geometries were studied. The welding parameters can be seen in Table 33 and the geometry specific factors can be seen in Table 34.

Table 33. Welding parameters for the weave geometry study.

Filler Material	Shielding Gas	Synergic Line	WFS	ALC	Dyn. Corr.	Burn Back	Crater Fill	FR
			ipm	%	%	sec.	sec. and %	mm/min
ER308	98/2	CMT 0908	95	15	-1.2	0.05	0.7s at 40%	Varried

Table 34. Stainless steel weave geometry study 1 parameters.

Factors		Parameters		
	Geometry	Step over (mm)	FR Reduction	Feed Rate (mm/min)
		E R 3 0 8	Modified Square	3, 0.5
Zig Zag 1	1.25		↓60 mm/min for 0.5 mm	720
Ladder	2			550
Concave	1.75			571
Parallel Bead	2.5			407
Zig Zag 2	1.75		↓40 mm/min for 0.5 mm	536

The results of this preliminary study showed that the zig zag geometry again produced the best weld. The concave geometry followed in order of appearance but the weld sounded very unstable when arcing back over the middle of the bead, for this reason the path was altered to be a convex geometry, traveling out and over instead of back. Similar results were found for ER308 as were observed for ER70S-6, therefore only the zig-zag and convex geometries will be evaluated further.

The second iteration of the stainless weave geometry study further evaluated the zig zag and convex geometries. All of the information on the paths studied and the feed rates and dwells used can be seen in Table 35 along with the measured results. The zig zag paths evaluated were the 1.25-mm step over and 1.75-mm step over. Using the constant volume material deposition from the ER70S-6 geometry study, the feed rates were calculated for each path such that each would deposit the same amount of wire. The feed

rate for the 1.75 mm zig zag path was calculated to be 536 mm/min, but additionally was run at 720 mm/min, the same as the 1.25-mm path. The two 1.25-mm zig zag paths varied in their feed rate reductions, with one having a large reduction for a short interval and the other having a smaller reduction for a longer interval. The difference can be seen in the nine second difference in layer time. Both of the convex paths used the same step over and feed rate reductions but the paths differed in their arc angles, with the first 83-degrees and the second at 90-degrees.

Table 35. Stainless steel weave geometry study 2 parameters.

Factors		Parameters			Measurables		
	Geometry	Step over (mm)	FR Reduction	Feed Rate (mm/min)	Layer Time (s)	Width (mm)	Height (mm)
E R 3 0 8	Zig Zag 1.25_1	1.25	↓30 mm/min for 0.25 mm	720	59.2	11.5	4.3
	Zig Zag 1.25_2	1.25	↓100 mm/min for 0.5 mm	720	50.6	10.3	4.1
	Convex_1	1.75, 83°	↓60 mm/min for 0.5 mm	563	51.9	11.75	4.0
	Convex_2	1.75, 90°	↓60 mm/min for 0.5 mm	571	52.0	11.75	4.2
	Zig Zag 1.75_1	1.75	↓40 mm/min for 0.5 mm	720	49.4	11.8	3.8
	Zig Zag 1.75_2	1.25	↓60 mm/min for 0.5 mm	536	52.0	11.8	4.0

From left to right in Figure 115, we have two iterations of zig zag with 1.25-mm step over, the two concave paths, and the two zig zags with 1.75-mm step over. These geometries were evaluated based on their deposition quality (i.e. undercutting, porosity, arc stability, visual appearance) and measurable results shown in Table 35. From a visual evaluation standpoint, they all looked similar. The 1.25-mm step over on the first zig zag paths resulted in the least amount of side roughness. The two concave beads were nearly identical, but both worse in quality than the zig zags. Therefore, concave would no longer be considered. The 1.75-mm zig zag beads results were of lower quality than the bead

printed in weave geometry study 1, therefore the lower feed rate of 536 with the higher feed rate reduction would move on to the next study. The 1.25-mm zig zags were almost indistinguishable and would both move on for further evaluation.

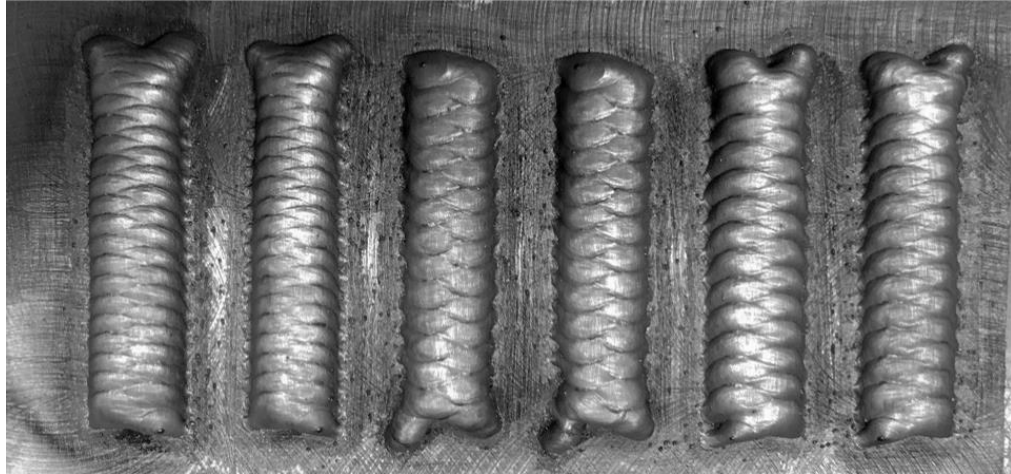


Figure 115. Stainless Steel Weave Geometry Test 2. From left to right, zig zag-1.25 1 & 2, convex 1 & 2, and zig zag-1.75 1 & 2.

Short Wall Study

The 1.25 and 1.75-mm zig zag geometries were selected, and shall be evaluated in the short wall study. This study will evaluate the ability of these three geometries to produce stable buildup and a clean machined surface. The study will also begin to look at the material properties to see if any variations exist. For each iteration, 8 layers will be printed. A summary of the geometry factors can be found in Table 37.

Table 37. Geometry factors used in stainless steel short wall study.

Factors		Parameters		
	Geometry	Step over (mm)	FR Reduction	Feed Rate (mm/min)
E R 3 0 8	Zig Zag_1.25_1	1.25	↓30 mm/min for 0.25 mm	720
	Zig Zag_1.25_2	1.25	↓60 mm/min for 0.5 mm	720
	Zig Zag_1.75_1	1.75	↓40 m/min for 0.5 mm	536
	Zig Zag_1.75_2	1.75	↓60 mm/min for 0.5 mm	536

The walls were printed in tandem, with zig zag 1.25_1 and 1.75_1 deposited at the same time then repeated for the other iteration. The walls were cut from their build plates and machined along the side to calculate the yield. Hardness testing was done in duplicate on the side of the walls. The results of the study can be seen in Table 36.

Table 36. Stainless short wall study results.

Factors		Measurables					
		Layer Time (s)	Width			Height	Hardness (HRB)
Geometry	Printed (mm)		Removed (mm)	% Yeild	Printed (mm)		
E R 3 0 8	Zig Zag_1.25_1	88.3	12.5	-0.8128	93.50%	29.3	85.25
	Zig Zag_1.25_2	87	12.5	-0.889	92.89%	28.7	87.5
	Zig Zag_1.75_1	87.4	12.65	-0.9144	92.77%	28.7	87.25
	Zig Zag_1.75_2	76.9	12.3	-0.9652	92.15%	27	92.75

The results indicate that the 1.25-mm geometry resulted in smoother surface, with a higher yield achieved in both compared to the 1.75-mm step over. The higher hardness

value observed in the second 1.75-mm test may indicate the effect of decreased thermal input from a shorter layer time and quicker dwell. For this reason, a conclusion on the best geometry cannot be made at this point and further analysis is needed. Between the two 1.25-mm zig zags, the second wall with a decrease in feed rate from 720 to 60 mm/min for 0.5 mm resulted in a better as-printed appearance and a lower temperature in print when monitoring it via a thermocouple. Therefore, this factor combination will be evaluated against the 1.75-mm zig zag with the same feed rate reduction.

Two Wall Study

For final analysis of the 1.25 and 1.75-mm zig zag geometries, two walls will be printed and dog bones machined to evaluate the monotonic tensile properties and difference in the walls. Dogbones will be machined in the longitudinal direction for both walls so that they can be directly compared. Walls were programed to be 120 mm long and 8 mm wide and printed simultaneously. A summary of the geometry factors can be found in Table 38.

Table 38. Stainless two wall study parameters.

Factors		Parameters		
	Geometry	Step over (mm)	FR Reduction	Feed Rate (mm/min)
E R 3 0 8	Zig Zag_1.25	1.25	↓60 mm/min for 0.5 mm	750
	Zig Zag_1.75	1.75	↓60 mm/min for 0.5 mm	535

Based on the results from prior analysis, the feed rate of the 1.25-mm zig zag was increased to 750 mm/min from 720 mm/min to decrease layer time and heat input. The walls were programed to be printed to about 60 mm in height, however, a problem was encountered at layer 11 and the print had to be stopped short. The main wire feeder was experiencing an abnormally high current and safeguards stopped the print here. The walls

were 10 layers tall at this point and while waiting on the Fronius technician to diagnose and repair the fault, the walls were machined to create tensile specimens. The results of the print can be found in Table 39.

Table 39. Stainless two wall study geometry results.

Factors		Measurables					
		Layer Time (s)	Width			Height	Length
Geometry			Printed (mm)	Removed (mm)	% Yield	Printed (mm)	Printed (mm)
E R 3 0 8	Zig Zag_1.25	108	10.1	-1.778	82.40%	39.75	124
	Zig Zag_1.75	94.2	9.6	-1.651	82.80%	34	123

As you can see, the difference in the yield percentage is negligible between the two walls. The layer times varied, with the 1.25-mm step over taking about 12 seconds longer to print a layer than the 1.75-mm. The height of the 1.25-mm zig zag was significantly taller.

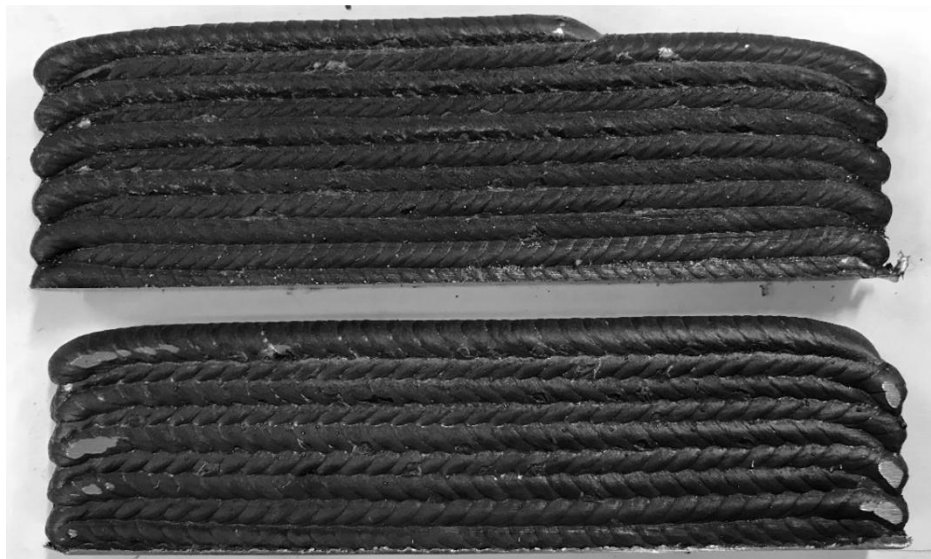


Figure 116. Stainless steel two wall study, zig zag 1.25-mm wall (top) and zig zag 1.75-mm wall (bottom)

For comparison of monotonic properties, two dog bones were machined from each wall and hardness tests were conducted prior to being pulled on the MTS Landmark Servohydraulic tensile testing machine at a rate of 0.15 ipm. The load, time, and extension were recorded at an interval of 0.01s, from which engineering stress/strain curves were generated and the ultimate tensile strength (UTS), yield strength, and Young’s modulus were calculated. A summary of the findings can be found in Table 40 and Figure 117.

Table 40. Stainless two wall study mechanical properties results.

	Sample	Yield Stress	Ultimate Tensile Strength	Modulus of Elasticity	Hardness	RA	True Fracture Strain	Toughness
	No.	ksi	ksi	ksi	HRB	%		$\int \sigma d\epsilon$
ZZ_1.25 mm	1	51.94	84.80	2369.40	86.25	55.33	0.806	387.5
	2	54.89	90.47	2567.08	91.5	47.16	0.638	423.3
ZZ_1.75 mm	1	53.47	85.13	2471.91	90.5	55.96	0.820	352.7
	2	59.10	92.83	2822.94	91.75	48.59	0.665	406.3
Manufacturers Spec		57 - 61	87 - 90			60		

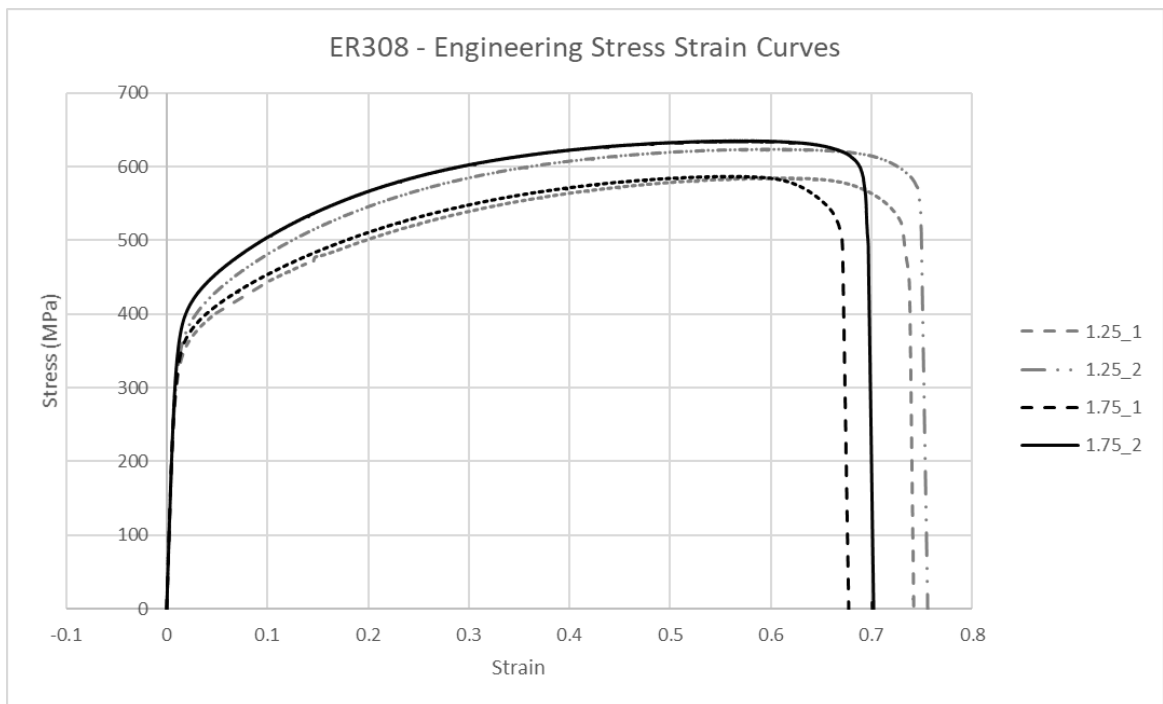


Figure 117. Stainless two wall study – engineering stress strain curves.

This study, although limited in its sample size, is insightful in the effect of varying geometry and location of tensile specimen and the effect on monotonic properties. Within each wall, the sample located closest to the top was denoted as the first sample, while the sample closest to the bottom was the second. As shown in Figure 117, the specimens from the bottom of the walls exhibited higher ultimate tensile strengths, higher yield stress, higher hardness values, and greater elongation at failure. The top samples exhibited greater reduction of area and true fracture strain. Between the walls, the 1.75-mm step over exhibited better mechanical properties than the 1.25-mm samples but as with the ER70S-6 two wall study, a lower toughness. Both the 1.25 and 1.75 walls both fell around the manufactures specs of 87 - 90 ksi ultimate tensile strength. In conclusion, the 1.25-mm geometry will be used, keeping consistent with the geometry selected for ER70S-6 and creating a “universal” path for ferrous alloys.

One observation made during the tensile testing, was the visual intrusions and extrusions occurring in the dog bones, as shown in Figure 118. These extrusions visible on the surface are a result of dislocations motion along the slip planes after the onset of plastic deformation. The degree of slip is primarily related to the crystallographic structure, i.e. ductility of the metal. A brittle metal will have limited slip, as the dislocations are restricted [53]. As observed, the presence of abundant intrusions and extrusions in the ER308 samples can be correlated to the high ductility due to the lower heat input of the CMT process. The directionality of the slip bands are aligned at 45-degree angle, the direction of maximum applied shear stress. This result was not seen in ER70S-6 and was observed only in stainless steel.

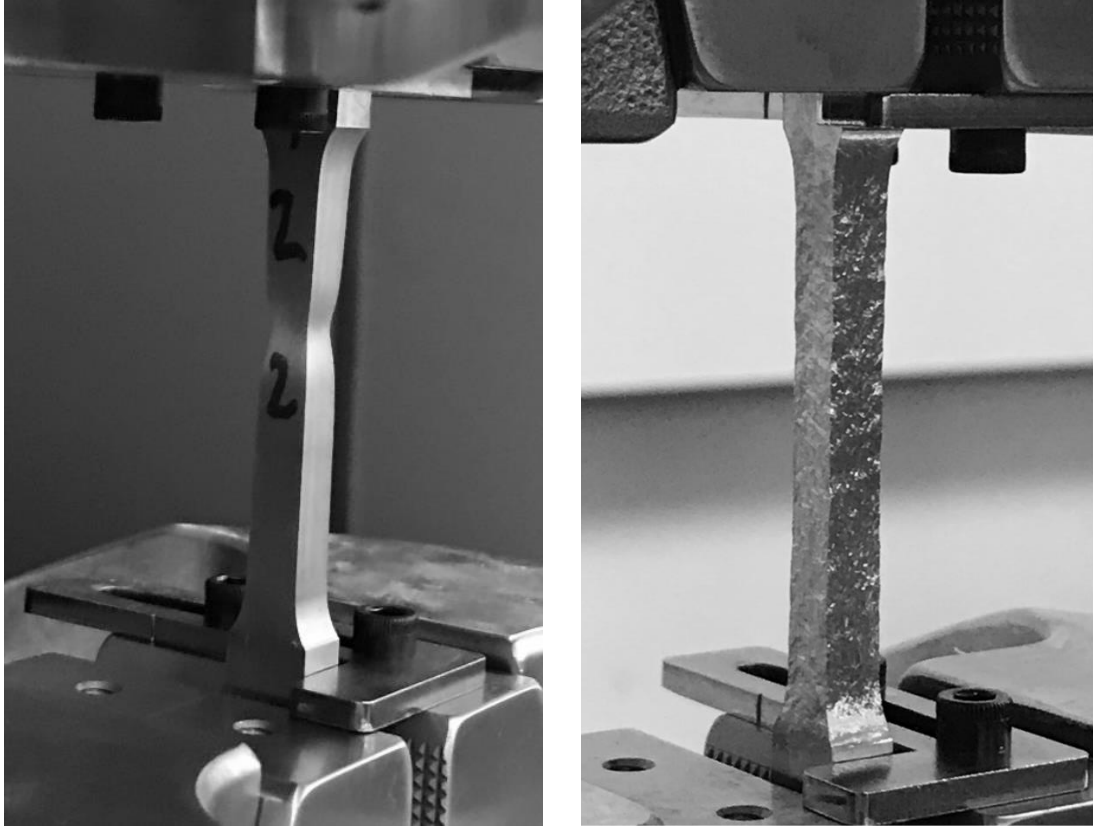


Figure 118. Dogbones of ER70S-6 (left) vs. ER308 (right).

ER4043 – Geometry Evaluation Results

Single-Bead Geometry Study

Working with Fronius representatives, aluminum deposition was studied for a cylinder geometry. Attempts to print aluminum single-bead geometry began with programming a simple cylinder. The cylinder was 85 mm in diameter and spiraled up at a rate of 2 mm per layer. The welding parameters used can be found in Table 41. The feed rate was set to 600 mm/min with a wire feed speed of 250 ipm initially.

Table 41. Welding parameters used for initial single-bead aluminum prints.

Filler Material	Shielding Gas	Synergic Line	WFS	ALC	EP/EN	Hot Start	Crater Fill	FR
			ipm	%	%	sec. and %	sec. and %	mm/min
ER4043	100%Ar	CMT1368 Adv	250↓190	0	-1.0	0.2s@140%	0.7s@50%	300

Wire feed speed was turned down to 190 ipm when the weld was observed to be getting too hot. The CMT Advanced synergic line 1368 was used. During the print, the CTWD decreased to the point where the weld had to be stopped around 20 mm tall. Moving quickly at this point, the program was paused, the z-axis zero reset, and the 2.5-mm step up G-code was loaded and restarted in an attempt to save the print. As seen on the back side of Figure 119, this resulted in a burnout of the weld and our contact tip was melted.



Figure 119. Aluminum single-bead cylinder.

Once new contact tips were received, aluminum deposition was again studied. Using the same welding parameters as the aluminum cylinder, two wall attempts shown in Figure 120, illustrate how the repeated heat input in a single location can affect the structure of a weld. The walls were produced by depositing a single-bead, 120-mm in length, followed by a step up of 2.5-mm, and welding back across the wall, similar to the method of welding for single-bead walls in steel. This method employed a constant welding path, with no starts and stops to avoid a burnout situation similar to the one experienced in the cylinder. The layers can be seen to slump off when deposited in succession like this as at the end of the walls, no cooling time was given prior to depositing another layer on top of

it. This problem can be alleviated through a pause at the end of the layer but re-starting the weld after it cools requires the use of the “hot-start” that may cause burn through. This issue can also be addressed by using a path approach, where the welder would not move back across the surface but instead continually move around the perimeter in one direction.

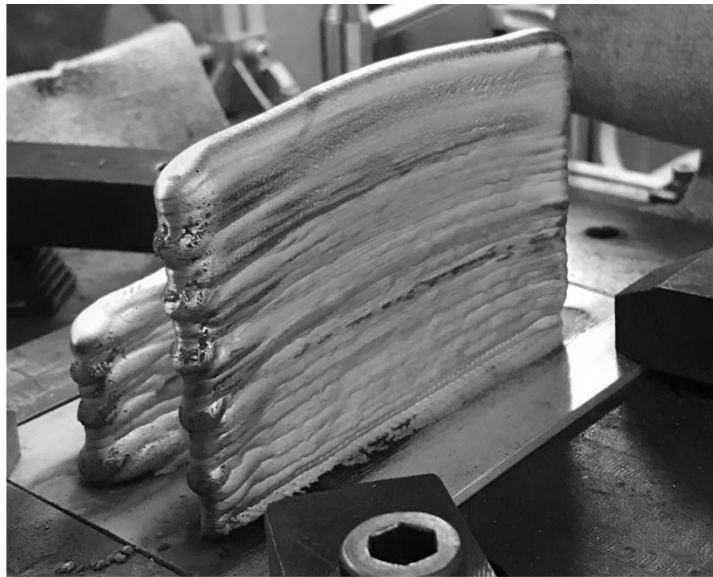


Figure 120. Excess heat effect on aluminum wall.

A method of producing walls in a circular manner was explored. The circle print above succeeds without pausing due to the high thermal conductivity of aluminum. The aluminum wants to shed heat quickly and solidify so by the time the welder makes it back around to the start point, that region is already solid and can be welded on top of. In order to study the buildup of walls and examine a flat surface, an oval shape would be needed. The “OvAl” was programmed with two parallel 100-mm segments 40-mm apart connected with half circles at each end. One end of the circle was deposited level, while the other end helixes up to the next layer height. The program was produced in HSMWorks by creating one layer and using the trace toolpath. For steel deposition, where welding was halted every few layers and a probe performed, programming multiple layers was as simple as copying

and pasting the first group of layers until the desired number of layers was reached. This was possible due to the probe resetting the zero on each layer. For aluminum, a constant weld path is desired, and therefore a probe cannot be used and the layers must be discretely programmed. By selecting enable axial offset passes trace settings, the toolpath can be repeated for each layer, avoiding the time-consuming task of drawing all the layers individually.

The first attempt was deposited with the welding parameters shown in Table 42 with a layer height of 1.85-mm. The feed rate used began at 600 mm/min and increased to 700 mm/min on layer 2, and again to 800 mm/min on layer 4. The wire feed speed started at 265 ipm and was decreased to 165 ipm on the second layer.

Table 42. Aluminum OvAl welding parameters.

Filler Material	Shielding Gas	Synergic Line	WFS	ALC	EP/EN	Hot Start	Crater Fill	FR
			ipm	%	%	sec. and %	sec. and %	mm/min
ER4043	100%Ar	CMT1368 Adv	250↓165	0	-1.0	0.2s@140%	0.7s@50%	600↑800

For the first attempt of the oval, shown in Figure 122, nine layers were deposited. The program was halted due to a decreasing CTWD. For the first oval attempt, the measured height after nine layers was 20.5 mm, or an average of 2.277 mm/layer. The bead thickness measured around the top was 4.25 mm.

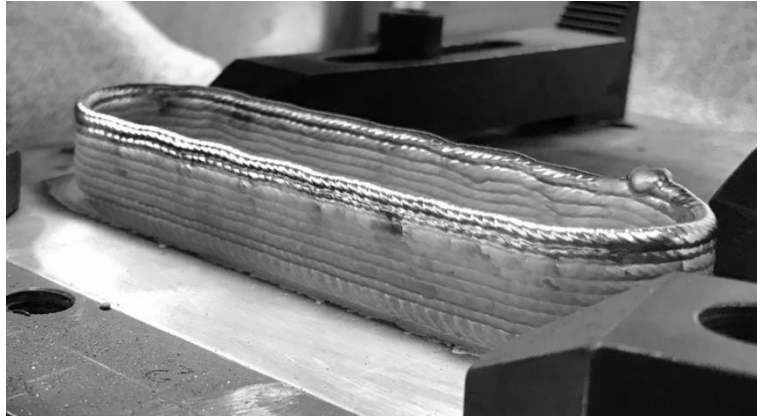


Figure 122. Aluminum OvAl 1

A second attempt at an aluminum oval was made using the average step-up distance of oval 1, 2.3 mm/layer. The welding settings were unchanged, however the crater fill was removed, as it was not needed and only resulted in a large glob at the end of the last layer, as seen on the right of Figure 122. In total 20 layers were printed in 9 minutes and 2 seconds. The result can be seen below in Figure 121.

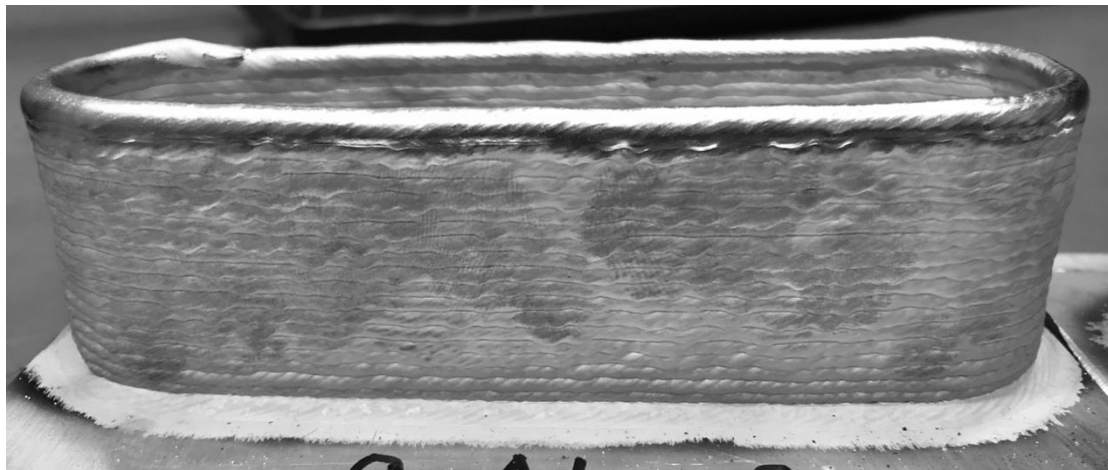


Figure 121. Aluminum OvAl 2.

During the second oval print, the CTWD was getting noticeably larger, so around layer 6, the feedrate was reduced from 800 mm/min to 720 mm/min to deposit more material. The as-printed height of the print was 42.037 mm, 4 mm shy of the programmed 46

mm and giving us an average layer height of 2.1 mm. The wall thickness measured at the top of the wall was 4.87 mm.

An additional study was conducted to consider the different synergic lines available for aluminum. Using the same parameters as oval 2, a third oval, oval 3, was printed to evaluate CMT Pulsed Advanced, synergic line 1369, against the CMT Advanced. The feedrate for this test was 600 at the start and increased to 700 mm/min on layer 2. The weld was completed in 9 minutes and 25 seconds.

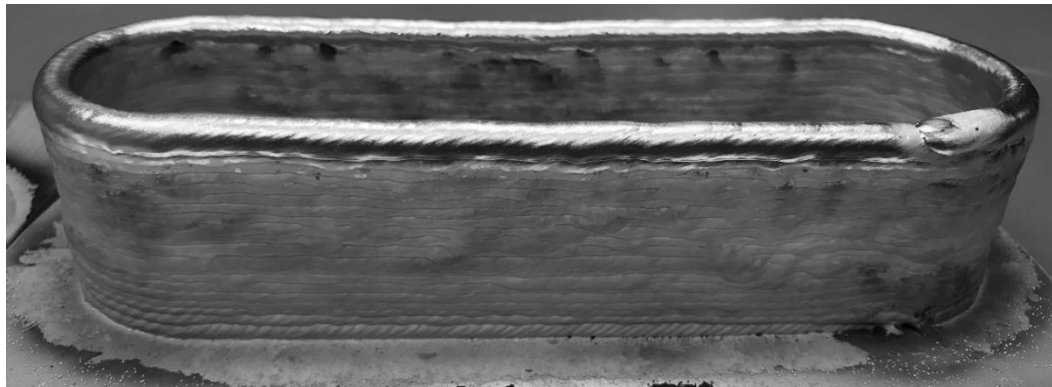


Figure 123. Aluminum Oval 3.

For oval 3, the measured wall thickness was 6.096 mm, a 25 % increase from oval 2. The height was measured to be 33.02 mm, with an average height of 1.651 mm /layer, much shorter than the programmed height of 46 mm. Although the CTWD was almost 27 mm by the end of the weld, the process remained very stable and was allowed to run to completion for this reason. The as welded surface reflects the effect of the higher heat input, with increased bead width and surface roughness compared to oval 2.

Evaluating the side of oval wall 1 using the Keyence 3D microscope revealed the waviness of the surface to be 0.362 mm. The area analyzed can be seen below in Figure 124. The top image reveals some porosity toward the bottom. The presence of small scratches can be seen but the cause is unknown.

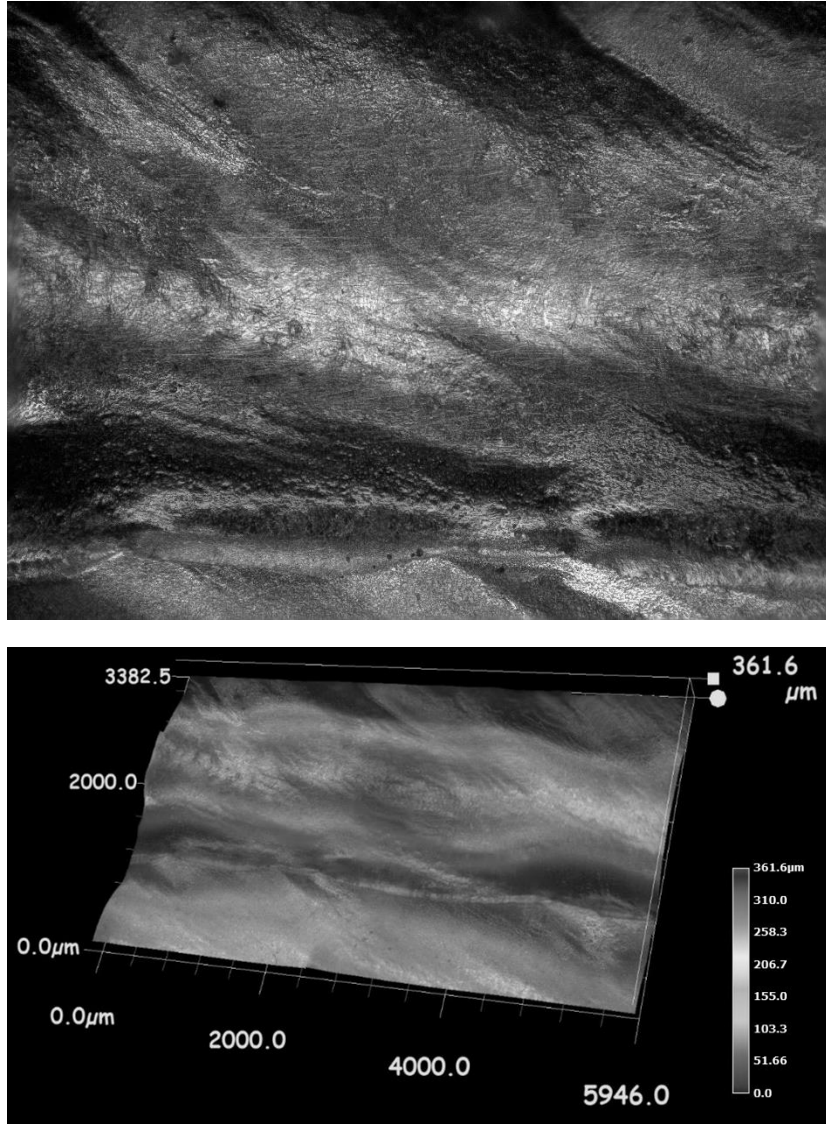


Figure 124. As welded macrostructure of the side of oval 1.

Overhang Geometry Study

To study the limitations of deposition with respect to angle from vertical in aluminum with a constant weld path, a cylindrical vase shape was chosen. The circular base for all tests had a diameter of 65 mm, and was programmed to weld with a helix with a pitch of 2.1 mm/revolution, per the oval results. A total of 20 layers would be deposited, making the programmed weld height 42 mm. A complete overview of the welding parameters can be found in Table 43.

Table 43. Welding parameters used in the overhang study.

Filler Material	Shielding Gas	Synergic Line	WFS	ALC	EP/EN	Hot Start	Crater Fill	FR
			ipm	%	%	sec. and %	sec. and %	mm/min
ER4043	100% Ar	CMT1368 Adv	250↓165	0	-1.0	0.2s@140%	0.0	600↑700

The first iteration of the overhang study can be seen below in Figure 125. This test was run with a programmed overhang of 15 degrees. The weld was run in 6 min and 57 seconds. The overhang was measured upon completion of the weld with the digital angle finder to be 17.5 degrees. The overall height was 42 mm tall and the bead width was 5.2 – 5.5 mm.



Figure 125. Aluminum single-bead 15-degree overhang.

The second test of overhang was programmed to spiral out with a 30-degree draft angle. The results of this test can be seen in Figure 126. The overhang ran for 8 minutes and 8 seconds and was measured to be right around 30 degrees. The height of the bowl measured 35.2 mm, a result of the larger angle of the print. The bead width remained constant with the prior study and was between 5.0 – 5.2 mm at the top. For the last couple of layers, the arc was sounding especially unstable, and visually left large black marks on the weld bead.

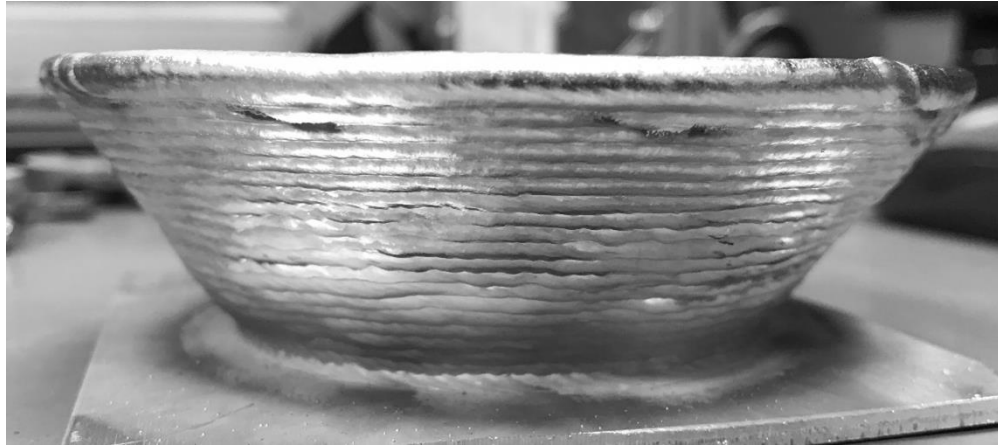


Figure 126. Aluminum single-bead 30-degree overhang.

Looking into the current and voltages over the last 200 seconds of welding, a slight difference can be seen between the overhang 15 test and the overhang 30 test, as shown in the images in Figure 127 below. While the average values of current and voltage are equal, the peaks in the voltage observed in the 30-degree overhang shows that this print was much less stable. The high peaking values toward the end of the path created the observed “burned” weld areas on Figure 126 above. For this reason, overhangs above 30 degrees will not be attempted.

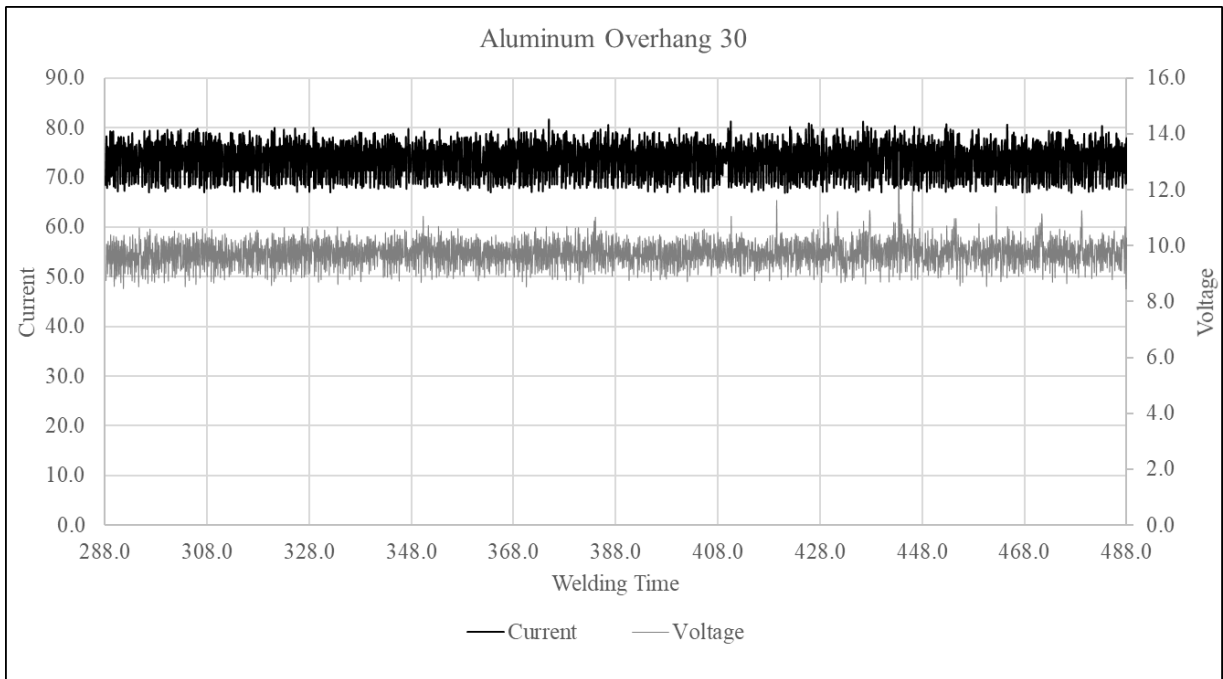
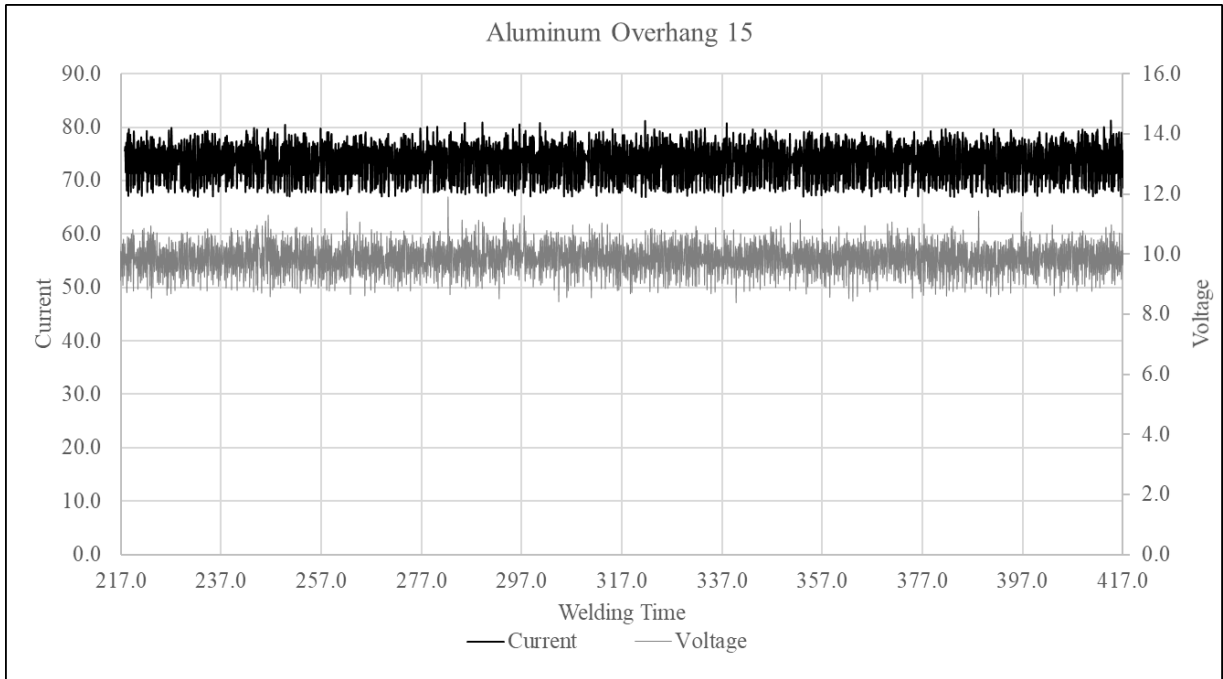


Figure 127. Welding current and voltage of the last 200 seconds of welding for aluminum overhang 15 and 30-degree shapes.

Thick-Bead Geometry Study

A weave geometry study similar to the one performed on ER70S-6 was attempted for aluminum with poor results. As shown in Figure 128, the square, zigzag, ladder, sine, concave, and parallel bead all were definitively ruled out as possible methods of producing thick beads. With the parallel bead geometry being “the best of the worst”, further testing shall continue tweaking the wire feed speed, travel speed, and step over for this one geometry.

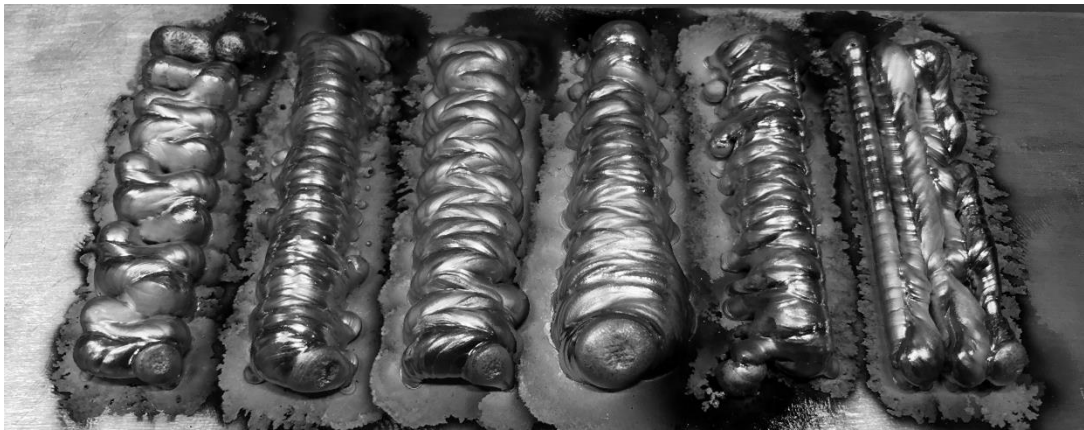


Figure 128. Aluminum thick-bead geometry evaluation, from right to left: square, zig zag, ladder, sine, concave, and parallel bead.

For the initial thick-bead test above, parallel bead was run with a step over of 3 mm, a wire feed speed of 165 ipm, at a feed rate of 615 mm/min. The initial portion of the bead looks promising, so therefore the issue may be entirely a heat issue. For deposition of a parallel bead using a continuous weld path, a flat spiral was chosen as the ideal candidate for testing. Using the flat spiral, a parallel bead method can be tested without reversals of direction, thus allowing the previously deposited material to cool before welding again in the same area.

A spiral with an outer diameter of 100 mm, a pitch of 3.5 mm, and an inner diameter of 72 mm was programmed. The results of the test can be seen in Figure 129. Two layers were deposited using a spiral out that followed the same path as the spiral in. Gaps between concentric beads were noticed on the first layer, indicating the pitch, or the step over between beads, was too large.

A second attempt was made using a spiral-in, spiral-up, spiral-out method that shifts the second layer slightly. Unlike the past attempt, welder would keep moving in the same direction, moving clockwise the entire time. In addition, the pitch of the spiral was reduced to 3-mm. The results of the second attempt can be seen in Figure 130.

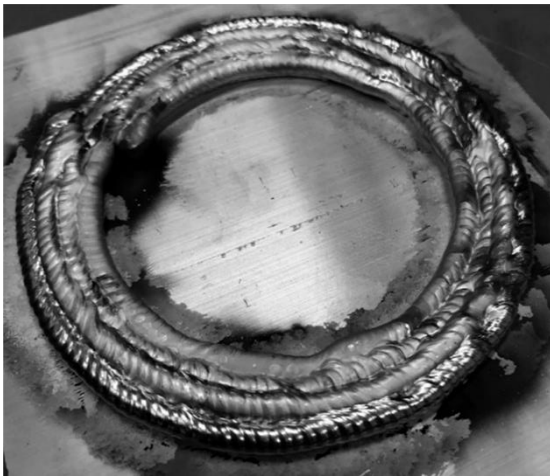


Figure 129. Aluminum flat spiral 1.



Figure 130. Aluminum flat spiral 2.

ER70S-6 – Mechanical Properties Evaluation Results

Temperature Study

Evaluation of temperature and the effect on mechanical properties was carried out by changing the duration of the pause after each layer. Four walls, 120 mm in length and 8 mm in width were programmed and printed at pause durations of 30, 90, 120, and 180 seconds between layers. A 1.25-mm zig zag weave was used with a feed rate of 720 mm/min and a feed rate reduction to 60 mm/min for 0.5-mm at the inflection points. A summary of the welding parameters used can be found below in Table 44.

Table 44. ER70S-6 temperature study welding parameters.

Filler Material	Shielding Gas	Synergic Line	WFS	ALC	Dyn. Corr.	Burn Back	Crater Fill	FR
			ipm	%	%	sec.	sec. and %	mm/min
ER70S-6	90/10	CMT 1362	95	15	-1.2	0.05	0.7s at 40%	720

The walls were printed one at a time and allowed to cool to room temperature before being removed from the base plate and machined. The machining process was similar to that of other walls, with the tops and bottoms machined parallel first, then the faces machined flat. The material removed on the sides to get a clean surface was recorded as a measure of waviness of the surface and used to calculate the yield. The as welded data for the walls including the layers printed, average layer time including pauses, height, width, length, layer height, and the yield is shown in Table 45.

Table 45. As-printed data for walls produced in the temperature study.

Wall ID	Layers Printed	Total Time	Average Layer Time	As Printed				Material Removed	Yield
				Height	Layer Height	Length	Width		
	#	min	s/layer	mm	mm/layer	mm	mm	in.	%
P30	29	75	155.2	-	-	122.8	13.25	0.0775	85.14%
P90	30	105	210.0	94.5	3.15	123.2	12.80	0.0600	88.09%
P120	31	127	245.8	-	-	123.0	12.40	0.0690	85.87%
P180	30	148	296.0	95.0	3.17	123.5	12.30	0.0700	85.54%

Once machined to a thickness of 0.25” +/- 0.005”, dog bone samples were machined from each wall in the longitudinal direction. Since the walls were taller than needed, the extra material from the tops of the walls was saved and used for microstructure evaluation. Hardness tests were done on each sample before being pulled.

An overview showing the yield stress, ultimate tensile strength, hardness, reduction of area and the true fracture strain can be seen in Table 46. A complete summary of the data can be found in Appendix I.

Table 46. ER70S-6 temperature study summary of mechanical property results.

Wall ID	Orientation	Yield Stress	Ultimate Tensile Strength	Hardness	RA	True Fracture Strain	Toughness
		ksi	ksi	HRB	%		$\int \sigma d\epsilon$
30	Longitudinal	49.45	69.32	70.25	74.08	1.35	255.57
90	Longitudinal	50.41	69.92	75.75	75.00	1.39	295.58
120	Longitudinal	50.00	70.51	74.25	73.49	1.33	252.67
180	Longitudinal	51.37	70.84	76.75	74.95	1.38	249.10

The graph below, shown in Figure 131, is a plot of ultimate tensile strength, S_u , versus inter-layer pause duration. Three outliers were removed, one from P30, P120, and P180 to get a better fit. The results indicate a drastic increase in ultimate tensile strength with pause duration from 30 to 90 to 120 seconds with diminishing increase for pause durations between 120 and 180 seconds. The results are fitted to a polynomial trendline correlating the values with a R^2 value of 0.8625, and can be summarized by the equation shown on the graph. Solving the equation for the pause time that gives us 70 ksi, or the manufactures spec for the ultimate tensile strength, we get a pause value of 98 second.

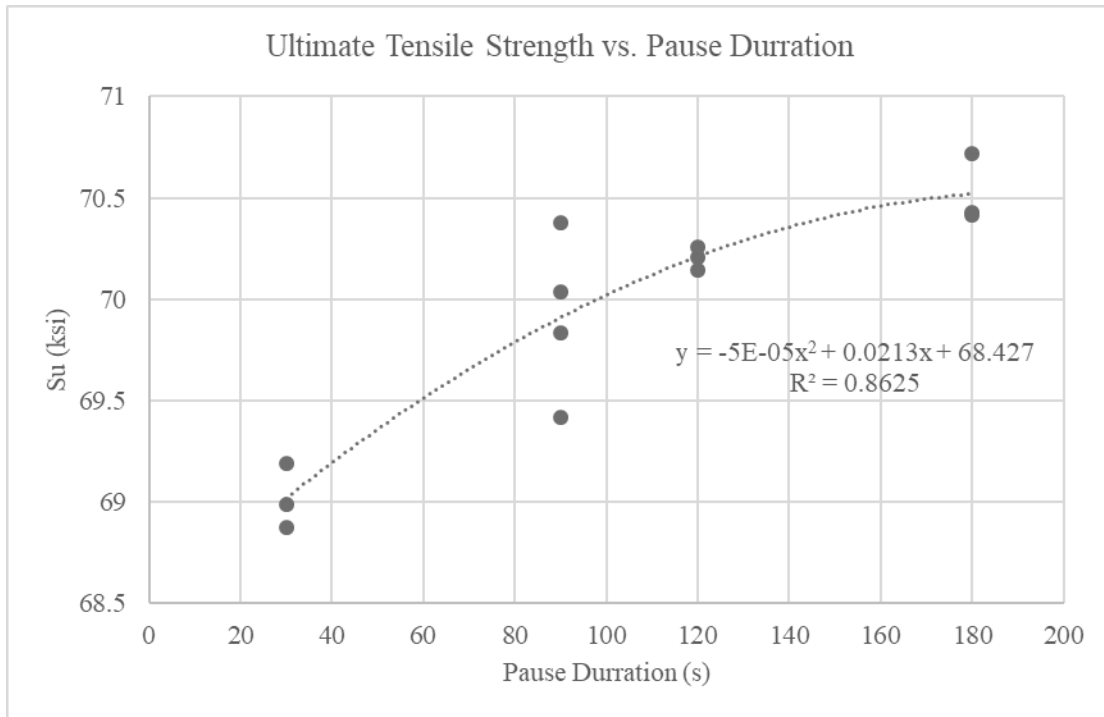


Figure 131. ER70S-6, the effect of pause duration on Ultimate Tensile Strength.

Wall P90, or 90 second pause wall, exhibited the ultimate tensile strength closest to the manufacturers spec and the lowest standard deviation of only 0.4 ksi, while the other walls were above 0.6 ksi. P90 also exhibited the highest toughness, with the walls at pause intervals before and after around 250 and P90 being around 295. The P120 and P180 walls both exhibited great mechanical properties, but the deposition rates were lower than practical, with both walls taking over 2 hours to print. All four walls had similar values for yield, with P90 having highest yield. For this reason, the P90 wall chosen as the ideal pause time and a second wall was deposited to examine the mechanical properties in the transverse direction. The weld and geometry print parameters remained constant, and the as-printed geometry can be seen in Table 47.

Table 47. Temperature study transverse wall as-printed data.

Wall ID	Layers Printed	Total Time	Average Layer Time	As Printed				Material Removed	Yield
				Height	Layer Height	Length	Width		
	#	min	s/layer	mm	mm/layer	mm	mm	in.	%
P90_T	35	120	205.7	106.0	3.03	123.0	13.00	0.0700	86.32%

Four dogbones were machined from the second wall, denoted P90_T, and pulled on the MTS Q-test load frame. A summary of the results can be seen in Table 48, comparing the longitudinal and transverse samples of the P90 Walls.

Table 48. ER70S-6 temperature study mechanical property results for longitudinal and transverse specimen.

Wall ID	Orientation		Yield Stress	Ultimate Tensile Strength	Hardness	RA	True Fracture Strain	Toughness
			ksi	ksi	HRB	%		$\int \sigma d\epsilon$
P90	Longitudinal	Average	50.41	69.92	75.75	75.00	1.39	295.58
		SD	2.59	0.40	0.65	1.41	0.06	95.76
P90_T	Transverse	Average	51.55	70.19	76.44	73.85	1.34	292.64
		SD	2.39	0.46	1.14	0.80	0.03	99.89

The results of this study indicate isotropic tensile properties, as the yield stress and ultimate tensile strength show statistically equal values independent of direction. The toughness value for the second P90 wall was equal to the first, and again was much higher than other walls. Generating an engineering stress strain curve for one of the longitudinal samples and one of the transverse samples reveals a difference in behavior after the ultimate tensile strength has been reached. As shown in Figure 132, the two lines are very similar up to ultimate tensile strength, but diverge in the behavior at high stress values.

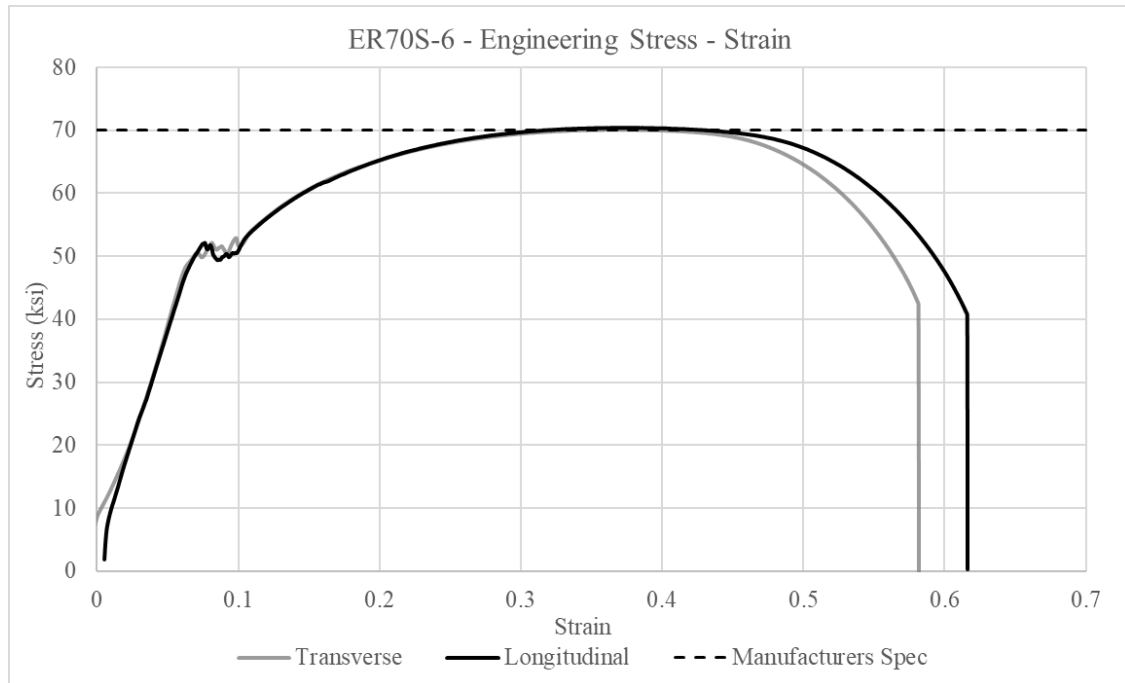


Figure 132. ER70S-6 transverse and longitudinal engineering stress strain curves.

The isotropic yield and ultimate tensile strength observed for ER70S-6 do not reveal the difference in behavior. Through the observation of the stress-strain curve, the non-uniform behavior after ultimate tensile strength becomes evident. This result may indicate some microstructural issues may be present and effect the toughness only when large plastic deformation occurs. The issue may be present at the layer interface and be due to contamination of the weld structure in-process. However, this difference in behavior should not overshadow the isotropic results up to ultimate tensile strength. The complete data set as well as the statistical results can be found in Appendix I and Appendix IV respectively.

ER308 – Mechanical Properties Evaluation Results

Temperature Study

Similar to the temperature study done for ER70S-6, evaluation of temperature and the effect on mechanical properties was carried out by changing the duration of the pause after each layer. Four walls, 120 mm in length and 8 mm in width were programmed and printed at pause durations of 30, 90, 120, and 180 seconds between layers. A 1.25-mm zig zag weave was used with a feed rate of 750 mm/min and a feed rate reduction to 60 mm/min for 0.5-mm at the inflection points. A summary of the welding parameters used can be found below in Table 49.

Table 49. Welding parameters used for ER308 Temperature Study.

Filler Material	Shielding Gas	Synergic Line	WFS	ALC	Dyn. Corr.	Burn Back	Crater Fill	FR
			ipm	%	%	sec.	sec. and %	mm/min
ER308	98/2	CMT 0908	95	15	-1.2	0.05	0.7s at 40%	750

The walls were printed one at a time and allowed to cool to room temperature before being removed from the base plate and machined. The as welded data for the walls including the layers printed, average layer time including pauses, height, width, length, layer height, and the yield is shown in Table 50.

Table 50. ER308 temperature study as-printed results.

Wall ID	Layers Printed	Total Time	Average Layer Time	Height	Layer Height	Width	Material Removed	Yield	Deposition Rate
	#	min	s/layer	mm	mm/layer	mm	in	%	kg/hr
P30	24	60	150.0	83	3.4583	11	0.075	0.82682	0.720
P90	24	83	207.5	83.7	3.4875	10.8	0.067	0.84243	0.520
P120	24	94	235.0	83.7	3.4875	10.9	0.07	0.83688	0.460
P180	24	116	290.0	84.2	3.5083	10.6	0.07	0.83226	0.372

The results from initial printing, machining, and measurement show a slight increase in layer height and decrease in width with pause duration. Yield percentage remained constant throughout the four walls, with a slight increase for wall P90. Four dogbones were machined from each wall and pulled on the MTS Servohydraulic load frame. A summary of the results can be seen below in Table 51, while the complete data set can be found in Appendix I.

Table 51. Stainless temperature study tensile properties results.

Sample		Yield Stress	Ultimate Tensile Strength	Modulus of Elasticity	RA	Ture Fracture Strain	Toughness
No.		ksi	ksi	ksi	%		$\int \sigma d\epsilon$
P30	Average	50.08	86.01	2351.43	49.03	0.68	417.64
	SD	0.61	1.93	192.13	6.03	0.12	15.45
P90	Average	50.53	86.78	2202.98	53.30	0.77	456.76
	SD	0.68	1.50	60.91	5.46	0.12	72.93
P120	Average	51.21	86.74	2252.27	52.78	0.75	421.73
	SD	0.82	1.33	35.41	4.41	0.09	36.57
P180	Average	51.33	86.61	2261.41	51.58	0.73	415.87
	SD	1.15	1.14	50.48	1.26	0.03	17.28
Manufacturers Spec		61	87-90		60		

Upon initial inspection, the data for stainless steel is quite constant regardless of pause duration, with only 0.77 ksi separating the highest and lowest average for ultimate tensile strength. Since the samples were pulled on the MTS Servohydraulic frame, issues with elongation measurement were subsided. Plots of the ultimate tensile strength, yield stress, and modulus of elasticity versus the pause duration can be in Figure 133.

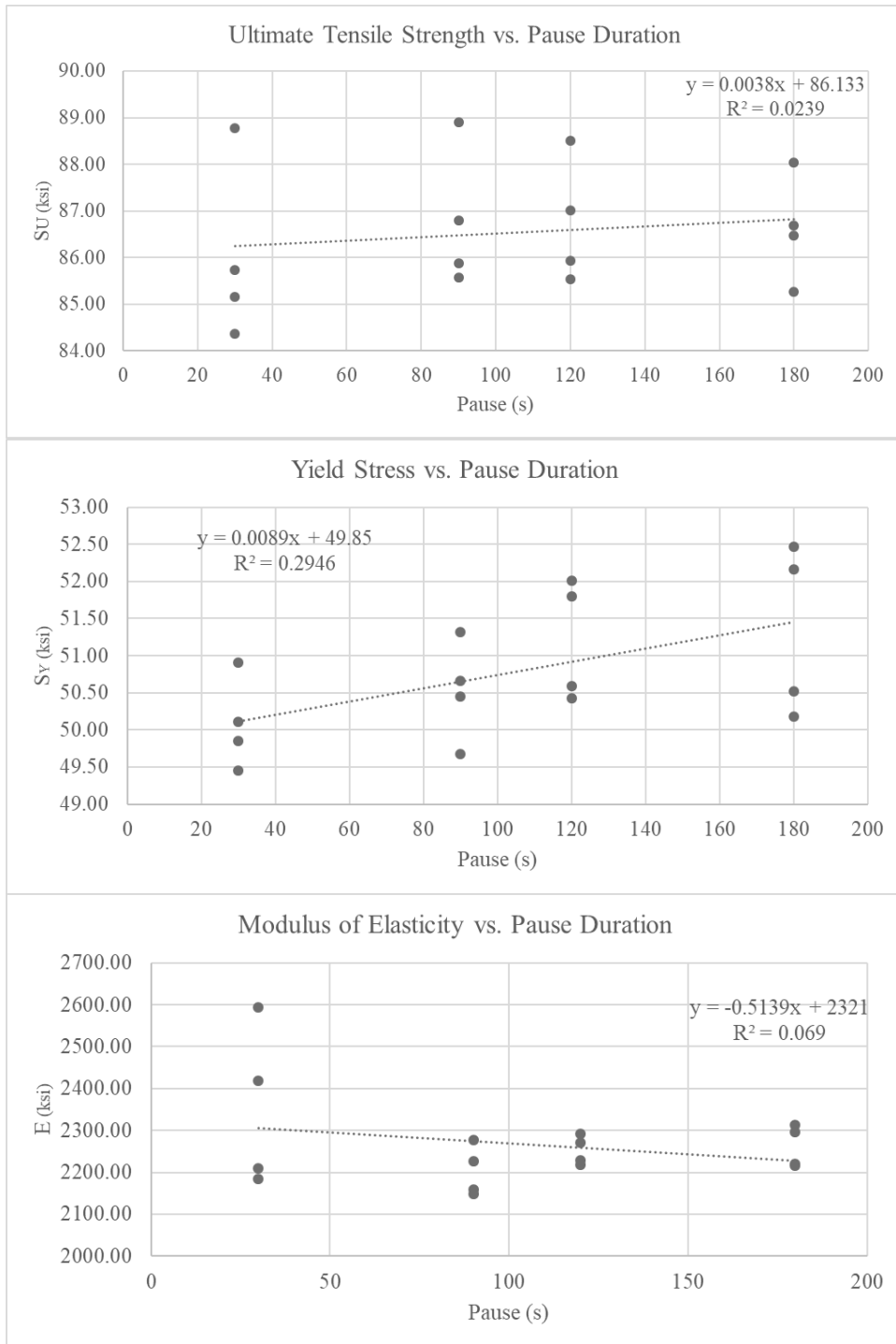


Figure 133. Ultimate tensile strength, yield stress, and modulus of elasticity vs. pause duration for ER308.

One clear observation from this data set is the high values obtained for toughness in the wall P90. The samples from wall P90 exhibited the highest average ultimate tensile strength, at 86.78 ksi right around the low end of the manufacturers spec of 87 – 90 ksi. Wall P90 obtained the largest reduction of area, with measured fracture surface area 53.3% or the original area. This reduction in area led to the high value for true fracture strain observed in wall P90 and thus the high toughness values.

To aid in the investigation of pause duration and the effect on temperature of each wall, a thermocouple was placed at the base of the wall and the temperatures after welding were recorded for each layer. The probe was placed around layer 4, once the wall was sufficiently built up, and remained stationary during the print. The temperature plot below, Figure 134, shows a plot of the data points and a linear trendline fit for each wall. As you can see, the difference between a thirty second pause and a 90 second pause is substantial, however the difference from 90 to 120 seconds is very minute.

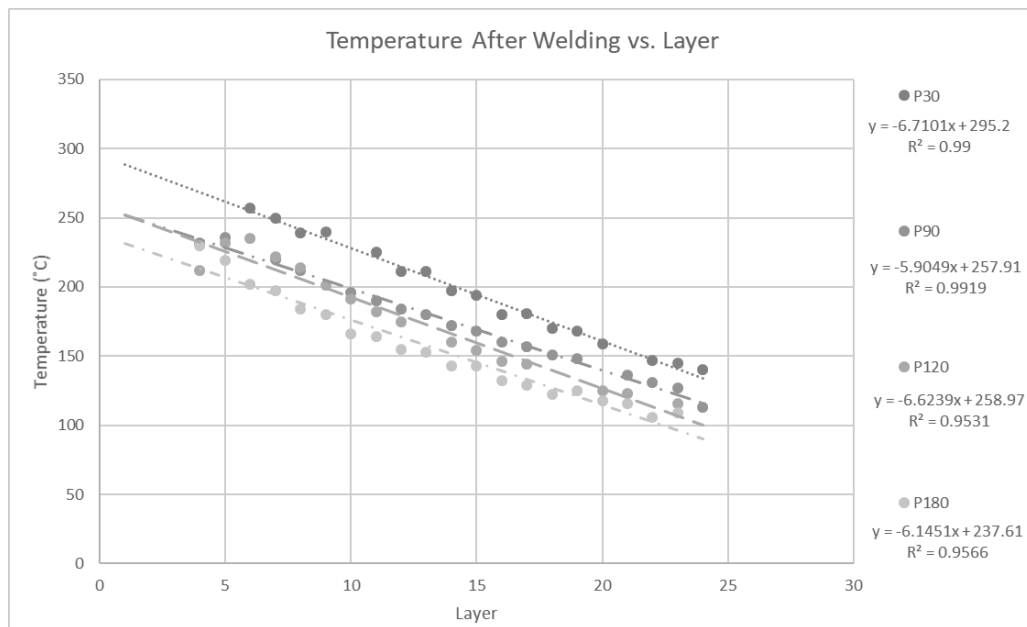


Figure 134. Temperature at the end of welding vs. layer number for the walls printed in the temperature study.

Long Wall

To complete the temperature study and evaluate the mechanical properties of stainless steel with respect to direction, another wall was deposited and transverse dogbones machined. Instead of printing another 120-mm long wall, a 250-mm long wall was programmed with a chosen 90-second interlayer pause. The wall was printed to be greater than 100 mm tall, so 30 layers were deposited. The total time of deposition was 160 minutes. An overview of the as-printed data can be found in Table 52 below while a complete summary of the data can be found in Appendix I. The as-printed wall can be seen in Figure 135. In printing a longer wall, residual stresses were minor, as shown with the small amount of build plate deflection.

Table 52. As-printed results for stainless long wall.

Wall ID	Layers Printed	Total Time	Average Layer Time	Height	Layer Height	Width	Material Removed	Yield	Deposition Rate
	#	min	s/layer	mm	mm/layer	mm	in	%	kg/hr
LW	30	160	320.0	106.5	3.5500	10.01	0.08	0.797	0.705

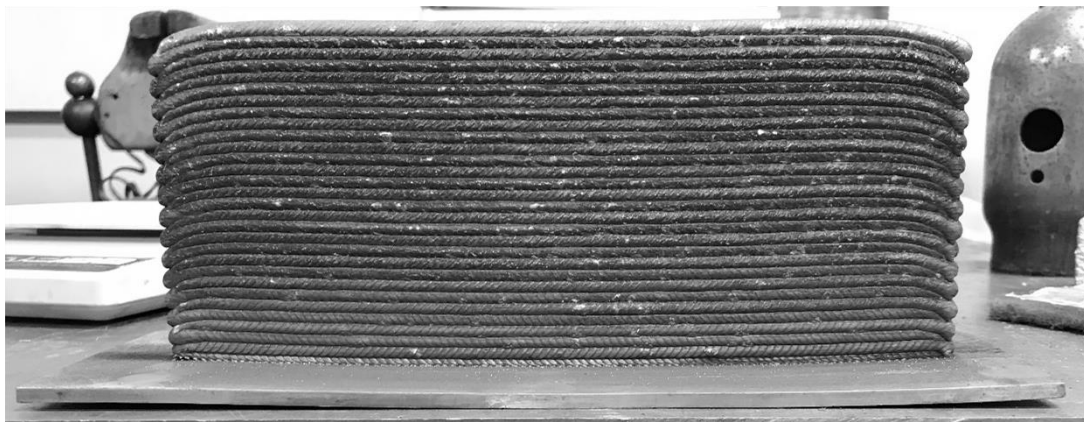


Figure 135. ER308 long wall showing minor residual stress bending.

Due to the longer weld path, the pause duration was a lower fraction of the overall printing time. With a layer time of 225 seconds and a pause time of 90 seconds, the welder was printing for 71 % of the time. This led to a higher deposition rate of 0.705 kg/hr when

compared to wall P90 (0.520 kg/hr), and is approaching the same deposition rate as wall P30 (0.720 kg/hr).

As shown in Figure 136, the location and orientation of the dogbones were chosen with two goals in mind: 1) Evaluate the mechanical properties in the transverse direction and 2) Evaluate the effect of residual stresses generated further out in the long wall by producing samples in the transverse direction from the outer edge in to the middle. A summary of the results of the tensile tests can be seen below in Table 53.

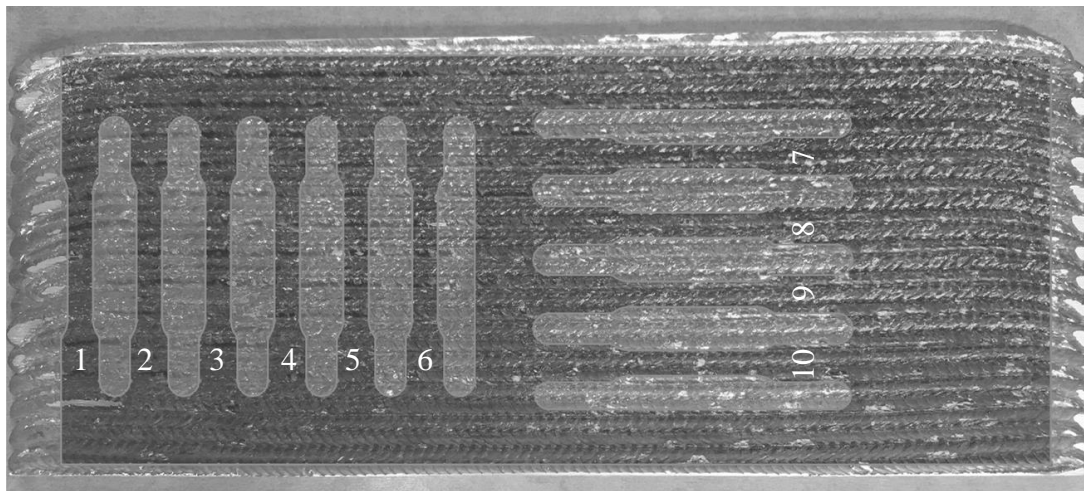


Figure 136. ER308 long wall showing the location of the tensile specimen.

Table 53. ER308 long wall tensile results grouped by orientation.

Sample		Yield Stress	Ultimate Tensile Strength	Modulus of Elasticity	RA	True Fracture Strain	Toughness
No.		ksi	ksi	ksi	%		$\int \sigma d\epsilon$
Transverse	Average	49.84	82.60	2251.56	63.90	1.02	426.11
	SD	2.30	1.46	137.54	2.57	0.07	24.22
Longitudinal	Average	53.40	89.46	2437.21	54.09	0.78	418.48
	SD	0.80	0.43	45.40	3.28	0.07	28.10
Manufacturers Spec		61	87 - 90		60		

Both values for the yield stress came in below the manufacturers spec. For UTS, the transverse direction was at 95% manufacturers spec and the longitudinal was at 100%. The results indicate that the yield stress and ultimate tensile strength are not statistically equal, with p-values of 0.019 and 0.0000188 respectively. Toughness between the transverse and longitudinal direction was statistically equal however, with a p-value of 0.658. The reason for this is the increased true fracture strain and reduction of area in the transverse direction compensating for the lower ultimate tensile strengths. Three graphs are shown below in Figure 137 that compare the data from the long wall study to the data from wall P90.

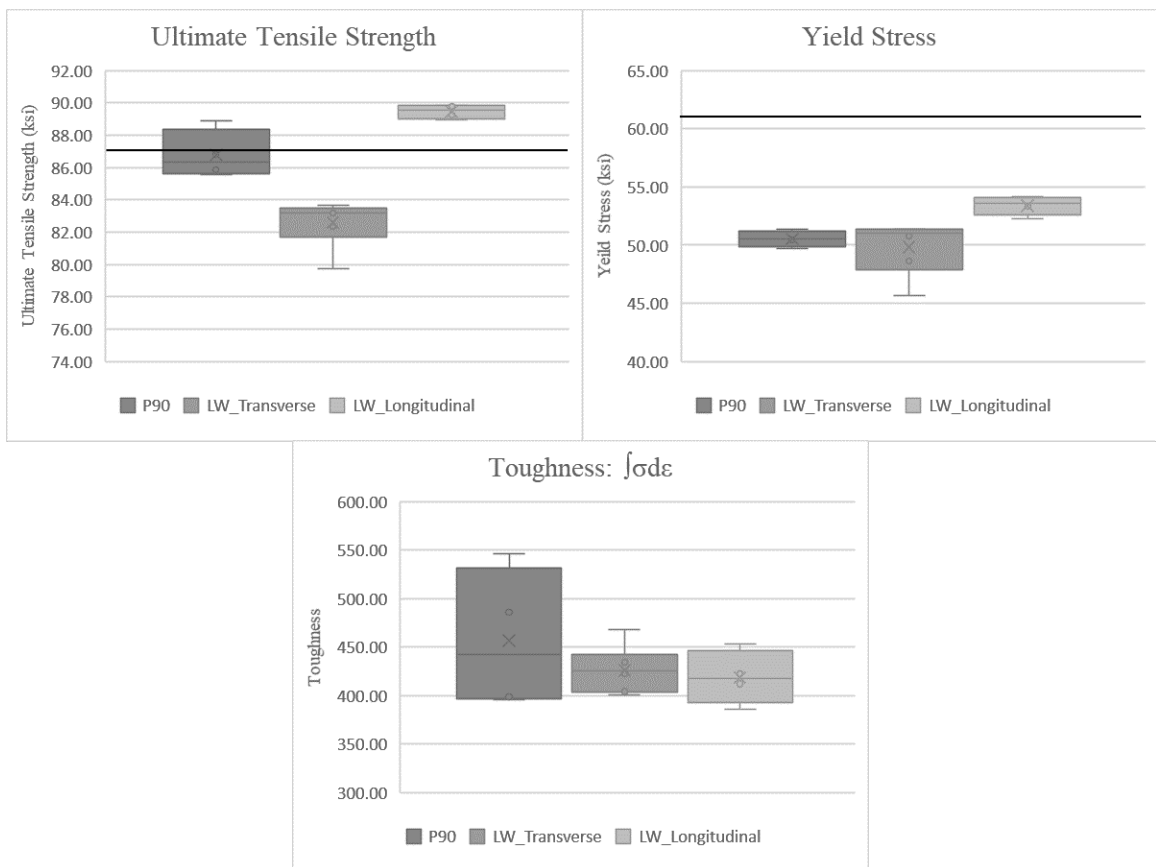


Figure 137. Ultimate tensile strength, yield stress, and toughness for wall P90, and long wall transverse and longitudinal. Lines denote manufacturers spec.

The engineering stress-strain curve below in Figure 138, plots two samples from the transverse direction (solid lines), and two samples from the longitudinal direction (dashed lines). The curve shows a very high level of repeatability between within each direction up to the ultimate tensile strength. The pairs of curves separate toward final fracture, with final fracture strain differing by around 0.05 within the same set. This result is comparable to the diverging values seen in the ER70S-6 shown in Figure 131 on page 191.

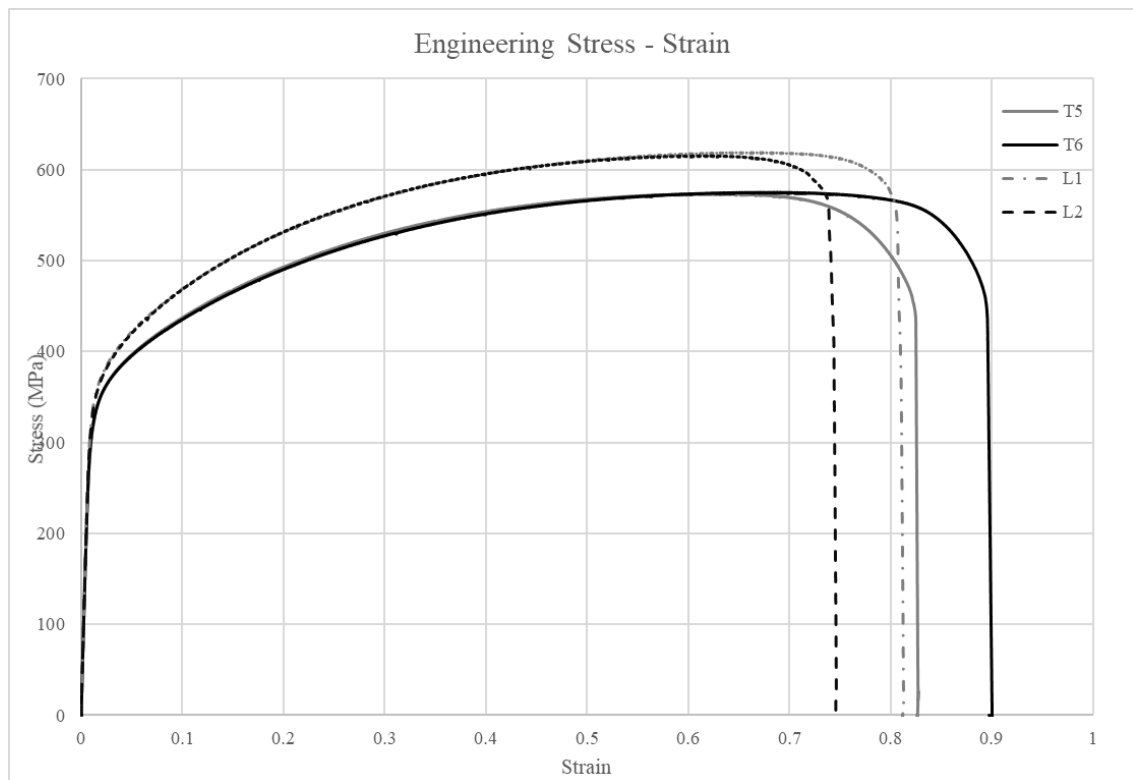


Figure 138. Long wall transverse vs. longitudinal engineering stress-strain curves.

The longitudinal direction consistently has a higher stress value than the transverse specimen at the same strains up until ultimate tensile strength is reached. The samples differ in their elongation with the longitudinal samples not elongating as much and failing before the transverse specimens. This difference is reflected in the true fracture strain and

reduction of area values between the orientations (Table 53). The larger true fracture strain and reduction of area observed is opposite of the expected results seen in ER70S-6, where the transverse direction had a slightly lower true fracture strain.

Evaluation of this observation continued with further analysis of the transverse tensile data with respect to specimen location, numbered from 1-6 from outside to inside, as well as longitudinal data, numbered 7-10 from top to bottom. As seen in the transverse data in Table 54, a trend of increasing yield stress and ultimate tensile strength can be seen moving in from the edge of the wall. The longitudinal data in Table 55 shows uniform mechanical properties with a much lower reduction in area and true fracture strain when compared to the transverse values.

Table 54. Stainless steel long wall transverse data with respect to location.

Sample	1	2	3	4	5	6
Sy (ksi)	45.7	48.6	50.8	51.4	51.3	51.3
Su (ksi)	79.8	82.3	83.2	83.7	83.2	83.4
RA (%)	67.9	60.8	65.2	61.8	64.7	63.0
Toughness	434	423	404	401	427	468
ϵ_f	1.14	0.94	1.06	0.96	1.04	0.99

Table 55. Stainless steel long wall longitudinal data with respect to location.

Sample	7	8	9	10
Sy (ksi)	54.2	53.8	53.3	52.3
Su (ksi)	89.8	89.3	89.0	89.9
RA (%)	52.7	50.1	57.0	56.5
Toughness	453.6	412.1	385.7	422.5
ϵ_f	0.749	0.695	0.845	0.833

The differences observed in the measured mechanical properties from the outside to inside can be attributed to the non-uniform cooling rate. The outer sample cools at a much faster rate and shows more ductility and toughness when compared to the adjacent sample. The difference in the mechanical properties between the transverse to longitudinal

results can be attributed to cooling rate as well. Jialuo Ding, of Cranfield University, used a finite element model to display the thermal gradient in multilayer buildup, as seen in Figure 49 on page 57. The center of the wall reaches steady state after the first initial layers. With very little thermal gradient, heat builds up at this location [5]. The reduction in ductility and lower true fracture strain can be likely due to the residual heat.

ER4043 – Mechanical Properties Evaluation Results

To produce an aluminum wall to machine dogbones out of, a continuous box print geometry was chosen as the most practical design, offering easy programming and four faces to machine for dogbones. Prior to programming, a square corner test was conducted with different feedrates through the corners to help avoid excess buildup. The ideal parameters were found to be 600 mm/min on the sides, increasing to 700 mm/min for 1-mm in the corner. When deciding on the size of the box, a large box was chosen so that heat would be less of an issue and transverse and longitudinal dogbones could be machined. The first print was programmed to be 210-mm by 100-mm. The welding parameters can be seen in Table 56 and the result of the print can be seen in Figure 140.

Table 56. Aluminum big box 1 welding parameters.

Filler Material	Shielding Gas	Synergic Line	WFS	ALC	EP/EN	Hot Start	Crater Fill	FR
			ipm	%	%	sec. and %	sec. and %	mm/min
ER4043	100%Ar	CMT1368 Adv	250 ↓165 ↓150	0	-1.0	0.2s@140%	0.0	600↑700

The first attempt at the big box was aborted due to a decreasing CTWD but not after printing 13 layers in 11 minutes and 40 seconds. Big box 1 measured between 30.1 and 31.5 mm in height and had a bead width of 4.2 mm at the top of the print. One major defect with the print was noticed on the second layer when the seam did not fill the gap left at the start. Usually, any excess weld height at the start point is slowly evened out as the layers

progress up, however from the start on big box 1, a gap was created and was bridged on each subsequent layer, propagating the gap up and along the side of the box.

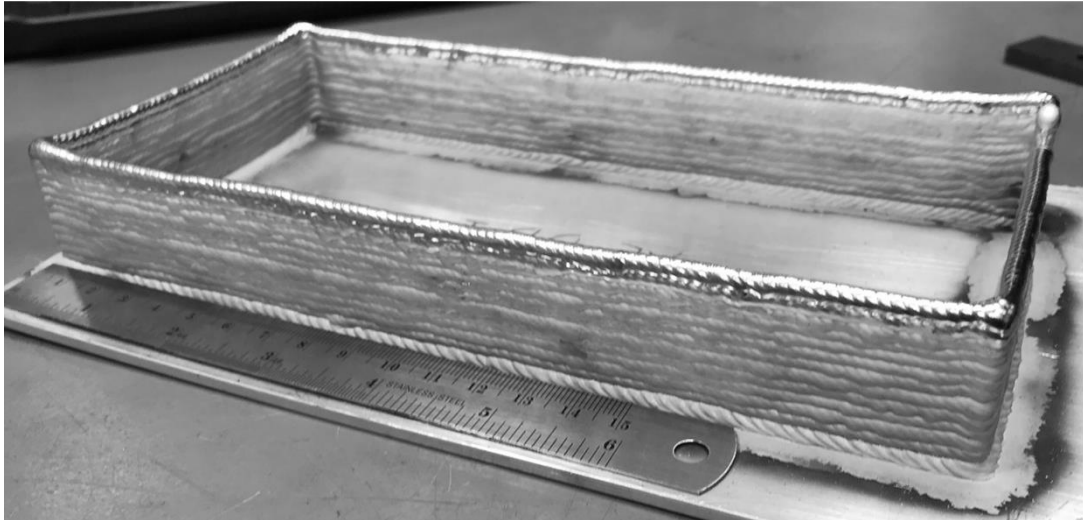


Figure 140. Aluminum big box 1.

As shown in Figure 139, the gap moves toward the left as the layers progress, as the corner gets excess material deposited on it every layer. This problem was not observed in other prints and may be alleviated by moving the start point out of the corner on the next trial.

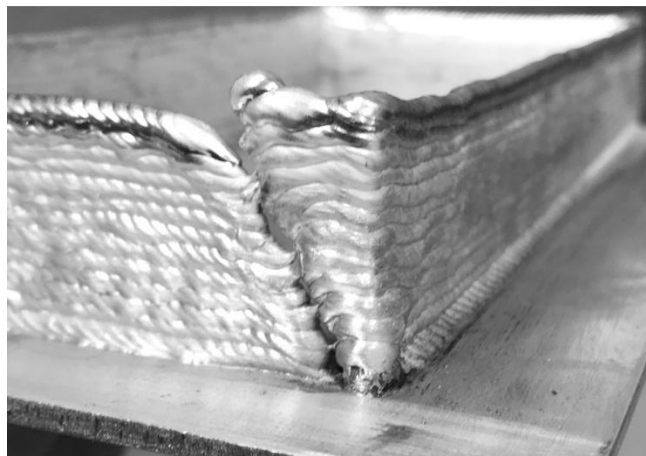


Figure 139. Start point gap bridge, big box 1.

For the deposition of big box 2, the geometry was changed to print a 210 by 50 mm box with the start point located in the middle, away from the corner. The welding parameters along with the wire feed speeds and feedrates used along with the layers can be seen below in Table 57.

Table 57. Aluminum big box 2 welding parameters.

Filler Material	Shielding Gas	Synergic Line	WFS	ALC	EP/EN	Hot Start	Crater Fill	FR
			ipm/layer	%	%	sec. and %	sec. and %	mm/min
ER4043	100%Ar	CMT1368 Adv	200 / 1	0	-1.0	0.2s@140%	0.0	600 / 1
			↓175 / 2					540 / 5
			↓165 / 4					509 / 14
			↓150 / 5					

In total, 40 layers were deposited in 39 min and 34 seconds. The result of the print can be seen in Figure 141, with arrows showing the start point at the bottom, and 25 layers up, where the program probed and restarted. A complete overview of the as-printed measurements can be seen in Table 58.

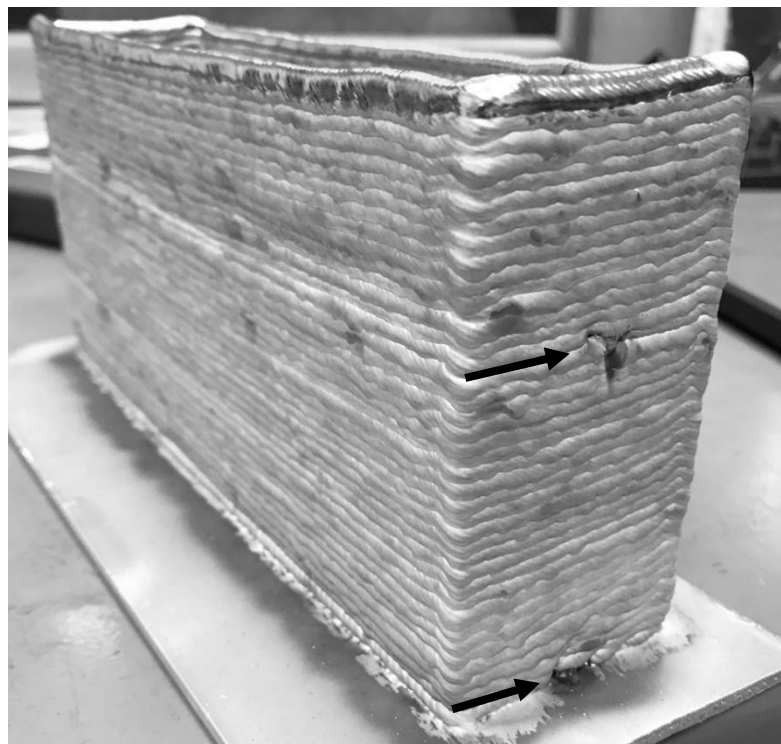


Figure 141. Aluminum big box 2. Arrows indicate start points.

Table 58. Aluminum big box 2 measured results.

E R 4 0 4 3	Mechanical Properties Study	Measurables							Deposition Rate
		Layers Printed	Total Time	Bead Width	Overall Width	Height	Layer Height	Overall Length	
			min	mm	mm	mm	mm/layer	mm	
	Big Box 2	40	39.57	5.5	54.99	102	2.55	213.36	0.9705

Tensile specimens were machined, from the sides and ends of the box. In order to create the thickest specimen possible, the gage section was machined flat and clean on both sides without regard for the condition in the grip region. This led to dogbones with visible unmachined surfaces as shown in Figure 142. This is expected to have no effect on the tensile results as it is outside the gage region. Since the samples were thin and susceptible to bending upon clamping in the vice, the gage surfaces were not machined completely flat and parallel. The thickness had slight taper from top to bottom. Referencing ASTM-E8, this was found to be allowable for use in monotonic tensile testing [48].



		Initial	
	Sample	Width	Thickness
	No.	in.	in.
Transverse	1	0.250	0.128
	2	0.250	0.127
	3	0.250	0.126
Longitudinal	4	0.250	0.122
	5	0.250	0.120
	6	0.250	0.121
	7	0.251	0.137
	8	0.250	0.120

Figure 142. Tensile specimen as-machined and a table of the measured sizes. Note that the specimens shown are transverse specimens 1, 2, and 3 and are incorrectly labeled.

In total, 3 samples in the transverse direction and 5 in the longitudinal direction were pulled on the MTS Q-Test 100. The results can be seen below in Table 59.

Table 59. Aluminum tensile test results.

Sample Orientation		Yield Stress	Ultimate Tensile Strength	Modulus of Elasticity	Reduction of Area	True Fracture Strain	Toughness
		ksi	ksi	ksi	%		$\int \sigma d\epsilon$
Transverse	Average	14.14	24.33	2415.6	27.58	0.32	44.12
	SD	0.95	0.05	1102.75	2.12	0.03	1.76
Longitudinal	Average	15.78	24.46	4543.0	28.04	0.33	47.87
	SD	1.33	0.64	643.11	3.21	0.04	5.06
Manufacturers Spec		18-10	27-20				

Analysis of the results indicated that for yield stress and ultimate tensile strength, isotropic properties were achieved with p-values of 0.115 and 0.729 respectively. The statistical data can be seen in Appendix IV. The ultimate tensile strengths seen fell inside the manufacturers spec, but the yield stress fell short. Looking at the engineering stress strain curve in Figure 143 below, all of the tensile the data can be seen plotted together. The data shows the transverse specimen are mixed in with the longitudinal samples at higher strain values. There is a large spread in the tensile results, with the fracture strain ranging from 0.26 to 0.36. The transverse specimens are closely grouped together at high strains towards failure but at low strains, these specimens yield before longitudinal samples and have smaller linear elastic regions. Overall the data is quite spread out when compared to the highly repeatable and uniform stress strain curves of other materials. The roughness of the curves, as seen clearly on the uppermost sample, raises some questions about the microstructure. This unsmooth stress strain behavior seems to only arise after plastic deformation has set in and will need to be explored further.

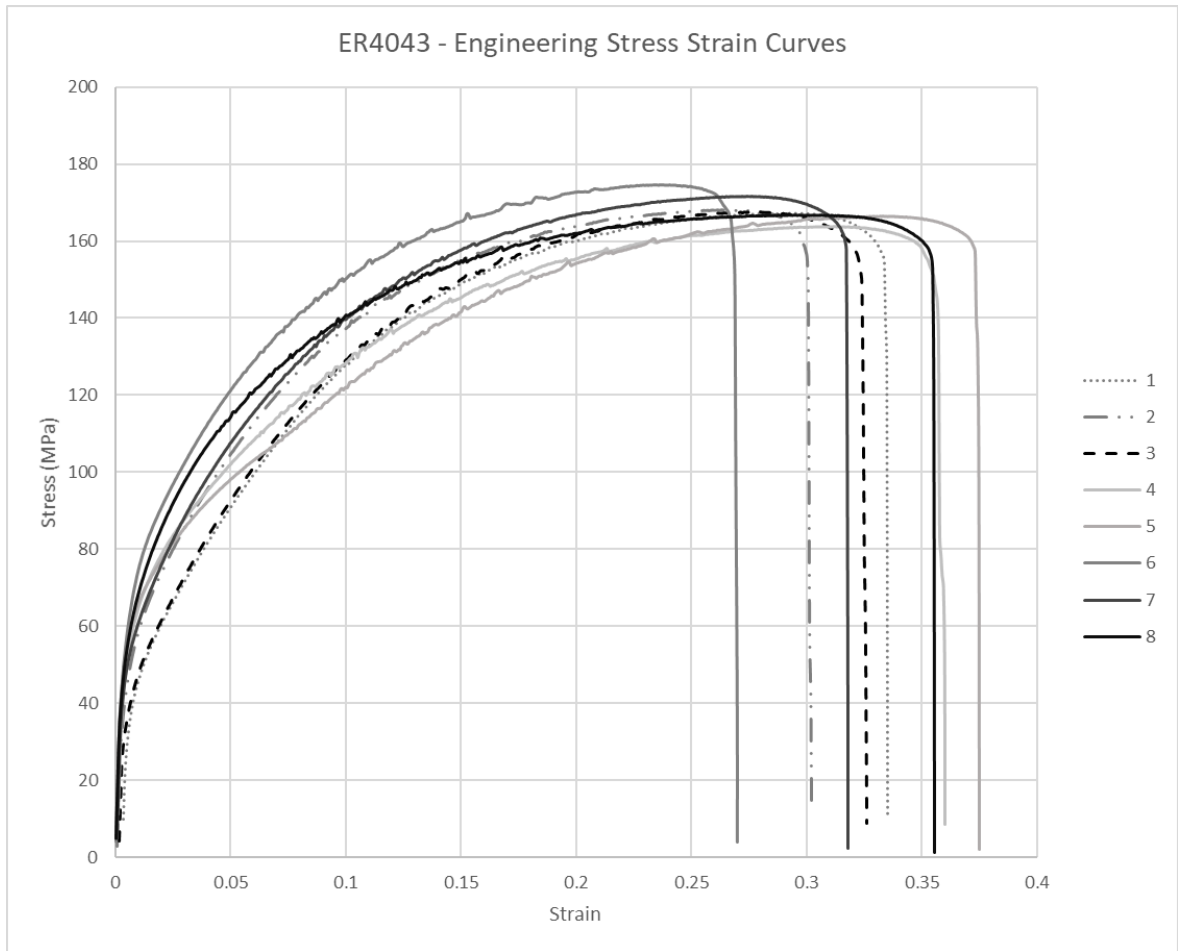


Figure 143. ER4043 engineering stress-strain curve, dashed lines are transverse orientation.

ER70S-6 – Microstructure Evaluation Results

For metallographic analysis of the microstructure of ER70S-6, ASM Handbook – Volume 9, on metallography and microstructure was used as reference, particularly the section on carbon and low-alloy steel castings [54]. Figure 144 below shows a typical microstructure observed in ER70S-6.

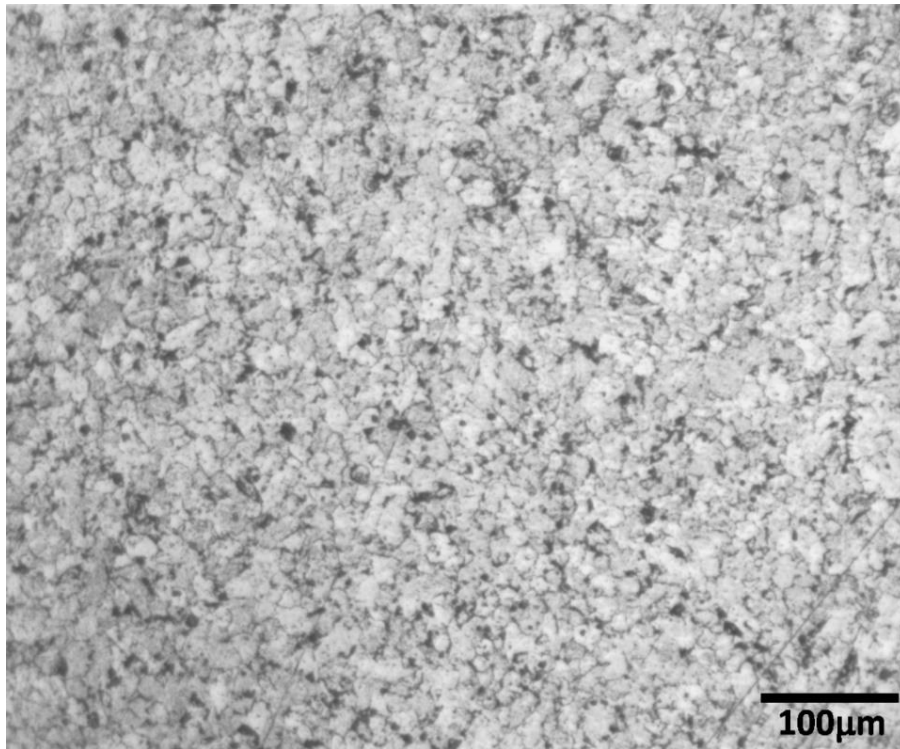


Figure 144. Grain structure of Temperature Study Wall P90

Evaluation of the microstructure at the layer interface indicates whether we can produce a welded microstructure structure that exhibits no evidence of layers. Microstructural images at the boundaries have been obtained by sectioning, mounting, and polishing samples while leaving the edge of the wall in tact in an as-printed condition. The dark areas on the images below in Figure 145 are the edges of the wall, with the triangle region being a layer interface and the meeting of two weld beads. Mounting the samples with an unmachined edge allows us to find, and look directly at this interface in detail. Prior results in Gaddes' research indicated a clear distinction and almost imperfect fusion at this region, however, that is not the case here. The welded layers have recrystallized as one bead and no line of separation can be seen.

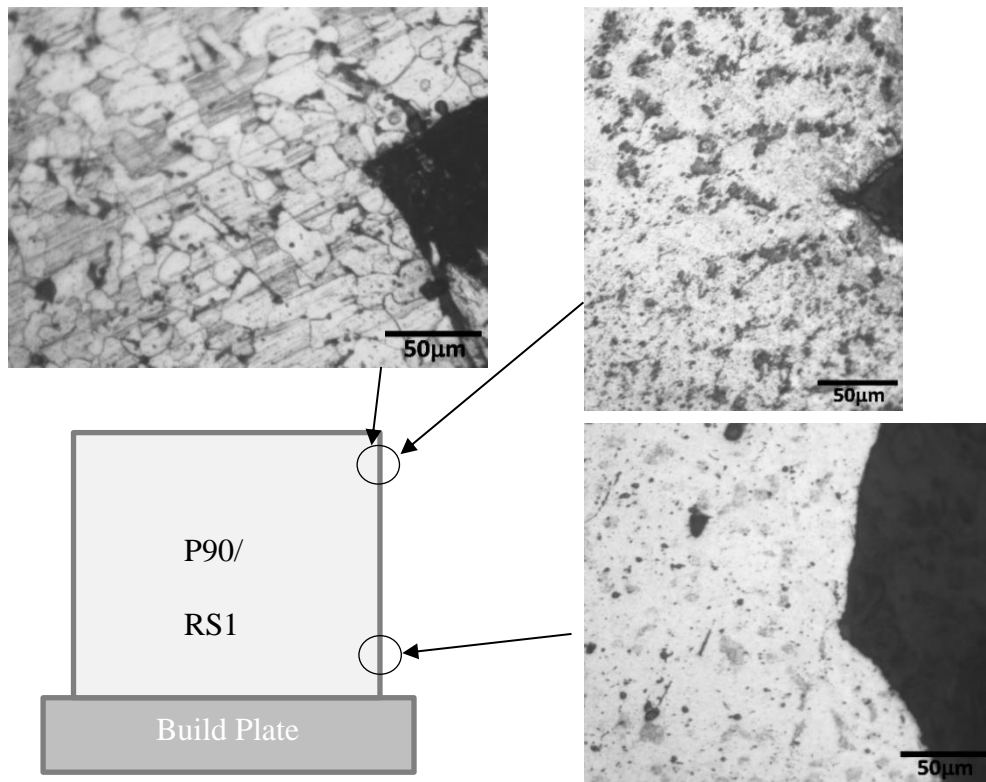


Figure 145. Layer interface from side of wall P90 (right images) and repeatability study wall 1 (left) and the locations of the samples on the original wall.

The images below in Figure 146 and Figure 147, are sampled from the wall built in repeatability study 1 and wall P30. The grain structure was evaluated at the top and the bottom of a wall to see the effect of repeated reheating and cooling. The results show this produced a non-uniform grain structure with the top of the weld exhibiting acicular ferrite with some regions of pearlite and bainite. This region was observed to only extend for the first few millimeters.

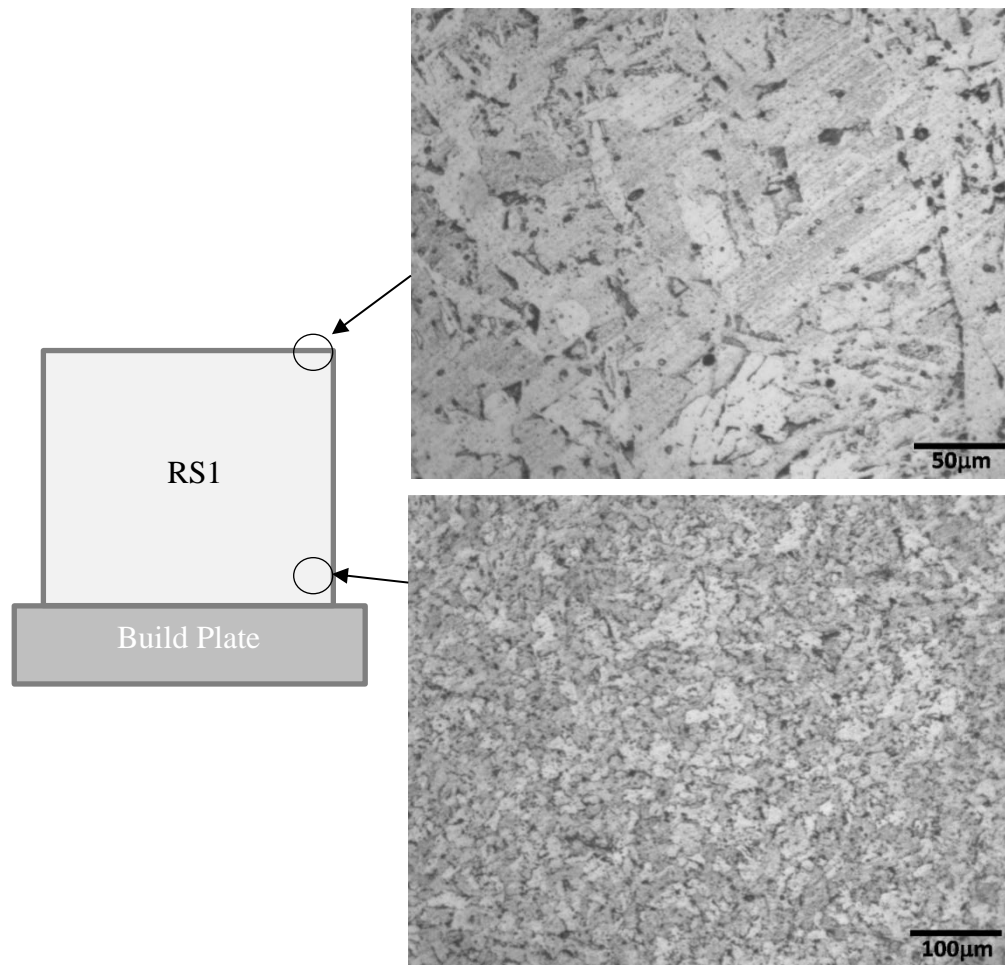


Figure 146. Microstructure of repeatability study 1 wall at top edge (top), and at the bottom of the wall, in from the edge (bottom)

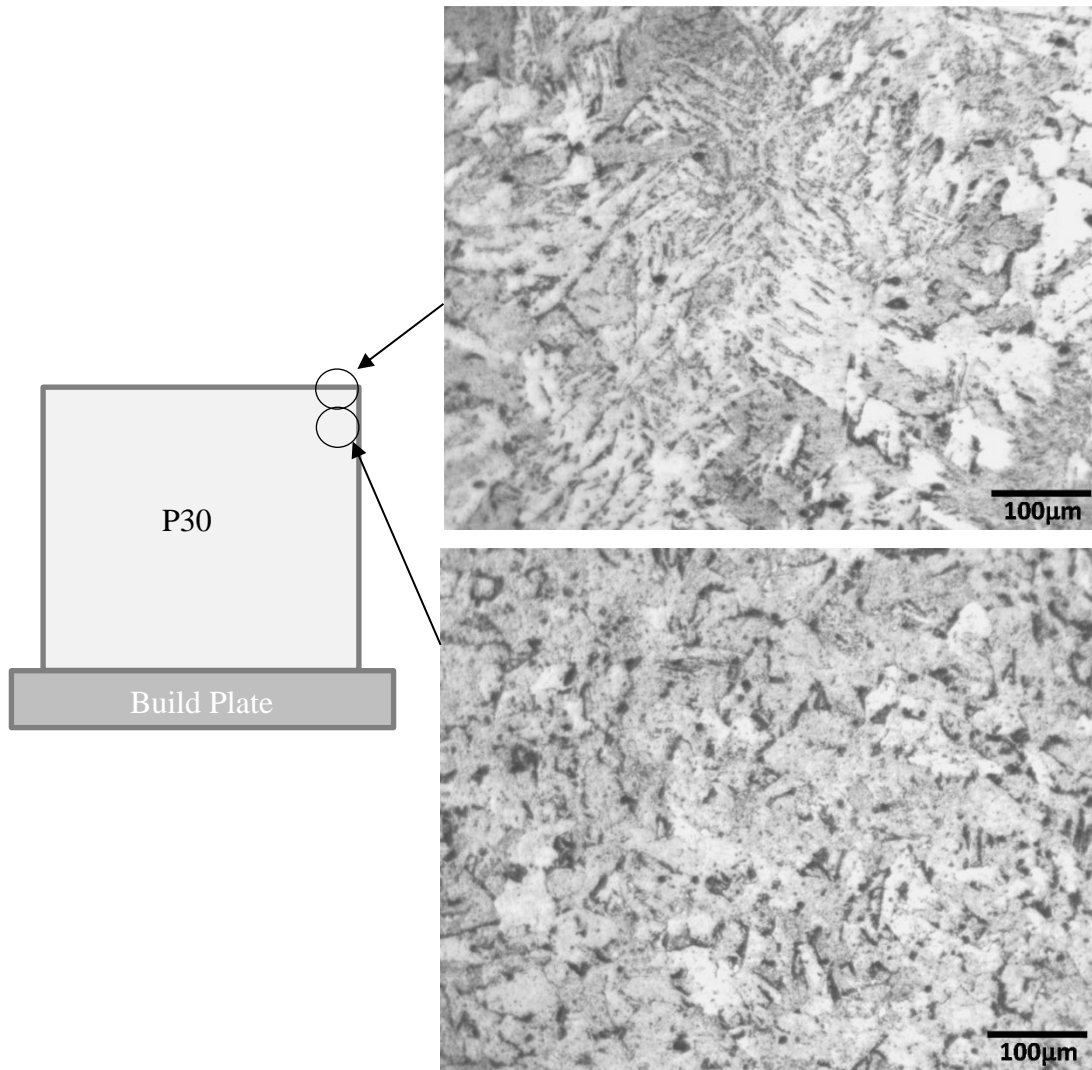


Figure 147. Microstructure of temperature study wall P30 at top edge (top), and just below the top edge (bottom)

The composite image shown in Figure 148, is from the top corner of repeatability study wall 1. An area of 1.7-mm in width and 6.6-mm in height was imaged for further analysis of the changing structure as it would cover at least two layers of the weld. The top of the image is the last layer deposited in the wall. The bottom and middle show previous layers with one, and possibly two reheating cycles. At the top of the image, Widmastatten ferrite can be clearly seen along with some acicular ferrite. Grain size starts to decrease and become uniform as you get closer to the bottom.

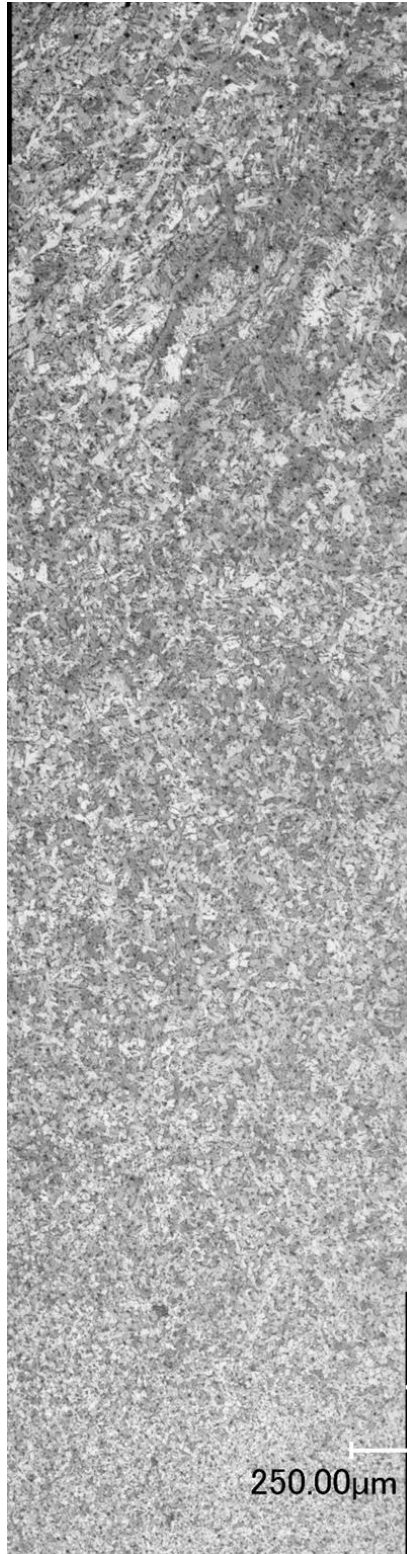


Figure 148. Repeatability Study Wall 1, composite micrograph from the top down, showing the multiple microstructures present.

Shown in Figure 149, a void measuring 37 μm was observed in the sample taken from wall P180. This was the largest void seen in all the samples. The void may be a slag inclusion which came free during polishing, leaving the void seen below.

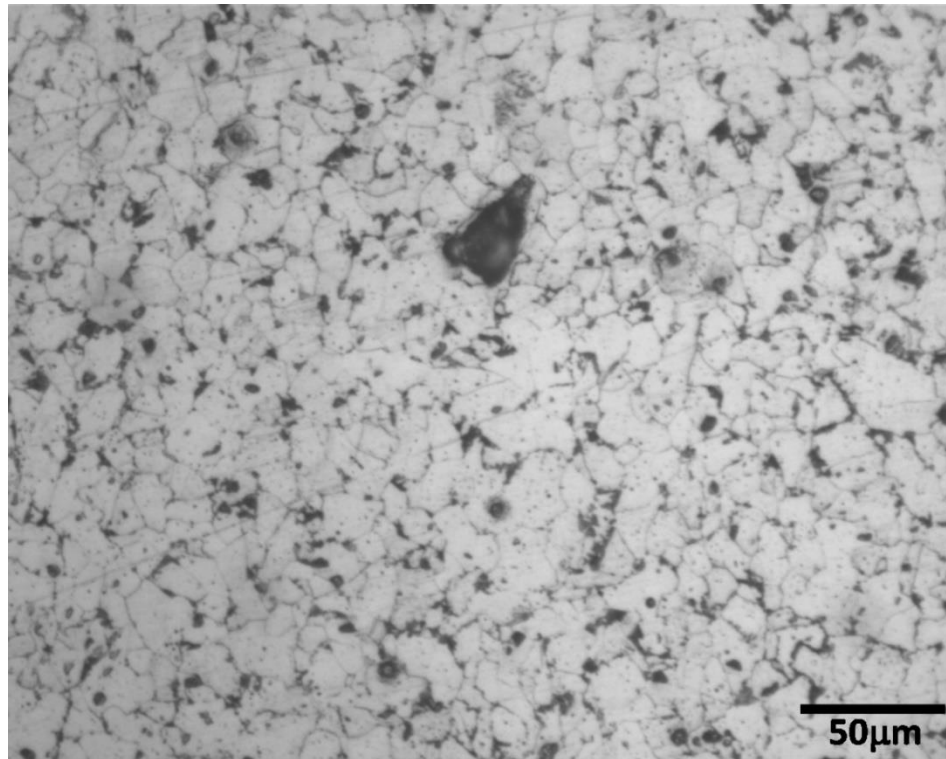


Figure 149. A 37 μm void seen on sample taken from wall P180.

ER308 – Microstructure Evaluation Results

The microstructure for stainless steel was evaluated next to stainless steel weldments of the ASM Handbook – Volume 9. Looking at the microstructure below in Figure 150, the handbook images of austenitic stainless steel weld material [54]. The microstructure is composed of skeletal δ -ferrite in an austenitic matrix.

The amount of δ -ferrite in stainless steel weld deposits is important because the microstructure of the steel influences many of its properties. Adverse effects of δ -ferrite might include increase in magnetic permeability of alloys containing ferrite, or reduction in impact strength during long-time high-temperature service through an increase in the rate of sigma phase formation which leads to hot cracking and embrittlement [55].

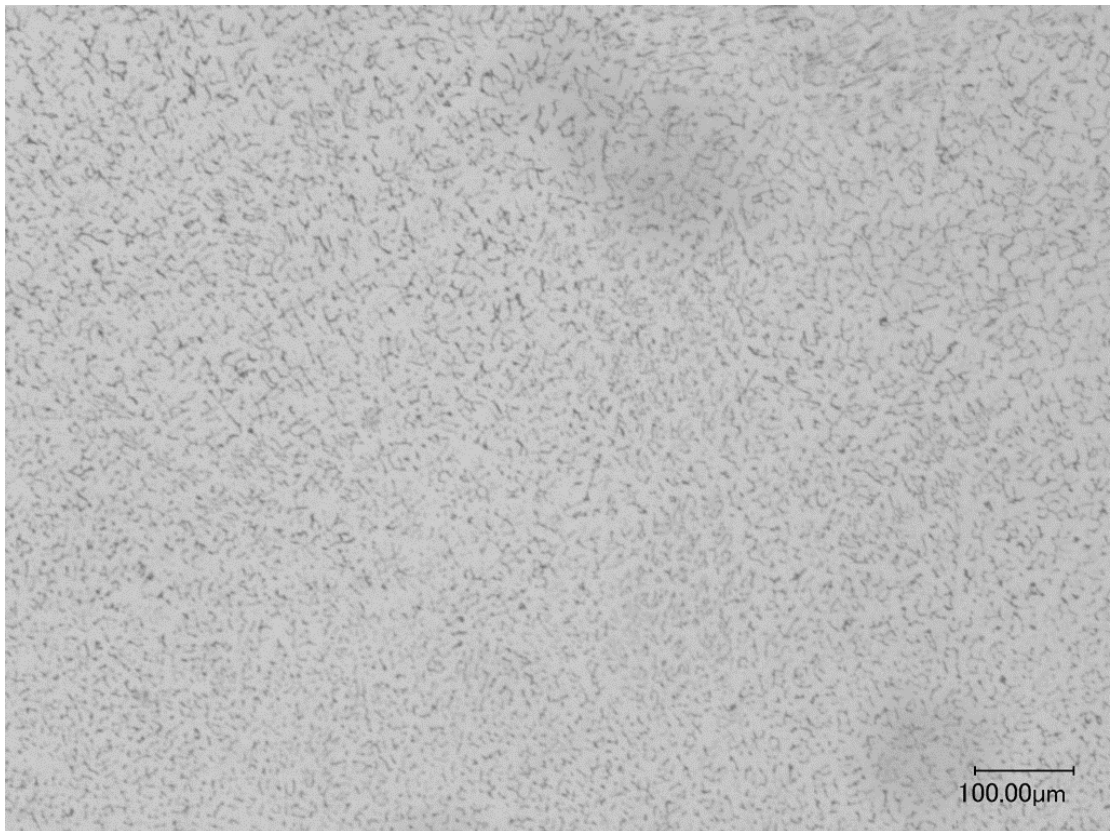


Figure 150. ER308 microstructure observed at the bottom of the long wall

To quantify the δ -ferrite composition of the weld microstructure shown in Figure 150, the image was calibrated and scaled down to a size of 427 μm by 804 μm using the ImageJ software. A particle size analysis was performed with the results outlined in Table 60 and Figure 151.

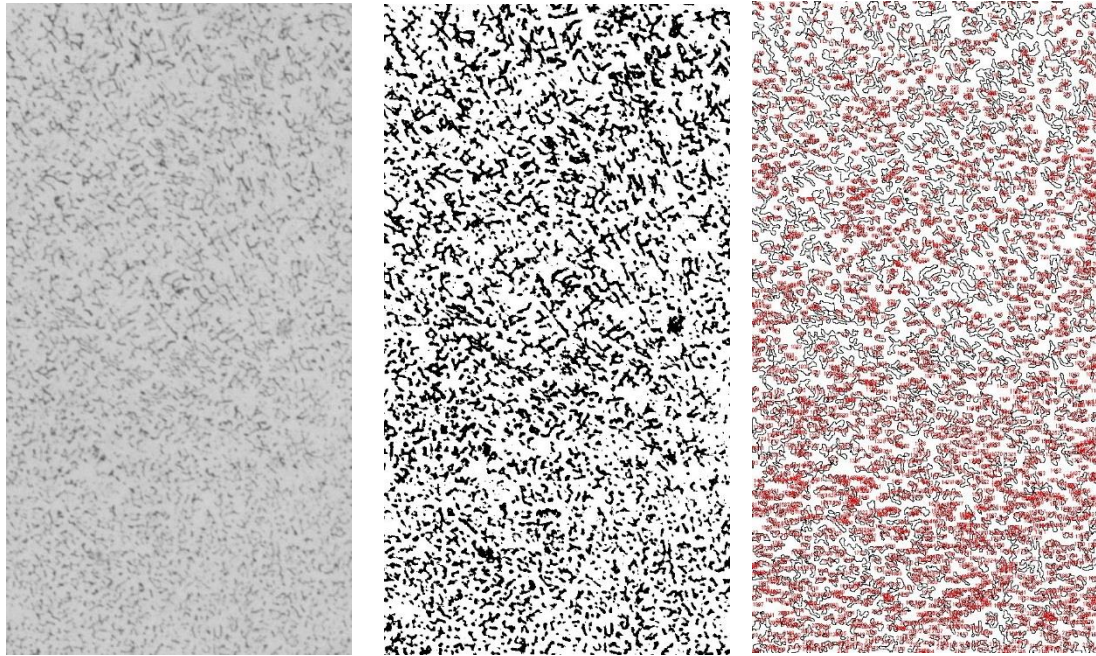


Figure 151. ER308 microstructure shown in Figure 150 processed with ImageJ, cropped (left), threshold applied (center), and particle size measurement (right).

Table 60. Summary of the particle size analysis.

Sample	Particle Count	Total Area (μm^2)	Average Size (μm^2)	Area %
ER308 Long Wall	2187	90889.75	41.559	26.535

These results quantify the δ -ferrite content to be around 25% of the microstructure by volume. Schaeffler produced a constitution diagram for weld metals that would allow the prediction of weld metal microstructure based on the chemical composition, using the equivalent chromium and nickel content, Cr_{eq} and Ni_{eq} of the weld material. The Schaeffler diagram is shown in Figure 152 [55]. For our ER308 filler material, Cr content is given as

a range between 19.5 – 22%, Si between 0.3 – 0.65%, Mo of max 0.75%, Ni between 9 – 11, Mn of 1 – 2.5 %, and C as 0.08% max. Using these ranges, the maximum and minimum possible values for chromium equivalent and nickel equivalent can be solved for to give a range of approximation. The values are shown plotted below, and correlate to an austenite and ferrite mixture of varying composition from 5 – 40%.

Following the analysis on the bottom of the wall, a sample from the top of the wall

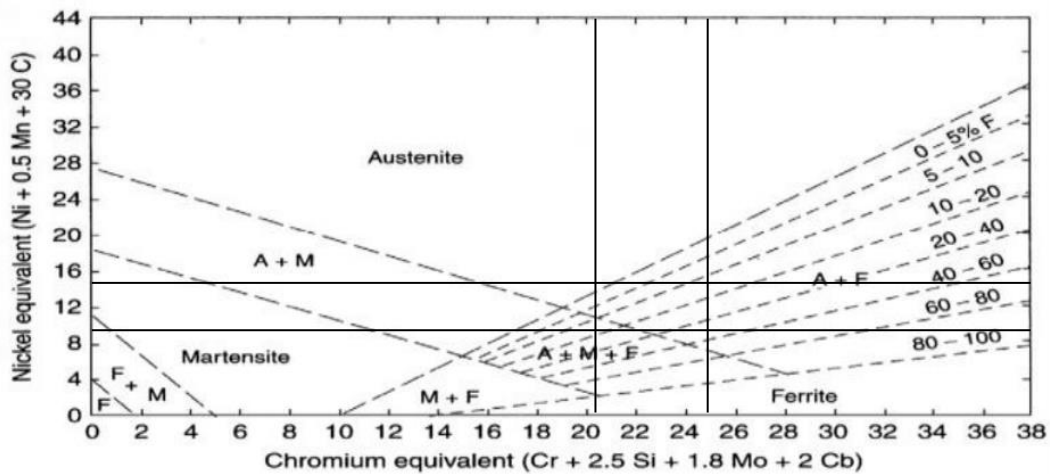


Figure 152. Schaeffler diagram of 1948, with linear boundaries [55]

Table 61. Summary of particle size analysis ER308 long wall (top)

Sample	Particle Count	Total Area (μm^2)	Average Size (μm^2)	Area %
ER308 Long Wall	14025	295507.4	21.07	14.631

was processed in a similar manner. The sample can be seen in Figure 153. Initial observation indicates a drop in the δ -ferrite content. Particle size analysis was performed on the image and the results can be seen in Table 61. A drop in ferrite content was noticed, with a reduction of approximately 45%. As you can also see, the average size of the ferrite particles was halved.

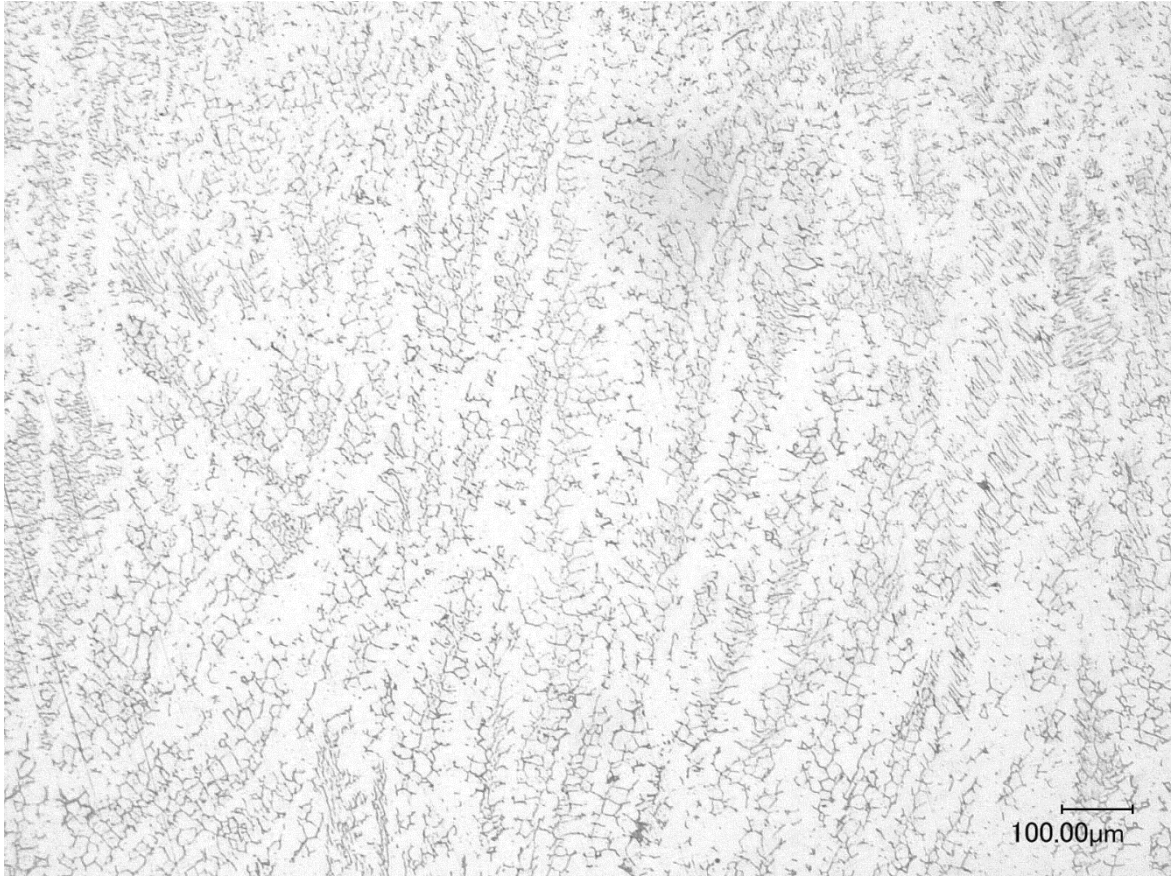


Figure 153. ER308 microstructure observed at the top of the long wall.

Figure 154 below, shows a detailed view of the interface of two layers, similar to the investigation done for ER70S-6 in the prior section. However, unlike the prior results, here we can clearly see a difference in the welded microstructure. The bottom of the image, or the layer deposited prior to the top bead, shows a similar microstructure to that observed throughout the weld. The top bead shows a fine circular grain structure, a possible indication that chromium is precipitating out of the weld pool and solidifying.

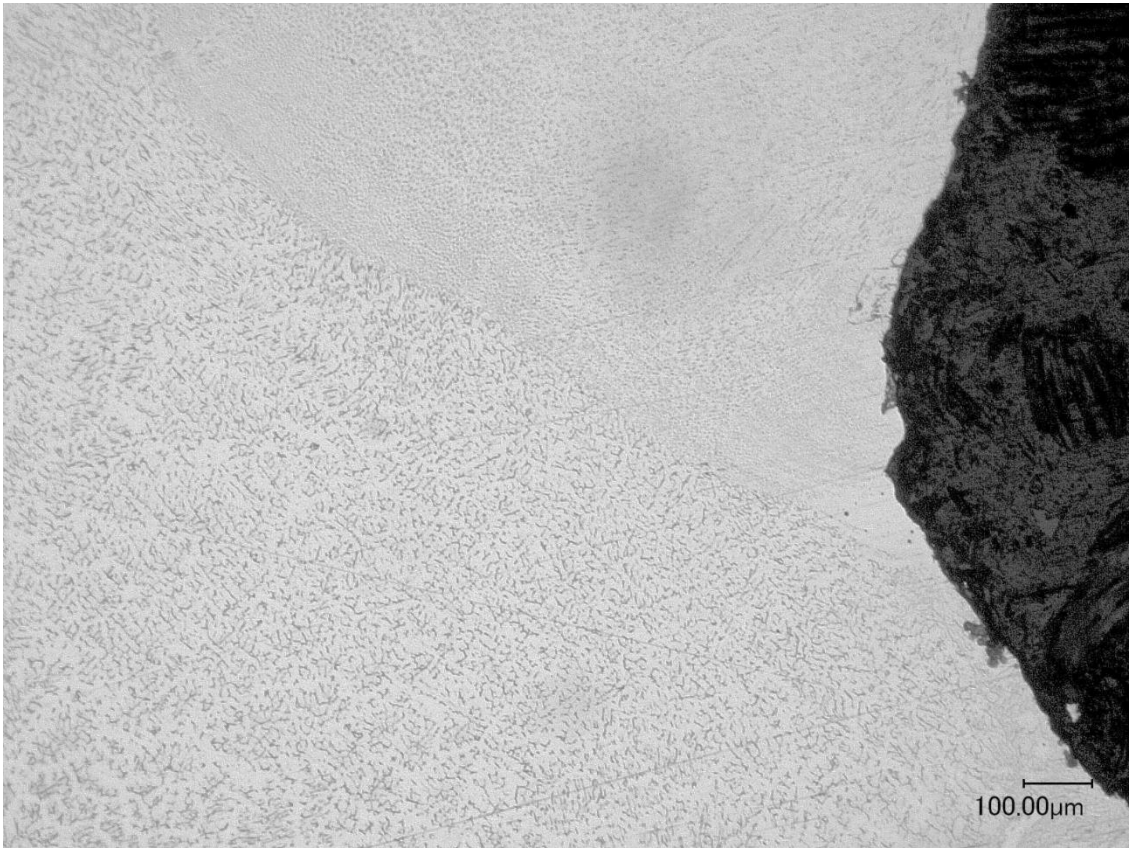


Figure 154. ER308 layer interface observed at the side of the long wall.

ER4043 – Microstructure Evaluation Results

When looking at the polished sample of ER4043 aluminum alloy, the layer boundaries could be seen with the naked eye during the polishing process, before etchant was applied, as shown in Figure 156. The interface could be seen throughout the sample, as shown in Figure 155 and Figure 158 at the side of the wall.

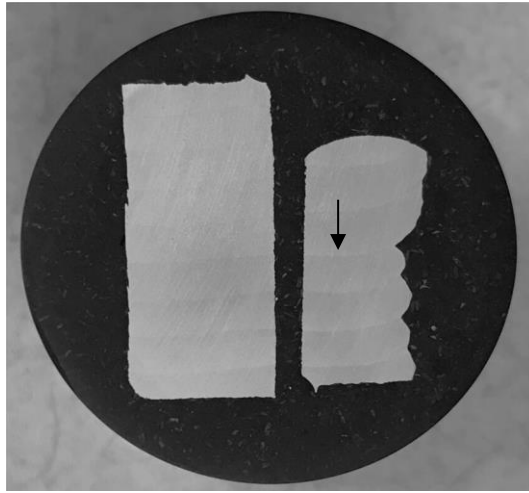


Figure 156. ER4043 samples mounted and polished.

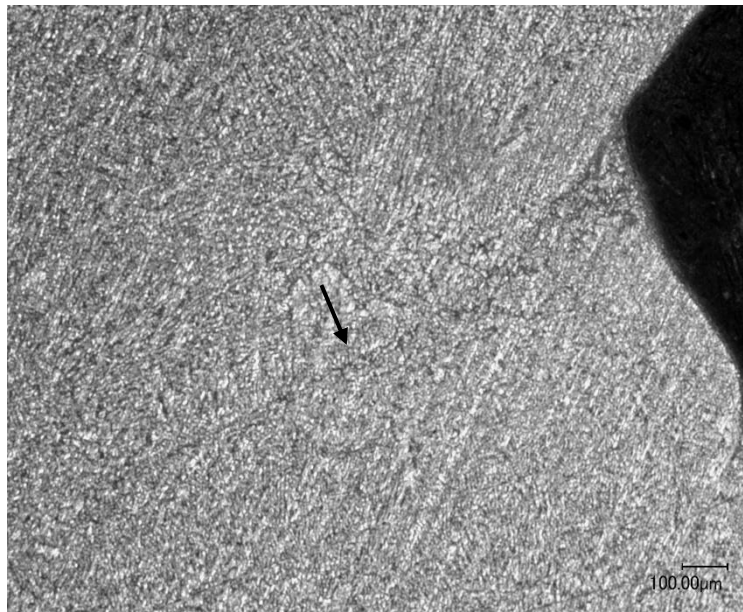


Figure 155. ER4043 layer boundary, on the side, at the top.

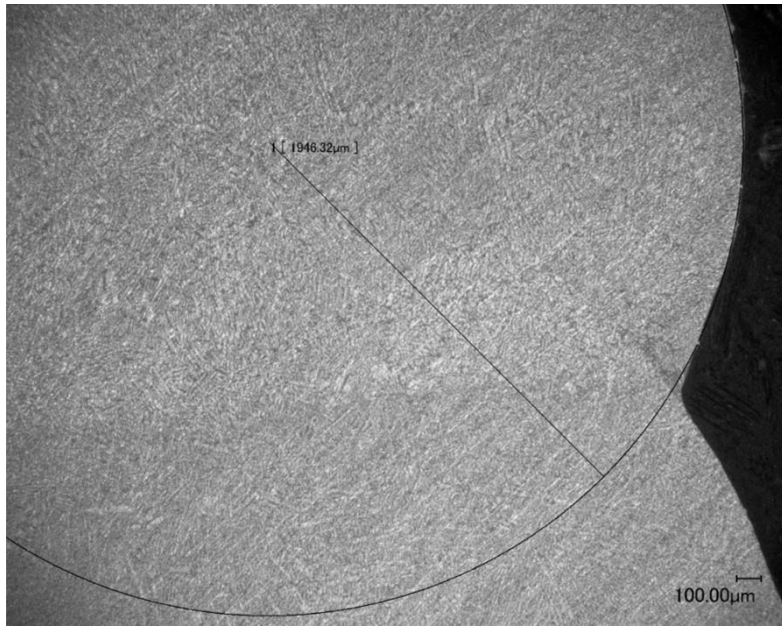


Figure 158. ER4043 side profile layer boundary, bottom. Radius =1.946 mm

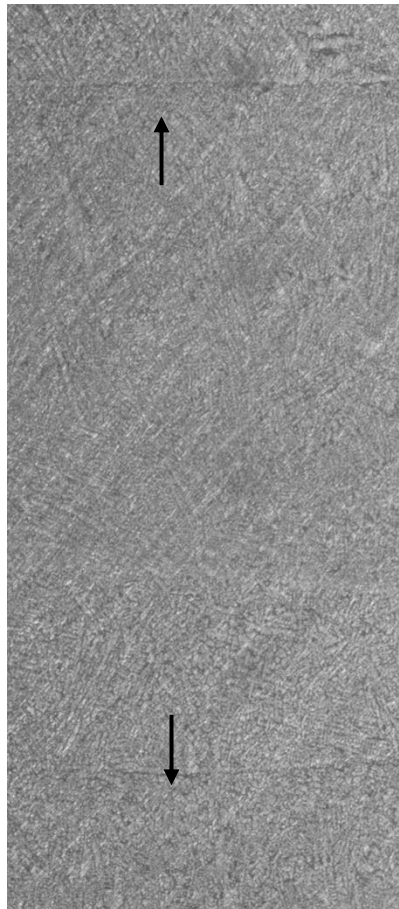


Figure 157. ER4043 stitched image of two layer boundaries 2.674 mm apart.

The image below in Figure 159 shows small equiaxed grain boundaries, seen throughout the aluminum samples taken.

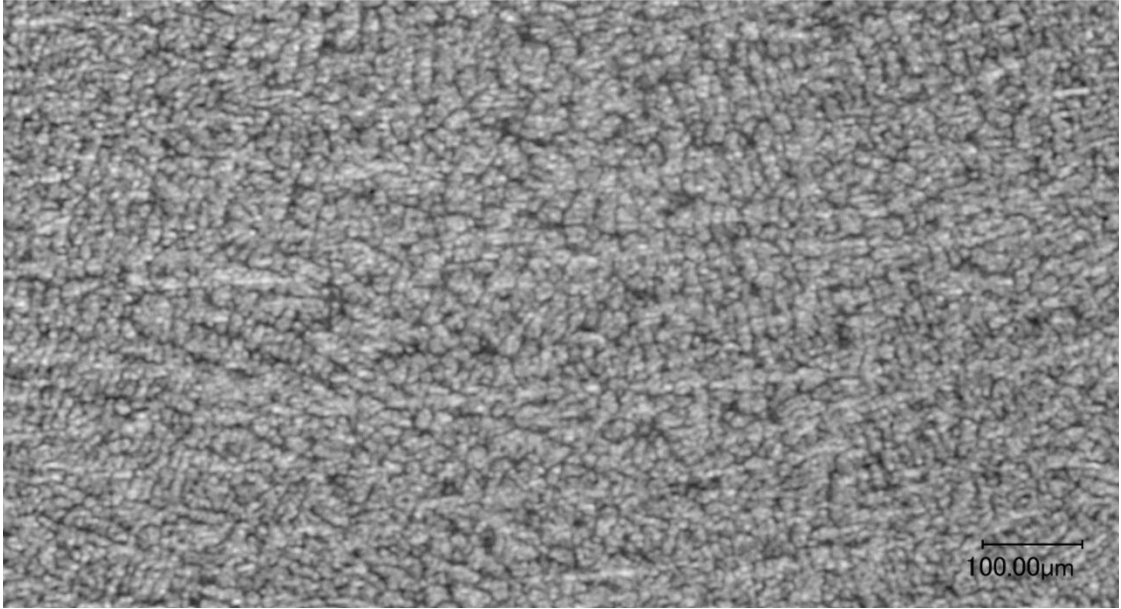


Figure 159. ER4043 top bead, viewing down toward the baseplate

Non-Planar Deposition Evaluation Results

To study the possible use of 3D toolpaths, paths where all three axes move at once, code was created using a zig zag path that built up a trapezoid shape with the sides angling in. Due to clearance issues, 45 degrees is the maximum that the welder can move relative to a surface maintain a CTWD of 14-mm. For this reason, the angles on the side of the trapezoid were set to 40 degrees and the path completed with a 3D zig zag across the entire surface. The test was performed using ER70S-6 and was to serve as a proof of concept. The results of the first attempt can be seen below, Figure 160.

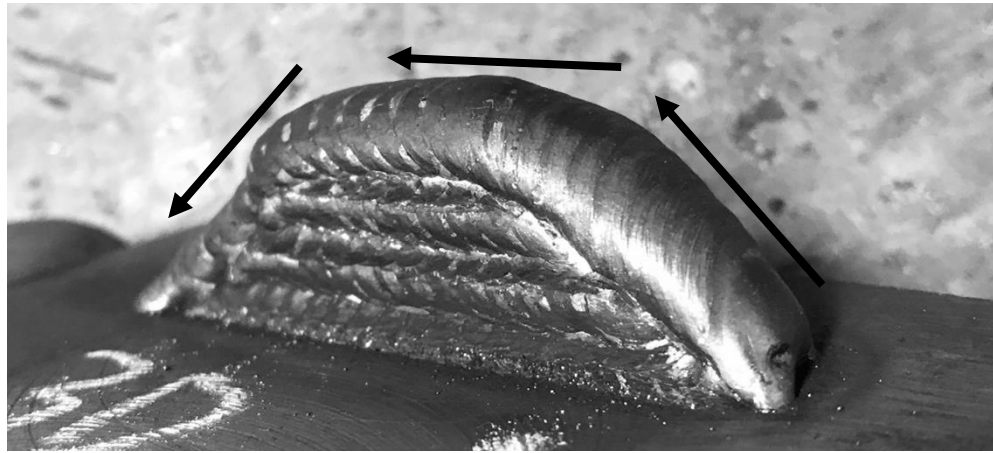


Figure 160. Non-planar toolpath examination results.

The foreground of the image shows the upward movement of the 3D path, the result of which was quite promising. The down slope on the back side proved to be an issue, with the arc becoming unstable as the welder attempted to bridge out on top of itself and build off of the bead currently being deposited rather than follow the slope down.

VII. Discussion

Analysis of the results found in the previous chapter allows a greater understanding of the process, its advantages, and improvement opportunities. A discussion of the results from each aspect of the project is found below.

CMT vs. GMAW Discussion

The addition of the CMT welder to the WAAM process was successful. The added process control was effective in eliminating spatter and creating perfect welds in multiple materials. The decreased heat input led to good results in aluminum while the increased stability allowed for deposition of larger structures with height no longer being an issue.

Closed Loop Process Controls Discussion

Prior to beginning the work presented in this thesis, the largest challenges faced in the deposition were the start point not arcing on command, and the increasing or decreasing CTWD. The implementation of the two feedback control loops, was successful in regard to reducing operator reliance to ensure the success of the print. Previously, when the CTWD was growing too large, the wire feed speed would be increased or the feed rate would be decreased in an attempt to deposit more material. Now that the print “re-zeros” itself after each layer or when programmed to, the operator is no longer needed except to monitor the status.

Controlling the start point used to be done via a short pause after a welding start command. While this succeeded in the short term, it often led to some layers with excess deposition at the start. The implementation of this feedback loop greatly increased the

accuracy of the deposition from the start of layer 1, which is the most crucial influence on the rest of the print.

Geometry Discussion

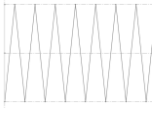
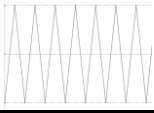
When beginning this research, following the recommendations of prior researchers, the 3D-printing slicing software Slic3r was used to create weld paths. This software had the most features and was suited to modification of parameters for our needs, however it was found to be an annoyance and therefore was abandoned completely. For most of the early work, G-code was scripted by hand until more complicated structures were to be made. At that point, the HSMWorks add-in for Solidworks was adapted and used to create G-code. This was found to be the best option, as the output was easy to post-process.

The most unexpected result of the geometry study was how beneficial the feed rate modification in HSMWorks was in the programming of weld paths. For both thick-walled structures and thin walled structures, the feed rate modification was used to create better bead profiles, and direct deposition where needed. The first use of this option was in the zig zag geometry when a feed rate reduction was investigated instead of programming a dwell time in at the inflection point. This led to decreased programming time, because now the dwells did not have to be added by hand.

The feed rate modification was also successfully added to single-bead squares, where a big issue previously was excess buildup at the corners. Using an increase in the feed rate going into the corner eliminated this problem and resulted in flat deposition.

This study has succeeded in its goal of developing a weld schedule and developing the best practices for printing ER70S-6, ER308, and ER4043. The complete guide can be found in Table 62.

Table 62. CMT-WAAM weld schedule.

Filler Material	Geometry	Parameters									Results	
		Stepover	Feed Rate	Feed Rate Reduction	Synergic Line	WFS	ALC	Dyn. Corr.	Crater Fill	Pause Time	Width	Layer Height
		mm	mm/min			ipm	%	%	sec. @ %	sec.	mm	mm/layer
ER70S-6	Single Bead	-	400	-	CMT 1362	125	15	-1.2	0.3s @ 50%	60	5.5	1.72
	Zig Zag 	1.25	720	↓60 mm/min for 0.5 mm		95	15	-1.2	0.7s @ 40%	90	12.80 (8mm)	3.15
ER308	Single Bead	-	440	-	CMT 0908	125	15	-1.2	0.3s @ 50%	60	4.5	1.7
	Zig Zag 	1.25	750	↓60 mm/min for 0.5 mm		95	15	-1.2	0.7s @ 40%	90	10.01 (8 mm)	3.55
ER4043	Single Bead	-	600 ↓510	-	CMT 1368 Adv.	200 ↓150	0	-1.0 (EP/E N)	Hotstart 0.2s @ 140%	-	5.5	2.55

The inability to successfully deposit thick-bead aluminum structures should not overshadow the results of the aluminum deposition study. One must also remember the benefit and usefulness of this technology is better suited to high strength, tough to machine, and expensive materials.

Non-Planar Toolpath Discussion

The results of the first trial showed promise in the use of non-planar deposition for 3D shapes. The toolpath should only be used to build upward, as it was found that welding downward against itself proved to be unstable. This has the promise to provide a “finishing pass” on 3D shapes.

Mechanical Properties Evaluation Discussion

When performing tensile testing on ER70S-6 and ER4043, isotropic results were achieved and within manufacturers spec. For ER308, this was not found to be the case, with the transverse direction and longitudinal direction being unequal at 95 and 100% manufacturers specification, respectively. A summary of the results can be found in Table 63.

Table 63. Mechanical property results for all three materials in each orientation.

ER70S-6 - Carbon Steel				
Orientation	Yield Stress	Ultimate Tensile Strength	Reduction of Area	True Fracture Strain
	ksi	ksi	%	
Longitudinal	50.41	69.92	75.00	1.39
Transverse	51.55	70.19	73.85	1.34
Spec	58.00	70.00	60.00	

ER308 - Stainless Steel				
Orientation	Yield Stress	Ultimate Tensile Strength	Reduction of Area	True Fracture Strain
	ksi	ksi	%	
Longitudinal	53.40	89.46	54.09	0.78
Transverse	49.84	82.60	63.90	1.02
Spec	61.00	87 - 90	60.00	

ER4043 - Aluminum				
Orientation	Yield Stress	Ultimate Tensile Strength	Reduction of Area	True Fracture Strain
	ksi	ksi	%	
Longitudinal	15.78	24.46	28.04	0.33
Transverse	14.14	24.33	27.58	0.32
Spec	18.00	20 - 27		

The mechanical properties observed and a lack of noticeable delamination in tension shows the benefit of the CMT process when compared to the results from previous work. The non-isotropic results for stainless steel and the non-uniform stress strain curves observed in plastic deformation show that there is still further work that needs to be done.

One of the biggest surprises of this research was the quality of the aluminum results. Depositing aluminum and building up a structure large enough to produce tensile specimens was a success, even if it did mean adjusting the geometry of the dogbones. In the machining of the dogbones the aluminum behaved in a very gummy manner, and left a poor surface finish. It was not free machining and did not produce a good chip when being cut.

Microstructure Examination Discussion

When investigating the microstructure of the steel, aluminum, and stainless steel, a general lack of porosity was noticed and uniform grain structure was seen outside the top layer. For ER308 and ER4043, layer boundaries could still be distinguished, indicating that the welding parameters could need modification. Further analysis into the effect of interpass cooling on stainless steel may offer a solution to the non-uniform grain structure observed at the layer interface. No evaluation of heat treatment, aging, or other post processing was evaluated in this research.

VIII. Conclusions and Recommendations for Future Work

In this analysis, a literature review was conducted to identify the current state of research in WAAM using a CMT based process. From the literature review, important process factors were extracted with the goal of implementing the best practices going forward. After improving upon the control of the additive manufacturing process, numerous tests were conducted to identify the ideal parameters for the deposition of thick walled and thin walled structures in carbon steel, stainless steel, and aluminum. The results of this experiment are listed below.

- A Fronius CMT welder was integrated into the existing 3-axis, gantry-style CNC 3D printer.
- New machine code was developed, adding greater functionality to the robot.
- Two feedback control loops were implemented to improve on process stability.
- An experimental record sheet was created for future researchers to use.
- Different deposition strategies for thicker buildup were studied.
- Ideal travel speeds and wire feed rates have been documented for single-bead and thick-bead deposition of ER70S-6, ER308, and ER4043.
- The ability to create standard geometric shapes has been refined and the best practices have been documented.
- Temperature and the effect of interpass cooling time on monotonic tensile properties has been studied for multilayer deposition,

- The tensile strength of steel, stainless steel, and aluminum was measured in the transverse and longitudinal direction, indicating isotropic behavior in steel and aluminum and near isotropic behavior in stainless steel.
- The microstructure was observed to be a fine equiaxed grain structure.
- The dimensional accuracy of multiple complex 3D shapes were compared to the models.
- Non-planar, 3D toolpaths were studied for feasibility.

Recommendations for Future Work

As shown in the experiments, further analysis is necessary to continue to refine and improve the process. This future work can be divided into improvements in the control, improvements in the robot, and improvements in process.

Methods of improving the control:

- Additional feedback loops should be added. Further capability of temperature monitoring would provide an automated method of pausing welding after each layer. Monitoring the voltage and current of the weld could be used to identify problems during the process as well as tweak the parameters on the fly.

Methods of improving the robot:

- Additional axes of motion are necessary for greater deposition capability and would expand upon the geometries capable of being produced. A two axis positioner (i.e. a trunnion and rotary table) would expand the capability but would increase the programming effort. Moving to a 6-axis robotic arm

may be easier going forward and will improve the manipulation of the weld pool.

Methods of improving the process:

- The addition of a water-cooled build plate would increase cooling rate and thus deposition rate.
 - Create a new fixture plate using a quick action edge-clamp to reduce distortion and better utilize the build plate area.
 - Develop an HSMWorks post processor to speed up the creation of G-Code.
- Develop a method of creating weave toolpaths directly from 3D models.

Omitted Objectives

The use of “rafts” as baseplates to increase ease of specimen removal was not studied. The first layer of the print is the most important and determines the quality of the rest of the deposition. If a problem is incurred in the first layer, depending on the severity and type, the print typically does not recover and the problem is propagated throughout. Placing a raft on top of the build plate would result in uneven first layer height and areas of incomplete baseplate fusion. I believe these would only have negative effects on the structure. The inconsistent fusion of the base plate would create non-uniform residual stress distributions and possible stress concentrations. In addition, the partially fused structure would still need to be removed from the baseplate using a saw.

References

- [1] Pinto, I. P. M. S., 2015, "Additive Manufacturing of Nickel Components Using CMT Process," Master of Science in Mechanical Engineering, Tecnico Lisboa.
- [2] Frazier, W. E., 2014, "Metal Additive Manufacturing: A Review," *Journal of Materials Engineering and Performance*, 23(6), pp. 1917-1928.
- [3] Gerhard Posch, K. C., Harald Chladil, 2017, "Material Properties of CMT-Metal Additive Manufactured Duplex Stainless Steel Blade-Like Geometries," *Weld World*, International Institute of Welding.
- [4] Gaddes, J. S., 2015, "Parametric Development of Wire 3D Printing," Master of Science, Auburn University.
- [5] Ding, J., 2012, "Thermo-mechanical Analysis of Wire and Arc Additive Manufacturing Process," PhD, Cranfield University.
- [6] Williams, S. W., Martina, F., Addison, A. C., Ding, J., Pardal, G., and Colegrove, P., 2016, "Wire + Arc Additive Manufacturing," *Materials Science and Technology*, 32(7), pp. 641-647.
- [7] Hasselberg, T. P., 2009, "A Feasibility Study of "Cold Metal Transfer" – Gas Metal Arc Welding (CMT-GMAW) Nickel Base Superalloy Inconel 718," MASTER OF SCIENCE, Rensselaer Polytechnic Institute.
- [8] P. M. Sequeira Almeida, S. W., 2010, "Innovative Process Model of Ti-6Al-4V Additive Layer Manufacturing Using Cold Metal Transfer (CMT)," *Annual*

International Solid Freeform Fabrication Symposium University of Texas at Austin.

- [9] Welding, M., 2012, "Guidelines for Gas Metal Arc Welding," 154 557 C, p. 20.
- [10] Fronius, "Cold Metal Transfer: The Technology ".
- [11] Baker, R., 1925, "Method of making decorative articles "U.S. Patent 1533300.
- [12] Eschholz, O. H., 1925, "Ornamental arc welding,"U.S. Patent 1533239.
- [13] Noble, P., 1933, "Method and apparatus for electric arc welding,"U.S. Patent 1898060.
- [14] R. Carpenter Otis, H. J. K., 1947, "Method and apparatus for metal coating metal pipes by electric fusion,"U.S. Patent 2427350.
- [15] White, J. W. D., 1964, "Pressure roller and method of manufacture,"U.S. Patent 3156968.
- [16] Ujiie, A., 1971, "Method of and apparatus for constructing substantially circular cross section vessel by welding,"U.S. Patent 3558846.
- [17] H. Brandi, H. L., 1976, "Method of making large structural one-piece parts of metal, particularly one-piece shafts,"U.S. Patent 3985995.
- [18] Acheson, R., 1990, "Automatic welding apparatus for weld build-up and method of achieving weld build-up,"U.S. Patent 4952769.
- [19] Almeida, P. M. S., 2012, "Process Control And Development In Wire And Arc Additive Manufacturing," PhD, Cranfield University.
- [20] Dr P M Dickens, D. M. S. P., Dr R C Cobb, Dr I Gibson and Mr G Dixon, 1992, "Rapid Prototyping Using 3-D Welding," Annual International Solid Freeform Fabrication Symposium, Department of Manufacturing Engineering and

Operations Management, and U. University of Nottingham, eds. University of Texas at Austin.

- [21] J D Spencer, P. M. D. a. C. M. W., 1998, "Rapid prototyping of metal parts by three-dimensional welding," Department of Manufacturing Engineering and Operations Management, The University of Nottingham, 212(Part B).
- [22] Ribeiro, F., Ogunbiyi, B., and Norrish, J., 1997, "Mathematical model of welding parameters for rapid prototyping using robot welding," Science and Technology of Welding and Joining, 2(5), pp. 185-190.
- [23] Ribeiro, F., Norrish, J., and McMaster, R. S., 1994, "Practical Case Of Rapid Prototyping Using Gas Metal Arc Welding" Cranfield University.
- [24] Wibelrs, F., 1998, "3D Printing with Metals," Computing & Control Engineering Journal, Rapid Prototyping.
- [25] Ribeiro, A. F., and Norrish, J., 1996, "Rapid Prototyping Using Robot Welding - Slicing System Development " DEI - Artigos em atas de congressos internacionais.
- [26] Norrish, F. R. a. P. J., 1996, "Case Study of Rapid Prototyping Using Robot Welding - Second 'Square to Round' Shape."
- [27] Fernando Ribeiro, P. J. N., 1996, "Metal Based Rapid Prototyping For More Complex Shapes," The Welding Institute.
- [28] Beardsley, R. K. a. H., 1998, "Process Control of 3D Welding as a Droplet-Based Rapid Prototyping Technique," Annual International Solid Freeform Fabrication Symposium, Southern Methodist University, Dallas, TX, University of Texas at Austin.

- [29] I. Kmecko, D. H. a. R. K., 1999, "Controlling heat input spatter and weld penetration in GMA welding for solid freeform fabrication," Annual International Solid Freeform Fabrication Symposium, D. Southern Methodist University, TX, ed. University of Texas at Austin.
- [30] YuMing Zhang, Y. C., Pengjiu Li, Alan T. Male, 2003, "Weld Deposition-Based Rapid Prototyping: A Preliminary Study," Journal of Materials Processing Technology, 135, pp. 347–357.
- [31] Song, Y.-A. P., Sehyung; Hwang, Kyunghyun; Choi, Doosun; Jee, Haeseong, 1998, "3D welding and milling for direct prototyping of metallic parts," Annual International Solid Freeform Fabrication Symposium, Korea Institute of Science and Technology KIST, CAD/CAM Research Center; Korea Institute of Machinery and Metals KIMM; Hongik University, Dept. of Mechanical Engineering, University of Texas at Austin.
- [32] Song, Y.-A., Park, S., Choi, D., and Jee, H., 2005, "3D welding and milling: Part I—a direct approach for freeform fabrication of metallic prototypes," International Journal of Machine Tools and Manufacture, 45(9), pp. 1057-1062.
- [33] Song, Y.-A., Park, S., and Chae, S.-W., 2005, "3D welding and milling: part II—optimization of the 3D welding process using an experimental design approach," International Journal of Machine Tools and Manufacture, 45(9), pp. 1063-1069.
- [34] Clark, D., Bache, M. R., and Whittaker, M. T., 2008, "Shaped Metal Deposition Of A Nickel Alloy For Aero Engine Applications," Journal of Materials Processing Technology, 203(1-3), pp. 439-448.

- [35] Anzalone, G. C., Chenlong, Z., Wijnen, B., Sanders, P. G., and Pearce, J. M., 2013, "A Low-Cost Open-Source Metal 3-D Printer," *IEEE Access*, 1, pp. 803-810.
- [36] Suryakumar, S., Karunakaran, K. P., Bernard, A., Chandrasekhar, U., Raghavender, N., and Sharma, D., 2011, "Weld bead modeling and process optimization in Hybrid Layered Manufacturing," *Computer-Aided Design*, 43(4), pp. 331-344.
- [37] Ding, J., Colegrove, P., Mehnen, J., Ganguly, S., Sequeira Almeida, P. M., Wang, F., and Williams, S., 2011, "Thermo-mechanical analysis of Wire and Arc Additive Layer Manufacturing process on large multi-layer parts," *Computational Materials Science*.
- [38] Jianglong Gu, B. C., Jialuo Ding, Stewart W. Williams, Yuchun Zhai, 2014, "Wire+Arc Additive Manufacturing of Aluminum," *Annual International Solid Freeform Fabrication Symposium, Welding Engineering and Laser Processing Centre, Cranfield University, UK; School of Materials and Metallurgy, Northeastern University, China; School of Mechanical Engineering and Automation, Beihang University, China, University of Texas at Austin*.
- [39] Posch Gerhard, K. F., Hackl Heinz, Chladil Harald, 2014, "Manufacturing of Turbine Blades by Shape Giving CMT-Welding," *Metal Additive Manufacturing Conference Vienna*.
- [40] Ding, D., Pan, Z., Cuiuri, D., and Li, H., 2015, "A multi-bead overlapping model for robotic wire and arc additive manufacturing (WAAM)," *Robotics and Computer-Integrated Manufacturing*, 31, pp. 101-110.
- [41] Institute, T. W., 2017, "Additive manufacture of aluminium alloy components using the Cold Metal Transfer (CMT) process," <http://www.twi-global.com/news->

[events/case-studies/additive-manufacture-of-aluminium-alloy-components-using-the-cold-metal-transfer-cmt-process-590/](#).

- [42] Xie, M., 1992, "Quality Assurance and Control for Robotic GMA Welding," PhD, Lund University, Sweden.
- [43] C.G. Pickin, S. W. W., M. Lunt, 2011, "Characterisation of the cold metal transfer (CMT) process and its application for low dilution cladding," *Journal of Materials Processing Technology*, 211(3), p. 15.
- [44] Ding, D., Pan, Z., Cuiuri, D., and Li, H., 2014, "A tool-path generation strategy for wire and arc additive manufacturing," *The International Journal of Advanced Manufacturing Technology*, 73(1), pp. 173-183.
- [45] Ding, D., Pan, Z., Cuiuri, D., and Li, H., 2015, "A practical path planning methodology for wire and arc additive manufacturing of thin-walled structures," *Robotics and Computer-Integrated Manufacturing*, 34, pp. 8-19.
- [46] Ding, D., Pan, Z., Cuiuri, D., Li, H., and Larkin, N., 2016, "Adaptive Path Planning For Wire-Feed Additive Manufacturing Using Medial Axis Transformation," *Journal of Cleaner Production*, 133, pp. 942-952.
- [47] ASTM, 2014, "F3122-14 Standard Guide for Evaluating Mechanical Properties of Metal Materials Made via Additive Manufacturing Processes," West Conshohocken, PA.
- [48] ASTM, 2016, "E8-Standard Test Methods for Tension Testing of Metallic Materials."
- [49] ASTM, 2017, "E18-16 - Standard Test Methods for Rockwell Hardness of Metallic Materials."

- [50] ASTM, 2013, "F2971-13 Standard Practice for Reporting Data for Test Specimens Prepared by Additive Manufacturing," West Conshohocken, PA.
- [51] ASTM, 2015, "A802-95 Standard Practice for Steel Castings, Surface Acceptance Standards, Visual Examination," West Conshohocken, PA.
- [52] Fronius, "MIG Welding Equipment: Operations Guide," p. 92.
- [53] R. I. Stephens, A. F., R. R. Stephens, H. O. Fuchs, 2001, Metal Fatigue in Engineering Wiley Inter-Science Canada.
- [54] International, A. S. f. M., 1985, "ASM Handbook - Volume 9: Metallography and Microstructures,"
- [55] Rati Saluja, K. M. M., 2015, "Formation, Quantification and Significance of Delta Ferrite for 300 Series Stainless Steel Weldments," International Journal of Engineering Technology, Management and Applied Sciences, 3, p. 14.

Appendix I: Data Results

Repeatability Study:

Sample No.	Width in	Thickness in	Yield Stress ksi	Ultimate Tensile Strength ksi	Modulus of Elasticity ksi	Hardness, Rockwell B						
						Top 1	Top 2	Avg. Top	Bottom 1	Bottom 2	Avg. Bottom	Average
Wall 1	1	0.252	51.80	67.90	6679.36	77.5	77.5	77.5	75.5	76	75.75	76.625
	2	0.253	57.24	67.51	6923.07	76	77	76.5	76	76.5	76.25	76.375
	3	0.253	54.57	67.94	7166.44	74.5	77.5	76	75	77	76	76
	4	0.253	52.91	68.10	6824.11	77.5	76	76.75	77	76.5	76.75	76.75
	5	0.252	52.38	68.23	6981.26	77.5	77.5	77.5	75.5	77	76.25	76.875
	6	0.252	51.12	67.73	6972.85	78	76	77	75	78	76.5	76.75
Wall 2	1	0.253	51.71	67.20	6196.92	77.5	77	77.25	75	77	76	76.625
	2	0.254	53.36	67.48	6989.13	76.5	77	76.75	74.5	75	74.75	75.75
	3	0.254	54.37	67.83	6914.91	76	76	76	74	74	74	75
	4	0.254	53.36	67.92	6947.85	76.5	77.5	77	77	77	77	77
	5	0.254	52.66	67.68	6943.16	76.5	75.5	76	76	77	76.5	76.25
	6	0.253	47.60	67.43	6244.91	76.5	77	76.75	77	76	76.5	76.625
Wall 3	1	0.251	57.05	69.88	885.29	77	77	77	76	76.5	76.25	76.625
	2	0.250	49.44	68.74	968.17	75.5	75.5	75.5	75	76	75.5	75.5
	3	0.251	49.59	68.50	1404.09	75.5	75	75.25	76	75.5	75.75	75.5
	4	0.250	51.20	68.82	1548.98	75.5	75	75.25	77	75.5	76.25	75.75
	5	0.250	50.01	69.94	1383.74	77	75.5	76.25	76	75.5	75.75	76
	6	0.250	51.60	71.23	1178.29	76.5	76	76.25	75	76.75	75.875	76.0625
Wall 4	1	0.252	48.33	69.30	1263.43	74.5	75	74.75	77.5	77.5	77.5	76.125
	2	0.251	50.81	68.28	1553.98	75.5	76.5	76	75.5	75.5	75.5	75.75
	3	0.251	50.68	68.58	1202.00	74.5	75.5	75	75	75	75	75
	4	0.251	50.00	68.65	1332.91	75.5	76	75.75	74.5	76	75.25	75.5
	5	0.250	51.41	69.63	1364.87	74.5	76.5	75.5	75.5	76.5	76	75.75
	6	0.250	51.23	70.49	1337.83	77	77.5	77.25	76	76	76	76.625

Travel Speed Calculations – Steel and Stainless Steel

Steel					
	WFS	95	ipm		
	WFS	2413	mm/min		
Iteration	Geometry	Path Length (mm)	FR (TS) (mm/min)	Wire Deposited (mm)	WFS/TS Ratio
ER70S-6 Weave Geometry Study					
1	Square	319.4	448.9	1717.0	5.4
1	Zig-zag	512.597	720.0	1717.9	3.4
1	Ladder	344.174	483.7	1717.0	5.0
1	Curlicue	350.148	492.1	1717.0	4.9
1	Concave	461.754	648.9	1717.0	3.7
1	Parallel	292	410.4	1717.0	5.9
1	Triangle	570.54	801.8	1717.0	3.0
1	Sine	332.4559	467.2	1717.0	5.2
2	Square	330	464.3	1715.0	5.2
2	Zig-zag	512	720.0	1715.9	3.4
2	Ladder	397	558.6	1715.0	4.3
2	Concave	407	572.6	1715.0	4.2
2	Triangle	476	669.7	1715.0	3.6
3	Square	330	464.3	1715.0	5.2
3	Zig-zag	512	720.0	1715.9	3.4
3	Concave	367	516.4	1715.0	4.7
3	Square	298	419.3	1715.0	5.8
3	Zig-zag	381	536.1	1715.0	4.5
3	Concave	445	626.1	1715.0	3.9
ER308 Weave Geometry Study					
SS1	Mod. Sq	330.2	464.0	1717.0	5.2
SS1	ZZ1	512.6	720.0	1717.9	3.4
SS1	Ladder	397.8	559.1	1717.0	4.3
SS1	Concave	407	572.0	1717.0	4.2
SS1	Parallel	290	407.6	1717.0	5.9
SS1	ZZ2	381.7	536.4	1717.0	4.5
SS2	ZZ_1.25_1	512.6	720.0	1717.9	3.4
SS2	ZZ_1.25_2	397.8	559.1	1717.0	4.3
SS2	Convex_1	401.3	564.0	1717.0	4.3
SS2	Convex_2	407	572.0	1717.0	4.2
SS2	ZZ_1.75_1	381.7	536.4	1717.0	4.5
SS2	ZZ_1.75_2	381.7	536.4	1717.0	4.5
Short Wall Study					
1	ZZ	1513.379	720.0	5071.9	3.4
1	Sq	892.163	424.5	5071.0	5.7
1	Con	1312.235	624.4	5071.0	3.9
Two Wall Print					
	ZZ 1.25	1616	720.0	5415.844444	3.351389
	ZZ 1.75	1175	523.59644	5415.000493	4.608511

Travel Speed Calculations – Aluminum

Aluminum					
	WFS	190	ipm		
	WFS	4826	mm/min		
Iteration	Geometry	Path Length (mm)	FR (TS) (mm/min)	Wire Deposited (mm)	WFS/TS Ratio
Aluminum Weave Geometry Study					
1	Square	319.4	673.70	2288.0	7.2
1	Zig-zag	512.1	1080.00	2288.3	4.5
1	Ladder	344.174	725.95	2288.0	6.6
1	Sine	332.4559	701.24	2288.0	6.9
1	Concave	451	951.28	2288.0	5.1
1	Parallel	292	615.91	2288.0	7.8

ER70S-6: Two Wall Study

	Sample	Yield Stress	Ultimate Tensile Strength	Modulus of Elasticity	Hardness	Reduction of Area	True Fracture Strain
	No.	ksi	ksi	ksi	HRB	%	
Wall 1.25	1	53.84	71.08	694.95	77.75	73.17	1.32
	2	53.28	71.11	702.96	77.50	73.12	1.31
	3	51.96	70.91	586.70	75.75	75.20	1.39
	4	51.22	72.17	618.53	76.00	73.17	1.32
	Average	52.57	71.32	650.79	76.75	73.67	1.33
	SD	1.20	0.58	57.22	1.02	1.02	0.04
Wall 1.75	1	54.51	71.86	623.38	76.50	75.20	1.39
	2	53.83	71.56	611.83	77.50	74.21	1.36
	3	52.16	71.47	706.51	76.50	76.19	1.44
	4	51.98	72.19	577.58	77.25	74.30	1.36
	Average	53.12	71.77	629.83	76.94	74.97	1.39
	SD	1.25	0.33	54.70	0.52	0.93	0.04
Manufacturers Spec		58	70			60	

ER70S-6: Temperature Study

Pause Time	Sample	Orientation	Yield Stress	Ultimate Tensile Strength	Hardness	RA	True Fracture Strain	Toughness
seconds	No.		ksi	ksi	HRB	%		$\int \sigma d\epsilon$
30	1	Longitudinal	48.89	68.99	71	73.07	1.31	257.71
	2	Longitudinal	49.56	68.87	69.5			253.43
	3	Longitudinal	49.45	69.19	66			252.78
	4	Longitudinal	49.89	70.22	74.5	75.10	1.39	258.34
90	1	Longitudinal	52.58	69.83	75	74.00	1.35	250.52
	2	Longitudinal	50.07	70.03	75.5			438.88
	3	Longitudinal	52.11	70.38	76			254.23
	4	Longitudinal	46.88	69.41	76.5	76.00	1.43	238.69
	1	Transverse	55.11	70.82	77.75	73.28	1.32	256.02
	2	Transverse	50.44	69.73	75.75			232.90
	3	Transverse	49.98	70.04	77			441.78
	4	Transverse	50.66	70.19	75.25	74.41	1.36	239.88
120	1	Longitudinal	50.62	70.21	73.5	72.47	1.29	249.80
	2	Longitudinal	49.88	70.26	75.5			251.21
	3	Longitudinal	49.30	70.15	73.5			253.07
	4	Longitudinal	50.21	71.41	74.5	74.51	1.37	256.61
180	1	Longitudinal	52.21	70.41	75.5	74.70	1.37	252.03
	2	Longitudinal	50.65	70.43	76.5			244.83
	3	Longitudinal	51.29	70.72	77			249.20
	4	Longitudinal	51.34	71.79	78	75.20	1.39	250.33

ER308: Temperature Study

	Sample	Width	Thickness	Ao	Ao	Fracture Width	Fracture Thickness	Af	Hardness
	No.	in	in	in ²	mm ²	mm	mm	mm ²	HRB
P30	1	0.245	0.252	0.062	39.832	4.25	4.55	19.338	82.5
	2	0.245	0.252	0.062	39.832	4.35	5.35	23.273	84.5
	3	0.245	0.252	0.062	39.832	4.15	5.05	20.958	82
	4	0.245	0.252	0.062	39.832	4.25	4.15	17.638	85.25
P90	1	0.245	0.255	0.062	40.306	5.15	3.80	19.570	86
	2	0.245	0.255	0.062	40.306	4.80	3.30	15.840	84.5
	3	0.245	0.255	0.062	40.306	4.70	4.00	18.800	85
	4	0.245	0.256	0.063	40.464	4.60	4.60	21.160	85.5
P120	1	0.245	0.253	0.062	39.990	4.20	4.90	20.580	84
	2	0.245	0.253	0.062	39.990	4.30	4.70	20.210	85.5
	3	0.245	0.253	0.062	39.911	4.00	4.40	17.600	83
	4	0.245	0.252	0.062	39.753	4.15	4.10	17.015	84.5
P180	1	0.245	0.248	0.061	39.121	4.40	4.15	18.260	85.5
	2	0.245	0.248	0.061	39.121	4.50	4.20	18.900	84
	3	0.245	0.248	0.061	39.121	4.20	4.60	19.320	85
	4	0.245	0.249	0.061	39.279	4.40	4.40	19.360	84.5

	Sample	Yield Stress	Ultimate Tensile Strength	Modulus of Elasticity	RA	True Fracture Strain	Toughness
	No.	ksi	ksi	ksi	%		$\int \sigma d\epsilon$
P30	1	50.90	85.74	2417.92	51.45	0.72	400.54
	2	49.85	85.16	2593.21	41.57	0.54	438.09
	3	49.46	84.35	2184.15	47.39	0.64	416.29
	4	50.11	88.78	2210.45	55.72	0.81	415.64
P90	1	50.45	86.80	2158.85	51.45	0.72	546.40
	2	49.68	85.57	2148.22	60.70	0.93	485.99
	3	50.66	85.87	2226.98	53.36	0.76	398.44
	4	51.32	88.90	2277.87	47.71	0.65	396.20
P120	1	51.80	87.00	2271.35	48.54	0.66	473.58
	2	52.02	85.53	2292.17	49.46	0.68	394.44
	3	50.59	85.93	2217.02	55.90	0.82	421.24
	4	50.43	88.50	2228.56	57.20	0.85	397.66
P180	1	52.16	86.69	2296.12	53.32	0.76	406.78
	2	52.47	86.46	2313.26	51.69	0.73	433.18
	3	50.18	85.26	2216.75	50.61	0.71	427.24
	4	50.53	88.03	2219.51	50.71	0.71	396.26
Manufacturers Spec		61	90		60		

ER308: Long Wall

	Sample	Width	Thickness	Ao	Ao	Fracture Width	Fracture Thickness	Af	Hardness	
	No.	in	in	in ²	mm ²	mm	mm	mm ²	Top, Left	Bottom, Right
Transverse	1	0.250	0.251	0.063	40.484	4.00	3.25	13.000	85.5	86
	2	0.250	0.252	0.063	40.645	4.25	3.75	15.938	87.5	88
	3	0.250	0.253	0.063	40.726	4.05	3.50	14.175	86.5	89
	4	0.250	0.253	0.063	40.806	4.10	3.80	15.580	88.5	85.5
	5	0.250	0.254	0.063	40.887	3.85	3.75	14.438	88	86.5
	6	0.250	0.254	0.064	40.968	4.15	3.65	15.148	87	87.5
Longitudinal	1	0.250	0.254	0.063	40.927	4.40	4.40	19.360	87.5	87
	2	0.250	0.254	0.064	41.008	4.65	4.40	20.460	87.5	86
	3	0.250	0.255	0.064	41.048	4.25	4.15	17.638	87.5	86.5
	4	0.250	0.255	0.064	41.048	4.25	4.20	17.850	86.5	86

	Sample	Yield Stress	Ultimate Tensile Strength	Modulus of Elasticity	RA	True Fracture Strain	Toughness
	No.	ksi	ksi	ksi	%		$\int \sigma d\epsilon$
Transverse	1	45.66	79.76	1987.37	67.89	1.14	434.41
	2	48.64	82.34	2214.73	60.79	0.94	423.05
	3	50.79	83.23	2304.85	65.19	1.06	404.04
	4	51.36	83.65	2334.09	61.82	0.96	400.57
	5	51.31	83.18	2325.85	64.69	1.04	427.07
	6	51.26	83.44	2342.49	63.03	0.99	467.51
Longitudinal	1	54.15	89.78	2476.44	52.70	0.75	453.62
	2	53.79	89.26	2456.66	50.11	0.70	412.06
	3	53.34	88.95	2443.54	57.03	0.84	385.67
	4	52.31	89.86	2372.21	56.51	0.83	422.55

Aluminum tensile data

Sample No.	Initial		Final		Yield Stress		Ultimate Tensile Strength		Modulus of Elasticity		RA %	True Fracture Strain	Toughness $\int \sigma d\epsilon$
	Width in.	Thickness in.	Width mm	Thickness mm	MPa	psi	MPa	psi	MPa	ksi			
Transverse	0.250	0.128	5.46	2.73	93.60	13575.70	167.37	24275.01	10359.20	1502.48	27.80	0.3257	45.7
	0.250	0.127	5.46	2.80	104.99	15227.54	168.11	24382.05	25102.00	3640.74	25.37	0.2926	42.2
	0.250	0.126	5.30	2.70	93.81	13605.72	167.70	24322.44	14504.00	2103.63	29.59	0.3508	44.4
Longitudinal	0.250	0.122	5.40	2.75	102.68	14892.36	163.84	23763.17	25278.90	3666.40	24.53	0.2815	49.9
	0.250	0.120	5.45	2.50	98.04	14219.53	166.53	24153.03	34772.00	5043.26	29.60	0.3510	51.9
	0.250	0.121	5.45	2.70	121.23	17582.52	174.68	25335.67	35253.00	5113.02	24.60	0.2824	39.9
	0.251	0.137	5.50	2.80	107.74	15626.10	171.64	24894.03	28021.00	4064.11	30.58	0.3651	45.9
	0.250	0.120	5.35	2.50	114.15	16555.80	166.69	24176.67	33290.00	4828.32	30.90	0.3696	51.8

Appendix II: Data Sheets

Data Sheet: ER70S-6 Temperature Study Walls P30 and P120

Conyers Coupled

WAAM Print/Sample Info Sheet

Bigger ↓

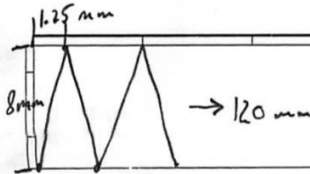
Date: 9/18/2017
Test Code Name: Pause Test

Geometry Printed: Wall
Data Save Location: ~~Agama Mechanical Properties Study~~ → Temperature.

Weld Parameters

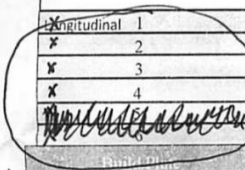
Material	Gas	Synergic Line	WFS (ipm)	ALC (%)	Dyn. Cor. (%)	BurnBack (s)	Crater fill
ER70S-6	90/10		95	15%	-1.2%	-0.03	0.75 @ 45%
ER308L	98/2						
ER4043	100 Ar						

Geometry Parameters



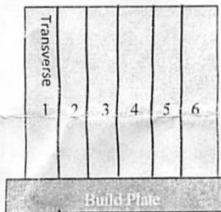
FR ↓ from 720 h	60 mm/min for 0.5m
FR	720 mm/min
Layer Time	110 sec

Post Weld Data



Wall ID	As Printed			Material Removed		% Yield	Layers	Tan Thk
	Height	Length	Width	Side 1	Side 2			
P30	~80	~122.8	13.25	0.045"	0.0325"	85%	29	1.12
P120	89.2	~123	12.4	-0.035"	-0.025"	87.7%	31	2.07

measure after cut on bandsaw



Wall ID	Sample #	DB Width	DB Thickness	Hardness	Surface
P30	1	250	251	71	✓
"	2	250	251	69.5	Scratches
"	3	250	251	66	lean scratches
"	4	250	254	74.5	Big scratch/dent
P120	1	250	255	73.5	✓
"	2	250	255	75.5	✓
"	3	250	255	73.5	✓
"	4	250	255	74.5	✓

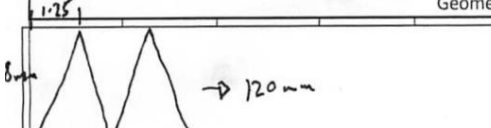
Give room to draw on, ~~blank~~ blank square. have place to draw surface defects.
Location of hardness test

Bigger add sandblasted grit col.

Data Sheet: ER70S-6 Temperature Study Walls P90 and P180

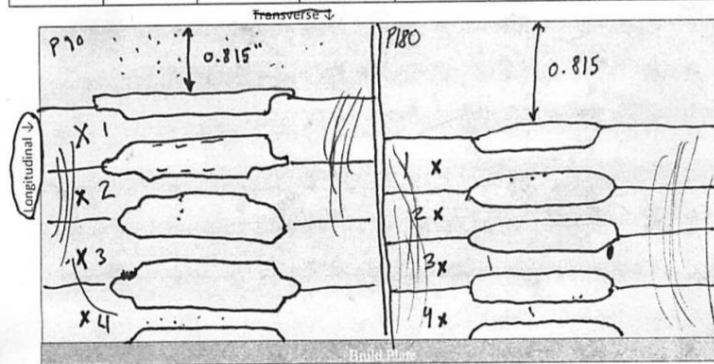
WAAM Print/Sample Info Sheet	
Name: CJC	Geometry Printed: WALL
Date: 9-22-17	Study: Mech. Properties → Temperature Study
Test Code Name: P90 / P180	Data Save Location:

Weld Parameters								
Material	Gas	Synergic Line	WFS (ipm)	ALC (%)	Dyn. Cor. (%)	Burn Back (s)	Crater fill	Notes
ER70S-6	90/10	CMT 1362	95	15	-1.2	-0.03	0.7s	
ER308L	98/2							
ER4043	100 Ar							

Geometry Parameters	
	FR/TS (mm/min) 720
	FR Reduction? 60 mm/min for 0.5mm
	Layer Time 110 - 111 Sec.
	Notes

Post Weld Data									
Wall ID	As Printed			Layers Printed	Total Time	Material Removed		% Yield	Notes
	Height	Length	Width			Side 1	Side 2		
P90	94-95	123.2	12.8	30	1:45	-0.025 - 50% -0.035 - bottom	-0.034		0.432 / 18mm ← thickness of weld
P180	95	123.5	12.3	30	2:28	-0.023 - top -0.033 - bot. X	-0.025 mm		0.420 / 10.7mm

Post Machining Data							
Wall ID	Sample #	Orientation	Dogbone		Hardness (HRB)	Sanding Grit	Surface Defects?
			Width	Thickness			
P90	1	Longitud.	250	250	75	600	Small mill defect on inside neck
"	2	"	250	250	75.5	"	"
"	3	"	250	250	76	"	Added the grip region with ball marker
"	4	"	250	250	76.5	"	3-4 indent on back from clasp reverse?
P180	1	"	252	250	75.5	"	Small indent on inside
"	2	"	252	250	76.5	"	
"	3	"	252	250	77	"	Lightest scratch, by marker in grip region
"	4	"	252	250	78	"	Light scratch, small indent on inside



Data Sheet: ER70S-6 Temperature Study Wall P90_T

WAAM Print/Sample Info Sheet	
Name: <u>Couyers Couland</u>	Geometry Printed: <u>Wall - Wene</u>
Date: <u>10/2/27</u>	Study: <u>Pause Study</u>
Test Code Name: <u>P90_T / Pause Study</u>	Data Save Location: <u>Mech weld Print -> Temp -> P90_T</u>

Weld Parameters								
Material	Gas	Synergic Line	WFS (ipm)	ALC (%)	Dyn. Cor. (%)	Burn Back (s)	Crater fill	Notes
<u>ER70S-6</u>	<u>90/10</u>	<u>CMT 1362</u>	<u>95</u>	<u>15%</u>	<u>-1.2 Z</u>	<u>-0.05</u>	<u>0.75</u>	
ER308L	98/2						<u>0.407</u>	
ER4043	100 Ar						<u>0.60%</u>	

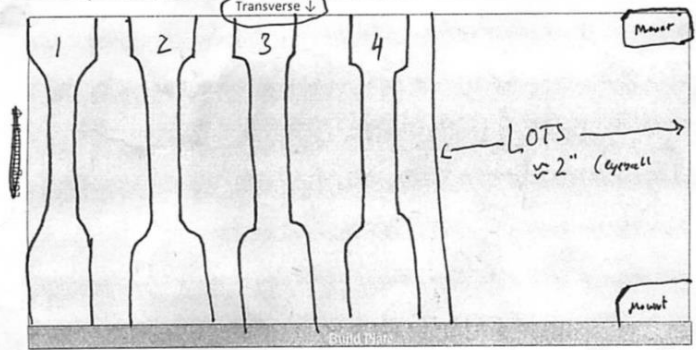
Geometry Parameters	
	FR/TS (mm/min) <u>720 mm/min</u> FR Reduction? <u>60mm for</u> Layer Time <u>110.8 sec</u> Notes: <u>Start time 11:42 AM, @ Seam 33 . JT 1:45</u>

Post Weld Data									
Wall ID	As Printed (mm)			Layers Printed	Total Time	Material Removed		% Yield	Notes
	Height (+0)	Length	Width			Side 1	Side 2		
<u>P90_T</u>	<u>106</u>	<u>123</u>	<u>13</u>	<u>35</u>	<u>2:00</u>	<u>-0.025 for 1st side</u> <u>-0.03 - TOTAL</u>	<u>-0.03 - PT 1</u> <u>-0.04 - TOT</u>	<u>10.8 / 13 = 83%</u>	<u>1.2 kg Defect (as printed)</u> <u>Thick areas = 0.6 kg / 4r</u> <u>0.425" / 10.8 mm</u>

→ To get spot where crater back occurred close

Post Machining Data								
Wall ID	Sample #	Orientation	Dogbone		Hardness (HRB)		Sanding Grit	Surface Defects?
			Width	Thickness	Top	Bottom		
<u>P90_T</u>	<u>1</u>	<u>Trans</u>	<u>250</u>	<u>253</u>	<u>77.5</u>	<u>78</u>	<u>—</u>	<u>as machined</u>
"	<u>2</u>	"	<u>256</u>	<u>254</u>	<u>74</u>	<u>77.5</u>	<u>—</u>	"
"	<u>3</u>	"	<u>250</u>	<u>254</u>	<u>76.5</u>	<u>77.5</u>	<u>—</u>	"
"	<u>4</u>	"	<u>256</u>	<u>254</u>	<u>74</u>	<u>76.5</u>	<u>—</u>	"

- Hardness test was done last time.



Sample #	Elongation to Failure
<u>P90_T-1</u>	<u>0.442</u>
<u>2</u>	<u>0.433</u>
<u>3</u>	<u>0.485</u>
<u>4</u>	<u>0.44</u>

Data Sheet: ER308 Two Wall Study Walls 1.25 and 1.75-mm

WAAM Print/Sample Info Sheet	
Name: <i>Coupons</i>	Geometry Printed: <i>Zig Zag Walls</i>
Date: <i>10/11/2017</i>	Study: <i>2 Wall Study</i>
Test Code Name: <i>2WS-SS</i>	Data Save Location: <i>Stanley Steel -> Mechanical Properties -></i>

Weld Parameters								
Material	Gas	Synergic Line	WFS (ipm)	ALC (%)	Dyn. Cor. (%)	Burn Back (s)	Crater fill	Notes
ER70S-6	90/10	<i>Co928</i>	<i>95</i>	<i>15%</i>	<i>-1.2%</i>	<i>-0.05</i>	<i>0.75</i>	<i>50%</i>
ER308L	<i>98/2</i>							
ER4043	100 Ar							

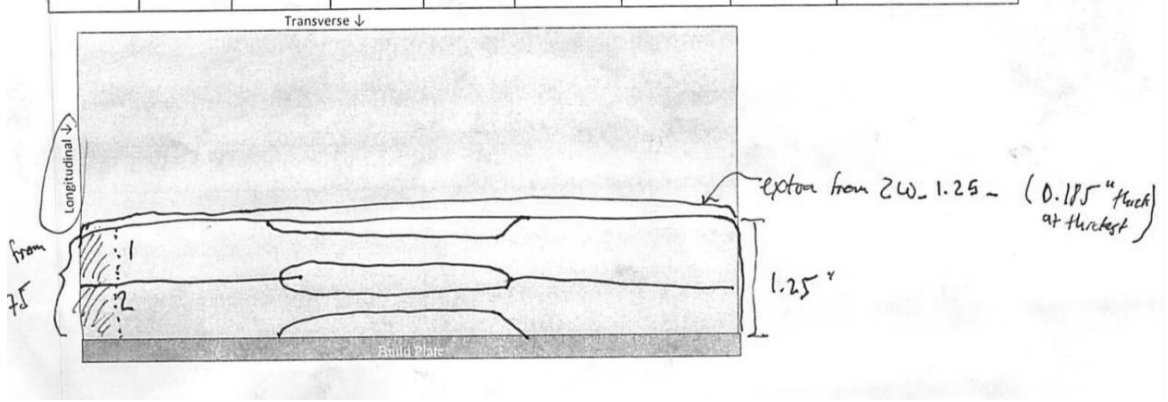
*Hotstart added on layer 10/11
0.2 sec @ 140% w/ 0.25 stroke
removed next layer*

Geometry Parameters	
1.25	1.75
FR/TS (mm/min) <i>750 mm/min</i>	<i>535 mm/min</i>
FR Reduction? <i>Co928/mm for 0.5 mm (both)</i>	
Layer Time <i>108 sec.</i>	<i>94.2 sec.</i>
Notes <i>Build plate wt: 655g -> after 1.265 kg = 0.61 kg/hr</i>	
<i>Start time 12:40</i>	

Post Weld Data									
Wall ID	As Printed			Layers Printed	Total Time	Material Removed		% Yield	Notes
	Height	Length	Width			Side 1	Side 2		
<i>2W-1.25</i>	<i>41.7/39.25</i>	<i>124</i>	<i>9.8-10.1</i>	<i>11.5</i>	<i>1:02</i>	<i>-0.035</i>	<i>-0.035</i>		<i>Really got super hot vehicle machining, may be effect on metall. properties.</i>
<i>2W-1.75</i>	<i>34</i>	<i>123</i>	<i>9.9-9.6</i>	<i>10</i>	<i>11</i>	<i>-0.035</i>	<i>-0.030</i>		<i>Both prob. have high residual stresses from machining.</i>

Post Machining Data								
Wall ID	Sample #	Orientation	Dogbone		Hardness (HRB)		Sanding Grit	Surface Defects?
			Width	Thickness				
<i>2W-1.25-1</i>	<i>long.</i>	<i>25.5</i>	<i>2.59</i>	<i>89</i>	<i>83.5</i>	<i>120</i>	<i>slump</i>	
<i>2W-1.25-2</i>	<i>"</i>	<i>25.4</i>	<i>2.55</i>	<i>90.5</i>	<i>92.5</i>	<i>"</i>	<i>pretty rough</i>	
<i>2W-1.75-1</i>	<i>"</i>	<i>25.4</i>	<i>2.55</i>	<i>90.5</i>	<i>90.5</i>	<i>120</i>	<i>Possible voids in area</i>	
<i>2W-1.75-2</i>	<i>"</i>	<i>25.4</i>	<i>2.57</i>	<i>92</i>	<i>91.5</i>	<i>"</i>	<i>pretty rough</i>	

*got entire extra
piece from top*



Data Sheet: ER308 Temperature Study Walls P30, P90, P120, and P180

WAAM Print/Sample Info Sheet									
Name: <u>Coupled Couplant</u>					Geometry Printed: <u>Wall</u>				
Date: <u>10/17/17</u>					Study: <u>Temperature Study</u>				
Test Code Name: <u>ER308 P# SS</u>					Data Save Location: <u>SS → Mech Prop → Temp Study</u>				
Weld Parameters									
Material	Gas	Synergic Line	WFS (ipm)	ALC (%)	Dyn. Cor. (%)	Burn Back (s)	Crater fill	Notes	
ER705-6	90/10	CMT 928	95	15	-1.2	-0.05	0.7 sec	changed to 0.5 sec on P90-SS	
ER308	98/2							50%	
ER4043	100 Ar								
Geometry Parameters									
FR/TS (mm/min)					750 → (10 from usual 720)				
FR Reduction?					↓ 600 mm/min for 0.5 mm				
Layer Time					109 seconds				
Notes: Build Plate 515g, Start time 1:52 PM									
Build Plate 2 585g, Start time 7:45 AM									
Post Weld Data									
Wall ID	Height	As Printed		Layers Printed	Total Time	Material Removed		% Yield	Notes
		Length	Width			for Side 1 (in)	Side 2 (in)		
P30-SS	83	126	121.75	24	1:00	-0.19	-0.035	-0.040	WT approx 1.235 kg
P90-SS	83.7	125.7	122.1	24	1:23		-0.035	-0.032	1.300 kg
P120-SS	83.7	125.2	120.9	24	1:34		-0.034	-0.030	
P180-SS	84.2	125.3	122.2	24	1:56		-0.035	-0.035	
Post Machining Data									
Wall ID	Sample #	Orientation	Dogbone (in x 10 ⁻³)		Hardness (HRa)	Sanding Grit	Surface Defects		Notes
			Width	Thickness			Fracture	Area (mm)	
P30-SS	1	Long.	245	252	82.5	120 (-)	4.25 x 4.55	0.225 - P30	
"	2	"	245	252	84.5	"	4.35 x 5.35		
"	3	"	245	252	82	"	4.15 x 5.05		
"	4	"	245	252	85.25	"	4.25 x 4.15		
P90-SS	1	"	245	255	86	"	5.15 x 3.8	0.216 - P90	
"	2	"	245	255	84.5	"	4.8 x 3.3	→ fracture surface	
"	3	"	245	255	85	"	4.7 x 3.8 / 4.2		
"	4	"	245	256	85.5	"	4.8 x 4.6		
P120-SS	1	"	246	253	84	"	4.15/4.3 x 4.8/5.1	0.295 - P120	
"	2	"	245	253	85.5	"	4.5/4.5 x 4.6/4.8	→ run before pro. 4	
"	3	"	245	252.5	83	"	4.0 x 4.4	→ broke up or	
"	4	"	245	251.5	84.5	"	4.15 x 4.2 / 4.05	→ normal	
P180-SS	1	transverse	245	247.5	85.5	"	4.9 x 4.2 / 4.1	0.310 - P180	
"	2	"	245	247.5	84	"	4.5 x 4.2		
"	3	"	245	247.5	85	"	4.05 / 4.5 x 4.6		
"	4	"	245	248.5	84.5	"	4.4 x 4.4		
EXTRA									

Data Sheet: ER308 Temperature Study Walls Long Wall

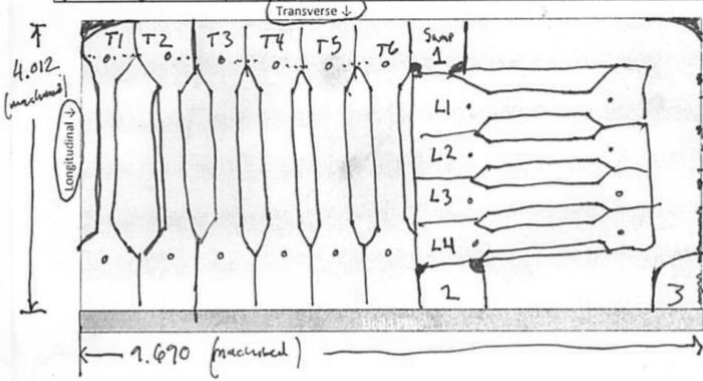
WAAM Print/Sample Info Sheet	
Name: <u>Conyers Coupland</u>	Geometry Printed: <u>Wall</u>
Date: <u>10/20/2017</u>	Study: <u>Stainless Steel Long Wall</u>
Test Code Name: <u>SSLW</u>	Data Save Location: <u>SS -> Mechanical Properties -> Long Wall</u>

Weld Parameters							
Material	Gas	Synergic Line	WFS (ipm)	ALC (%)	Dyn. Cor. (%)	Burn Back (s)	Crater fill
ER70S-6 (ER308)	90/10 (98/2)	<u>CMT928</u>	<u>95</u>	<u>15</u>	<u>-1.2</u>	<u>-0.05</u>	<u>0.75 @ 50%</u>
ER4043	100 Ar						

Geometry Parameters	
FR/TS (mm/min)	<u>750</u>
FR Reduction?	<u>60 for 0.5 mm</u>
Layer Time	<u>225.1 sec. -> 71.4% of time its printing</u>
Notes	<u>Build Plate wt before 1.055 kg. Start Time 3:56 PM</u> <u>After 2.935 kg = 1.88 kg ↓ End Time 6:38 PM</u>

Post Weld Data									
Wall ID	Height	As Printed		Layers Printed	Total Time	Material Removed		% Yield	Deposition Rate
		Length (in)	Width			Side 1	Side 2		
<u>SS_LW</u>	<u>106.5</u>	<u>10.02" (in)</u> <u>2.58" (mm)</u>	<u>10 ± 0.1</u>	<u>30</u>	<u>2:40 min</u> <u>(160 min)</u>	<u>-0.040</u>	<u>-0.040</u>		<u>0.705 kg/hr.</u>
-			<u>at Top 9.7 → 10</u>						
-			<u>at Bottom 9.8 → 9.5</u>						

Post Machining Data								
Wall ID	Sample #	Orientation	Dogbone		Hardness (HRB)		Sanding Grit	Surface Defects?
			Width	Thickness	Top/Left	Bot/Right		
<u>LW</u>	<u>T1</u>	<u>Transverse</u>	<u>250</u>	<u>.251</u>	<u>85.5</u>	<u>86</u>	<u>120</u>	
	<u>T2</u>			<u>.252</u>	<u>87.5</u>	<u>88</u>		
	<u>T3</u>			<u>.2525</u>	<u>86.5</u>	<u>89</u>		
	<u>T4</u>			<u>.253</u>	<u>88.5</u>	<u>88.5</u>		<u>Burr on during machining</u>
	<u>T5</u>			<u>.2535</u>	<u>88</u>	<u>86.5</u>		
	<u>T6</u>			<u>.254</u>	<u>87</u>	<u>87.5</u>		
	<u>L1</u>	<u>Long.</u>		<u>.25375</u>	<u>87.5</u>	<u>87</u>		
	<u>L2</u>			<u>.25425</u>	<u>87.5</u>	<u>86</u>		
	<u>L3</u>			<u>.2545</u>	<u>87.5</u>	<u>86.5</u>		
	<u>L4</u>			<u>.2545</u>	<u>86.5</u>	<u>86</u>		



Goals of this print is to get transverse dogbones and to see if size effects properties.

look at this for skull walls too.

when machining the top, after bottom two high points, about 0.02"

increased wall size = greater magnitude of residual stresses. Want to machine longitudinal & Transverse samples, and also have key areas to monitor & polish for microstructure.

Roughed to 9.7" wide (246.4 mm)

↳ Clean up one side, left the other machined but still soft of enough to see the layers on microscope

Data Sheet: ER4043 Big Box 2

WAAM Print/Sample Info Sheet	
Name: <u>Comers</u>	Geometry Printed: <u>Box</u>
Date: <u>10/28/17</u>	Study: <u>AL MECH Prop</u>
Test Code Name: <u>AL-BB</u>	Data Save Location: <u>→ BB Box</u>

Weld Parameters							
Material	Gas	Synergic Line	WFS (ipm)	WFS ALC (%)	Dyn. Cor. (%)	Burn Back (s)	Notes
ER70S-6	90/10	1368 Adv	200/1	0	-1	-0.5	Hot Start
ER308L	98/2		175/2				0.26 @ 140%
ER4043	100 Ar		165/4				0.15 slope

Geometry Parameters	
FR/TS (mm/min)	<u>600 mm/min ↓ 540 (5) ↓ 509 (14)</u>
FR Reduction?	<u>↑ 700 mm/min @ corners</u>
Layer Time	
Notes	<u>Build plate 23.152/in. 0.640 kg deposited - 0.97 kg/hr</u>

Post Weld Data									
Wall ID	As Printed		Dog	Layers Printed	Total Time	Material Removed		% Yield	Notes
	Height	Length				Side 1	Side 2		
AL-BB-2	101.5	overall	5.5	40	39:34s				
	102.5		8.4"			overall 2.165"			

Post Machining Data								
Wall ID	Sample #	Orientation	Dogbone		Hardness (HRB)	Sanding Grit	Surface Defects?	
			Width	Thickness				
BB-2	1	T	255	0.090	68	67.5	YES	
	2	T		0.094	68			
	3	T		.096	70			
	4	T		.098	68.5			
	5	T	250	0.128	68	67	120 150	5.46 2.75
	6	T		0.127	69.5	67.5		5.46 2.80
	7	T		0.126				5.30 2.70
	8	L	0.250	0.122				5.4 2.75
	9	L		0.120				5.45 2.5
	10	L		.121				5.45 2.7
	11	L		0.137	68			5.5 2.7
	12	L		2.56	0.120			5.35 2.50

Appendix III: Mach3 M-Codes

M111 – Welding Start

```
ActivateSignal(OUTPUT1) ; Activate signal, X2:4 on ROB 5000
Do Until IsActive(Input1) ; Until Arc Stable signal received
DoOEMButton(1001) ;Feedhold
Sleep(50) ;Pause for 50 ms
Loop ; Loop
DoOEMButton(1000) ;Cycle Start to resume program
```

M110 – Welding Stop

```
DeactivateSignal(OUTPUT1) ; Deactivate signal, X2:4 on ROB 5000
```

M121 – Quick Stop (Active Low)

```
ActivateSignal(OUTPUT2) ; Activate signal, X2:5 on ROB 5000
```

M120 – Robot Ready

```
DeactivateSignal(OUTPUT2) ; Deactivate signal, X2:5 on ROB 5000
```

M131 – Gas Test Start

```
ActivateSignal(OUTPUT3) ; Activate signal, X2:7 on ROB 5000
```

M130 – Gas Test Stop

```
DeactivateSignal(OUTPUT3) ; Deactivate signal, X2:7 on ROB 5000
```

M141 – Touch Sensing

```
ActivateSignal(OUTPUT4) ; Activate signal, X8:7 on ROB 5000
CurrentFeed = GetOEMDRO(818) ; Get current feed rate of program
If Not IsActive(Input1) Then ; If arc stable is not active (not touching)
Code("G31 Z0 F100") ; G-code probing cycle, feed rate 100
mm/min
```

```

While IsMoving()           ; While probing, do nothing
Wend                       ; While loop end

ZProbePos = GetVar(2002)   ; Probed Z value where probe touched
Code("G0 Z" &ZProbePos)   ; Move z-axis to that position, rapid
While IsMoving()           ; While moving, do nothing
Wend                       ; While loop end

Code("G92 Z0")             ; Zero the z-axis at the probed position
Code("G4 P0.25")           ; Pause for 0.25 seconds
Code("F" &CurrentFeed)     ; Reset the feed rate to the prior feed rate
Code("G1 Z3")              ; Move the z-axis up 3 mm
End If                     ; End the probing loop

DeactivateSignal(OUTPUT4) ; Deactivate signal, X8:7 on ROB 5000

```

M151 – Wire Retract Start

```

ActivateSignal(OUTPUT5)   ; Activate signal, X14:6 on ROB 5000

```

M150 – Wire Retract Stop

```

DeactivateSignal(OUTPUT5) ; Deactivate signal, X14:6 on ROB 5000

```

M161 – Source Error Reset

```

ActivateSignal(OUTPUT6)   ; Activate signal, X8:5 on ROB 5000
Sleep(1000)               ; Pause for 1 second
DeactivateSignal(OUTPUT6) ; Deactivate signal to reset welder

```

M171 – Blow Through

ActivateSignal(OUTPUT7) ; Activate signal, X14:5 on ROB 5000
Sleep(5000) ; Pause for 5 seconds
DeactivateSignal(OUTPUT7) ; Deactivate signal, X14:5 on ROB 5000

M181 – Wire Feed Start

ActivateSignal(OUTPUT8) ; Activate signal, X2:11 on ROB 5000

M180 – Wire Feed Stop

DeactivateSignal(OUTPUT8) ; Deactivate signal, X2:11 on ROB 5000

Appendix IV: Statistical Analysis

Repeatability Study – Hardness Wall 1 Top vs. Wall 2 Top

Two-Sample T-Test and CI: W1_T, W2_T

Method

μ_1 : mean of W1_T

μ_2 : mean of W2_T

Difference: $\mu_1 - \mu_2$

Equal variances are assumed for this analysis.

Descriptive Statistics

Sample	N	Mean	StDev	SE Mean
W1_T	6	76.875	0.586	0.24
W2_T	6	76.625	0.518	0.21

Estimation for Difference

Difference	Pooled StDev	95% CI for Difference
0.250	0.553	(-0.462, 0.962)

Test

Null hypothesis $H_0: \mu_1 - \mu_2 = 0$

Alternative hypothesis $H_1: \mu_1 - \mu_2 \neq 0$

T-Value	DF	P-Value
0.78	10	0.452

Repeatability Study – Hardness Wall 1 Bottom vs. Wall 2 Bottom

Two-Sample T-Test and CI: W1_B, W2_B

Method

μ_1 : mean of W1_B

μ_2 : mean of W2_B

Difference: $\mu_1 - \mu_2$

Equal variances are assumed for this analysis.

Descriptive Statistics

Sample	N	Mean	StDev	SE Mean
W1_B	6	76.250	0.354	0.14
W2_B	6	75.79	1.17	0.48

Estimation for Difference

Difference	Pooled StDev	95% CI for Difference
0.458	0.862	(-0.650, 1.567)

Test

Null hypothesis $H_0: \mu_1 - \mu_2 = 0$

Alternative hypothesis $H_1: \mu_1 - \mu_2 \neq 0$

T-Value	DF	P-Value
0.92	10	0.379

Repeatability Study – Hardness Wall 3 Left vs. Wall 4 Left

Two-Sample T-Test and CI: W3_L, W4_L

Method

μ_1 : mean of W3_L
 μ_2 : mean of W4_L
 Difference: $\mu_1 - \mu_2$

Equal variances are assumed for this analysis.

Descriptive Statistics

Sample	N	Mean	StDev	SE Mean
W3_L	6	75.917	0.701	0.29
W4_L	6	75.708	0.886	0.36

Estimation for Difference

Difference	Pooled StDev	95% CI for Difference
0.208	0.799	(-0.820, 1.236)

Test

Null hypothesis $H_0: \mu_1 - \mu_2 = 0$
 Alternative hypothesis $H_1: \mu_1 - \mu_2 \neq 0$

T-Value	DF	P-Value
0.45	10	0.661

Repeatability Study – Hardness Wall 3 Right vs. Wall 4 Right

Two-Sample T-Test and CI: W3_R, W4_R

Method

μ_1 : mean of W3_R
 μ_2 : mean of W4_R
 Difference: $\mu_1 - \mu_2$

Equal variances are assumed for this analysis.

Descriptive Statistics

Sample	N	Mean	StDev	SE Mean
W3_R	6	75.896	0.300	0.12
W4_R	6	75.875	0.891	0.36

Estimation for Difference

Difference	Pooled StDev	95% CI for Difference
0.021	0.665	(-0.834, 0.876)

Test

Null hypothesis $H_0: \mu_1 - \mu_2 = 0$
 Alternative hypothesis $H_1: \mu_1 - \mu_2 \neq 0$

T-Value	DF	P-Value
0.05	10	0.958

Repeatability Study Hardness – Tukey-Kramer Multiple Comparison of Means

```

Tukey multiple comparisons of means
 95% family-wise confidence level

Fit: aov(formula = H.Average ~ wall, data = RepStudy)

$wall
              diff          lwr          upr          p adj
wall 2-wall 1 -0.3541667 -1.2088282 0.50049488 0.6580256
wall 3-wall 1 -0.6562500 -1.5109115 0.19841155 0.1720193
wall 4-wall 1 -0.7708333 -1.6254949 0.08382821 0.0863416
wall 3-wall 2 -0.3020833 -1.1567449 0.55257821 0.7570879
wall 4-wall 2 -0.4166667 -1.2713282 0.43799488 0.5348068
wall 4-wall 3 -0.1145833 -0.9692449 0.74007821 0.9814685

> confint(fm.aov)
              2.5 %          97.5 %
(Intercept) 76.1121057 77.0128943
wallwall 2  -0.9911204  0.2827870
wallwall 3  -1.2932037 -0.0192963
wallwall 4  -1.4077870 -0.1338796
    
```

Repeatability Study – Hardness Power Analysis

Power analysis on hardness test data for estimation of statistical sample size based on hardness averages from repeatability test. Four hardness tests required to be 95% confident results are within one standard deviation of the mean.

Sample Size for Estimation

Method

Parameter	Mean
Distribution	Normal
Standard deviation	0.794 (population value)
Confidence level	95%
Confidence interval	Two-sided

Results

Margin of Error	Sample Size
0.794	4

Repeatability Study – Ultimate Tensile Strength Wall 1 vs. Wall 2

Two-Sample T-Test and CI: UTS_W1, UTS_W2

Method

μ_1 : mean of UTS_W1

μ_2 : mean of UTS_W2

Difference: $\mu_1 - \mu_2$

Equal variances are assumed for this analysis.

Descriptive Statistics

Sample	N	Mean	StDev	SE Mean
UTS_W1	6	67.900	0.257	0.11
UTS_W2	6	67.590	0.269	0.11

Estimation for Difference

Difference	Pooled StDev	95% CI for Difference
0.310	0.263	(-0.028, 0.648)

Test

Null hypothesis $H_0: \mu_1 - \mu_2 = 0$

Alternative hypothesis $H_1: \mu_1 - \mu_2 \neq 0$

T-Value	DF	P-Value
2.04	10	0.068

Repeatability Study – Ultimate Tensile Strength Wall 3 vs. Wall 4

Two-Sample T-Test and CI: UTS_W3, UTS_W4

Method

μ_1 : mean of UTS_W3

μ_2 : mean of UTS_W4

Difference: $\mu_1 - \mu_2$

Equal variances are assumed for this analysis.

Descriptive Statistics

Sample	N	Mean	StDev	SE Mean
UTS_W3	6	69.52	1.04	0.42
UTS_W4	6	69.155	0.822	0.34

Estimation for Difference

Difference	Pooled StDev	95% CI for Difference
0.363	0.936	(-0.840, 1.567)

Test

Null hypothesis $H_0: \mu_1 - \mu_2 = 0$

Alternative hypothesis $H_1: \mu_1 - \mu_2 \neq 0$

T-Value	DF	P-Value
0.67	10	0.516

Repeatability Study – Ultimate Tensile Strength Walls 1 & 2 vs. Walls 3 & 4

Two-Sample T-Test and CI: UTS_W1/2, UTS_W3/4

Method

μ_1 : mean of UTS_W1/2
 μ_2 : mean of UTS_W3/4
 Difference: $\mu_1 - \mu_2$

Equal variances are assumed for this analysis.

Descriptive Statistics

Sample	N	Mean	StDev	SE Mean
UTS_W1/2	12	67.745	0.299	0.086
UTS_W3/4	12	69.336	0.912	0.26

Estimation for Difference

Difference	Pooled StDev	95% CI for Difference
-1.591	0.679	(-2.166, -1.017)

Test

Null hypothesis $H_0: \mu_1 - \mu_2 = 0$
 Alternative hypothesis $H_1: \mu_1 - \mu_2 \neq 0$

T-Value	DF	P-Value
-5.74	22	0.000008879

Repeatability Study UTS – Tukey-Kramer Multiple Comparison of Means

Tukey multiple comparisons of means
 95% family-wise confidence level

Fit: aov(formula = UTS ~ wall, data = RepStudy)

```
$wall
```

	diff	lwr	upr	p adj
wall 2-wall 1	-0.3101842	-1.4103630	0.7899945	0.8585110
wall 3-wall 1	1.6408359	0.5406571	2.7410146	0.0024309
wall 4-wall 1	1.2545926	0.1544139	2.3547714	0.0218700
wall 3-wall 2	1.9510201	0.8508414	3.0511989	0.0004025
wall 4-wall 2	1.5647769	0.4645981	2.6649556	0.0037757
wall 4-wall 3	-0.3862432	-1.4864220	0.7139355	0.7607778

```
> confint(fm.aov)
```

	2.5 %	97.5 %
(Intercept)	67.3203837	68.4799403
wallwall 2	-1.1301146	0.5097461
wallwall 3	0.8209055	2.4607662
wallwall 4	0.4346623	2.0745230

Repeatability Study – Ultimate Tensile Strength Power Analysis

Power analysis on tensile test data for estimation of statistical sample size based on averages from UTS from repeatability test. Four tensile samples required to be 95% confident results are within one standard deviation of the mean.

Sample Size for Estimation

Method

Parameter	Mean
Distribution	Normal
Standard deviation	299 (population value)
Confidence level	95%
Confidence interval	Two-sided

Results

Margin of Error	Sample Size
299	4

Repeatability Study – Tukey-Kramer Multiple Comparison of Means

Tukey multiple comparisons of means
95% family-wise confidence level

Fit: aov(formula = Yield ~ wall, data = Repstudy)

```
$wall
      diff      lwr      upr    p adj
wall 2-wall 1 -1.1614157 -4.801627 2.4787961 0.8085185
wall 3-wall 1 -1.8363956 -5.476607 1.8038162 0.5067433
wall 4-wall 1 -2.9275269 -6.567739 0.7126849 0.1437657
wall 3-wall 2 -0.6749799 -4.315192 2.9652319 0.9535466
wall 4-wall 2 -1.7661112 -5.406323 1.8741006 0.5387354
wall 4-wall 3 -1.0911313 -4.731343 2.5490805 0.8353269
```

```
> confint(fm.aov)
      2.5 %    97.5 %
(Intercept) 51.417299 55.2539774
wallwall 2  -3.874357  1.5515254
wallwall 3  -4.549337  0.8765454
wallwall 4  -5.640468 -0.2145859
```

ER70S-6: Two Wall Study. Yield Stress Wall 1 vs. Yield Stress Wall 2

Two-Sample T-Test and CI: YS-W1, YS-W2

Method

μ_1 : mean of YS-W1
 μ_2 : mean of YS-W2
 Difference: $\mu_1 - \mu_2$

Equal variances are assumed for this analysis.

Descriptive Statistics

Sample	N	Mean	StDev	SE Mean
YS-W1	4	52573	1199	600
YS-W2	4	53119	1247	623

Estimation for Difference

Difference	Pooled StDev	95% CI for Difference
-546	1223	(-2662, 1571)

Test

Null hypothesis $H_0: \mu_1 - \mu_2 = 0$
 Alternative hypothesis $H_1: \mu_1 - \mu_2 \neq 0$

T-Value	DF	P-Value
-0.63	6	0.551

ER70S-6: Two Wall Study. Ultimate tensile strength Wall 1 vs. Wall 2

Two-Sample T-Test and CI: UTS-W1, UTS-W2

Method

μ_1 : mean of UTS-W1
 μ_2 : mean of UTS-W2
 Difference: $\mu_1 - \mu_2$

Equal variances are assumed for this analysis.

Descriptive Statistics

Sample	N	Mean	StDev	SE Mean
UTS-W1	4	71319	577	288
UTS-W2	4	71771	326	163

Estimation for Difference

Difference	Pooled StDev	95% CI for Difference
-452	468	(-1262, 358)

Test

Null hypothesis $H_0: \mu_1 - \mu_2 = 0$
 Alternative hypothesis $H_1: \mu_1 - \mu_2 \neq 0$

T-Value	DF	P-Value
-1.36	6	0.221

ER70S-6: Temperature Study

UTS family-wise comparison of means

```

Tukey multiple comparisons of means
 95% family-wise confidence level

Fit: aov(formula = UTS ~ Pause, data = Tempstudy)

$Pause
      diff      lwr      upr    p adj
P90-P30  597.8800 -611.84164 1807.6016 0.5623819
P120-P30 1188.3675  -21.35414 2398.0891 0.0553258
P180-P30 1521.7000  311.97836 2731.4216 0.0108967
P90_T-P30  876.4633 -333.25838 2086.1849 0.2190361
P120-P90  590.4875 -619.23414 1800.2091 0.5734856
P180-P90  923.8200 -285.90164 2133.5416 0.1806593
P90_T-P90  278.5833 -931.13838 1488.3049 0.9507229
P180-P120  333.3325 -876.38914 1543.0541 0.9101472
P90_T-P120 -311.9042 -1521.62588  897.8174 0.9277454
P90_T-P180 -645.2367 -1854.95838  564.4849 0.4924298

> confint(fm.aov)
              2.5 %    97.5 %
(Intercept) 68726.77083 69907.659
PauseP90    -237.13415 1432.894
PauseP120    353.35335 2023.382
PauseP180    686.68585 2356.714
PauseP90_T    41.44911 1711.477

```

Yield Stress family-wise comparison of means

```

Tukey multiple comparisons of means
 95% family-wise confidence level

Fit: aov(formula = Tempstudy$yeild.stress ~ Tempstudy$Pause)

$`Tempstudy$Pause`
      diff      lwr      upr    p adj
P90-P30  964.285 -3040.950 4969.52008 0.9426165
P120-P30  556.655 -3448.580 4561.89008 0.9921753
P180-P30 1927.190 -2078.045 5932.42508 0.5861479
P90_T-P30 -2127.491 -6132.727 1877.74365 0.4962852
P120-P90  -407.630 -4412.865 3597.60508 0.9976362
P180-P90  962.905 -3042.330 4968.14008 0.9428955
P90_T-P90 -3091.776 -7097.012  913.45865 0.1732944
P180-P120 1370.535 -2634.700 5375.77008 0.8251775
P90_T-P120 -2684.146 -6689.382 1321.08865 0.2824344
P90_T-P180 -4054.681 -8059.917  -49.44635 0.0465667

> confint(fm.aov)
              2.5 %    97.5 %
(Intercept) 47490.5642 51400.3358
Tempstudy$PauseP90 -1800.3411 3728.9111
Tempstudy$PauseP120 -2207.9711 3321.2811
Tempstudy$PauseP180  -837.4361 4691.8161
Tempstudy$PauseP90_T -4892.1175  637.1346

```

ER308: Temperature Study

UTS family-wise comparison of means

```
Tukey multiple comparisons of means
95% family-wise confidence level

Fit: aov(formula = UTS ~ Pause, data = TempStudy)

$Pause
      diff      lwr      upr    p adj
P90-P30 -0.12660847 -3.286242 3.033025 0.9993626
P120-P30 -0.73220155 -3.891835 2.427432 0.8997016
P180-P30  0.04531278 -3.114321 3.204946 0.9999706
P120-P90 -0.60559307 -3.765227 2.554040 0.9394156
P180-P90  0.17192125 -2.987712 3.331555 0.9984129
P180-P120 0.77751432 -2.382119 3.937148 0.8829822

> confint(fm.aov)
      2.5 %    97.5 %
(Intercept) 85.100071 88.379332
PauseP90    -2.445396  2.192179
PauseP120   -3.050989  1.586586
PauseP180   -2.273474  2.364100
```

Yield Stress family-wise comparison of means

```
Tukey multiple comparisons of means
95% family-wise confidence level

Fit: aov(formula = TempStudy$YS ~ TempStudy$Pause)

$`TempStudy$Pause`
      diff      lwr      upr    p adj
P90-P30  0.1260911 -1.635270 1.8874521 0.9964177
P120-P30 -1.1283379 -2.889699 0.6330231 0.2777053
P180-P30 -0.6813009 -2.442662 1.0800601 0.6683612
P120-P90 -1.2544290 -3.015790 0.5069320 0.2033762
P180-P90 -0.8073920 -2.568753 0.9539690 0.5448930
P180-P120 0.4470370 -1.314324 2.2083980 0.8734627

> confint(fm.aov)
      2.5 %    97.5 %
(Intercept) 50.294314 52.1223619
TempStudy$PauseP90 -1.166534  1.4187162
TempStudy$PauseP120 -2.420963  0.1642872
TempStudy$PauseP180 -1.973926  0.6113242
```

ER308: Long Wall

UTS: Longitudinal vs. Transverse

Two-Sample T-Test and CI: UTS_T, UTS_L

Method

μ_1 : mean of UTS_T

μ_2 : mean of UTS_L

Difference: $\mu_1 - \mu_2$

Equal variances are assumed for this analysis.

Descriptive Statistics

Sample	N	Mean	StDev	SE Mean
UTS_T	6	82.60	1.46	0.60
UTS_L	4	89.464	0.433	0.22

Estimation for Difference

Difference	Pooled StDev	95% CI for Difference
-6.864	1.184	(-8.626, -5.101)

Test

Null hypothesis $H_0: \mu_1 - \mu_2 = 0$

Alternative hypothesis $H_1: \mu_1 - \mu_2 \neq 0$

T-Value	DF	P-Value
-8.98	8	0.000018852

Yield Strength: Longitudinal vs. Transverse

Two-Sample T-Test and CI: YS_T, YS_L

Method

μ_1 : mean of YS_T
 μ_2 : mean of YS_L
 Difference: $\mu_1 - \mu_2$

Equal variances are assumed for this analysis.

Descriptive Statistics

Sample	N	Mean	StDev	SE Mean
YS_T	6	49.84	2.30	0.94
YS_L	4	53.398	0.799	0.40

Estimation for Difference

Difference	Pooled StDev	95% CI for Difference
-3.56	1.88	(-6.36, -0.76)

Test

Null hypothesis $H_0: \mu_1 - \mu_2 = 0$
 Alternative hypothesis $H_1: \mu_1 - \mu_2 \neq 0$

T-Value	DF	P-Value
-2.94	8	0.019

Toughness: Longitudinal vs. Transverse

Two-Sample T-Test and CI: Toughness_T, Toughness_L

Method

μ_1 : mean of Toughness_T
 μ_2 : mean of Toughness_L
 Difference: $\mu_1 - \mu_2$

Equal variances are assumed for this analysis.

Descriptive Statistics

Sample	N	Mean	StDev	SE Mean
Toughness_T	6	426.1	24.2	9.9
Toughness_L	4	418.5	28.1	14

Estimation for Difference

Difference	Pooled StDev	95% CI for Difference
7.6	25.7	(-30.7, 46.0)

Test

Null hypothesis $H_0: \mu_1 - \mu_2 = 0$
 Alternative hypothesis $H_1: \mu_1 - \mu_2 \neq 0$

T-Value	DF	P-Value
0.46	8	0.658

Aluminum Yield Stress, Transverse vs. Longitudinal

Two-Sample T-Test and CI: YS_T, YS_L

Method

μ_1 : mean of YS_T
 μ_2 : mean of YS_L
 Difference: $\mu_1 - \mu_2$

Equal variances are assumed for this analysis.

Descriptive Statistics

Sample	N	Mean	StDev	SE Mean
YS_T	3	14136	945	546
YS_L	5	15775	1332	596

Estimation for Difference

Difference	Pooled StDev	95% CI for Difference
-1639	1217	(-3813, 536)

Test

Null hypothesis $H_0: \mu_1 - \mu_2 = 0$
 Alternative hypothesis $H_1: \mu_1 - \mu_2 \neq 0$

T-Value	DF	P-Value
-1.84	6	0.115

Aluminum UTS, Transverse vs. Longitudinal

Two-Sample T-Test and CI: UTS_T, UTS_L

Method

μ_1 : mean of UTS_T
 μ_2 : mean of UTS_L
 Difference: $\mu_1 - \mu_2$

Equal variances are assumed for this analysis.

Descriptive Statistics

Sample	N	Mean	StDev	SE Mean
UTS_T	3	24326.5	53.6	31
UTS_L	5	24465	635	284

Estimation for Difference

Difference	Pooled StDev	95% CI for Difference
-138	520	(-1067, 791)

Test

Null hypothesis $H_0: \mu_1 - \mu_2 = 0$
 Alternative hypothesis $H_1: \mu_1 - \mu_2 \neq 0$

T-Value	DF	P-Value
-0.36	6	0.729

Appendix V: Weld Wire Data Sheets

AWS A5.9 ER308L

Quote This

ER308L or **Alloy 308L** has the same analysis as type 308 except the carbon content has been held to a maximum of .03% to reduce the possibility of intergranular carbide precipitation. Balanced chromium and nickel levels provide enough ferrite in the weld for high resistance to hot cracking.

ER308L Applications

ER308L is used to weld metals with similar composition, such as 304L in wrought and cast forms. Ideal for welding Types 304L, 321, and 347 stainless steels. This is a suitable wire for applications at cryogenic temperatures.

Specifications:

- AWS A5.9 ER308L
- UNS S30880

Nominal Chemistry Composition (%)								
C	Cr	Ni	Mn	Si	P	S	Mo	Cu
0.03 max	19.5-22.0	9.0-11.0	1.0-2.5	0.30-0.65	0.03 max	0.03 max	0.75 max	0.75 max

Mechanical Properties

Tensile Strength (psi) 87,000

Yield Strength (psi) 57,000

Elongation (no units) 34%



70S-6 Carbon Steel Welding Wire and Rod

U.S. ALLOY CO.
 dba Washington Alloy
 7010-G Reames Rd.
 Charlotte, NC 28216
www.weldinewire.com



ALLOY DESCRIPTION AND APPLICATION;

70S-6 is commonly a copper coated carbon steel that contains high levels of manganese and silicon for stronger deoxidizing power and has excellent welding results on mild steels where poor fit-up, rust and oils may be present.

TYPICAL GMAW WELDING PROCEDURES; DCEP Short Circuit ⁽¹⁾ 98Ar/2O₂

Wire Diameter	Wire Speed (ipm)	Amps	Volts	Travel speed (ipm)	CO ₂ (cfh)
0.023	80-350	30-85	14-19	10-15	20-25
0.030	110-340	40-130	15-20	12-24	20-25
0.035	100-520	60-235	16-25	11-40	20-30
0.045	70-270	90-290	18-23	12-22	25-35
<i>Spray</i> 0.035	320-600	160-300	23-26	11-22	⁽¹⁾ 25-35
0.045	170-550	170-375	23-29	12-21	⁽¹⁾ 25-35
1/16"	175-350	275-475	25-31	9-19	⁽¹⁾ 25-35

TYPICAL GTAW WELDING PROCEDURES; DCEN with EWTh-2 truncated conical tip

Filler Wire Size	Tungsten	Amps	Volts	Gas Cup Size	Argon (cfh)	Base thickness
1/16"	1/16"	100-160	12	3/8"	20	1/16-3/32"
1/16-3/32"	3/32"	120-250	12	3/8"	20	1/8- 3/16"
1/8"	1/8"	150-300	12	1/2"	25	1/4-1/2"

Procedures may vary with change in position, base metals, filler metals, equipment and other changes.

TYPICAL WIRE CHEMISTRY (%) AND WELD METAL PROPERTIES; 100%CO₂

	AWS Spec.	70S-6		AWS Spec	Typical
Carbon	0.06-0.15	0.10	Tensile Strength (psi)	70,000 min.	90,000
Manganese	1.40-1.85	1.70	Yield Strength (psi)	58,000 min.	73,000
Silicon	0.80-1.15	1.00	Elongation in 2"	22% min.	25%
Phosphorus	0.025 max.	0.010	Charpy V-notch at -20°F	20 ft-lbs min.	28 ft-lbs
Sulfur	0.035 max.	0.015	Reduction of area	n/a	60%
Copper contents and coating	0.5 max.		Average Brinell Hardness	n/a	160

AVAILABLE SIZES: TC 70S-6 = Spools of .023, .030, .035, .040, .045, .052, 1/16

TT 70S-6 = Cut lengths of .030, .035, .045, 1/16, 3/32, 1/8, 5/32

SPECIFICATIONS; ANSI/AWS A5.18 ER 70S-6

ASME SFA 5.18 ER 70S-6

EAST COAST
 7010-G Reames Rd
 Charlotte, NC 28216
 Tel (888) 522-8296
 Fax (704)598-6673

GULF COAST
 4755 Alpine Drive #100A
 Stafford, TX 77477
 Tel (877) 711-9274
 Fax (281)313-6332

WEST COAST
 8535 Utica Ave
 Rancho Cucamonga, CA 91730
 Tel(800)830-9033
 Fax (909)291-4586



dc2012

Warehouse Distribution Center – Dayton, Ohio

Head Office – Puyallup, Washington

Washington Alloy Company believes that all information and data given is correct. Use this information to assist in making your own evaluations or decisions and this information should not be mistaken as an expressed or implied warranty. U.S. ALLOY CO. assumes no liability for results or damages incurred from the use of any information contained herein, in whole or in part.

ALLOY 4043 WELD DATA SHEET

TYPICAL APPLICATIONS

- Welding Filler Wire
- Spray and Flame Metallizing Wire

GENERAL INFORMATION

- Trade Designation: Almigweld and Altigweld
- Non-Heat treatable
- Similar to AISi5 (Germany), BS N21 (United Kingdom)
- EN ISO 18273 designation AISi5
- Principle alloying element: Silicon
- Applicable specifications: ANSI/AWS A5.10 (ER & R), AMS 4190 (Chemistry Only)

WELDING APPROVALS

- Canadian Welding Bureau Lloyd's Register
- CE DB

TYPICAL PROPERTIES

Melting range: 1065 - 1170°F Resistance to corrosion: B (Gen) A (SCC)
 Conductivity: 42 % IACS (-O) Anodize Color: Gray
 Density: .097 lbs./cu. in.

CHEMISTRY

SILICON	IRON	COPPER	MANGANESE	MAGNESIUM	CHROMIUM	ZINC	TITANIUM	BERYLLIUM	OTHERS		ALUM REM
									EACH	TOTAL	
4.5-6.0	0.8	0.30	0.05	0.05	—	0.10	0.20	0.0003	0.05	0.15	

NOTE: SINGLE VALUES ARE MAXIMUM UNLESS OTHERWISE NOTED.

TYPICAL MECHANICAL PROPERTIES OF GTAW GROOVE JOINT WELDS

BASE ALLOY	BASE ALLOY PROPERTIES			AS WELDED			POSTWELD HEAT-TREATED AND AGED ¹		
	UTS (KSI)	UYS (KSI)	ELONG (%)	UTS (KSI)	UYS (KSI)	ELONG (%)	UTS (KSI)	UYS (KSI)	ELONG (%)
2014-T6	70	60	13	34	26	4	50	—	2
6061-T4	35	21	22	27	18	8	35 ²	—	8 ²
6061-T6	45	40	12	27	18	8	44	40	5
6063-T4	25	22	22	20	10	12	30	—	13

(1) REQUIRES SUFFICIENT DILUTION OF BASE METAL INTO WELD POOL FOR HEAT TREAT AND/OR AGE RESPONSE. REFER TO ALCOTECHNIC CONCERNING ALLOY 4643 FOR ADDITIONAL INFORMATION

(2) POSTWELD AGED ONLY.

ALLOY CHARACTERISTICS

ALLOY 4043 IS ONE OF THE OLDEST AND MOST WIDELY USED WELDING AND BRAZING ALLOYS. Almigweld AND Altigweld 4043 CAN BE CLASSIFIED AS A GENERAL PURPOSE TYPE FILLER ALLOY. THE SILICON ADDITIONS RESULT IN IMPROVED FLUIDITY (WETTING ACTION) TO MAKE THE ALLOY A PREFERRED CHOICE BY WELDERS. THE ALLOY IS LESS SENSITIVE TO WELD CRACKING AND PRODUCES BRIGHTER, ALMOST SMUT FREE WELDS.

Typical Semiautomatic GMA Procedures for Fillet and Lap Welding Aluminum

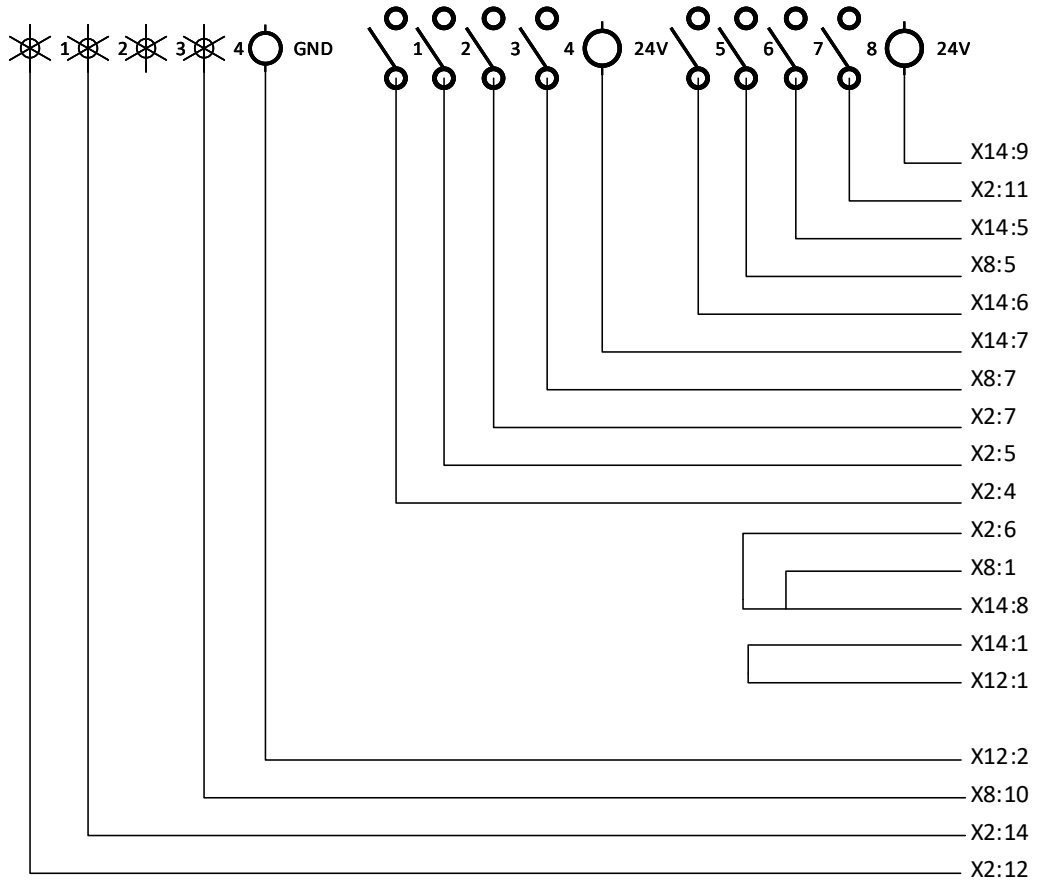
Wire Dia Inches	DC(EP) ³ Range		Base ¹ Thickness Inches	DC(EP) Suggested		Wire Feed IPM	Argon Gas Flow CFH	Approximate Consumption ² Lbs/100Ft
	Amps	Volts		Amps	Volts			
.030	100-130	18-22	.094	100	22	500	30	0.75
	125-150	20-24	.125	120	22	600	30	1
.035	85-120	20-23	.094	110	22	480	30	0.75
	125-150	20-24	.125	130	22	568	30	1
	170-190	21-26	.250	170	23	740	35	4
.047	125-150	20-24	.125	150	23	380	30	1
	180-210	22-26	.187	180	23	410	30	2.3
	170-240	24-28	.250	190	24	470	40	4
.062	190-260	21-26	.250	200	23	285	50	4
	240-300	22-27	.375	230	24	300	50	9
	260-310	22-27	.500	260	26	340	60	16
	280-320	24-28	.750	280	27	385	65	36
	290-340	26-30	1.000	300	28	420	70	64
.094	280-360	26-30	.750	320	29	170	60	36
	300-400	26-32	1.000	330	30	180	80	64

1. Metal thickness of 3/4" or greater for fillet welds sometimes employs a double vee bevel of 50 deg or greater included vee with 3/32 to 1/8 inch land thickness on the abutting member.
2. Electrode consumption given for weld on one side only and based on leg length equal to plate thickness.
3. For 5XXX series electrodes use a welding current in the high side of the range given and an arc voltage in the lower portion of the range. 1XXX, 2XXX, and 4XXX series electrodes would use the lower currents and higher arc voltages.

THIS INFORMATION IS BASED ON DATA DEVELOPED UNDER LABORATORY CONDITIONS AND IS DESIGNED AS A GUIDELINE ONLY. INDIVIDUAL CONDITIONS, WELDING EQUIPMENT AND ENVIRONMENT CAN AFFECT SUGGESTED SETTINGS.

Appendix VI: Wiring Diagram

Sealevel RS-485 Modbus RTU



ROB 5000